



UNIVERSITY of
TASMANIA



IMAS
INSTITUTE FOR MARINE
& ANTARCTIC STUDIES



Manganese biogeochemistry in the Southern Ocean

By

Pauline Marie Aurélie Latour (BSc, MSc)

Under the supervision of Andrew R. Bowie, Kathrin Wuttig, Pier van der Merwe and

Robert F. Strzepek

This thesis is submitted in fulfillment of the requirements for the degree of

Doctor of Philosophy

Institute of Marine and Antarctic Studies,
University of Tasmania

July, 2022

“I walk around like everything is fine, but deep down, inside my shoe, my sock is sliding off.”

– Unknown source–

Here’s to 3 years and 9 months of struggle, joy and intense learning.

Statements and declarations

Declaration of originality

I, Pauline Latour, declare that this thesis entitled, “Manganese biogeochemistry in the Southern Ocean” contains no material that has been accepted for a degree or diploma by the University or any other institution, except by way of background information and duly acknowledged in this thesis and to the best of my knowledge and belief, no material previously published or written by another person except where due acknowledgement is made in the text of the thesis, nor does this thesis contain material that infringes copyright.

Signed:

(Pauline Latour)

Date: January 27, 2022

Statement of authority of access

This thesis may be made available for loan and limited copying and communication in accordance with the Copyright Act 1968.

Signed:

(Pauline Latour)

Date: January 27, 2022

Statement regarding published work contained within the thesis

The publisher of the paper comprising Chapter 1 holds the copyright for that content and access to that material should be sought from this journal. The remaining nonpublished content of the thesis may be made available for loan and limited communication in accordance with the copyright Act 1968.

Signed:

(Pauline Latour)

Date: January 27, 2022

Publications results from research completed during candidature

Published or in preparation

Latour, P.; Wuttig, K.; van Der Merwe, P.; Strzepek, R. F.; Gault-Ringold, M.; Townsend, A. T.; Holmes, T. M. ; Corkill, M. & Bowie, A. R. (2021). **Manganese biogeochemistry in the Southern Ocean, from Tasmania to Antarctica**. *Limnology and Oceanography*, [Doi 10.1002/lno.11772](https://doi.org/10.1002/lno.11772)

Latour, P.; van Der Merwe, P.; Wuttig, K.; Corkill, M.; Townsend, A. T.; M.; Holmes, T. M.; Rintoul, S. R.; Schlitzer, R.; Weldrick, C.; Noble, T. L.; Strzepek, R. F.; Gault-Ringold, & Bowie, A. R. (2022). **Biological uptake, water mass dilution and scavenging prevent transport of manganese-rich waters from the Antarctic shelf**. *Submitted to Global Biogeochemical Cycles*.

Latour, P.; Strzepek, R. F.; Wuttig, K.; van Der Merwe, P.; Eggins, S.; Bach, L.; Boyd, P.; Ellwood, M. J. & Bowie, A. R. (2022). **Seasonality of phytoplankton growth limitation by iron and manganese in subantarctic waters**. Published as a preprint: <https://doi.org/10.1002/essoar.10511502.1>; also in review in *Frontiers in Marine Science*.

Latour, P.; Eggins, S.; van Der Merwe, P.; Bach, L.; Boyd, P.; Ellwood, M. J.; Wuttig, K.; Bowie, A. R. & Strzepek, R. F. (*in prep*). **Characterization of a Southern Ocean deep chlorophyll maximum: responses of phytoplankton to light, iron and manganese**.

Statement of co-authorship

The following people and institutions contributed to the publication of work undertaken as part of this thesis.

Paper 1: Manganese biogeochemistry in the Southern Ocean, from Tasmania to Antarctica: Located in Chapter 2

Pauline Latour – Institute for Marine and Antarctic Studies (IMAS), University of Tasmania
Kathrin Wuttig – Antarctic Climate and Ecosystems Cooperative Research Centre (ACE CRC)
Pier van der Merwe – Institute for Marine and Antarctic Studies, University of Tasmania
Robert F. Strzpek – Antarctic Climate and Ecosystems Cooperative Research Centre (ACE CRC); Antarctic Gateway Partnership (AGP), University of Tasmania; Australian Antarctic Program Partnership (AAPP), University of Tasmania
Melanie Gault-Ringold – Antarctic Climate and Ecosystems Cooperative Research Centre (ACE CRC)
Ashley T. Townsend – Central Science Laboratory (CSL), University of Tasmania, Hobart
Thomas M. Holmes – Antarctic Climate and Ecosystems Cooperative Research Centre (ACE CRC)
Matthew Corkill – Institute for Marine and Antarctic Studies (IMAS), University of Tasmania
Andrew R. Bowie – Institute for Marine and Antarctic Studies (IMAS), University of Tasmania

Author contributions

PL, KW, PvdM, MGR, TMH, MC and ARB collected the data. PL, KW, PvdM, MGR, TMH, MC analysed the samples. PL, KW, PvdM, RFS and ARB worked on the data interpretation. The manuscript was written by PL and reviewed by all authors. ARB secured funding for field work and sample analysis.

Paper 2: Biological uptake, water mass dilution and scavenging prevent transport of Mn-rich waters from the Antarctic shelf: Located in Chapter 3

Pauline Latour – Institute for Marine and Antarctic Studies (IMAS), University of Tasmania
Pier van der Merwe – Institute for Marine and Antarctic Studies, University of Tasmania
Kathrin Wuttig – Antarctic Climate and Ecosystems Cooperative Research Centre (ACE CRC)
Matthew Corkill – Institute for Marine and Antarctic Studies (IMAS), University of Tasmania
Ashley T. Townsend – Central Science Laboratory (CSL), University of Tasmania, Hobart
Thomas M. Holmes – Antarctic Climate and Ecosystems Cooperative Research Centre (ACE CRC)
Steve R. Rintoul – Australian Antarctic Program Partnership (AAPP), University of Tasmania; CSIRO Oceans & Atmosphere
Reiner Schlitzer – Alfred Wegener Institute for Polar and Marine Research
Christine Weldrick – Australian Antarctic Program Partnership (AAPP), University of Tasmania
Taryn L. Noble – Institute for Marine and Antarctic Studies (IMAS), University of Tasmania
Robert F. Strzpek – Antarctic Climate and Ecosystems Cooperative Research Centre (ACE CRC); Antarctic Gateway Partnership (AGP), University of Tasmania; Australian Antarctic Program Partnership (AAPP), University of Tasmania
Melanie Gault-Ringold – Antarctic Climate and Ecosystems Cooperative Research Centre (ACE CRC)
Andrew R. Bowie – Institute for Marine and Antarctic Studies (IMAS), University of Tasmania

Author contributions

PL, KW, PvdM, MGR, TMH, MC, CW and ARB collected the data. PL, KW, PvdM, MGR, TMH, MC analysed the samples. SRR, RS and TLN helped for specific data analyses. PL, PvdM, KW, MC, SRR and ARB worked on the data interpretation. The manuscript was written by PL and reviewed by all authors. ARB secured funding for field work and sample analysis.

Paper 3: Seasonality of phytoplankton growth limitation by iron and manganese in subantarctic waters: Located in Chapter 4

Pauline Latour – Institute for Marine and Antarctic Studies, University of Tasmania
Robert F. Strzpek – Antarctic Climate and Ecosystems Cooperative Research Centre (ACE CRC); Antarctic Gateway Partnership (AGP), University of Tasmania; Australian Antarctic Program Partnership (AAPP), University of Tasmania
Kathrin Wuttig – Antarctic Climate and Ecosystems Cooperative Research Centre (ACE CRC)

Pier van der Merwe – Institute for Marine and Antarctic Studies, University of Tasmania
Sam Eggs – Research School of Earth Sciences, Australian National University
Lennart Bach – Institute for Marine and Antarctic Studies, University of Tasmania
Philip Boyd – Institute for Marine and Antarctic Studies (IMAS), University of Tasmania
Michael J. Ellwood - Research School of Earth Sciences, Australian National University
Terry Pinfold - Menzies Research Institute Tasmania, University of Tasmania
Andrew R. Bowie - Institute for Marine and Antarctic Studies (IMAS), University of Tasmania

Author contributions

Experiments were designed by RFS and PL. PL, RFS, SE and MJE collected the data and analysed the samples. LB and TP helped for specific sample and data analyses. PL, RFS, PvdM, and KW worked on the data interpretation. The manuscript was written by PL and reviewed by all authors. Funding for field work and sample analysis was secured by RFS, ARB and PB.

Paper 4: Characterization of a Southern Ocean deep chlorophyll maximum: responses of phytoplankton to light, iron and manganese: Located in Chapter 5

Pauline Latour – Institute for Marine and Antarctic Studies, University of Tasmania
Sam Eggs – Research School of Earth Sciences, Australian National University
Pier van der Merwe – Institute for Marine and Antarctic Studies, University of Tasmania
Lennart Bach – Institute for Marine and Antarctic Studies, University of Tasmania
Philip Boyd – Institute for Marine and Antarctic Studies (IMAS), University of Tasmania
Michael J. Ellwood - Research School of Earth Sciences, Australian National University
Kathrin Wuttig – Antarctic Climate and Ecosystems Cooperative Research Centre (ACE CRC)
Andrew R. Bowie - Institute for Marine and Antarctic Studies (IMAS), University of Tasmania
Robert F. Strzpek – Antarctic Climate and Ecosystems Cooperative Research Centre (ACE CRC); Antarctic Gateway Partnership (AGP), University of Tasmania; Australian Antarctic Program Partnership (AAPP), University of Tasmania

Author contributions

The experiment was designed by RFS, PB, MJE, SE and PL. PL, RFS, SE and MJE collected the data and analysed the samples. LB helped for specific sample and data analyses. PL, RFS and PvdM, worked on the data interpretation. The manuscript was written by PL and reviewed by all authors. Funding for field work and sample analysis was secured by PB, RFS and MJE.

We the undersigned agree with the above stated “proportion of work undertaken” for each of the above published peer-reviewed manuscripts contributing to this thesis:

Pauline Latour

Candidate
IMAS
University of Tasmania

Date: 27/01/2022

Andrew R Bowie

Primary Supervisor
IMAS
University of Tasmania

Date: 27/01/2022

Pete Strutton

Head of School
IMAS
University of Tasmania

Date: 27/01/2022

General abstract

Manganese biogeochemistry in the Southern Ocean

By Pauline Latour (University of Tasmania)

Manganese (Mn) is a redox-active metal essential for most life on Earth. In photosynthetic microalgae (phytoplankton), Mn is used in the oxygen evolving complex of photosystem II, and in the superoxide dismutase enzyme to detoxify reactive oxygen species. Thus, phytoplankton have a strict Mn requirement for growth. In the Southern Ocean, the largest High-Nutrient Low-Chlorophyll (HNLC) region, phytoplankton growth is strongly limited by the micronutrient iron (Fe), but recent evidence shows Mn can (co-)limit phytoplankton growth in both coastal and open ocean regions. These results conflict with earlier studies that found Mn levels in Southern Ocean waters were sufficient to support phytoplankton growth. Hence, there is a need to constrain the distribution of Mn in Southern Ocean waters, to describe its sources and sinks and to identify potential regions of limitation. Here, we aim to tackle this problem by firstly describing Mn distribution along a meridional transect between Tasmania and Antarctica. Secondly, we study the zonal distribution of Mn near major Antarctic coastal sources with a focus on the northward supply of fertilised waters into HNLC waters. Finally, we use ship-based bioassays to test Mn limitation of Southern Ocean phytoplankton in subantarctic and polar waters.

Manganese concentrations were measured in the Australian sector of the Southern Ocean, following the GEOTRACES-SR3 meridional transect, from Tasmania (Australia) to Antarctica. Manganese distribution was related to two external sources: sediment and hydrothermal inputs. We found both dissolved and particulate Mn concentrations were extremely low along this transect, despite strong inputs from Tasmanian and Antarctic shelf sediments, and hydrothermal vents. The presence of a cold-core eddy induced upward movement of Mn enriched waters. However, this enrichment did not reach surface waters where it could fertilize Mn depleted waters.

At the southern end of the SR3 section, we studied the potential export of Mn-enriched shelf waters to Southern Ocean open waters. This was done in the context of the complex oceanography near the shelf break. We found that despite high Mn concentrations present on the shelf (> 0.25 nM), export toward depleted open waters was limited. This was due to three processes: biological uptake decreased dissolved Mn concentrations in surface waters while dilution of Mn-rich Antarctic Bottom Waters with Mn-depleted Low Circumpolar Deep Water and scavenging processes decreased concentrations in bottom waters. The latter finding was unexpected considering elevated Mn concentrations are commonly observed near the seafloor, implying constant sediment inputs and increase of Mn concentrations in bottom waters. However, additional bottom water measurements remain necessary to evaluate Mn oxidation rates.

As very low surface dissolved Mn concentrations were observed in this region, we performed repeated field bioassays in subantarctic waters to study the seasonality of Fe- and Mn (co-)limitation. To the best of our knowledge, only one other study has looked at Fe- and Mn (co-)limitation in subantarctic waters, and no other study has looked at the potential seasonality of this limitation. To evaluate this, surface seawater was incubated with additions of Fe and Mn in austral spring, summer, and autumn. After eight days of incubation, we collected samples for macronutrient concentrations, photophysiology, phytoplankton community composition measured by flow cytometry, and Fe/carbon uptake. We found no clear signal of Mn limitation at any season. However, we observed strong seasonality in Fe and silicic acid limitation of phytoplankton growth. Iron limited phytoplankton growth in summer while silicic acid levels limited diatom growth in autumn. In spring, neither Fe nor silicic acid limited phytoplankton growth. Carbon uptake measurements suggested a slight stimulation by Mn in both spring and summer. In spring, the combined addition of Fe and Mn resulted in significant carbon uptake stimulation in the medium size class (composed of multiple species: small diatoms, cyanobacteria and prymnesiophytes). Similarly, during the summer, only the addition of both Fe and Mn led to significantly higher carbon uptake in the large size class (comprised primarily of large diatoms and/or dinoflagellates), indicating that only part of the community may have been (co-)limited by Mn. This latter result suggests Mn limitation may be missed during conventional field bioassays.

We repeated the subantarctic field experiment south of the Polar Front to study the response of the phytoplankton community collected from a deep chlorophyll maximum to increases in light, Fe and Mn conditions. To the best of our knowledge, no other study has looked at Mn limitation of phytoplankton growth in deep chlorophyll maxima. We tested the hypothesis that phytoplankton Mn requirement may vary with changing light or Fe conditions. Seawater was collected from a diatom-dominated deep chlorophyll maximum and incubated at ambient and elevated irradiances (1 and 12% of incident irradiance, respectively). We observed that the community was primarily light limited. Once light limitation was alleviated Fe became the limiting factor and adding Fe primarily stimulated the growth of large diatoms. We did not observe evidence of Mn limitation, suggesting natural Mn levels (0.33 nM) were sufficient to support phytoplankton growth. However, we observed a small shift in phytoplankton community composition when both Fe and Mn were added, indicating that some phytoplankton species, within the nanoeukaryote size class, may have benefited from Mn additions.

In conclusion, this work described the first set of dissolved and particulate Mn concentrations along a full depth meridional transect in the Australian sector of the Southern Ocean where trace metal (especially Mn) datasets are limited. Low Mn levels observed across the transect contrasted with potential inputs from the Antarctic shelf. However, we conclude that the export of Mn from the East Antarctic shelf adjacent to open waters was limited by biological uptake, water masses mixing and scavenging processes. We tested the hypothesis that low Mn concentrations limit phytoplankton growth in subantarctic waters with a potential seasonal variability. No seasonal signal of Mn (co-)limitation

was observed at the subantarctic site. However, we did observe some responses to Mn addition: stimulation of carbon uptake and phytoplankton communities shifts that indicated Mn may control the primary productivity of a sub-set of phytoplankton taxa. In addition, we investigated the hypothesis that Mn may limit phytoplankton growth from a polar deep chlorophyll maximum. Again, no clear signal of Mn limitation was observed but subtle responses suggested some population benefited from Mn additions. Overall, identifying limiting parameters of phytoplankton growth remains essential to predict the future evolution of the ocean carbon cycle. Our results suggest Mn (co-)limitation is nuanced and may be hard to capture, particularly when Fe limits much of the phytoplankton community. This points to the need for further study on the Mn requirements of Southern Ocean phytoplankton and their interaction with other variables such as light and Fe.

Acknowledgements

It is with great sentiment that I would like to thank all the people that helped and supported me both prior to and during my PhD, it was surely an exciting and intense adventure.

I first would like to thank my supervisory team, without whom this work would not have been possible. Four years ago, I arrived in Tassie to participate to a research voyage. This is when my Australian adventure began. Andy, I owe you a huge thanks for giving me a chance at this PhD, especially considering I had no skills in trace metal work, and for allowing me to customise the direction of this project to my preference. I really appreciate the opportunities this PhD has given me! Pier, while it took me a while to understand your accent at first, I thank you for your constant support and availability which made this work much more enjoyable. Being part of the sunrise shift with you, Christine, and Tom during SR3 has been an amazing experience and was a pivoting point in my choice to stay here for a PhD. For this, I am extremely grateful. Kathrin, your guidance as the “Mn supervisor” has been amazing, even from another continent. Thank you so much for your patience in the lab when I started, but also for being so motivated to talk about this *under-loved* element. Robert, I am so glad I was encouraged to come and see you for a potential collaboration. I hope that almost 4 years later, after many meetings, field, and lab hours you are still as excited to be part of the team. I surely know that my thesis would have been very different without you. I thank you for your eternal patience, support and company on the boat. I feel very lucky to have participated to three voyages with you, and I strongly hope there will be more (on the Nuyina?).

During this PhD, I participated to four voyages, resulting in almost five months at sea. I feel extremely lucky to have had so much field work and would like to thank the people who made this possible: my supervisory team, of course, for allowing me to go but also Philip Boyd for welcoming me on SOTS2019 and SOLACE. These times at sea would not have been the same without the scientists, crew people and MNF organization; thanks for making these times memorable. In addition, some of this work would not have been complete without extra help, thanks Sam, Michael, Pam, Rob, the hydrochem team and Svenja (for moral support on 3 voyages!). Pam, thank you so much for your eternal patience for all (too many) lab-related questions and chat. Ash and Delphine, even without being part of my supervisory team you always made time to have a chat when I needed it and your inputs has always been extremely helpful, thank you so much. Wen, having your inputs on all the side-administrative work was a great help during this PhD, thank you for all your patience and time.

I also would like to give a special thanks to my partner, Floriaan. Being both simultaneously at the end of our PhDs was not easy but you have been my rock. Of course, I could not go without thanking my Tassie family. Doing a PhD abroad is already not easy but adding a pandemic on top of it surely made it ‘memorable’. Without these people, my time in Tassie would not have been the same: Layla, Noémie, Abi, Romain, Sam, Matt, Ghom, Yannick, Emiliano, Cristina, Sahan, Nick, Teleah, Katy, Laurent, Rita,

Eric, Jake, Paolo, Phil, Tina, Ole, Vero. Special thanks to la baguette & the triplettes, spending time with you have made me feel at home and I am so grateful for this. Abi, it goes without saying that this PhD would have been much harder without you as my trace metal PhD buddy. Cristina, I also want to give you a special thanks for supporting me throughout the thesis and increase my love for chemistry or, as you call it, 'magic'. In addition, big thanks to the people who took the time to read and correct this thesis: Layla, Noémie, Samantha, Matt, Sahan, Romain, Floriaan, Nick, Abi and Katy.

Far from view but close to the heart: Louise, Victor, Lucile, Mathou and Myrtille; you have provided me with great support from distance. I am grateful we found time for each other in this awkward time zone difference.

Finally, I would like to thank my family for their constant support. My two brothers, Philippe and Fabrice, my godmother, Marie, and my cousins, Lynda and Francois, who supported my move to Tassie but also for your excitement and support when I learned this exciting news of a PhD on the other side of the planet. The pandemic has made the distance particularly difficult, but you all guided me at distance. *Dad*, I wish you were still present to see me coming through this final study step. *Maman*, I would never be the person I am today without your constant support; you have never doubted me and you have provided me with unconditional support and reassurance in all my choices, this thesis is for you.

Table of content

List of figures.....	XIV
List of tables.....	XIX
List of abbreviations.....	XXI
1. CHAPTER 1 – General introduction, aims and thesis structure	1
1.2. The evolution of early life and Earth’s oceans	1
1.3. The Southern Ocean	3
1.4. Factors limiting phytoplankton growth in the Southern Ocean	5
1.5. Oceanic manganese distribution.....	7
1.6. Manganese speciation	12
1.7. Phytoplankton Mn requirements	14
1.8. Thesis objectives and structure.....	16
2. CHAPTER 2 – Manganese biogeochemistry in the Southern Ocean, from Tasmania to Antarctica.....	19
2.1. Introduction	19
2.2. Material and methods	21
2.2.1. <i>SAMPLING</i>	21
2.2.2. <i>TRACE-METAL SAMPLE PROCESSING</i>	22
2.2.3. <i>HYDROGRAPHIC DATA AND MACRONUTRIENTS</i>	23
2.2.4. <i>TRACE METAL PRECONCENTRATION AND ANALYSIS</i>	23
2.2.5. <i>STATISTICAL ANALYSIS</i>	24
2.3. Results and discussion.....	24
2.3.1. <i>HYDROGRAPHY</i>	24
2.3.2. <i>UNIFORMLY LOW MN CONCENTRATIONS</i>	27
2.3.3. <i>BIOLOGICAL CONTROL OF SURFACE DISSOLVED MN</i>	30
2.3.4. <i>MN REINTRODUCTION IN THE SYSTEM</i>	34
2.4. Conclusion.....	40
3. CHAPTER 3 – Biological uptake, water mass dilution and scavenging prevent transport of manganese-rich waters from the Antarctic shelf	41
3.1. Introduction	41
3.2. Material and methods	43
3.2.1. <i>SAMPLING AREA</i>	43
3.2.2. <i>SAMPLE PROCESSING AND ANALYSIS</i>	44
3.2.3. <i>HYDROLOGY</i>	45
3.3. Results and discussion.....	45
3.3.1. <i>HYDROLOGY</i>	45
3.3.2. <i>MANGANESE CYCLE OF THE ADÉLIE AND GEORGE V LANDS</i>	47
3.4. Conclusion.....	56
4. CHAPTER 4 – Seasonality of phytoplankton growth limitation by iron and manganese in subantarctic waters	58
4.1. Introduction	58
4.2. Material and Methods.....	60

4.2.1. SAMPLING.....	60
4.2.2. ANALYSIS	62
4.2.3. STATISTICAL TESTS	63
4.3. Results.....	64
4.3.1. INITIAL HYDROGRAPHIC AND NUTRIENT CONDITIONS	64
4.3.2. MACRONUTRIENT DRAWDOWN	65
4.3.3. PHOTOPHYSIOLOGY	67
4.3.4. FLOW CYTOMETRY.....	68
4.3.5. IRON AND CARBON UPTAKE.....	70
4.4. Discussion	73
4.4.1. DIFFERING HYDROGRAPHIC CONDITIONS.....	73
4.4.2. SEASONALITY OF IRON LIMITATION.....	74
4.4.3. SIGNAL OF IRON-MANGANESE CO-LIMITATION.....	76
4.5. Conclusion.....	78
5. CHAPTER 5 – Characterization of a Southern Ocean deep chlorophyll maximum: responses of phytoplankton to light, iron and manganese.....	79
5.1. Introduction	79
5.2. Material and methods	81
5.2.1. EXPERIMENTAL SET UP.....	81
5.2.2. SAMPLE COLLECTION	83
5.2.3. SAMPLE ANALYSIS	84
5.2.4. STATISTICAL ANALYSES	85
5.3. Results.....	85
5.3.1. CHARACTERISTICS OF THE DCM	85
5.3.2. LOW AMBIENT DCM LIGHT TREATMENT.....	89
5.3.3. HIGH LIGHT TREATMENT	96
5.4. Discussion	98
5.4.1. LIGHT CONTROLS PHYTOPLANKTON GROWTH AT THE DCM	99
5.4.2. ONCE LIGHT SHINES, IRON LIMITS	100
5.4.3. RESPONSES TO MANGANESE ADDITIONS.....	101
5.5. Conclusion.....	103
6. CHAPTER 6 – Summary and future directions	105
6.1. Summary of key results.....	105
6.2. Significance of findings	106
6.2.1. NEW KNOWLEDGE REGARDING THE MANGANESE CYCLE.....	106
6.2.2. IMPORTANCE FOR GLOBAL CARBON CYCLE.....	107
6.3. Future directions.....	108
Appendices	111
References	138

List of figures

Figures are labelled according to Chapter and figure order within a chapter. For example, 'Figure 4.2' is Figure 2 in Chapter 4.

Figure 1.1: Structure of photosystem II from Sproviero et al. (2007). The oxygen evolving complex (OEC in illustration) has four Mn atoms, providing electrons during the step of water oxidation..... 2

Figure 1.2: Schematic representation of the reaction pathway from water to oxygen (photosynthesis) and oxygen to water (respiration) with intermediates reactive oxygen species: superoxide (O_2^-), hydrogen peroxide (H_2O_2) and hydroxyl radical ($HO\bullet$) from Wuttig 2013..... 3

Figure 1.3: Overview of the oceanic carbon pump from Chisholm (2000). This illustrates the biological carbon pump (left), including the transfer of carbon dioxide from the atmosphere into the ocean which is induced by phytoplankton photosynthesis and sinking organic matter and the solubility pump (right), consisting of mixing and equilibration between the ocean and atmosphere. 4

Figure 1.4: Map of surface chlorophyll-*a* distribution in the Southern Ocean, from Deppeler and Davidson (2017). Chlorophyll-*a* concentrations were measured by satellites (MODIS-Aqua from the austral summer season 2002/03 and 2015/16 at 9 km resolution). Oceanographic fronts (from Orsi et al. 1995) are indicated with black lines: Subtropical Front (STF), Subantarctic Front (SAF), Polar Front (PF) and Southern Antarctic Circumpolar Front (SACCF). 5

Figure 1.5: Typical depth profiles of Mn concentrations, observed in most ocean basins, published by Sunda and Huntsman (1988). a) Depth profiles of dissolved Mn (dMn) and b) particulate Mn (pMn) measured in the Sargasso Sea. 8

Figure 1.6: Sources and sinks of dissolved Mn (dMn) and particulate Mn (pMn) in the Southern Ocean. Both phases can be supplied by multiple sources: sediment resuspension, hydrothermal vents, glacial and sea-ice melting and aerosols depositions. Photoreduction of Mn oxides in surface waters may also increase dMn concentrations. However, this process has not yet been studied in the Southern Ocean waters. 11

Figure 1.7: Illustration of dMn and pMn depth profiles with expected internal reactions impacting Mn speciation and the distinction between the Southern Ocean and other ocean basins. The last panel shows real dMn concentrations measured in the Weddell Sea by Middag et al. (2013). Reactions showing a gain of dMn are shown with full arrows, reactions showing a loss of dMn are shown with dashed arrows. (1) photoreduction of MnOx, this reaction can be mediated by reactive oxygen species. (2) Biological uptake of dMn. (3) Oxidation of Mn(II) to MnOx, this reaction can be mediated by microbes or humic substances. (4) Scavenging of dMn onto MnOx or other particles. Near the seafloor, sediment (*or other sources such as hydrothermal inputs) can increase dMn and pMn concentrations..... 13

Figure 1.8: Map of GEOTRACES cruises in the Southern Ocean. The yellow, black and red lines indicate completed cruises, International Polar Year cruises and planned cruises, respectively. This map can be found at: https://www.bodc.ac.uk/geotraces/cruises/section_maps/southern_ocean/. In Chapters 2 and 3 of this thesis, we describe data collected along the GS01 transect (yellow line between Tasmania and Antarctica), sampled during the IN2018-V01 voyage onboard RV *Investigator*. 18

Figure 2.1: Chlorophyll-*a* map showing details of the stations sampled during IN2018-V01 along SR3. The coloured dots represent different station types. Black dots: shallow casts with high resolution (surface to 1500m depth); yellow dots: deep casts with lower resolution deep casts (surface to seafloor). Oceanographic fronts are indicated as: STF: Subtropical Front; SAF: Subantarctic Front; N-PF: North Polar Front; S-PF: South Polar Front; SACCF: Southern Antarctic Circumpolar Front. The background image colour shading represents satellite average Chlorophyll-*a* concentration data (MODIS-Aqua,

monthly average 4 km) for the period January-February 2018 (<https://giovanni.gsfc.nasa.gov/giovanni/#>)..... 21

Figure 2.2: Absolute salinity (A), conservative temperature (B), and oxygen (C) distribution along the 2018 SR3 transect. The colour represents the parameter value (absolute salinity, conservative temperature and oxygen). The contour lines represent the neutral densities ($\text{kg}\cdot\text{m}^{-3}$). Fronts: Subtropical Front (STF), Subantarctic Front (SAF), North-Polar Front (N-PF), South-Polar Front (S-PF) and Southern Antarctic Circumpolar Current Front (SAACF). Biogeochemical regions: Subtropical Zone (STZ), Subantarctic Zone (SAZ), the Polar Frontal Zone (PFZ), Polar Front Waters (PFW), Antarctic Zone (AZ) and Antarctic slope (AS). The extent of the Antarctic Circumpolar Current is indicated as ACC. Water masses: Antarctic Intermediate Water (AAIW), Upper and Lower Circumpolar Deep Water (UCDW – LCDW), Antarctic Surface Water (AASW) and Antarctic Bottom water (AABW). The arrows show a simplified flow. The red dotted rectangle indicates the position of a cyclonic eddy observed during the voyage. 26

Figure 2.3: Section of dissolved Mn (dMn) concentrations along the SR3 transect from North to South for 0-500 m (A) and 0-5000 m (B) and section of total particulate Mn (tot pMn) for 0-5000 m (C). Stations numbers are indicated at top (double numbers for super-stations). The bathymetry comes from the GEBCO_2014_Grid, version 20141103, <http://www.gebco.net>. Fronts: Subtropical Front (STF), Subantarctic Front (SAF), North-Polar Front (N-PF), South-Polar Front (S-PF) and South Antarctic Circumpolar Current Front (SAACF). Biogeochemical regions: Subtropical Zone (STZ), Subantarctic Zone (SAZ), the Polar Frontal Zone (PFZ), Polar Front Waters (PFW), Antarctic Zone (AZ) and Antarctic slope (AS). The extent of the Antarctic Circumpolar Current is indicated as ACC. The red dotted rectangle indicates the position of a cyclonic eddy observed during the voyage. We identified at least two hydrothermal plumes (indicated on 3B) but we suspect there may be multiple plumes present. 30

Figure 2.4: Box and whisker plots of labile to total particulate Mn ratio (%) for each region along SR3: Subantarctic Zone (SAZ); Polar Front Waters (PFW); Antarctic Zone (AZ); Antarctic Slope (AS). A: Mixed Layer Depth; B: 0 - 1500 m. The mean is represented with a filled diamond shape for each region. 30

Figure 2.5: Depth profiles of dissolved Mn (dMn) (A) and total particulate Mn (totpMn) (B) measured above the Antarctic slope for stations 30 – 36. All stations display an increase of dMn and pMn with depth, likely due to sedimentary sources. 35

Figure 2.6: Depth profiles of temperature ($^{\circ}\text{C}$) (red), turbidity (NTU) (blue), salinity (PSU) (green) and dissolved Mn (nM) for stations 8, 9 & 10, 13 & 14 and 17 & 18 between 1000 and 4500 m. 37

Figure 2.7: Depth profiles of dissolved Mn (dMn) (A) and total particulate Mn (totpMn) (B) for stations 19, 21, 24 and 27. The southern extension can be observed for stations 19-24 considering dMn, and for all stations for total pMn, suggesting further extension in the pMn fraction. 39

Figure 3.1: Map of the study area showing the bathymetry background colour (from Arndt et al. 2013) overlaid with TMR station locations (black dots) (a). The triangle shows stations where in-situ pumps were deployed. The large arrows indicate bottom water movement characterized in this region by Foppert et al. (2021): in red the Ross Sea Bottom Water (RSBW) and in black the Adelie Land Bottom Water (ALBW). On the right panel (b), the colour shows the change in sea-ice persistence between November and December 2017, prior to our occupation (Spren et al., 2008). A value of 0 indicates no change in the proportion of sea-ice occurred between November and December while a value of -1 indicate that where sea-ice was present for all of November, it was absent for all of December. Overlaid small black arrows represent the average sea-ice velocity for November and December (Kimura 2004). The South Antarctic Circumpolar Front and the Antarctic Slope Front are indicated on each panel. ... 43

Figure 3.2: Potential temperature-salinity plot for a) the full dataset and b) the same dataset focusing on bottom waters, with salinities ranging from 34.5 to 34.75. Overlaid coloured dots represent dissolved Mn concentrations.....	46
Figure 3.3: Depth profiles of dissolved Mn (dMn) along each transect, the colours represent the position of the station relative to both fronts, the slope and the shelf, the shape represents the four transects: 132, 140 and 150 (three main) and S4 which joins all the transects.....	48
Figure 3.4: Scatter plot showing the evolution of salinity (A), dMn (B) and the ratio between dMn:salinity (C) with distance from the coast. Logarithmic regression lines are added in panel B and C with the corresponding equation and R-squared. The colours represent the water masses: AASW, Antarctic Surface Water; WW, Winter Water, CDW; Circumpolar Deep Water and DSW/AABW for Dense Shelf Water/Antarctic Bottom Water.....	49
Figure 3.5: Depth profiles of fluorescence (F_o) (a), Photosynthetic Active Radiation (PAR in $\mu\text{mol photons m}^{-2} \text{sec}^{-1}$) (b) and transmittance (trans. in %) (c) between 0-200 m, north of the SACCF, where the lower surface dMn concentrations were observed.	50
Figure 3.6: Dissolved manganese (dMn) concentrations measured in Antarctic Bottom Water (AABW) against the fraction of Low Circumpolar Deep Water (LCDW) in AABW. Linear regression with 95% confidence interval, R^2 and p-value are displayed. The theoretical dilution line (TDL) is shown for a theoretical mixture of AABW and LCDW with dMn endmembers set as the mean of all off shelf dMn observations within each water mass. The TDL assumes no losses or enrichments during mixing.....	52
Figure 3.7: Ratio between labile particulate manganese (labilepMn) to total particulate manganese (totpMn) in % with distance from the coast. The colours represent the position of the station relative to both fronts, the slope and the shelf.	53
Figure 3.8: Depth profiles of oxygen concentrations (in μM) measured by the CTD sensors for the three main transects and the three 3 shelf stations with overlaid coloured dots showing dissolved Mn concentrations (in nM). The black circle shows low oxygen concentrations coincident with relatively high dMn concentrations.....	55
Figure 3.9: 3D plot showing dissolved Mn concentrations (in nM) along the three perpendicular sections measured (132, 140 and 150). While dMn seem elevated in bottom waters, we observed a decrease of dMn with distance from the coast. We suggest subsurface dMn maxima may represent an important source of dMn for surface waters.....	56
Figure 4.1: Sites sampled for each experiment. The background image colour shading represents the average surface chlorophyll-a concentrations measured by satellite (MODIS-Aqua, 8-day average 4 km) for the month when each of the bioassay experiments was performed. A: phytoplankton incubations at PS2 during the spring voyage (IN2018-V04), monthly average for September 2018. B: phytoplankton incubations at SOTS during the summer voyage (IN2020-V08), monthly average for December 2020. C: phytoplankton incubations at SOTS during the autumn voyage (IN2019-V02), monthly average for March 2019.	60
Figure 4.2: Temperature (A), salinity (B) and silicic acid concentrations (C) depth profiles measured at the sites of the incubations: PS2 (spring, in green) and SOTS (summer in blue and autumn in brown).	64
Figure 4.3: Phosphate (A) and silicic acid (B) concentrations (μM) measured in the initial water incubated ("Initial"), and after seven days of incubations for each treatment: Control ("Control"), +Fe ("Fe"), + Mn ("Mn"), +FeMn ("FeMn"). The colour represents the season of the experiment: green for spring, blue for summer and brown for autumn. Error bars represent the standard deviations and are smaller than the symbols when not visible (n = 3, except for the initial treatment where n = 1).	66

Figure 4.4: A) Photochemical efficiency of photosystem II (F_v/F_m) and B) functional absorption cross section of PSII (σ_{PSII}) in $\text{nm}^2 \text{ quanta}^{-1}$, measured for the initial algal communities incubated (“Initial”) and after 7 days of incubation, in each treatment: Control, +Fe (“Fe”), + Mn (“Mn”), +FeMn (“FeMn”). The three colours show the different seasons: green for spring, blue for summer and brown for autumn. Error bars represent the standard deviations ($n = 3$, except for the initial treatment where $n = 1$). 68

Figure 4.5: Relative contribution of four gated populations compared to all phytoplankton cells captured by the instrument: large phytoplankton (microeukaryotes), nanoeukaryotes, picoeukaryotes and cyanobacteria in terms of population size (FSC), as defined in equation (1) for summer (A) and autumn (B). These values were calculated according to the equation of Bach et al. (2018). Error bars represent the standard deviations ($n = 3$, except for the initial treatment where $n = 1$). 69

Figure 4.6: Fe uptake (pM d^{-1}) measured in each size fraction and for the three seasons: spring in green, summer in blue and autumn in brown. During the autumn experiment, only two datapoints were recorded for the +Fe treatment. Error bars represent the standard deviations and are smaller than the symbols when not visible ($n = 3$). 70

Figure 4.7: Carbon uptake ($\mu\text{M d}^{-1}$) measured in each size fraction and for the three seasons: spring in green, summer in blue and autumn in brown. Due to a manipulation mistake during the autumn experiment, only one datapoint was recorded for the +Fe treatment. For the other treatments, error bars represent the standard deviations and are smaller than the symbols when not visible ($n = 3$). 71

Figure 4.8: Iron to carbon (Fe:C) uptake ratio ($\mu\text{mol mol}^{-1}$) measured in each size fraction and for the three seasons: spring in green, summer in blue and autumn in brown. The Fe:C ratio from the +Fe treatment in autumn was not included due to missing data. Error bars represent the standard deviations and are smaller than the symbols when not visible ($n = 3$). 72

Figure 5.1: Photosynthetic Active Radiation (PAR in $\mu\text{mol photons m}^{-2} \text{ s}^{-1}$) showing the decrease in PAR with depth. The two red points represent the two depths used for the calculation of the light attenuation coefficient K. 82

Figure 5.2: Depth profiles of A) fluorescence (F_o) measured by the CTD sensors; B) chlorophyll-*a* (Chl-*a*) concentrations in mg m^{-3} ; C) ratio of fluorescence per chlorophyll-*a* ($F_o:\text{Chl-}a$) D) biogenic silicate (BSi) concentrations in μM ; E) ratio of chlorophyll-*a* per particulate organic carbon (Chl:C) in mmol mol^{-1} ; F) silicic acid concentrations (μM); G) net primary productivity (NPP) measured through carbon uptake ($\mu\text{M d}^{-1}$); H) intracellular Fe uptake (pM d^{-1}). The legend of shapes only relates to the different sizes measured for the NPP and Fe uptake (G and H). 87

Figure 5.3: A) Cell counts (cell mL^{-1}) and B) relative importance in terms of chlorophyll-*a* fluorescence (%) for the three main populations gated: picoeukaryotes (“Peuks”), nanoeukaryotes (“Nanos”), large phytoplankton (“Large phyto”) at the initial TMR cast where the DCM was sampled (at 87 m). The white pie slices indicate cells that were not included in the three main gates. 88

Figure 5.4: Concentrations of nitrate (A), phosphate (B), silicic acid (C), chlorophyll-*a* (D), particulate organic carbon (POC, E) and biogenic silicate (BSi, F) measured in the initial water incubated (“Initial”) and after 10 days of incubations, in each treatment: Control, +Fe (“Fe”), + Mn (“Mn”), +FeMn (“FeMn”). The two colours represent the light treatments: light grey for high light (HL) and dark grey for low light (LL). 90

Figure 5.5: Relative contributions to chlorophyll-*a* fluorescence of the three main gated phytoplankton populations: large phytoplankton (“Large phyto”), nanoeukaryotes (“Nanos”) and picoeukaryotes (“Peuks”) for the initial communities incubated (“Initial”) and after 10 days of incubation in each treatment: Control, +Fe (“Fe”), + Mn (“Mn”), +FeMn (“FeMn”). The results are separated by light treatments. 93

Figure 5.6: Carbon uptake in $\mu\text{M d}^{-1}$ (A-C), Fe uptake in pM d^{-1} (D-F) and Fe:C ratios in $\mu\text{mol mol}^{-1}$ (G-I) per size class (0.2-2 μm , 2-20 μm , >20 μm), treatment (Control, Mn, Fe, FeMn) and light condition (low light, LL vs high light, HL) assessed over a 24 h period on subsamples collected after 10 days of incubation. 94

Figure 5.7: Cellular carbon uptake in $\mu\text{mol cell}^{-1} \text{d}^{-1}$ (A-C), cellular Fe uptake in $\text{pmol cell}^{-1} \text{d}^{-1}$ (D-F) and cellular Fe:C ratios in $\mu\text{mol mol}^{-1}$ (G-I) per size class (0.2-2 μm , 2-20 μm , >20 μm), treatment (Control, Mn, Fe, FeMn) and light condition (low light, LL vs high light, HL) assessed over a 24 h period on subsamples collected after 10 days of incubation..... 95

List of tables

Tables are labelled according to Chapter and Table order within a chapter. For example, 'Table 4.2' is Table 2 in Chapter 4.

Table 2.1: Average dissolved Mn concentrations (nM) measured across the whole water column and within the mixed layer depth (MLD) for each area along SR3: Subtropical zone (STZ) n= 41 and 11; Subantarctic zone (SAZ) n= 102 and 27; Polar Front Zone (PFZ) n= 24 and 8; Polar Front Waters (PFW) n=84 and 20; Antarctic Zone (AZ) n= 53 and 11; Antarctic Slope (AS) n= 67 and 16..... 27

Table 2.2: Average total, labile and refractory particulate Mn concentrations (nM) measured across the whole water column for each area along SR3: Subantarctic zone (SAZ) n= 40, 24 and 24; Polar Front Waters (PFW) n=38, 8 and 8; Antarctic Zone (AZ) n= 30, 16 and 16; Antarctic Slope (AS) n= 38, 16 and 16..... 28

Table 2.3: Relations calculated between dissolved Mn (dMn) and dissolved PO₄³⁻, above the dMn subsurface maximum, for the Subantarctic Zone (SAZ), the Polar Front Waters (PFW), the Antarctic Zone (AZ) and the Antarctic Slope (AS) data. Asterisk (*) indicate a p-value below 0.05. 31

Table 2.4: Means and standard deviations of Mn:P ratios ($\times 10^{-3}$ mol mol⁻¹) in the labile and total particulate fraction for the Subantarctic Zone (SAZ), the Polar Front Waters (PFW), the Antarctic Zone (AZ) and the Antarctic Slope (AS) data, above the dissolved Mn subsurface maximum 32

Table 3.1: Dissolved and particulate Mn concentrations with various ratios in the dissolved and total particulate fractions between Mn, P and Ti, measured in Antarctic Surface Waters (AASW). 51

Table 4.1: Initial mean dFe and dMn concentrations with standard deviations measured in (or near) the seawater incubated for the three experiments and the calculated Mn* according to Browning et al. (2021): spring at PS2 in 2018 (n = 2), summer at SOTS in 2020 (n = 1) and autumn at SOTS in 2019 (n = 3). *Single measurements were performed for dFe and dMn in summer and dMn in autumn, in these cases the method error is indicated. In autumn, both dFe and dMn values came from a near cast. 65

Table 4.2: Average uptake rates of phosphate and silicic acid ($\mu\text{M week}^{-1}$) and standard deviations for each treatment calculated over the 7-day incubation period for each experiment (n=3). *In summer, all final silicic acid concentrations were below the detection limit (0.2 μM) and hence replaced with 0.2 μM . Consequently, the calculated uptake rate is identical in each treatment and cannot be interpreted. 67

Table 4.3: Counts of phytoplankton cell (cell mL⁻¹) measured in the main gated populations: picoeukaryotes ("Picoeuk."), cyanobacteria ("Cyano."), nanoeukaryotes ("Nanos."), large phytoplankton ("Large phyto.") and bacteria for the summer and autumn experiments, in each treatment. The mean value along with the standard deviation (n=3) is presented. 68

Table 5.1: Incident irradiance (I_0), factor of attenuation depth (AD) and derived depth (m) calculated for the different light treatments used during the field incubations. For the present work, we used either 1- (high light) or 3-layers (low light) of mesh to attenuate light. 83

Table 5.2: Characteristics of the DCM and overlying waters: dissolved Fe (dFe), dissolved Mn (dMn), chlorophyll-*a* concentrations (Chl-*a*), temperature ("Temp."), chlorophyll-*a* concentrations per cell (Chl:cell), biogenic silica (BSi), particulate organic carbon (POC or C in ratio), photochemical efficiency of PSII (F_v/F_m) and functional absorption cross section of PSII (σ_{PSII}). '/' indicates no data were collected. 88

Table 5.3: Nutrient consumption rates of nitrate (ΔN), phosphate (ΔP), silicic acid (ΔSi) in $\mu M d^{-1}$ and rate of chlorophyll-*a* ($\Delta Chl-a$) and POC production in $mg m^{-3} d^{-1}$ and $\mu M/day$, respectively. 91

Table 5.4: Multiple variables characterising phytoplankton communities at the DCM prior to and after 10 days of incubations in each treatment and under the two light treatments with F_o : fluorescence, *Chl-a*: chlorophyll-*a*, C: particulate organic carbon, BSi: biogenic silica, Si: silicic acid, N: nitrate, P: phosphate, F_v/F_m : photochemical efficiency of PSII and σ_{PSII} : functional absorption cross section of PSII. The units are as: *Chl-a*:C ($mmol mol^{-1}$); BSi:C ($mol mol^{-1}$); BSi:*Chl-a* ($mol mol^{-1}$); Si:N ($mol mol^{-1}$); N:P ($mol mol^{-1}$) and σ_{PSII} ($nm^2 quanta^{-1}$). 92

Table 5.5: Cell counts ($cell mL^{-1}$) for the four gated populations for the initial community incubated (“Initial”) and after 10 days of incubation in each treatments: Control, +Fe (“Fe”), + Mn (“Mn”), +FeMn (“FeMn”), separated by light conditions. 93

List of abbreviations

Abbreviation	Meaning	Abbreviation	Meaning
ACC	Antarctic Circumpolar Current	SCM	Subsurface chlorophyll maximum
AS	Antarctic Slope	SFM	Subsurface fluorescence maximum
AZ	Antarctic Zone	SOD	Superoxide dismutase enzyme
BSi	Biogenic silica	STZ	Subtropical Zone
Ca	Calcium	Ti	Titanium
Chl-a	Chlorophyll-a	TMR	Trace metal rosette
CO₂	Carbon dioxide	Zn	Zinc
Co	Cobalt		
Cu	Copper		
DCM	Deep Chlorophyll maximum		
dFe	Dissolved iron		
dMn	Dissolved manganese		
Fe	Iron		
Fo	Fluorescence		
F_v/F_m	Photochemical efficiency of PSII		
H₂O₂	Hydrogen peroxide		
HO[•]	Hydroxyl radical		
HNLC	High Nutrient Low Chlorophyll		
Mn	Manganese		
O₂	Oxygen		
O₂⁻	Superoxide		
PAR	Photosynthetic active radiation		
PFW	Polar Front Waters		
PFZ	Polar Front Zone		
POC	Particulate organic carbon		
pMn	Particulate Mn		
PSII	Photosystem II		
ROS	Reactive oxygen species		
σ_{PSII}	Functional absorption cross section of PSII		
SAZ	Subantarctic Zone		

1. CHAPTER 1 – General introduction, aims and thesis structure

1.2. The evolution of early life and Earth's oceans

It is hypothesized that early life on Earth began within the oceans and that transition metals, such as iron (Fe) and manganese (Mn), played a crucial role in determining the fate of microbial evolution (Nisbet and Sleep 2001). Microbial life began on Earth more than 3.5 billion years ago (Ga), with putative evidence suggesting up to 3.8 Ga, during the Archean period (Kasting and Siefert 2002). During this time, conditions within the oceans were mostly anoxic, characterized by low oxygen concentrations, and reduced (Lyons et al. 2014). Anoxic conditions favoured high concentrations of transition metals, which were mainly present in their lower reduction/oxidation (redox) forms (e.g., Fe(II) and Mn(II)) (Walker and Brimblecombe 1985; Fischer and Knoll 2009). In fact, Fe and Mn were present in such great abundance that nearly all early microscopic life integrated these elements as electron donors/acceptors in their metabolic systems (Widdel et al. 1993; Ehrenreich and Widdel 1994; Raven et al. 1999; Fischer et al. 2015), with Fe being the dominant electron donor and acceptor (Fischer and Knoll 2009). In addition, both metals were integrated in oxygen defence enzymes, present in a common ancestor before the divergence of eukaryotes and bacteria (May and Dennis 1989; Wintjens et al. 2004). However, about 2.3 Ga ago, our planet underwent major changes following the appearance of photosynthesis (Kasting and Siefert 2002).

Firstly, anoxygenic photosynthesis allowed the use of light as an additional energy source, with sulphur used as reductant by multiple bacteria (e.g., purple bacteria or green bacteria) (Nisbet and Sleep 2001). Following this, oxygenic photosynthesis evolved with the most notable difference residing in the use of water as an electron donor, leading to the production of oxygen (Nisbet and Sleep 2001). Oxygenic photosynthesis was only permitted through the development of the oxygen evolving complex, which contains four Mn atoms, one calcium (Ca) atom, and resides in the photosystem II (PSII) reaction centre (Figure 1.1; Sauer 1980; McEvoy and Brudvig 2006; Sproviero et al. 2007; Armstrong 2008). There is also a high requirement for Fe during oxygenic photosynthesis, as it is used in the electron transport chain and in carbon and nitrogen fixation (Raven 1990; Twining and Baines 2013). Manganese and Fe were therefore two important elements, at the centre of the rise of Earth's oxygen levels, commonly referred to as the Great Oxidation Event (Kopp et al. 2005; Kirschvink and Kopp 2008; Planavsky et al. 2014).

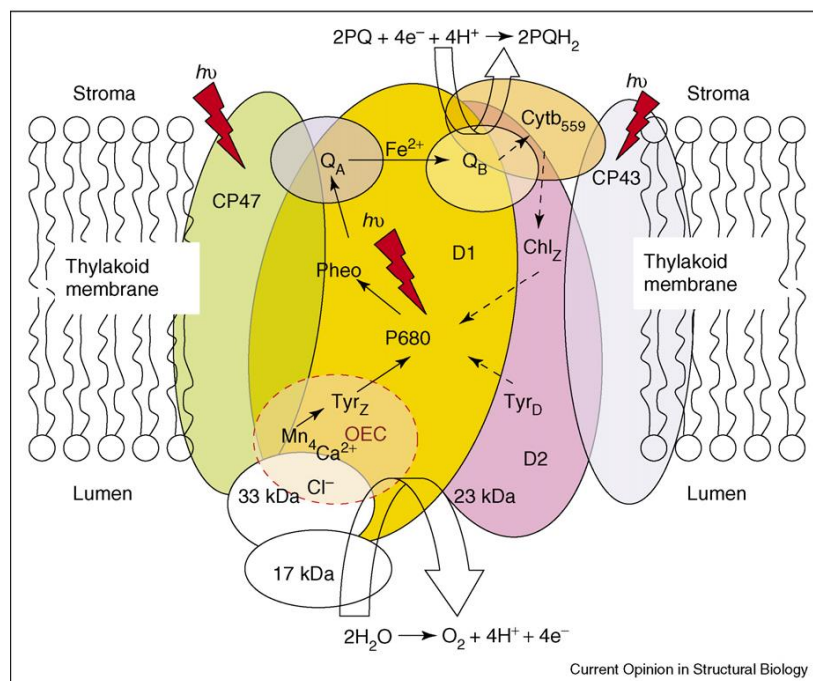


Figure 1.1: Structure of photosystem II from Sproviero et al. (2007). The oxygen evolving complex (OEC in illustration) has four Mn atoms, providing electrons during the step of water oxidation.

With the continued expansion of oxygenic photosynthesis amongst other taxa, the Earth's hydrosphere and atmosphere rapidly accumulated substantial amounts of oxygen, becoming strongly oxidized environments (Nisbet and Sleep 2001; Armstrong 2008), toxic for anaerobic life but also for photosynthetic organisms due to reactive oxygen biproducts (Lesser 2006). Directly linked to the surrounding oxygen concentration is the production of reactive oxygen species (ROS) by biological systems (Jamieson et al. 1986). Reactive oxygen species include singlet oxygen (1O_2), superoxide (O_2^-), hydrogen peroxide (H_2O_2) and the most reactive and damaging ROS, the hydroxyl radical (HO^\bullet) (Figure 1.2; Lesser 2006). These highly reactive molecules result from the reduction of oxygen, commonly in the photosynthetic electron transport chain of photoautotrophs, and can easily damage the cellular constituents such as lipids, proteins and/or DNA (Figure 1.2; Cadenas 1989; Fridovich 1998; Lesser 2006). Reactive oxygen species are countered by antioxidant molecules (Cadenas 1989; Fridovich 1998; Lesser 2006). Iron and Mn are both used in the superoxide dismutase (SOD) enzyme which lessens O_2^- concentrations by catalysing its transformation to H_2O_2 and dioxygen (O_2) (McAdam et al. 1977; Cadenas 1989; Bull et al. 1991; Stallings et al. 1991; Fridovich 1998; Lesser 2006). Manganese-SOD are found in mitochondria and bacteria while Fe-SOD are found in chloroplasts and bacteria, forming the Fe/Mn SOD family (Cadenas 1989; Fridovich 1997; 1998; Lesser 2006). Other SOD classes which perform similar functions have also been observed, differentiated by other metal co-factors: the Cu/Zn-SOD and Ni-SOD (Fridovich 1997; Lesser 2006; Morel et al. 2020).

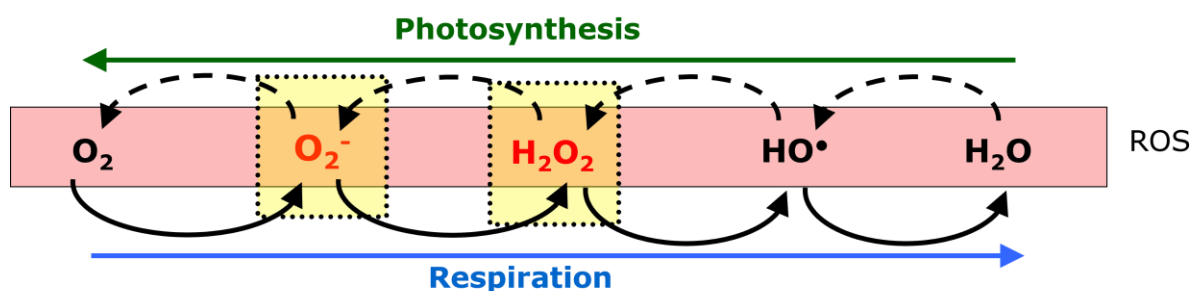


Figure 1.2: Schematic representation of the reaction pathway from water to oxygen (photosynthesis) and oxygen to water (respiration) with intermediates reactive oxygen species: superoxide (O_2^-), hydrogen peroxide (H_2O_2) and hydroxyl radical (HO^\bullet) from Wuttig 2013.

In releasing vast amounts of oxygen and oxygen byproducts, the Great Oxidation Event impacted all life on Earth, but it also modified many elemental cycles. In the presence of oxygen, Mn(II) and Fe(II) can be oxidized to insoluble species such as oxides, for example Mn(III)/Mn(IV)Ox, which form particles that sink through the water column (Sunda and Huntsman 1983; Kirschvink et al. 2000; Konovalov et al. 2004; van Hulst et al. 2017). Consequently, ocean oxygenation resulted in a strong decrease in dissolved Mn and Fe concentrations, as shown by large manganese deposits, such as the Kalahari Mn field in South Africa (Cairncross and Gutzmer 1997; Kirschvink et al. 2000; Kopp et al. 2005). Low metal concentrations (in the nanomolar range; 10^{-9} molar) are currently observed in the modern oceans. Several oceanic regions with high macronutrient concentrations but surprisingly low biomass and particularly low trace metal concentrations, especially Fe, have been identified for several decades (Martin 1990, Martin 1991; Behrenfeld et al. 1996). Analytical techniques only improved sufficiently by the end of the 20th century to allow the detection of trace metal concentrations without contamination (Landing and Bruland 1987; Martin and Gordon 1988), and to demonstrate that Fe is limiting phytoplankton growth in these regions (Martin 1990; Behrenfeld et al. 1996; Boyd et al. 2000). These oceanic regions are now referred to as High-Nutrient Low-Chlorophyll or HNLC areas and are located in the Equatorial Pacific, North Pacific and Southern Ocean (Martin et al. 1989). This thesis focusses on the latter and largest HNLC area.

1.3. The Southern Ocean

Circling the Antarctic continent, the Southern Ocean connects the Pacific, Atlantic and Indian ocean basins through the Antarctic Circumpolar Current (ACC), forming a unique environment on Earth (Boyd et al. 2000; Rintoul 2018). Identified as a region of deep water formation, the Southern Ocean strongly influences global oceanic circulation (Rintoul 1998; 2018), but also the carbon cycle, and therefore the climate at a macro-scale (Sarmiento et al. 1998; Boyd et al. 2000; Lenton et al. 2013). Previous studies have estimated that the Southern Ocean is responsible for one third of the uptake of anthropogenically generated carbon dioxide (CO_2) (Caldeira and Duffy 2000; Sarmiento and Gruber 2002; Gruber et al. 2009). This uptake occurs through two processes (Figure 1.3): i) the physical carbon pump (or solubility carbon pump), which consists of constant equilibration between the atmosphere and

the surface ocean and ii) the biological carbon pump wherein CO_2 is absorbed by phytoplankton photosynthesis (Ducklow et al. 2001; Herndl and Reinthaler 2013; McKinley et al. 2016) and carbon is exported to the deep ocean through sinking particles (e.g., aggregated phytoplankton, faecal pellets or zooplankton carcasses) (Turner 2002; Boyd et al. 2019; Halfter et al. 2021).

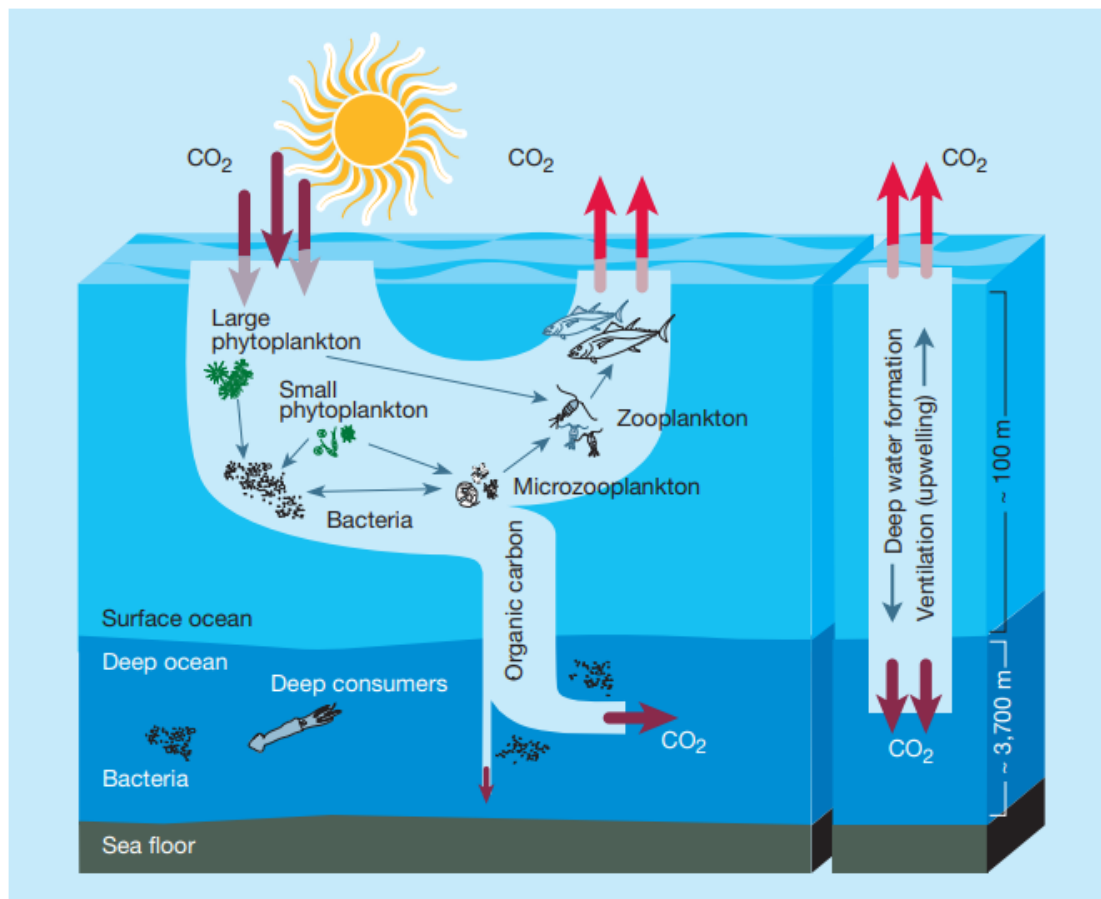


Figure 1.3: Overview of the oceanic carbon pump from Chisholm (2000). This illustrates the biological carbon pump (left), including the transfer of carbon dioxide from the atmosphere into the ocean which is induced by phytoplankton photosynthesis and sinking organic matter and the solubility pump (right), consisting of mixing and equilibration between the ocean and atmosphere.

The intensity of the biological carbon pump varies spatially between the different Southern Ocean regions (Lenton et al. 2013). The Southern Ocean is divided into several biogeochemical regions, characterized by contrasting hydrographic and nutrients conditions and separated by fronts (Orsi et al. 1995). From North to South, these regions are usually referred to as: Subantarctic zone (SAZ), Polar Front Zone (PFZ), Antarctic Zone (AZ) and Seasonal Ice Zone (SIZ) (Figure 1.4; Deppeler and Davidson 2017). Depending on the season, these regions can either act as sinks or sources of CO_2 (Lenton et al. 2013). During the austral summer, they usually act as sinks due to the growth of phytoplankton (Ishii et al. 1998; Metzl et al. 1999; Bakker et al. 2008; Takahashi et al. 2012; Landschützer et al. 2014). However, phytoplankton growth differs amongst these Southern Ocean biogeochemical regions, because of different physical and chemical constraints.

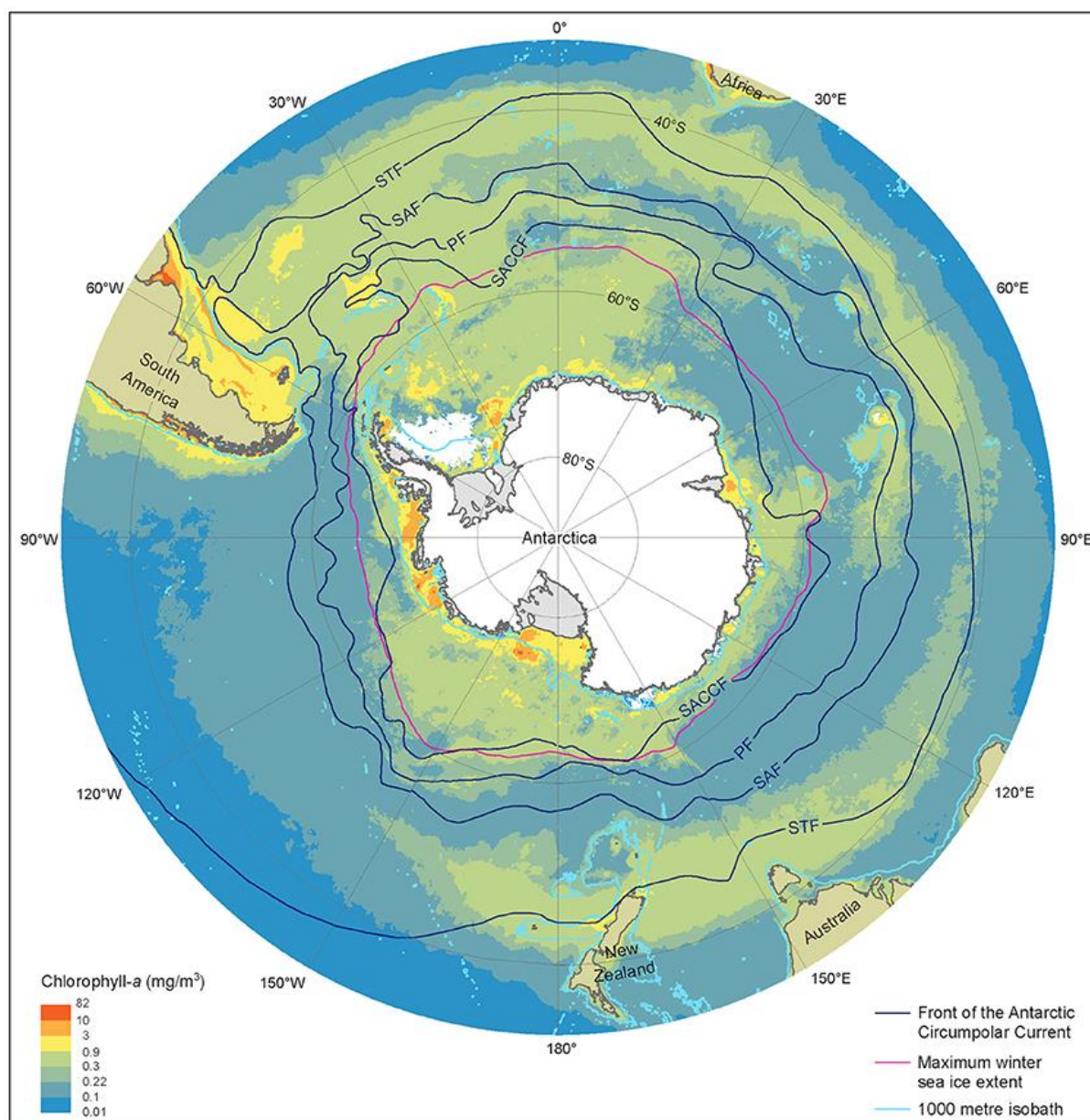


Figure 1.4: Map of surface chlorophyll-*a* distribution in the Southern Ocean, from Deppeler and Davidson (2017). Chlorophyll-*a* concentrations were measured by satellites (MODIS-Aqua from the austral summer season 2002/03 and 2015/16 at 9 km resolution). Oceanographic fronts (from Orsi et al. 1995) are indicated with black lines: Subtropical Front (STF), Subantarctic Front (SAF), Polar Front (PF) and Southern Antarctic Circumpolar Front (SACCF).

1.4. Factors limiting phytoplankton growth in the Southern Ocean

Various parameters have been observed to limit phytoplankton growth in Southern Ocean waters. Low Fe concentrations have now been widely described in this region (Martin 1990; Behrenfeld et al. 1996; Boyd et al. 2000; Henley et al. 2020) and Fe limitation of phytoplankton growth has been demonstrated through bottle incubation and artificial fertilisation experiments (Behrenfeld et al. 1996; Boyd et al. 2007). Overall, phytoplankton are expected to be Fe-limited south of the Subtropical Front (STF) (Deppeler and Davidson 2017), but other parameters can also control phytoplankton growth in this region, such as low temperature (Boyd 2002) and low silicic acid concentrations north of the Polar Front

(Bowie et al. 2009; Lannuzel et al. 2011; Eriksen et al. 2018). Light limitation can also be observed under deep seasonal mixing (Mitchell et al. 1991; Nelson and Smith 1991; Boyd 2002) although adaptations of Southern Ocean phytoplankton to low Fe conditions have resulted in specific ways to counter low light (Strzepek and Harrison 2004; Strzepek et al. 2012). In addition, high-light stress has also been observed during deep mixing events when phytoplankton are submitted to highly variable irradiances (Alderikamp et al. 2010), highlighting the complexity of light control on Southern Ocean phytoplankton growth. Hence, many parameters have been observed to control phytoplankton growth in this region.

More recently, interest has been given to the possibility of several simultaneous trace metal limitations during which phytoplankton growth would not be limited by only one element (e.g., Fe) but by a combination of two or more elements. The concept of trace metal co-limitation is complex and has been divided into three types: i) type I: “independent nutrient co-limitation”, within which two elements present in very low concentrations and used in different biochemical functions can limit phytoplankton growth; type II: “biochemical substitution co-limitation”, where two metals can substitute each other within a metalloenzyme and type III: “biochemically dependant co-limitation”, where the growth limitation by one element result from the limitation of another element (Saito et al. 2008). The first identification of Fe as a limiting parameter of phytoplankton growth (in part) led to the creation of the GEOTRACES program (<https://www.geotraces.org/>), which aims to identify processes controlling trace metal distributions, quantify their fluxes and predict their evolution considering changing environmental conditions. This motivated the efforts to acquire multiple datasets of various trace metals concentrations in the global ocean, including Mn in the Southern Ocean (Middag et al. 2011, 2013).

As a bioactive trace metal, Mn has received interest due to its central roles in photosynthesis and defence against ROS (Middag et al. 2011, 2013; Browning et al. 2014). Saito et al. (2008) suggested Mn may be involved in type II co-limitation: “Biochemical substitution co-limitation”, as Fe and Mn can substitute for one another in the superoxide dismutase enzyme. In the Southern Ocean, Mn was recently observed to co-limit phytoplankton growth in both coastal regions and open waters (Wu et al. 2019; Browning et al. 2021). Conversely, studies with trace metal additions performed in the 1990s indicated natural levels of Mn were high enough to support phytoplankton growth in the Weddell-Scotia Seas, the Atlantic sector of the Southern Ocean and in the Ross Sea (Martin et al. 1990; Buma et al. 1991; Scharek et al. 1997; Sedwick et al. 2000). This suggests Mn (co-)limitation is not pervasive within Southern Ocean waters and complicates our understanding of its role in controlling primary productivity and hence, the carbon cycle. Furthermore, the seasonality of potential Mn limitation has not been studied. Identifying where and when phytoplankton can be Mn-limited remains essential to inform biogeochemical models such as PISCES (Aumont et al. 2015), which aim to predict changes in the oceanic carbon cycle. This emphasises the need for additional knowledge on Mn concentrations, its cycle and chemistry but also its seasonal variations in all biogeochemical regions of the Southern Ocean.

1.5. Oceanic manganese distribution

Manganese is the twelfth most abundant element in the Earth's crust (Wedepohl, 1995). Comparatively, its concentrations in seawater are much lower, within the nanomolar range (Landing and Bruland 1980; Landing and Bruland 1987; Middag et al. 2011). Manganese concentrations are usually described with a separation between its dissolved phase, which goes through a 0.2 μm filter and its particulate phase, which remains on the filter (Cutter 2017). More focus has been given to its dissolved phase, as it is considered more available for phytoplankton uptake (Tebo et al. 2007; van Hulst et al. 2017). Dissolved Mn (dMn) concentrations can be supplied to seawater through multiple external sources, such as atmospheric deposition and dissolution (Wuttig et al. 2013; Xu and Gao 2014; Perron et al. 2020), riverine inputs (Landing and Bruland 1980; Bruland and Lohan 2003; Aguilar-Islas and Bruland 2006), land runoff (Shiller 1997), sea-ice melting (Grotti et al. 2005; Middag et al. 2013; Lannuzel et al. 2014), hydrothermal vents (Klinkhammer and Hudson 1986; Fitzsimmons et al. 2017; Holmes et al. 2017) or sediment inputs (Landing and Bruland 1980; Middag et al. 2013; Cheize et al. 2019; Smith et al. 2021). Dissolved Mn is lost from the water column through biological uptake in the photic zone, microbially-mediated oxidation below the photic zone and scavenging onto particles at depth (Klinkhammer and Bender 1980; Sunda and Huntsman 1988; Westerlund and Öhman 1991; Sunda and Huntsman 1994; Bruland and Lohan 2003; Middag et al. 2011). These interactions between sources and sinks result in a typical dissolved (dMn) depth profile, characterized as “scavenged-type” in most ocean basins (Figure 1.5; Bruland and Lohan 2003). A surface maximum is commonly observed, resulting from external inputs to the surface ocean, ranging from low nanomolar values in open ocean to higher nanomolar/micromolar values near continents (Sunda and Huntsman 1988; Aguilar-Islas and Bruland 2006; Wuttig et al. 2013; van Hulst et al. 2017). In addition, high dMn surface concentrations are typically maintained by internal processes such as photoreduction of Mn oxides (MnOx) (Sunda and Huntsman 1988, 1994). Below surface maxima, dMn decrease with depth due to scavenging, a ubiquitous process decreasing trace metal concentrations (Turekian, 1977; Sunda and Huntsman 1994, Van Hulst et al. 2017). This results in uniformly low dMn concentrations in the deep ocean, ranging between 0.1-0.2 nM (Landing and Bruland 1980; Middag et al. 2011; van Hulst et al. 2017) with an associated relatively short residence time, between 100 and 1000 years (Bruland and Lohan 2003). Near the seafloor, increasing concentrations are commonly observed due to sediment resuspension (Middag et al. 2011). Southern Ocean dMn depth profiles differ from those typical to most other ocean basins.

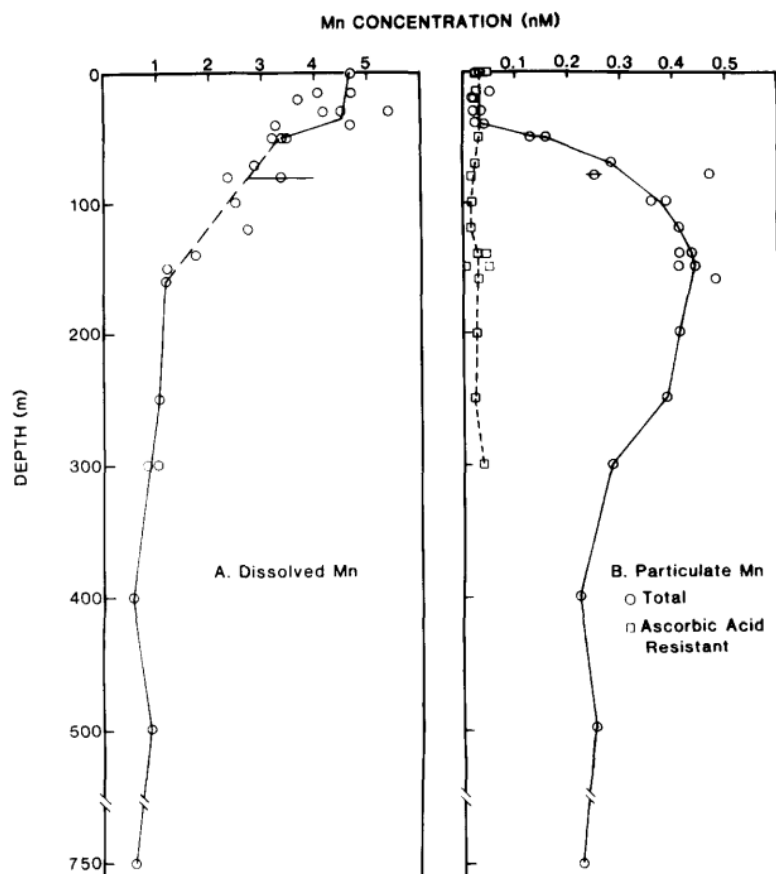


Figure 1.5: Typical depth profiles of Mn concentrations, observed in most ocean basins, published by Sunda and Huntsman (1988). a) Depth profiles of dissolved Mn (dMn) and b) particulate Mn (pMn) measured in the Sargasso Sea.

In the Southern Ocean, Mn sources and sinks are similar to other ocean basins (Figure 1.6). Yet, vast distance from continents results in a decrease in magnitude of some sources, for example atmospheric deposition (Wagener et al. 2008). Southern Ocean dMn distributions have only been described by a few studies and a different depth profile shape was observed in contrast to continent-influenced regions (Westerlund and Öhman 1991; Middag et al. 2011; Middag et al. 2013). No surface maximum and as a result very low surface dMn concentrations (< 0.5 nM) were reported and attributed to biological uptake combined with few external inputs (Klinkhammer and Bender, 1980; Westerlund and Öhman 1991; Middag et al. 2011). The lowest known dMn concentrations have been measured in the Southern Ocean: 0.03 nM in the Drake Passage (Browning et al. 2014) and 0.04 nM in the Atlantic sector of the Southern Ocean (Middag et al. 2011). Below these low surface concentrations, dMn concentrations were observed to increase until a subsurface maximum, located between 100 and 200 m and attributed to particle remineralization (Middag et al. 2011). Under this subsurface dMn maximum, decreasing dMn concentrations were observed with depth and attributed to scavenging processes. Near the seafloor, increasing dMn concentrations were associated with sediment inputs (Middag et al. 2011).

In the ocean, particulate Mn (pMn) can be composed of MnOx, Mn within phytoplankton cells or adsorbed onto particles and Mn within minerals (Sunda and Huntsman 1994; Canfield et al. 2005). Concentrations of pMn can be locally increased by external sources introducing dMn into the system, such as sediment inputs, hydrothermal vents or melting sea-ice (Fitzwater et al. 2000; Corami et al. 2005; Fitzsimmons et al. 2017; Lannuzel et al. 2014). In the Sargasso Sea, Sunda and Huntsman (1988) reported pMn data (Figure 1.5) with a depth profile opposite to a typical dMn depth profile, with low surface concentrations increasing with depth. Low surface pMn concentrations were maintained by photoreductive processes which induced a reduction of MnOx to Mn(II) and increased dMn concentrations. Below the photic zone, dMn increases due to lower rates of photoreduction of MnOx and a decrease in photoinhibition of bacterially-mediated oxidation of Mn(II) to MnOx (Sunda and Huntsman 1988). Combined with scavenging of Mn(II) onto MnOx and other particles, pMn concentrations are observed to increase with depth (Sunda and Huntsman 1988). The few studies looking at the different fractions of pMn have shown that MnOx dominates the particulate pool in the open ocean and that it is mostly labile (Sunda and Huntsman 1988; Twining et al. 2015). The labile particulate fraction is considered more bioavailable for biological uptake while the refractory fraction is expected to be inaccessible (Berger et al. 2008). Near shore and in proximity to lithogenic inputs, pMn can have a higher refractory ratio, considered less bioavailable and associated with lithogenic material and mineral particles. An increase in lability is expected with distance from sources due to the higher relative density of lithogenic particles which settle out preferentially to the biogenic particles (van der Merwe et al. 2019). Previous studies on both Mn phases have shown differing profiles in the ocean circling the Antarctic continent (Middag et al. 2011; Middag et al. 2013).

Particulate Mn distributions have rarely been described in the Southern Ocean (Westerlund and Öhman 1991; Fitzwater et al. 2000; Corami et al. 2005) and even less-so in open ocean waters (Bowie et al. 2009; 2010). Bowie et al. (2009) reported very low pMn concentrations south of 48°S (<0.03 nM) between 0 and 400 m. Near shore, increasing pMn concentrations can be observed due to external sources (Fitzwater et al. 2000; Corami et al. 2005; Bowie et al. 2009; 2010). To the best of our knowledge, no deep pMn concentrations have been reported in the Southern Ocean. However, work presented here has shown low pMn concentrations (< 0.1 nM) with a local increase resulting from deep sources, such as hydrothermal vents or sediment resuspension (see Chapter 2).

Very few seawater Mn concentrations have been reported in the Australian sector of the Southern Ocean. Discrete dMn and pMn concentrations have been reported south of Tasmania (Sedwick et al. 1997; Bowie et al. 2009; 2010) and above the East Antarctic shelf in sea-ice and surrounding seawater (Lannuzel et al. 2011, 2014; Duprat et al. 2020; Smith et al. 2021). These studies showed results in accordance with previous Southern Ocean research. However, additional datasets including Mn concentrations were published in 2021 during the GEOTRACES Intermediate Data Product (IDP, 2021).

CHAPTER 1 – General introduction, aims and thesis structure

This thesis will analyse one of the datasets added to the IDP 2021, following the GS01 section, between Tasmania and Antarctica (see Chapters 2 and 3).

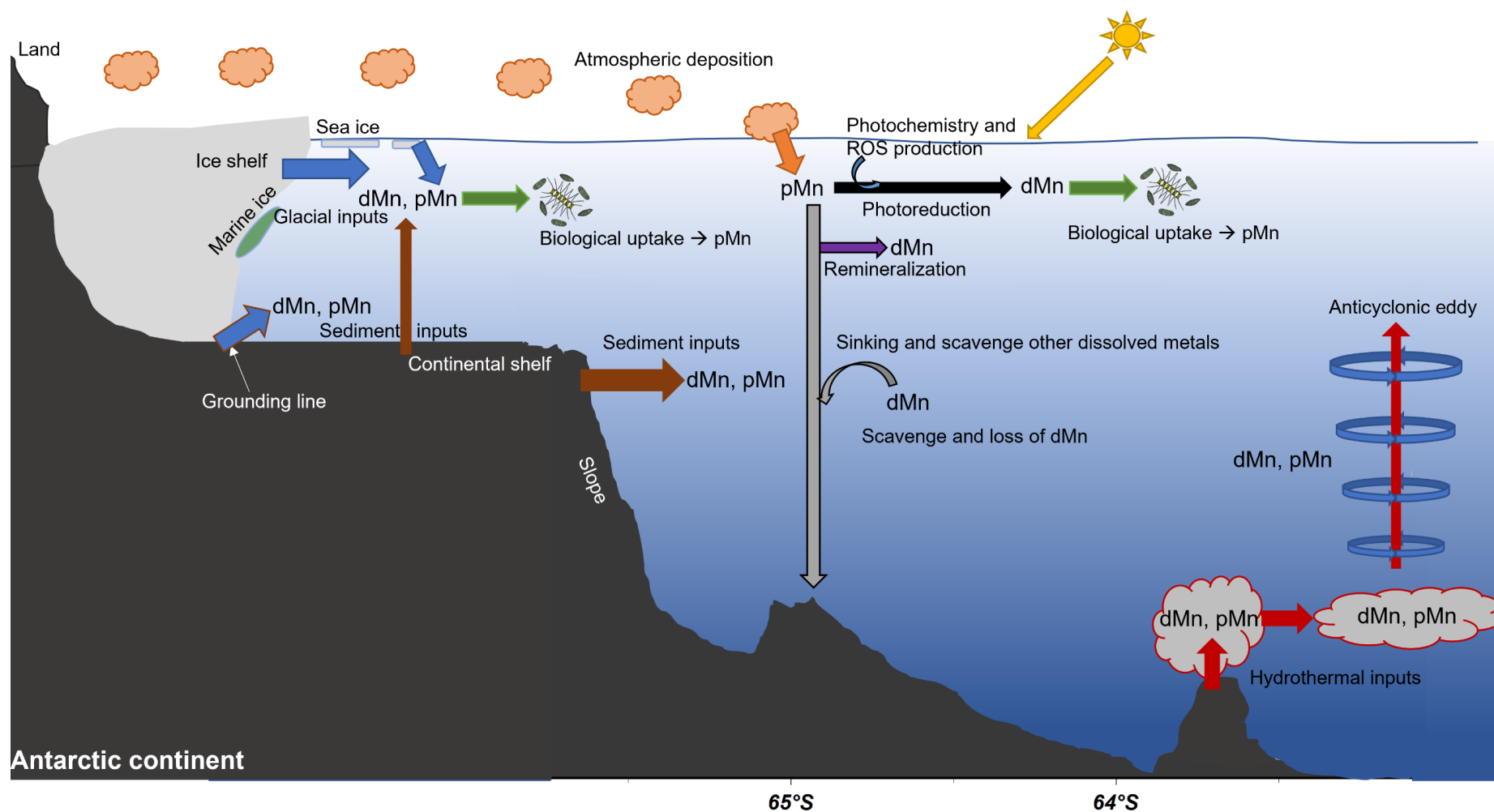


Figure 1.6: Sources and sinks of dissolved Mn (dMn) and particulate Mn (pMn) in the Southern Ocean. Both phases can be supplied by multiple sources: sediment resuspension, hydrothermal vents, glacial and sea-ice melting and aerosols depositions. Photoreduction of Mn oxides in surface waters may also increase dMn concentrations. However, this process has not yet been studied in the Southern Ocean waters.

1.6. Manganese speciation

In aquatic environments, Mn is characterized by three oxidation states: Mn(II), Mn(III) and Mn(IV), facilitating rich redox chemistry (Wuttig et al. 2013). Despite Mn(IV) being the stable oxidation state under oxygenated conditions (Tebo et al. 2004), Mn(II) is dominant in the ocean, as the soluble free aqueous ion $MnCl^+$. This is due to slow reaction kinetics with oxygen and photochemical reactions involving ROS, such as the reduction of MnOx to Mn(II) by O_2^- or H_2O_2 (Sung and Morgan 1981; Sunda and Huntsman 1994; Morgan 2005; Luther 2010). The two other oxidation states are less soluble and more commonly found in particles, as Mn(III)/Mn(IV) oxides. Many reactions can influence Mn speciation and cycling in seawater. In the surface ocean, sunlit-influenced reaction favour the presence of Mn(II), due to photoreduction of MnOx and photoinhibition of microbially-mediated Mn(II) oxidation (Sunda and Huntsman 1994). Conversely, Mn(II) oxidation by O_2 was observed to be slow at seawater pH (Morgan 2005) but other processes can speed up this reaction. Among them, microbial oxidation of Mn(II) has been extensively studied and is expected to occur below the photic zone in open waters (Sunda and Huntsman 1988, 1994; Tebo et al. 2004). In addition, the presence of metal oxides can influence Mn(II) oxidation (Davies and Morgan 1989) and Mn(II) photo-oxidation can also be mediated by humic substances and subsequent production of O_2^- and singlet molecular oxygen (1O_2) (Nico et al. 2002). This may be important in Southern Ocean waters considering humic substances have been observed in greater excess compared to Fe (and hence dMn) concentrations (Whitby et al. 2020). These reactions are briefly summarised in Figure 1.7.

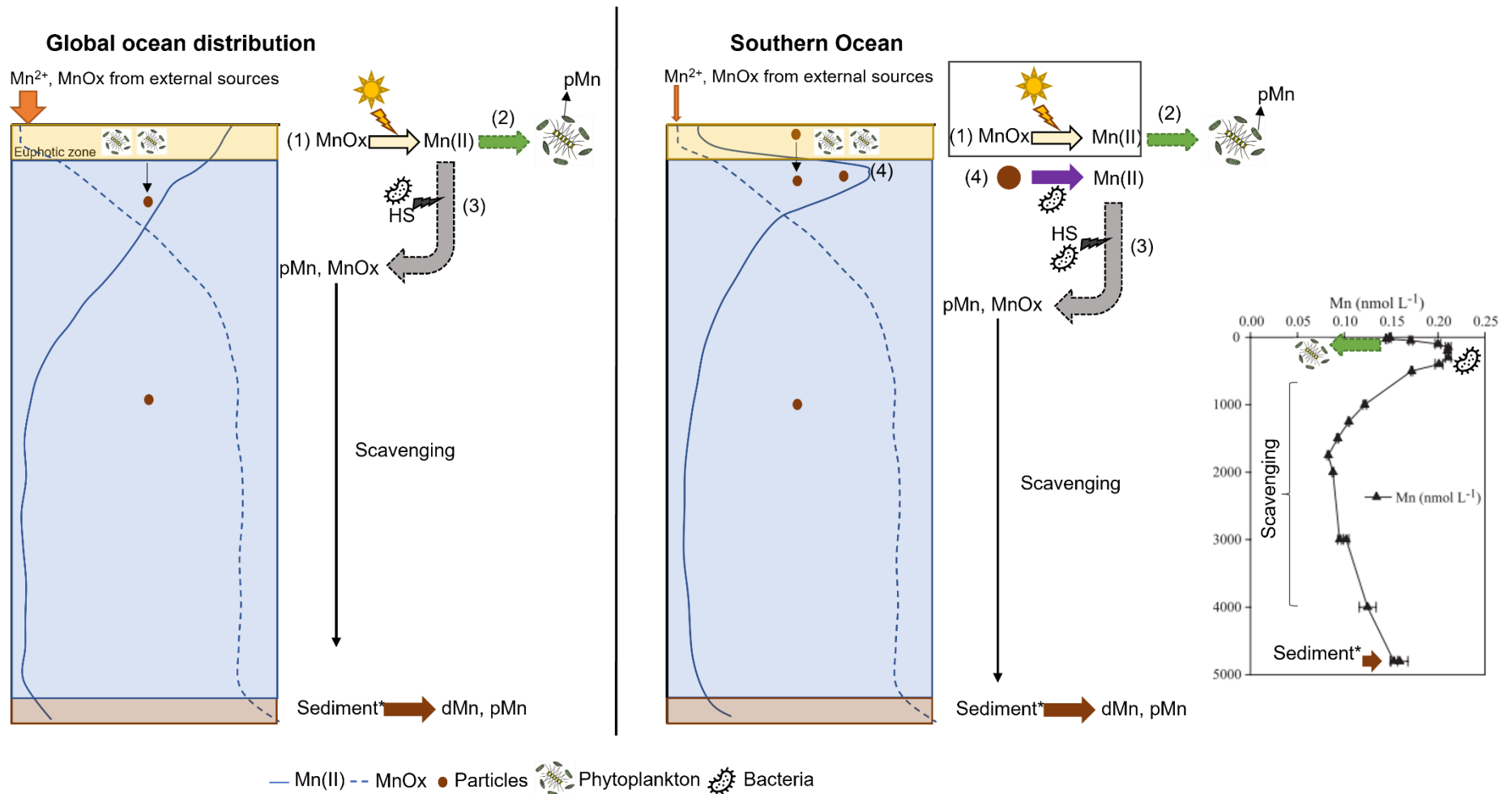


Figure 1.7: Illustration of dMn and pMn depth profiles with expected internal reactions impacting Mn speciation and the distinction between the Southern Ocean and other ocean basins. The last panel shows real dMn concentrations measured in the Weddell Sea by Middag et al. (2013). Reactions showing a gain of dMn are shown with full arrows, reactions showing a loss of dMn are shown with dashed arrows. (1) photoreduction of MnOx, this reaction can be mediated by reactive oxygen species. (2) Biological uptake of dMn. (3) Oxidation of Mn(II) to MnOx, this reaction can be mediated by microbes or humic substances. (4) Scavenging of dMn onto MnOx or other particles. Near the seafloor, sediment (*or other sources such as hydrothermal inputs) can increase dMn and pMn concentrations.

Intermediate to many of these reactions is the species Mn(III), which was assumed to be unstable in seawater and to quickly disproportionate to Mn(II) or Mn(IV) (Luther 2005, 2016). The development of a new spectrophotometric method showed that Mn(III) can be maintained in seawater, when bounded to strong ligands as Mn(III)-L complexes, for example in sediment porewaters (Madison et al. 2011). Additional studies showed that these complexes tend to dominate the dissolved Mn pool in suboxic and anoxic waters (Trouwborst 2006; Madison et al. 2013; Oldham et al. 2015). Subsequent analytical improvements and lowering of the detection limit has allowed the measurement of Mn(III)-L complexes in oxygenated waters, where they were previously unexpected (Oldham et al. 2017).

In the Southern Ocean, Mn speciation has been described primarily in terms of its dissolved/particulate phases rather than complexation by organic ligands (Fitzwater et al. 2000; Corami et al. 2005; Middag et al. 2011; Middag et al. 2013). For example, the study of Mn(III)-L complexes in Southern Ocean waters was previously prevented due to the instrument detection limits being higher than dMn concentrations. In 2021, the first study looking at Mn(III)-L complexes in Antarctic coastal waters was published and showed that these complexes can make up to 100% of the dMn pool (Oldham et al. 2021). In addition, the authors found a unique Mn redox cycle in the Ross Sea, inducing the formation and stabilization of Mn(III)-L complexes at the expense of MnOx formation, which were not detected. The discovery of these Mn(III)-L complexes in Southern Ocean waters may have important implications for other trace metals cycles. For instance, the affinity of Mn(III) for similar ligands to Fe(III) implies that Mn(III) may compete with Fe(III) for the same ligands (Kostka et al. 1995; Luther et al. 2015; Oldham et al. 2017). Still, ligands were observed in excess of dMn and dFe concentrations in the Southern Ocean (Gerringa et al. 2008), suggesting that such competition between both species may not strongly impact the Fe cycle. In addition, the lack (or decrease) of MnOx may impact other trace elements depth profiles. Manganese oxides are strong scavengers, meaning that lower MnOx concentrations may induce an increase in surrounding dissolved trace metal concentrations, due to the reduction in scavenging and adsorption of metals such as Fe, cobalt (Co) and zinc (Zn) onto MnOx (Goldberg 1954; Murray 1975; Tonkin et al. 2004; Oldham et al. 2021). However, additional measurements of Mn(III)-L complexes are necessary to confirm the results of this speciation study. Overall, previous studies have resulted in a preliminary understanding of Mn concentrations, cycling and speciation in the Southern Ocean. The main difference between the Southern Ocean and other ocean basins is the very low dMn concentrations measured in surface waters. This raises fundamental questions about phytoplankton Mn requirements in this region.

1.7. Phytoplankton Mn requirements

Currently, little is known about Southern Ocean phytoplankton Mn requirements. Cellular needs for Mn are directly linked to photosynthesis, as Mn is used in the oxygen evolving complex of PSII (Raven 1990; Sproviero et al. 2007; Armstrong 2008) and to detoxify the damaging ROS by-products of photosynthesis using the SOD enzyme (Peers and Price 2004; Wolfe-Simon et al. 2006; Aguirre and

Culotta 2012; MnCain and Bertrand 2022). No photosynthetic organism has yet been observed to substitute Mn with a different metal within the oxygen evolving complex. This implies a strict minimum Mn requirement for all phytoplankton species (Raven 1990). However, some external variables such as changes in Fe concentrations or light conditions may modify the number of PSII units found within an organism (Sunda and Huntsman 1997; Strzepek et al. 2019). This may influence Mn requirements for phytoplankton growth. To the best of our knowledge, no study has investigated the variation of Southern Ocean phytoplankton Mn requirement under various light and Fe conditions. Additionally, the Mn requirement associated with SOD synthesis can vary amongst species as not all phytoplankton taxa use a Mn-SOD. As previously mentioned, three SOD families are observed in organisms, all using a redox-active metal to convert O_2^- into H_2O_2 and O_2 : Fe/Mn-SOD, Cu/Zn-SOD and Ni-SOD (Aguirre and Culotta 2012). Many species have been observed to use the Fe/Mn-SOD, likely derived from a common ancestor (May and Dennis 1989; Wintjens et al. 2004). Among them, diatoms and cyanobacteria have been observed to rely on Mn-SOD for ROS detoxification (Peers and Price 2004; Perelman et al. 2006; Wolfe-Simon et al. 2006; Allen et al. 2007; Zhao et al. 2007; Schoffman et al. 2016) and haptophytes such as *Phaeocystis* sp. are also expected to rely on Mn-SOD (Schoemann et al. 2001). Diatoms and *Phaeocystis* sp. are key Southern Ocean phytoplankton groups (Deppeler and Davidson 2017) that strongly influence carbon export (DiTullio et al. 2000; Rembauville et al. 2015; Rigual-Hernández et al. 2015). As very low surface dMn concentrations are known to occur in this region, it is reasonable to hypothesise that Mn may influence the strength of the Southern Ocean biological carbon pump to some degree.

In the past decades, laboratory-based studies have confirmed that Mn requirements vary amongst phytoplankton species. Amongst coccolithophores, Brand et al. (1983) observed higher Mn requirements in neritic species compared to their oceanic relatives. However, they did not observe this difference in diatoms, which are more easily limited by Mn than the coccolithophores (Brand et al. 1983). Yet, the diatom species used in their study was isolated from the Gulf of Mexico and hence was likely not adapted to Mn-depleted waters. More recently, Pausch et al. (2019) studied the effects of Fe and Mn co-limitation on the diatom *Chaetoceros debilis*. They found that under relatively low dMn (< 0.59 nM) and dFe (0.84 nM) concentrations, the growth, photosynthetic efficiency, and carbon production of this species were impacted. In addition, as these dMn and dFe concentrations were “high” compared to Southern Ocean levels (Westerlund and Öhman 1991; Middag et al. 2011, 2013; Browning et al. 2014), Mn limitation is possible in Southern Ocean phytoplankton species with similar Mn requirements.

In recent field experiments, Wu et al. (2019) observed Fe/Mn co-limitation in the haptophyte *Phaeocystis antarctica* from the Ross Sea, using proteomic techniques. Specifically, they observed physiological stress during their experiment in January (austral summer), when dFe and dMn concentrations were depleted: 0.48 and 0.22 nM, respectively. Co-limitation was not observed during

their previous experiment performed a month earlier, where higher dFe and dMn concentrations were measured (1.03 and 0.27 nM, respectively). Consequently, their study was the first to suggest a range of dMn concentrations (0.22 – 0.27 nM) within which dMn concentrations become too low for the optimal growth of *Phaeocystis antarctica*. In the Drake passage, repeated bioassays demonstrated spatial variations in Fe/Mn co-limitation of bulk phytoplankton growth (Browning et al. 2021). In their study, the authors observed Mn (co-)limitation in open ocean waters, whereas Fe-limited sites were found mostly near the coast. When Mn stress was alleviated, they observed changes in carbon and biogenic silicate accumulation, nutrient drawdown, photophysiology and chlorophyll production. They also defined a new parameter Mn* to describe dMn deficiency relative to dFe deficiency for phytoplankton growth, using the following equation: $Mn^* = dMn - dFe / R_{Fe:Mn}$, where dFe is dissolve Fe concentrations and $R_{Fe:Mn}$ is the assumed average Fe:Mn ratio of phytoplankton derived by Moore (2013). Overall, observations of Mn (co-)limitation of natural phytoplankton growth suggest Mn may control primary productivity in specific Southern Ocean region, where the Mn supply does not meet phytoplankton demand. In addition, Mn limitation may vary seasonally as both dFe and dMn concentrations will decrease over the growth season following winter mixing. Hence, we performed the first study of the seasonality of Fe and Mn limitation of phytoplankton growth through repeated field incubations in subantarctic waters, presented in Chapter 4. We also aimed to address how changes in light and Fe conditions can modify Mn requirement by studying deep phytoplankton communities responses to Mn and Fe additions under various light conditions, presented in Chapter 5.

1.8. Thesis objectives and structure

This thesis aims to fill key gaps in our understanding of Mn biogeochemistry by looking at this element distribution in the under-studied Australian sector of the Southern Ocean. In addition, we aim to study the potential role of Mn in limiting phytoplankton growth in this region. To address this, the present work is divided in four data chapters (Chapters 2, 3, 4 and 5). Chapters 2 and 3 focus on Mn distribution/chemistry and Chapters 4 and 5 address Mn's control of primary productivity in this region.

In Chapter 2, dissolved and particulate Mn concentrations are described along the full-depth GEOTRACES-SR3 transect (GS01 in Figure 1.8), between Tasmania and Antarctica. This transect allowed the study of Mn distributions relative to multiple external sources (e.g. hydrothermal vents, sediment resuspension) and highlighted the extremely low dMn concentrations in this region. This work is published in *Limnology and Oceanography* (Latour et al. 2021). The research in Chapter 3 aims to address the hypothesis that the East Antarctic region, specifically George V and Adélie Lands, is exporting Mn-enriched coastal waters toward depleted open Southern Ocean waters. Despite the presence of high Mn concentrations over the East Antarctic shelf, little Mn export occurred through westward/northward coastal current and bottom water transport. This chapter has been submitted as a paper to *Global Biogeochemical Cycles* (GBC).

Considering the very low dMn concentrations observed in the Australian sector of the Southern Ocean (see Chapter 2), the seasonality of Mn limitation of phytoplankton growth was studied in Chapter 4. Three field bioassay experiments were performed in subantarctic waters to look at the seasonality of Fe/Mn co-limitation in this region. We found that Mn(co-)limitation was hard to capture and easily masked by strong responses to Fe additions. However, some interesting responses were observed with Mn additions, such as strengthened summer carbon fixation from microplankton (>20 μm) and autumnal stimulation of picocyanobacteria. In Chapter 5, another bioassay performed in waters south of the PFZ allowed us to gain insights about the natural occurrence of the deep chlorophyll maximum (DCM), a common Southern Ocean feature. We studied the initial conditions of this DCM using a suite of physical, chemical and biological parameters and investigated the effects of Fe, Mn and light on stimulating natural phytoplankton communities.

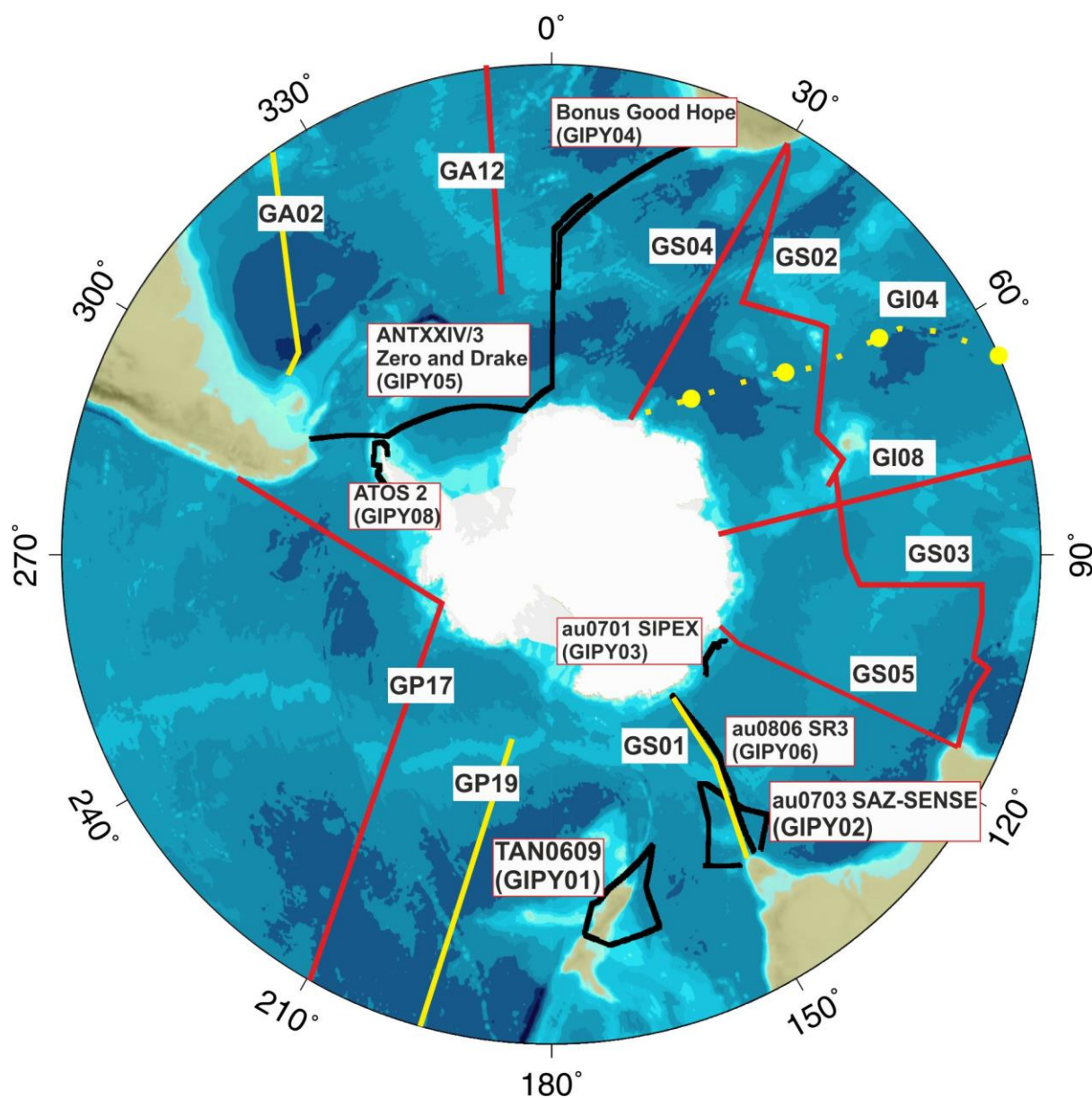


Figure 1.8: Map of GEOTRACES cruises in the Southern Ocean. The yellow, black and red lines indicate completed cruises, International Polar Year cruises and planned cruises, respectively. This map can be found at: https://www.bodc.ac.uk/geotraces/cruises/section_maps/southern_ocean/. In Chapters 2 and 3 of this thesis, we describe data collected along the GS01 transect (yellow line between Tasmania and Antarctica), sampled during the IN2018-V01 voyage onboard RV *Investigator*.

Overall, this thesis improves our understanding of Mn biogeochemistry in the Southern Ocean. With this valuable new dataset added to the GEOTRACES database, we gained insights on Mn chemistry in this region and on important external sources, notably with the identification of deep inputs from hydrothermal vents. Finally, this thesis provides knowledge on how Mn concentrations control primary productivity in this region and highlights the need to study the Mn requirements of Southern Ocean phytoplankton to further our current understanding of the biological component of the Mn cycle.

2. CHAPTER 2 – Manganese biogeochemistry in the Southern Ocean, from Tasmania to Antarctica

The following chapter has been published in *Limnology and Oceanography*.

Latour, P.; Wuttig, K.; van Der Merwe, P.; Strzepek, R. F.; Gault-Ringold, M.; Townsend, A. T.; Holmes, T. M. ; Corkill, M. & Bowie, A. R. (2021). **Manganese biogeochemistry in the Southern Ocean, from Tasmania to Antarctica**. *Limnology and Oceanography*, [Doi 10.1002/lno.11772](https://doi.org/10.1002/lno.11772)

2.1. Introduction

The control of ocean primary productivity by trace metals has been intensively studied for the last three decades after Martin (1990) hypothesized that low iron (Fe) concentrations could limit phytoplankton growth in High-Nutrient, Low-Chlorophyll (HNLC) areas (e.g. Boyd et al. 2000; Bowie et al. 2009). These HNLC areas are characterized by very low primary productivity despite high concentrations of macronutrients present, such as nitrate and phosphate (PO_4^{3-}). The Southern Ocean is the largest HNLC area and has great influence on the global marine carbon cycle, and therefore on climate (Boyd et al. 2000; Pardo et al. 2017). However, carbon uptake in this region varies greatly over space and time (Pardo et al. 2017). An understanding of the parameters that limit phytoplankton growth in this region is essential to help constrain the sensitivity of the biological carbon pump to changing ocean conditions.

Earlier studies have determined the role of Fe, as well as light and silicic acid (north of the Polar Front) in limiting phytoplankton growth (e.g. Boyd et al. 2000; Bowie et al. 2009). Recent studies have suggested that trace metal co-limitation in the Southern Ocean and Antarctic waters may be more important than previously thought (Middag et al. 2011; Browning et al. 2014; Wu et al. 2019). Trace metals such as cobalt (Co), copper (Cu), Mn, nickel (Ni) and zinc (Zn), are required in various proportions relative to Fe for essential cellular functions. Co-limitation occurs when these trace metals are not present in high enough concentrations to allow full utilisation of macronutrients by phytoplankton (Saito et al. 2008; Twining and Baines 2013).

Among the studies published on co-limitation, and despite some contradictory results (Buma et al. 1991; Scharek et al. 1997; Sedwick et al. 2000), Mn is considered important (Coale 1991; Middag et al. 2013; Browning et al. 2014) due to its essential role in photosynthesis (Sunda and Huntsman 1983) and protection against oxidative stress from reactive oxygen species (ROS), especially for diatoms (Peers and Price, 2004; Wolfe-Simon et al. 2006). After Fe and Zn, Mn is an equal third with Ni and Cu in terms of biological requirement (Twining and Baines 2013). A recent study on Southern Ocean phytoplankton species provided evidence of strong physiological effects of Fe and Mn co-limitation (Wu et al. 2019). Changes in protein expression were observed during lab-based experiments on *Phaeocystis antarctica*, related to the availability of both Fe and Mn. These proteomic changes were applied as a tool to identify Fe and Mn stress in natural populations in the coastal surface waters of Antarctica (Wu et al. 2019). Another study demonstrated the potential for Fe and Mn co-limitation,

observing higher growth and carbon fixation rates in the Southern Ocean diatom, *Chaetoceros debilis*, only when both Fe and Mn were replete (Pausch et al. 2019). These results suggest that Mn availability may play a key role in Southern Ocean productivity.

Manganese is characterized by three oxidation states in seawater (Mn(II), Mn(III), Mn(IV)) and a rather complex cycle in aquatic environments, impacted by multiple redox reactions (Wuttig et al. 2013). Additionally, Mn concentrations can be affected by external inputs, such as aerosols (Xu and Gao 2014), sedimentary (Cheize et al. 2018), hydrothermal vents (Klinkhammer and Bender 1980; Holmes et al. 2017), rivers (Aguilar-Islas and Bruland 2006) and melting sea ice (Sedwick et al. 2000; Middag et al. 2013). The vertical distribution of its dissolved phase, long considered to be mainly Mn(II), is usually characterized by higher concentrations at the surface, maintained chiefly by the photoreduction of Mn(III/IV) oxides (MnOx) and by the photoinhibition of microbially-mediated Mn(II) oxidation to MnOx (Sunda and Huntsman 1994). Underlying these high surface concentrations, dissolved Mn (dMn) decreases with depth due to scavenging processes (Sunda and Huntsman 1994). Several Southern Ocean studies have shown vertical distributions of dMn that differ from the typical profile: relatively low dMn concentrations (i.e. 0.03 – 0.04 nM) were measured in surface waters, which are thought to be due to phytoplankton uptake and few external inputs; low concentrations are maintained with increasing depth due to scavenging processes (Klinkhammer and Bender 1980; Westerlund and Öhman 1991; Middag et al. 2011); and near the seafloor, dMn concentrations can increase due to sedimentary inputs (Middag et al. 2011).

Compared to dMn, few studies have looked at the concentrations of particulate Mn (pMn) in Southern Ocean waters (Westerlund and Öhman 1991; Fitzwater et al. 2000; Bowie et al. 2009) and there is, to our knowledge, no study that has looked at the different fractions of pMn (e.g. labile and refractory) in these waters. Particulate Mn – composed of MnOx, Mn adsorbed onto particles, Mn within lattices of minerals and Mn inside phytoplankton – is usually characterized by very low concentrations in surface waters that increase with depth (Sunda and Huntsman 1994). This increase is thought to be mainly biotic and related to the decrease of the photoreduction and photoinhibition processes below the photic zone, allowing microbes to oxidize Mn(II) to MnOx (Sunda and Huntsman 1994).

The oceanographic circulation and low sea-ice extension along the SR3 section, between Tasmania and Antarctica, offers an interesting area to study the distribution of trace metals in the Southern Ocean (Sedwick et al. 2008). This section crosses various biogeochemical regions and oceanographic fronts (Sokolov and Rintoul 2002), allowing characterisation of a wide range of external sources. The physical oceanography of this area has been studied in detail since the early 1990s (Rintoul and Bullister 1999), and Fe, along with other trace metals such as Cd, Co, Ni and Zn, have been studied on or near this transect since the late 1990s (Sedwick et al. 1997; Sedwick et al. 2008; Butler et al. 2013). However, comparatively few Mn data have been reported (Sedwick et al. 1997; Bowie et al. 2009).

In this study, processes controlling Mn distributions are studied along the SR3 transect. Correlations between Mn and PO_4^{3-} observed in the dissolved and particulate phases are used to study the biological control of surface dMn. Links between the dissolved and particulate pools are investigated. We also aimed to identify the external sources which supply dMn and pMn along this transect.

2.2. Material and methods

2.2.1. SAMPLING

Samples were collected onboard the R/V *Investigator* in the Austral summer of 2018 (10th January – 22nd February) during the GEOTRACES expedition IN2018_V01 along the SR3 section (44°S-65.7°S, 140-147°E), in the Australian sector of the Southern Ocean, between Tasmania and Antarctica (Figure 2.1).

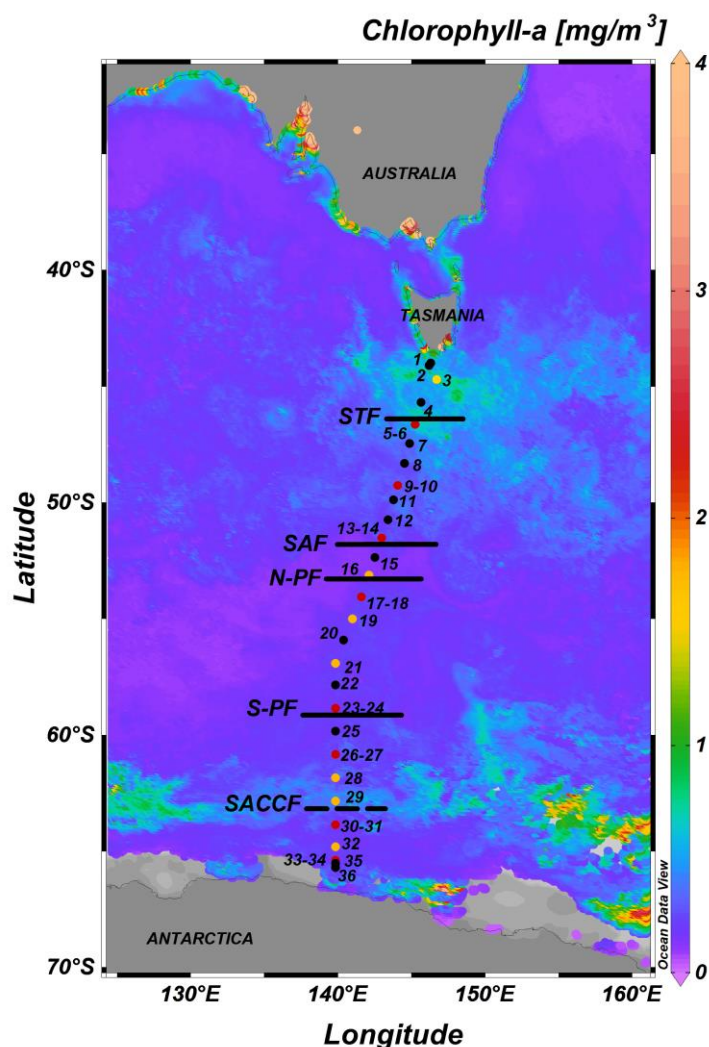


Figure 2.1: Chlorophyll-*a* map showing details of the stations sampled during IN2018-V01 along SR3. The coloured dots represent different station types. Black dots: shallow casts with high resolution (surface to 1500m depth); yellow dots: deep casts with lower resolution deep casts (surface to seafloor). Oceanographic fronts are indicated as: STF: Subtropical Front; SAF: Subantarctic Front; N-PF: North Polar Front; S-PF: South Polar Front; SACCF: Southern Antarctic Circumpolar Front. The background image colour shading represents satellite

average Chlorophyll-a concentration data (MODIS-Aqua, monthly average 4 km) for the period January-February 2018 (<https://giovanni.gsfc.nasa.gov/giovanni/#>).

Of the 28 sites sampled along SR3, 13 stations were shallow trace metal rosette (Sea-bird Scientific) casts with high resolution sampling in the top 1500 m of the water column, seven stations were deep trace metal rosette casts with lower sample resolution but a complete profile to the bottom of the ocean, and eight were “super-stations” sampled with two trace metal rosette casts: one shallow focusing on the first 1500 m of the water column and a second sampling between 1500 m and the seafloor (Figure 2.1). The trace metal rosette was equipped with 12 x 12 L externally-closing Teflon-coated Niskin bottles (Ocean Test Equipment) that were cleaned following GEOTRACES recommendations (Cutter et al. 2017) and initially conditioned with an open ocean seawater test cast at 300 m. Every trace metal rosette deployment was undertaken with strict adherence to trace metal clean precautions to minimise external contamination sources (Cutter et al. 2017). Samples for both dissolved and particulate trace metals were collected from the trace metal rosette.

Eight in-situ pumps (McLane Research Laboratories, WTS-LV) were also deployed at the super-stations for complementary high-volume sampling of suspended trace-metal particle concentrations. Subsamples of the 0.8 µm porosity SUPOR® filters were used to qualitatively observe phytoplankton assemblages under the microscope.

2.2.2. TRACE-METAL SAMPLE PROCESSING

All dissolved trace-metal samples were collected following the GEOTRACES protocols including sample bottle and sampling equipment preparation, sample handling, and storage (Cutter et al. 2017). After sample collection, all Niskin bottles were immediately transferred into an ISO Class 5 containerized cleanroom. Seawater filtration was performed using a 0.2 µm trace-metal clean filter cartridge (AcroPak™ 200, Pall), under a continuous laminar flow of HEPA filtered air. Filter cartridges were acid-cleaned, rinsed three times with Ultra High Purity water, and rinsed three times with seawater before each sampling (Cutter et al. 2017). Low density polyethylene bottles (Nalgene) were used to sample dissolved trace metals. These bottles were previously washed using Decon 90 for one week followed by 6 M reagent grade hydrochloric acid (HCl) for four weeks and were stored with 1 M trace-metal grade HCl for a minimum of four weeks. Sample bottles were also rinsed three times with filtered seawater before sample collection. Filtered seawater samples were then acidified with HCl, previously distilled using a Savillex PFA distillation system (DST-1000) to a final concentration of 0.024 M (pH = 1.8), double bagged and stored at room temperature, until analyses onshore at the Institute for Marine and Antarctic Studies (Hobart, Australia).

For total particulate trace-metal samples, Niskin bottles were inverted several times to homogenise the particles and an unfiltered subsample was then decanted into 4L acid-washed low density polyethylene bottles (Nalgene) and placed into a custom-made filtration apparatus (see Materials and Methods in van

der Merwe et al. 2019). The samples were then drawn under vacuum through paired 25 mm acid-cleaned 0.8 µm SUPOR® (PES) filters, with an effective 0.4 µm size cut-off (Bishop et al. 2012). After filtration, each pair of filters were stored in acid-cleaned petri-dishes at -20°C until analyses onshore. Subsamples from in situ pumps were subjected to a chemical leach as described in Berger et al. (2008) to separate the chemically labile from the refractory fractions while the filters from the direct filtration of the Niskin bottles were analysed for total elemental composition as detailed below. At some stations, due to the lower sampling resolution of the in situ pumps (e.g. 3 data points in the Antarctic zone, above the depth of dMn remineralization), elemental ratios were calculated in both the total and labile particulate fractions.

2.2.3. HYDROGRAPHIC DATA AND MACRONUTRIENTS

All stations presented in this study (Figure 2.1) and additional hydrography- and macronutrient-only stations were sampled using a 36-bottle Conductivity-Temperature-Depth rosette that also measured oxygen (Sea-Bird Electronics sensors: SBE4C, SBE3T, SBE9plus, and SBE43). All sensors were calibrated prior to the voyage and subsequently quality controlled by the Australian Marine National Facility. Dissolved macronutrients (nitrate, nitrite, PO₄³⁻, silicic acid and ammonia) were analysed onboard using segmented flow analysis (Rees et al. 2018).

2.2.4. TRACE METAL PRECONCENTRATION AND ANALYSIS

Dissolved trace-metal samples were preconcentrated onshore prior to analysis using an automated *seaFAST* system (SC-4 DX *seaFAST* S2 / pico, ESI, USA) in offline mode. This system uses two columns filled with Nobias PA1 resin, one for buffer clean-up and the second one for trace metal preconcentration (a preconcentration factor of 40-67-fold was employed) and matrix removal, following the method of Wuttig et al. (2019). Each batch of samples (usually three stations per day) included a standard addition seawater calibration, multiple blanks, certified reference material (NASS-6), community GEOTRACES reference samples (GEOTRACES deep water GD, GEOTRACES Pacific surface seawater GSP and GEOTRACES coastal surface seawater GSC), and an in-house seawater standard, collected during the SR3 voyage. Controls were analysed repeatedly at regular intervals throughout the processing period to ensure continued accuracy and precision of the method. Manganese showed good column recoveries following *seaFAST* preconcentration (average recoveries 98 ± 8 %, n=20). After preconcentration, dissolved trace metal concentrations were determined using a Thermo Fisher ELEMENT 2 Sector Field Inductively Coupled Plasma Mass Spectrometry (SF-ICP-MS) (Central Science Laboratory, University of Tasmania). Increased (“medium”) spectral resolution was employed for the analysis of Mn, with Rhodium (Rh) used as an internal standard. The detection limit for dMn was 0.002 nM at both preconcentration factors of 40 and 67 (n=30 and n=51, respectively). Data generated from the SF-ICP-MS were processed using the *seaFAST* R script (Rijkenberg 2016).

More details on the procedure, analytical techniques and a critical method evaluation have been presented in Wuttig et al. (2019).

Total particulate trace-metal samples were measured using a SF-ICP-MS, after digesting the paired filters following Bowie et al. (2010). Briefly, concentrated and ultrapure acids were used: HCl, nitric acid and hydrofluoric acid in pre-cleaned 15mL Teflon PFA vials (Savillex Corp., USA). Acidified samples were digested at 120°C for 12 h and dried overnight at 90°C. Residues were resuspended in 10% nitric acid (including an Indium internal standard) before analysis following van der Merwe et al. (2019). For this method, the recoveries were checked with a total digestion of certified reference material BCR414 samples with an average recovery of 90 ± 0.1 % ($n = 3$) for Mn during this analytical run.

The filter pairs from the in situ pumps were subjected to a chemical leach to separate the refractory trace metal component from the chemically labile fraction (Berger et al. 2008; van der Merwe et al. 2019). The chemically labile fraction is considered to be more bio-available while the refractory fraction is considered insoluble and unavailable to phytoplankton (Berger et al. 2008). The labile fraction was extracted from subsampled filters with acetic acid and hydroxylamine hydrochloride solution, and finally analysed via SF-ICP-MS in a 10 % nitric acid matrix. The refractory fraction was analysed via total digestion of the leachate residue on each filter, using a mixed solution of HCl, nitric and hydrofluoric acid. The Berger leach was verified by comparing the sum of the labile and refractory fraction with the total digest of a subsample. The recoveries were on average 107 ± 13.4 % ($n = 4$) for Mn. During data processing, all values below the detection limit (after blank subtraction) were removed.

2.2.5. STATISTICAL ANALYSIS

To evaluate biological control over the Mn cycle, dMn concentrations were plotted against dissolved PO_4^{3-} concentrations using a linear regression model from the R “stats” package (R Core Team, 2020). Only values above the dMn subsurface maximum were used, according to the methods of Middag et al. (2011, 2013). Briefly, dMn concentrations at the subsurface maximum are assumed to be influenced by remineralization, while values above the subsurface maximum are assumed to be mainly impacted by biological uptake (Middag et al. 2013).

To compare this dataset with Mn:P ratios measured in phytoplankton samples from the literature, the means and standard deviations of pMn divided by particulate phosphorus were calculated for the total and labile particulate fraction.

2.3. Results and discussion

2.3.1. HYDROGRAPHY

Salinity, temperature and oxygen values measured along the SR3 2018 transect were used to identify the water masses, as well as to define the position of the oceanographic fronts (Figure 2.2). Five

biogeochemical areas were defined according to the fronts: the Subtropical Zone, the Subantarctic Zone, the Polar Frontal Zone, the waters between the northern and southern branch of the Polar Front, hereafter referred to as Polar Front Waters and the Antarctic Zone. The Subtropical Front separates the warm ($>11^{\circ}\text{C}$) and salty ($>35\text{ g kg}^{-1}$) surface waters of the Subtropical Zone from the colder and fresher Subantarctic Zone waters ($9\text{-}11^{\circ}\text{C}$ and $<35\text{ g kg}^{-1}$) (Pardo et al. 2017). The delineation of the Subantarctic Front, south of the Subantarctic Zone, was complicated in this study by the presence of a cyclonic eddy, that transported cooler and fresher waters from the south toward the north (P. C. Pardo, pers. comm.). The deep and strong signature of the eddy is visible along the transect (Figure 2.2), highlighted by the red dashed rectangle. South of the Subantarctic Front, the Polar Frontal Zone waters were even colder ($<7^{\circ}\text{C}$) with salinities below 34 g kg^{-1} . The Polar Front crossed the SR3 section twice during IN2018-V01, as previously described (Sokolov and Rintoul 2002; 2009). Therefore, the two intersections with SR3 will be referred to as North-Polar Front and South-Polar Front, defined as the northern extension of the surface oxygen maximum (North-Polar Front) and as the northernmost limit of the 0 to 1°C isotherms (South-Polar Front) (Sokolov and Rintoul 2002). One last area was considered south of the South-Polar Front, the Antarctic Zone, with water temperatures typically below 2.5°C , but reaching negative values close to Antarctica. The extent of the Antarctic Circumpolar Current is also illustrated (Figure 2.2), reaching from the Subtropical Front to the Southern Antarctic Circumpolar Current Front. The Southern Antarctic Circumpolar Current Front was identified as the southern extension of subsurface oxygen minimum concentration. The Antarctic Zone south of the Southern Antarctic Circumpolar Current Front will be referred to as the Antarctic slope. The deep water masses along the SR3 section have also previously been described and discussed in detail (Sokolov and Rintoul 2002; Pardo et al. 2017).

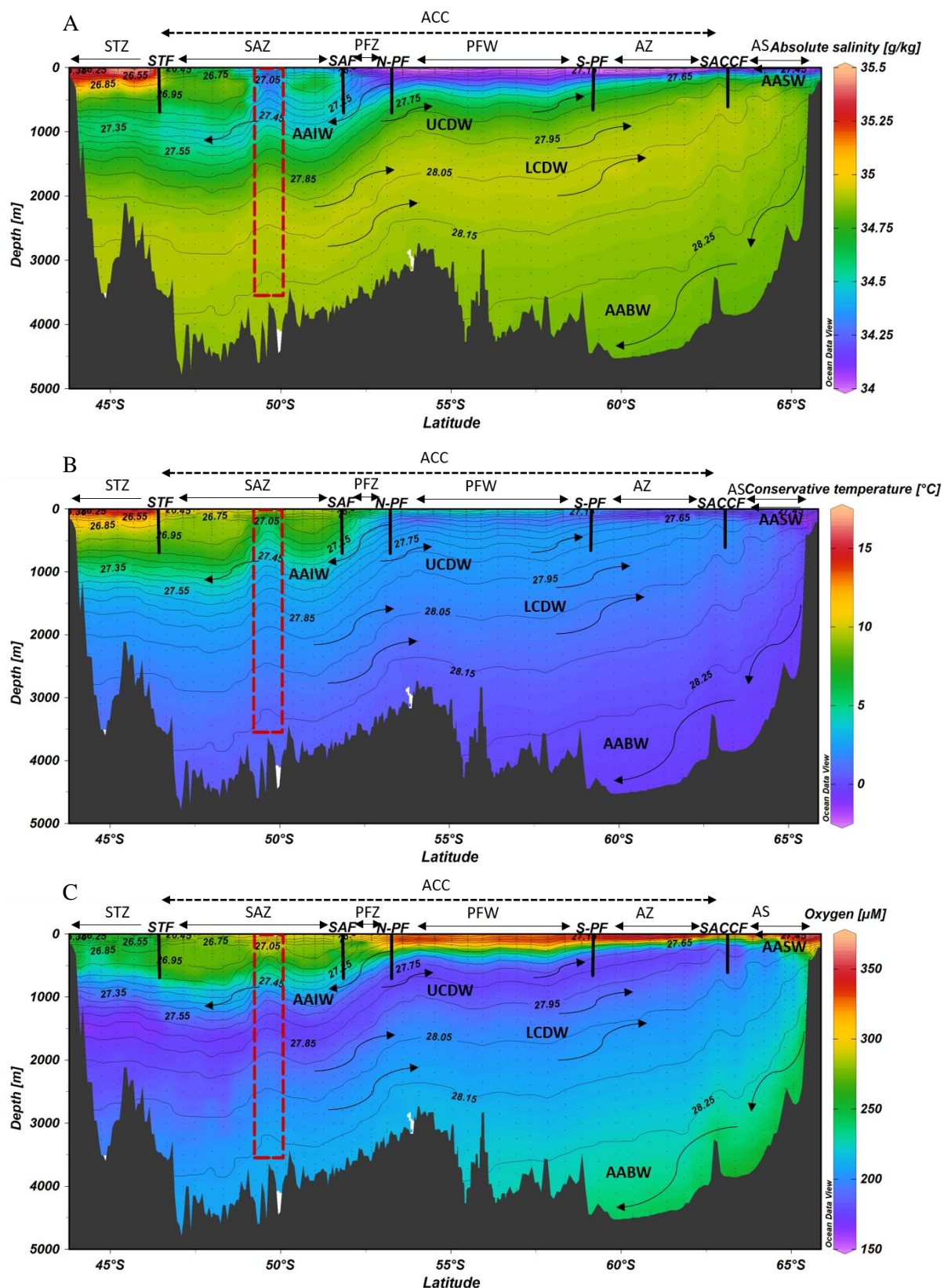


Figure 2.2: Absolute salinity (A), conservative temperature (B), and oxygen (C) distribution along the 2018 SR3 transect. The colour represents the parameter value (absolute salinity, conservative temperature and oxygen). The contour lines represent the neutral densities ($\text{kg}\cdot\text{m}^{-3}$). Fronts: Subtropical Front (STF), Subantarctic Front (SAF), North-Polar Front (N-PF), South-Polar Front (S-PF) and Southern Antarctic Circumpolar Current Front (SAACF). Biogeochemical regions: Subtropical Zone (STZ), Subantarctic Zone (SAZ), the Polar Frontal Zone (PFZ), Polar

Front Waters (PFW), Antarctic Zone (AZ) and Antarctic slope (AS). The extent of the Antarctic Circumpolar Current is indicated as ACC. Water masses: Antarctic Intermediate Water (AAIW), Upper and Lower Circumpolar Deep Water (UCDW – LCDW), Antarctic Surface Water (AASW) and Antarctic Bottom water (AABW). The arrows show a simplified flow. The red dotted rectangle indicates the position of a cyclonic eddy observed during the voyage.

2.3.2. UNIFORMLY LOW MN CONCENTRATIONS

Low dMn concentrations were found along most of the SR3 transect (Figure 2.3; total average: 0.32 ± 0.28 nM, $n=371$, Table 2.1). This is typical for Southern Ocean and Antarctic coastal waters. Previous studies have measured dMn concentrations ranging from 0.03 to 3.1 nM, but mostly below 0.5 nM, especially in open ocean waters (Klinkhammer and Bender 1980; Middag et al. 2011; Browning et al. 2014). In this study, dMn depth profiles in the open ocean (from the Subantarctic Zone to the Antarctic Zone) followed the same shape as reported in the literature previously (Sedwick et al. 1997; Middag et al. 2011) with minimum dMn concentrations measured in surface waters, as low as 0.06 nM measured in the Antarctic Zone, followed by a subsurface maximum, more or less pronounced, observed between 100 and 200 m and attributed to particle remineralization (Middag et al. 2011). Below these subsurface maxima, deep dMn concentrations were generally low (mostly < 0.25 nM). The lowest deep dMn concentrations were observed in the Polar Front Waters and Antarctic Zone as shown by the full-depth average values (Table 2.1).

Table 2.1: Average dissolved Mn concentrations (nM) measured across the whole water column and within the mixed layer depth (MLD) for each area along SR3: Subtropical zone (STZ) $n= 41$ and 11 ; Subantarctic zone (SAZ) $n= 102$ and 27 ; Polar Front Zone (PFZ) $n= 24$ and 8 ; Polar Front Waters (PFW) $n=84$ and 20 ; Antarctic Zone (AZ) $n= 53$ and 11 ; Antarctic Slope (AS) $n= 67$ and 16 .

Area	STZ	SAZ	PFZ	PFW	AZ	AS
Average conc. (full depth)	0.66	0.32	0.29	0.26	0.19	0.31
SD	± 0.45	± 0.20	± 0.10	± 0.36	± 0.06	± 0.13
Average conc. (within MLD)	0.80	0.24	0.23	0.16	0.11	0.21
SD	± 0.14	± 0.08	± 0.05	± 0.05	± 0.05	± 0.06

The total pMn concentrations were also very low (Figure 2.3C and Table 2.2), characterized in the open ocean by low surface minima, a common feature due to the photoreduction of MnOx (Sunda and Huntsman 1994). However, the low surface dMn concentrations might also suggest that the supply of MnOx to the surface waters of this Southern Ocean region is low. Following this surface minimum, slightly increasing total pMn concentrations were observed with depth, likely due to the oxidation of Mn(II) to MnOx (Sunda and Huntsman 1994). The ratio of labile to total pMn shows that the labile fraction accounted for 51 to 63 % (regional averages) of pMn in the upper 1500 m along the transect (Figure 2.4). This ratio is lower than the previously reported labile fraction of over 70 % of the total pMn in the North Atlantic (Twining et al. 2015). This may suggest either: 1) less MnOx inputs in this region as MnOx are thought to dominate labile pMn (Sunda and Huntsman 1988; Twining et al. 2015) or 2) the observed pMn increase with depth may result from processes other than Mn(II) oxidation. These results also indicate that pMn composition in the Southern Ocean might differ from other ocean basins, possibly due to higher lithogenic or refractory fraction.

Table 2.2: Average total, labile and refractory particulate Mn concentrations (nM) measured across the whole water column for each area along SR3: Subantarctic zone (SAZ) n= 40, 24 and 24; Polar Front Waters (PFW) n=38, 8 and 8; Antarctic Zone (AZ) n= 30, 16 and 16; Antarctic Slope (AS) n= 38, 16 and 16.

Area	SAZ	PFW	AZ	AS
Average conc.	0.044	0.058	0.039	0.074
total				
SD	±0.03	±0.05	±0.03	±0.07
Average conc.	0.027	0.022	0.029	0.025
labile				
SD	±0.019	±0.012	±0.013	±0.016
Average conc.	0.021	0.013	0.017	0.023
refractory				
SD	±0.013	±0.007	±0.009	±0.016

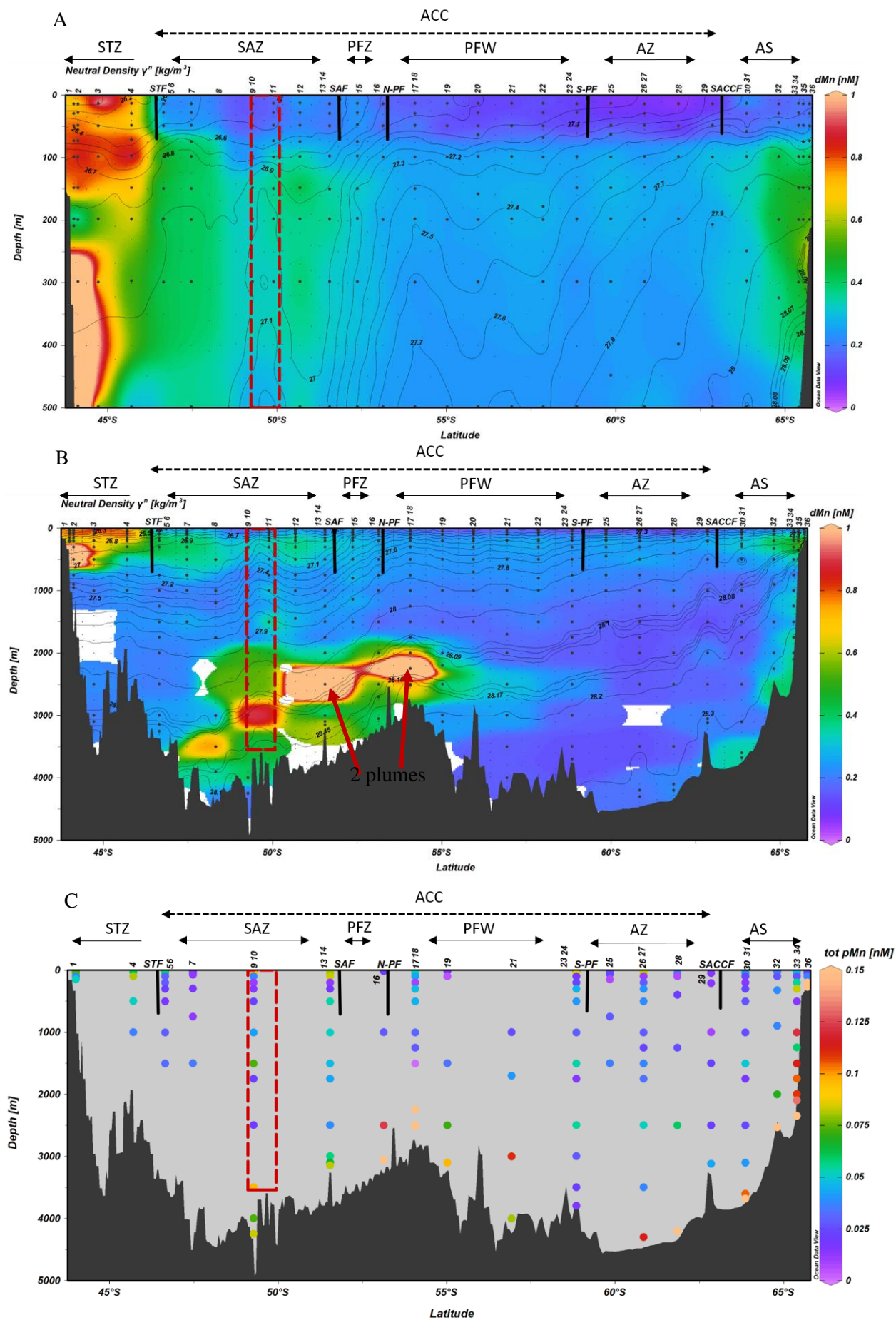


Figure 2.3: Section of dissolved Mn (dMn) concentrations along the SR3 transect from North to South for 0-500 m (A) and 0-5000 m (B) and section of total particulate Mn (tot pMn) for 0-5000 m (C). Stations numbers are indicated at top (double numbers for super-stations). The bathymetry comes from the GEBCO_2014_Grid, version 20141103, <http://www.gebco.net>. Fronts: Subtropical Front (STF), Subantarctic Front (SAF), North-Polar Front (N-PF), South-Polar Front (S-PF) and South Antarctic Circumpolar Current Front (SAACF). Biogeochemical regions: Subtropical Zone (STZ), Subantarctic Zone (SAZ), the Polar Frontal Zone (PFZ), Polar Front Waters (PFW), Antarctic Zone (AZ) and Antarctic slope (AS). The extent of the Antarctic Circumpolar Current is indicated as ACC. The red dotted rectangle indicates the position of a cyclonic eddy observed during the voyage. We identified at least two hydrothermal plumes (indicated on 3B) but we suspect there may be multiple plumes present.

Significant negative correlations between dMn and labile pMn were observed over the entire water column in the Subantarctic Zone ($R^2 = 0.32$; $p < 0.05$; $n = 23$), Polar Front Waters ($R^2 = 0.39$; $p < 0.05$; $n = 16$) and Antarctic Zone ($R^2 = 0.65$; $p < 0.05$; $n = 7$). These results support both following hypotheses: 1) dMn is transformed into labile pMn through biological uptake or scavenging by biogenic particles and 2) the deep production of MnOx is through bacterially-mediated Mn(II) oxidation. Further Southern Ocean MnOx measurements remain essential to confirm the second hypothesis. The strongest correlation between dMn and labile pMn was observed in the Antarctic Zone, which is the region least impacted by external inputs (see next section). Few external inputs are one factor explaining the low dMn surface concentrations commonly observed in the Southern Ocean (Klinkhammer and Bender 1980; Middag et al. 2013). Biological uptake is likely the other major process maintaining low dMn surface concentrations in this region (Sedwick et al. 1997; Middag et al. 2011, 2013), which is supported by the negative correlations between dMn and labile pMn reported here.

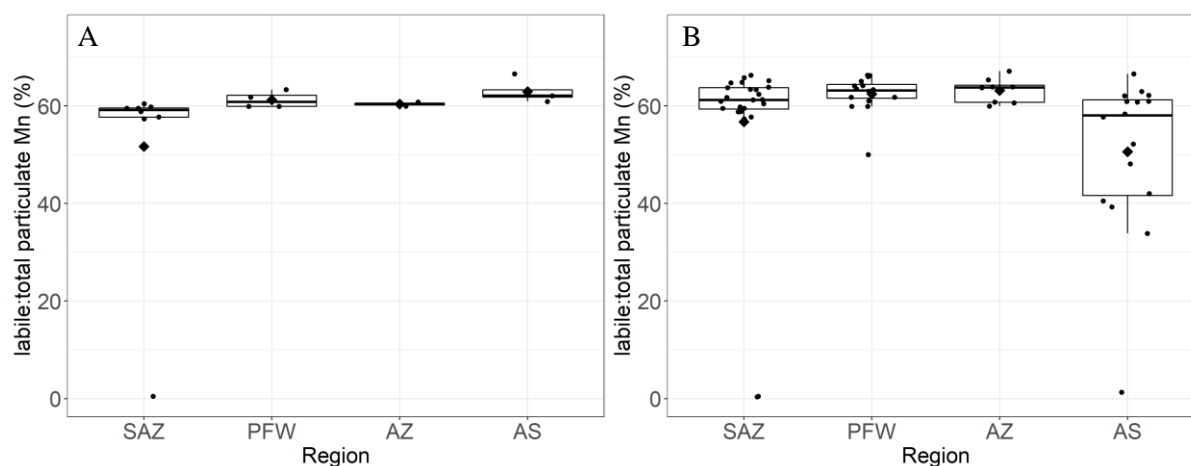


Figure 2.4: Box and whisker plots of labile to total particulate Mn ratio (%) for each region along SR3: Subantarctic Zone (SAZ); Polar Front Waters (PFW); Antarctic Zone (AZ); Antarctic Slope (AS). A: Mixed Layer Depth; B: 0 - 1500 m. The mean is represented with a filled diamond shape for each region.

2.3.3. BIOLOGICAL CONTROL OF SURFACE DISSOLVED MN

The correlation between dMn and dissolved PO_4^{3-} above the dMn subsurface maximum was compared using a linear regression along SR3, divided by biogeochemical regions (Table 2.3). The Subantarctic Zone and Polar Front Waters (the latter included both stations from the Polar Frontal Zone) exhibited significant but weak relationships between dMn and dissolved PO_4^{3-} ($R^2 = 0.21$, $p < 0.05$, $n = 23$ and

$R^2 = 0.32$, $p < 0.05$, $n = 27$, respectively). Further south, the Antarctic Zone showed a much stronger relationship between dMn and dissolved PO_4^{3-} ($R^2 = 0.72$, $p < 0.05$, $n = 12$), as well as a very low dMn patch at the surface (Figure 2.3A), with a 0.06 nM dMn minimum (station 28 at 14 m). This value is close to the lowest dMn concentrations ever measured: 0.034 nM in the surface waters of the Drake passage (Browning et al. 2014) and 0.04 nM in the Atlantic sector of the Southern Ocean (Middag et al. 2013). This region was characterized by high total pMn surface concentrations with 0.09 nM measured at 30 m at station 26 (Figure 2.3C), indicating transfer from dMn to pMn, due to biological uptake. The strongest interaction between dMn and dissolved PO_4^{3-} was located above the Antarctic slope ($R^2 = 0.81$, $p < 0.05$, $n = 21$) and coincided with high total pMn values at station 30, with 0.06 nM measured at 20 m.

Table 2.3: Relations calculated between dissolved Mn (dMn) and dissolved PO_4^{3-} , above the dMn subsurface maximum, for the Subantarctic Zone (SAZ), the Polar Front Waters (PFW), the Antarctic Zone (AZ) and the Antarctic Slope (AS) data. Asterisk (*) indicate a p-value below 0.05.

Region	Equation (dMn vs dPO_4^{3-})	R^2	n
SAZ	$\text{dMn} = 0.20 * \text{dPO}_4^{3-} - 0.02$	0.21*	23
PFW	$\text{dMn} = 0.20 * \text{dPO}_4^{3-} - 0.16$	0.32*	27
AZ	$\text{dMn} = 0.21 * \text{dPO}_4^{3-} - 0.24$	0.72*	12
AS	$\text{dMn} = 0.62 * \text{dPO}_4^{3-} - 0.95$	0.81*	21

The significance of the correlations between dMn and dissolved PO_4^{3-} supports the hypothesis of biological influence over the dMn surface distributions, which seems to strengthen from north to south. The slope of the relationship between dMn and dissolved PO_4^{3-} was used to calculate Mn to PO_4^{3-} (Mn:P) slope derived uptake ratios. These ranged from 0.20 to $0.62 \times 10^{-3} \text{ mol mol}^{-1}$, showing a greater variance along the SR3 transect compared to the relatively constant Mn:P ratio of 0.36 to $0.39 \times 10^{-3} \text{ mol mol}^{-1}$ observed in the Atlantic sector of the Southern Ocean and the central Weddell Sea (Middag et al. 2011). This could suggest differences in the Mn requirements of the phytoplankton communities and/or additional processes controlling the dMn cycle along SR3 (e.g. external sources).

The Mn:P ratio in phytoplankton is a useful tool for estimating biological Mn requirements. In the Southern Ocean, Twining et al. (2004) reported ratios ranging from $0.14 \times 10^{-3} \text{ mol mol}^{-1}$ for heterotrophic cells to $0.42 \times 10^{-3} \text{ mol mol}^{-1}$ for diatoms via synchrotron x-ray fluorescence techniques. Although this method was not used in the present study, bulk analysis of particulates can provide some insights. Along SR3, the labile particulate Mn:P ratios vary from 0.33 to $0.71 \times 10^{-3} \text{ mol mol}^{-1}$ (Table 2.4). The lowest ratio was measured in the Antarctic Zone and falls within the range of the Mn:P ratio measured in diatoms (Twining et al. 2004). On the other hand, the highest ratio was measured in the

Subantarctic Zone and is closer to the labile particulate Mn:P ratio measured nearby at the Southern Ocean Time Series (SOTS, 46.80°S, 141.884°E) station in the upper 75 m, in autumn 2018 ($1.34 \pm 0.74 \times 10^{-3} \text{ mol mol}^{-1}$; B. Twining, pers. comm.). Labile particulate Mn:P ratios calculated from filtered material have been observed to overestimate the biogenic Mn due to scavenging of MnOx onto particles (Twining et al. 2015). Therefore, this high Subantarctic Zone labile Mn:P ratio may indicate either an actual higher phytoplankton Mn:P ratio or excess of MnOx, resulting from 1) direct MnOx input in this region, likely Australian continental sources or 2) dMn inputs in this region and transfer of dMn toward labile pMn through Mn(II) oxidation. The same hypothesis can be made for the high labile particulate Mn:P ratio observed above the Antarctic slope (Table 2.4).

Table 2.4: Means and standard deviations of Mn:P ratios ($\times 10^{-3} \text{ mol mol}^{-1}$) in the labile and total particulate fraction for the Subantarctic Zone (SAZ), the Polar Front Waters (PFW), the Antarctic Zone (AZ) and the Antarctic Slope (AS) data, above the dissolved Mn subsurface maximum

Fraction	Region	Means	SD	n
Labile	SAZ	0.71	0.31	8
	PFW	0.34	0.88	5
	AZ	0.33	0.24	3
	AS	0.58	0.27	6
Total particulate	SAZ	0.62	0.12	11
	PFW	0.36	0.11	7
	AZ	0.38	0.15	7
	AS	1.27	1.50	11

The total particulate Mn:P ratios range from 0.36 to $1.27 \times 10^{-3} \text{ mol mol}^{-1}$ (Table 2.4). The Subantarctic Zone displays a lower Mn:P ratio in the total particulate fraction compared to the Mn:P ratio in the labile fraction. In this region, the proportion of labile to total pMn ($56.7 \pm 17.5 \%$, Figure 2.4) was higher than the proportion of labile to total particulate phosphorus ($50.4 \pm 2.34 \%$), suggesting that the relatively high proportion of labile Mn in this total particulate pool is driving the variation between the two Mn:P ratios. In the Subantarctic zone, higher contribution of labile pMn may suggest MnOx formation or advection, MnOx scavenging onto particles, or uptake by cells susceptible to the weak chemical leach used in this method. Conversely, over the Antarctic slope, the total particulate Mn:P ratio is much higher ($1.27 \times 10^{-3} \text{ mol mol}^{-1}$) than the labile particulate Mn:P ratio ($0.58 \times 10^{-3} \text{ mol mol}^{-1}$) (Table 2.4). In this region, the proportions of labile to total pMn and phosphorus are both close to 50 % and the wide range displayed in the labile to total pMn over the Antarctic slope (Figure 2.4B) may indicate lithogenic or other deep inputs with lower chemical lability (van der Merwe et al. 2019). In this

case, non-labile pMn seems to drive the variation between the two Mn:P ratios. In contrast, the total particulate and labile particulate Mn:P ratios measured in the Polar Front Waters and Antarctic Zone are comparable (Table 2.4). Their similarity to the ratios measured by Twining et al. (2004) in Fe-stressed diatoms ($0.42 \times 10^{-3} \text{ mol mol}^{-1}$) may indicate the presence of such communities along SR3. Iron limiting conditions are expected along SR3 in late summer, as the dissolved Fe (dFe) concentrations are strongly decreased during the bloom season (Bowie et al. 2009). The production of ROS is enhanced under Fe-limiting conditions, which may lead to a higher Mn requirement for diatoms if they rely on the Fe/Mn class of superoxide dismutase for ROS detoxification (Peers and Price 2004). Additionally, ROS production can increase in the case of photoinhibition, which has been suggested to be important in Southern Ocean waters characterized by deep mixed layer depth (Alderkamp et al. 2010). Qualitative microscopic observations of filtered phytoplankton assemblages during this cruise support the hypothesis of diatom dominance along SR3, however, these observations do not replace a quantitative study of the natural phytoplankton assemblage in this region. Non-silicified species such as haptophytes or flagellates are poorly conserved on high volume filtration systems, as used in this study, which may bias microscopic results toward diatoms. Additionally, derived Mn:P ratios from bulk particulate samples have already been shown to be difficult to interpret because the phytoplankton elemental composition varies with the taxonomic assemblage, the cellular growth rate, the environmental trace metal concentrations (Twining et al. 2004) and the inclusion of labile oxides (Twining et al. 2015). The use of other techniques such as synchrotron x-ray fluorescence (Twining et al. 2004) would provide deeper insights into phytoplankton Mn requirements in this region.

The dMn requirements of Southern Ocean phytoplankton are poorly understood. Wu et al. (2019) observed that coastal phytoplankton from the McMurdo Sound, Ross Sea, experienced physiological stress due to both low Fe and Mn conditions in mid-January. At this time, the surface dFe and dMn concentrations were depleted (dFe = 0.48 nM and dMn = 0.22 nM) in comparison to an earlier experiment in late December, where 0.27 nM of dMn was considered as replete conditions. In the present study, dMn values measured within the mixed layer above the Antarctic slope were on average $0.21 \pm 0.06 \text{ nM}$, $n = 16$, with dFe concentrations below 0.12 nM considering 12 of the 16 dFe samples were below the detection limit ($< 0.05 \text{ nM}$). This suggests strong Fe stress conditions at the southern end of the SR3 section. Therefore, it is possible that the low dMn concentrations measured above the Antarctic slope were due to enhanced Mn uptake resulting from Fe limitation (Peers and Price 2004). This agrees with the high uptake ratios calculated above the Antarctic slope. Additionally, we cannot exclude the possibility that dMn concentrations were low enough to co-limit with Fe the growth of the Antarctic coastal phytoplankton communities.

The threshold at which the dMn concentrations becomes limiting has not yet been defined and it will likely vary with environmental conditions, such as Fe concentrations and among taxa (Brand et al. 1983; Sunda and Huntsman 1983). However, for Antarctic coastal phytoplankton species, this threshold

appears to be between 0.22 and 0.27 nM (Wu et al. 2019). Using the lower value of 0.22 nM as the threshold for Mn limitation, the potential for Mn co-limitation could be extended to other regions of the SR3 line, such as the Polar Front Waters and Antarctic Zone with average dMn concentrations of 0.16 and 0.11 nM in the mixed layer depth, respectively (Table 2.1). This could suggest uniform Mn (co-)limitation of phytoplankton growth in the Australian sector of the Southern Ocean, south of the North-Polar Front. However, different Mn requirements between neritic and oceanic species are expected as was previously observed in coccolithophores (Brand et al. 1983) and diatom species (Sunda and Huntsman 1983). Further information on Mn limitation remains crucial, hence the need for lab-based experiments studying the minimum Mn requirement for different Southern Ocean phytoplankton species, in order to determine if the low dMn concentrations in the Polar Front Waters and Antarctic Zone may have been co-limiting phytoplankton growth during this voyage.

Previous field studies in the Southern Ocean and Antarctic coastal waters have shown contradictory results, with sometimes little to no stimulation of phytoplankton growth upon Mn addition (Buma et al. 1991; Scharek et al. 1997; Sedwick et al. 2000). Several reasons may explain these contradictory results, such as different initial conditions (e.g. in situ dMn and dFe), differing Mn requirement among phytoplankton taxa, or different interactions between Mn and other trace metals. Targeted field bioassay experiments would be useful to determine the spatial and temporal extent and variability of Mn limitation in Southern Ocean waters. Additionally, describing Mn distribution and its potential sources in this Southern Ocean region remain necessary to understand its potential limiting role.

2.3.4. MN REINTRODUCTION IN THE SYSTEM

Manganese is introduced into the water column through different external and recycled sources, such as remineralization (recycled), sedimentary (a mix of recycled and external) and hydrothermal inputs (external). These sources play a major role in supplying Mn to low Mn Southern Ocean waters.

Sedimentary inputs

Along the SR3 transect, sedimentary inputs were observed in the Subtropical Zone, extending from the Tasmanian shelf to the Subantarctic Front, highlighting the importance of advective movement of Sub-Tropical trace metal enriched waters from the north (Bowie et al. 2009). Sedimentary inputs can occur through sediment resuspension and/or direct dMn fluxes from porewaters (Klinkhammer and Bender 1980; Butler 2006). To differentiate these two processes, pMn concentrations proximal to the seafloor and downstream of seafloor interactions can be used as an indicator of sediment resuspension. Focusing on the upper 500 m of the water column across the transect (Figure 2.3A), two dMn subsurface maxima were observed in the Subtropical Zone. The upper dMn maximum extended from the surface to about 150 m (0.65 to 1.13 nM) and the deeper dMn subsurface maximum between 250 and 500 m with a concentration maximum of 2.2 nM. High total pMn concentrations were also measured at stations 1 and 4 (Figure 2.3C), adding evidence that these maxima are associated with sedimentary inputs from the

Tasmanian shelf. Previous studies have identified high Mn content in Tasmanian shelf composition (Prasada Rao and Jayawardane 1994; Butler 2006), which supports the theory of sedimentary inputs within the Subtropical Zone.

Sedimentary inputs were also observed in the Polar Front Waters and Antarctic Zone, just above the seafloor (Figure 2.3C), with high total pMn concentrations, indicating sediment resuspension. However, the other major sedimentary inputs were observed at the southern end of the SR3 transect, where sources of both dMn and pMn were observed along the Antarctic shelf, in proximity to the seafloor (Figure 2.3B, 2.3C). Additionally, the full-depth labile to total pMn ratio shows inputs of non-labile material (e.g. refractory) above the Antarctic slope (Figure 2.4B), which indicates lithogenic inputs (van der Merwe et al. 2019) likely of sedimentary origin in this region. The depth profiles of dMn and pMn along the Antarctic shelf also support the hypothesis of sedimentary inputs, with increasing concentrations close to the seafloor (Figure 2.5).

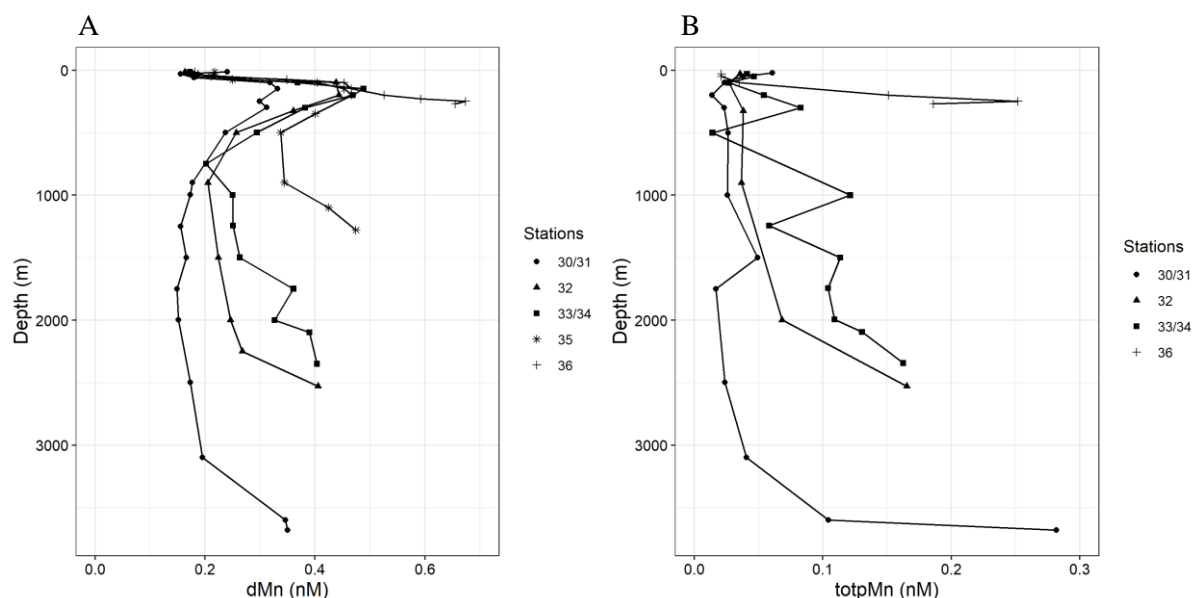


Figure 2.5: Depth profiles of dissolved Mn (dMn) (A) and total particulate Mn (totpMn) (B) measured above the Antarctic slope for stations 30 – 36. All stations display an increase of dMn and pMn with depth, likely due to sedimentary sources.

The release of dMn from sediments has already been documented in the Southern Ocean, particularly from sediment composed of biogenic silicate and calcite around the Kerguelen plateau (Cheize et al. 2018). Sedimentary inputs of dFe have also been previously observed at the end of the SR3 line (Sedwick et al. 2008). The Mn inputs observed here could be produced locally along the shelf or transported downward by dense shelf waters, sinking to form the Antarctic Bottom Water (Wijk and Rintoul 2014). As the Antarctic Bottom Water is partly composed of waters from the Ross Sea (Wijk and Rintoul 2014), it is interesting to compare results from this study with previous measurements from this region. Corami et al. (2005) measured summer dMn concentrations ranging from 0.34 to 0.78 nM

in the western sector of the Ross Sea, in good accordance with our study. Total pMn concentrations have also been previously measured in the Ross Sea and ranged from 0.01 to 0.51 nM (Fitzwater et al. 2000; Corami et al. 2005). In this study, the total pMn concentrations varied between 0.01 and 0.25 nM along the shelf, which is slightly lower than the previous measurements. Therefore, the high Mn concentrations observed along the shelf could also have originated from seafloor interactions in the Ross Sea and lateral advection through dense shelf water transport.

Hydrothermal inputs

In the Subantarctic Zone, Polar Frontal Zone and Polar Front Waters, strong dMn and pMn inputs were observed from the seafloor to about 2000 m depth (Figure 2.3B and 2.3C). Stations 17 & 18 were located above the Southeast Indian Ridge where several hydrothermal signatures have previously been observed, west of the present study (130-139°30'E), including dMn inputs (Boulart et al. 2017). Manganese is a known non-conservative but effective tracer for hydrothermal vents (Holmes, Chase, van der Merwe, et al. 2017), which provides strong evidence of hydrothermalism in this region. These inputs support the hypothesis that hydrothermal vents act as a source of Mn in this region of the Southern Ocean and could represent one of the major processes supplying Mn to deep Southern Ocean waters.

In their study, Boulart et al. (2017) observed different kinds of hydrothermal fluid close to our location (about 395 to 534 km west and slightly north, between 50 and 50.5°S). On the George V Fracture Zone, the closest feature to our study (139°30'E), they suggested the plume signal originated from ultramafic low-temperature hydrothermal circulation, supported by the absence of turbidity, a significant methane (CH₄) anomaly and potential redox (Eh) decrease (Boulart et al. 2017). Further west on the ridge, they observed high-temperature hydrothermal inputs, indicated by turbidity and temperature anomalies, and confirmed by strong Eh and salinity anomalies. This high-temperature system was accompanied by high dMn concentrations (12 – 30 nM).

In the present study, at least two dMn plumes can be observed (Figure 2.3B). To compare the present system with the study from Boulart et al. (2017), the depth profiles of temperature, turbidity, salinity and dMn for four stations crossing the plumes were studied (Figure 2.6). Results did not reveal an increase in the turbidity where elevated dMn concentrations were observed. However, station 8 shows a slight increase in temperature and salinity between 3400 and 3750 m in the vicinity of the high dMn concentration (0.77 nM at 3500 m) (Figure 2.6). This could indicate a hydrothermal plume originating from high-temperature venting (Boulart et al. 2017). A similar feature was not observed for the other stations, which could suggest different sources of two (or more) dMn plumes observed on the SR3 transect. The neutral densities in which the plumes reside also support the theory of different plume sources. The plume at super-station 13 & 14 sits in less dense waters, with neutral densities ranging from 28.00 to 28.09 kg m⁻³, in comparison to the plume at super-station 17 & 18, which sits between

isopycnals ranging from 28.09 to 28.17 kg m⁻³ (Figure 2.3B). The two other dMn maxima, observed at stations 8 and 10, sit in similar neutral densities as noted for the southern plume (super-station 17 & 18).

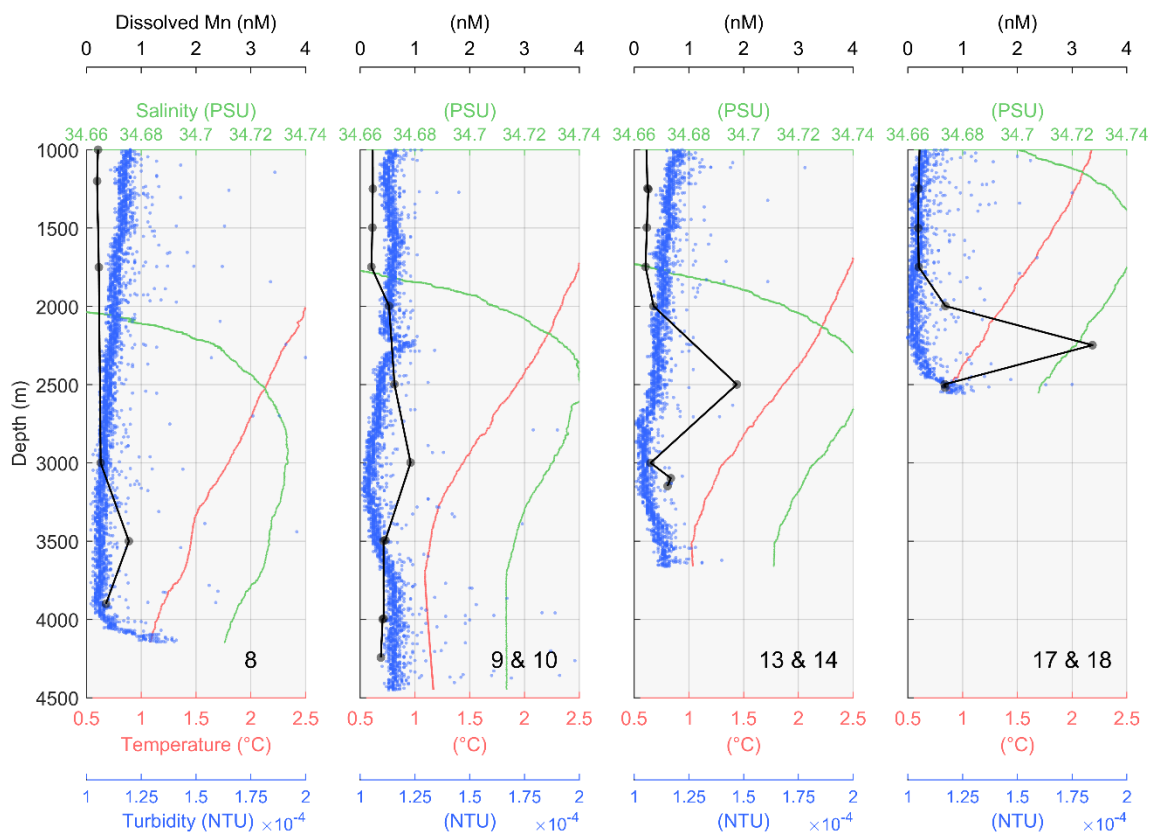


Figure 2.6: Depth profiles of temperature (°C) (red), turbidity (NTU) (blue), salinity (PSU) (green) and dissolved Mn (nM) for stations 8, 9 & 10, 13 & 14 and 17 & 18 between 1000 and 4500 m.

The plume observed at the super-station 17 & 18 had a maximum dMn concentration value of 3.37 nM at 2250 m. The plume observed further north, at super-station 13 & 14, had a lower maximum value of 1.88 nM and the dMn maxima observed at stations 8 and 10 were even lower with 0.77 and 0.92 nM, respectively. These dMn maxima remain low compared to the nearby study (Boulart et al. 2017), suggesting either that the type of hydrothermal circulation is not associated with high dMn concentrations (e.g. low-temperature hydrothermal circulation) or that both sources of these plumes could be located west of the SR3 section and that plumes were diluted with distance from their sources. In the latter case, these two (or more) plumes would then be dispersed towards the east across the SR3 section, due to the influence of the ACC (Sokolov and Rintoul 2009). This second hypothesis is also supported by previous studies (Klinkhammer and Hudson 1986; Fitzsimmons et al. 2017) which observed lateral dispersion of hydrothermally produced Mn over hundreds of kilometres (up > 3000 km) away from their sources, located at the East Pacific Rise.

Manganese is known to be supplied hydrothermally as Mn(II) and its residence time in the neutrally buoyant plume varies from weeks to years (Dick et al. 2009). After mixing with surrounding waters, Mn(II) transfers to the particulate form through chemical and microbial oxidation and scavenging (Klinkhammer and Hudson 1986; Dick et al. 2009), forming pMn. The fastest process is the microbially-mediated oxidation of Mn(II) to MnOx, by metal-depositing capsuled bacteria (Dick et al. 2009). These organisms, identified in hydrothermal plumes, have an extracellular capsule composed of polymers, which tend to become overlain with metal deposits, such as MnOx. Manganese oxides are strong scavengers, enhancing the removal of Mn(II) and other trace metals (Dick et al. 2009).

The movement of hydrothermally enriched waters is still not fully constrained. High dMn and pMn concentrations were observed (at about 2500 m), extending south from the strong plume signals to approximately 60-62°S (Figure 2.3B, 2.3C). The depth profiles of dMn concentrations showed higher concentrations for stations 19, 21, 24 but not for station 27, indicating the limit of this southward extension of the enriched dMn plume (Figure 2.7A). The pMn depth profiles showed similar results, except for station 27, which also had high pMn concentration at 2500 m (Figure 2.7B). The higher pMn concentrations at station 27 are likely related to continuous removal of dMn to pMn in the plume through microbially-mediated oxidation of Mn(II), limiting the extension of dMn. Further extension of the pMn compared to the dMn plume was also observed at the East Pacific rise (Fitzsimmons et al. 2017). In this study, the authors hypothesised that the lower specific gravity of the bacterial capsule prevent the settling of pMn in comparison to other metals such as Fe. This apparent transport of dMn and pMn follows the Low Circumpolar Deep Water flow path (Figure 2.2) which seems to move trace metal enriched waters toward the southern end of the SR3 section. However, despite this southern movement, the enriched waters do not seem to move upward from the Low Circumpolar Deep Water to the Upper Circumpolar Deep Water, suggesting that these Mn enriched waters remain confined by the isopycnals in which they originated (Figure 2.3B). Some features, such as flow-topography interactions associated with eddy activity or vertical mixing, could potentially disturb the isopycnals and force an upward movement of the Mn-enriched water toward the Upper Circumpolar Deep Water limit (Tamsitt et al. 2017; Ardyna et al. 2019).

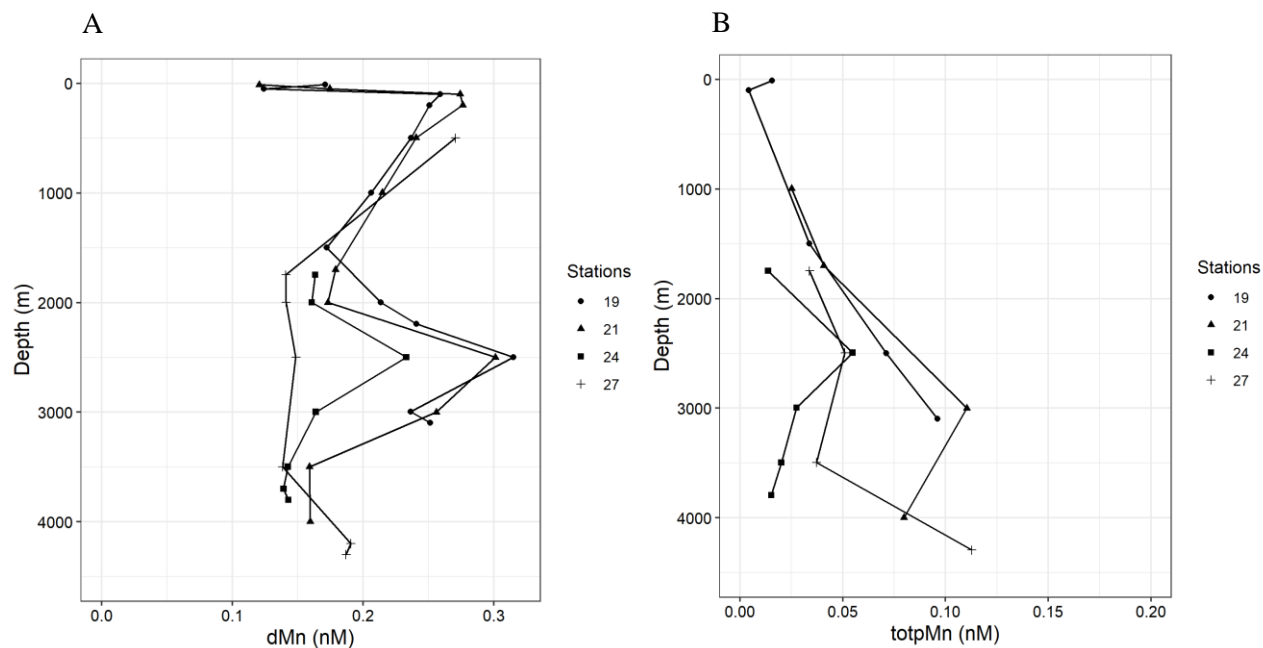


Figure 2.7: Depth profiles of dissolved Mn (dMn) (A) and total particulate Mn (totpMn) (B) for stations 19, 21, 24 and 27. The southern extension can be observed for stations 19-24 considering dMn, and for all stations for total pMn, suggesting further extension in the pMn fraction.

Upward transport of Mn

The upward transport of trace metals supplied by hydrothermal vents, over long distances, is still not fully characterized (Holmes et al. 2017). A recent modelling study has suggested that Fe, supplied by hydrothermal vents, can trigger phytoplankton blooms in Southern Ocean surface waters (Ardyna et al. 2019). The authors modelled the development of two phytoplankton blooms in Southern Ocean waters, located downstream of the Southwest Indian ridge, where strong signatures of hydrothermal vents have been measured in previous studies (Ardyna et al. 2019). This may also happen in our study area because of the presence of a cyclonic eddy bringing up deep waters, enriched in trace metals, through both hydrothermal and advective processes. Satellite data provided more information on this eddy. Formed from the Subantarctic Front in November 2017, this cyclonic eddy was sampled during a declining-life state in January 2018 (Patel et al. 2020).

Elevated dMn concentrations originating from hydrothermal inputs can be observed from the plume up to approximately 1000 m (Figure 2.3B). At depths above 500 m, the high dMn concentrations observed in the Subantarctic Zone appears to be advected upwards between 100 and 300 m (Figure 2.3A). However, strong stratification is observed at the base of the mixed layer at 100 m. Therefore, at the time of sampling, the eddy was not supplying dMn into the surface layer and the low surface dMn concentrations support this finding (Figure 2.3A). It is possible that prior to the eddy's decline, dMn inputs to the surface layer may have occurred if doming isopycnals induced by the younger eddy reached the surface. If so, the higher dMn concentrations brought to the surface may have been consumed through biological uptake prior to the present sampling period. Supporting this hypothesis,

high biomass was observed in the core of the eddy during the voyage, (Patel et al. 2020) and total pMn was enriched, relative to surrounding waters (0.11 nM at 30 m, Figure 2.3C). This supports the theory of previous dMn inputs to surface waters, during an earlier life-stage of the eddy. Additionally, deep mixing events, such as entrainment, may supply dMn concentrations accumulated under the surface mixed layer. This constitutes a possible mechanism for supply of dMn and other trace metals into euphotic waters of the Subantarctic Zone. Further south, total pMn concentrations are elevated from the plumes up to 1750 m at super-station 13 & 14 (Figure 2.3C). This suggests that the total pMn, likely composed of MnOx, results from the eddy moving from the Subantarctic Front. Eddies are common features of the Australian sector of the Southern Ocean (Patel et al. 2020), which could likely aid vertical transport of deep dMn towards the mixed layer.

2.4. Conclusion

This study describes the first detailed measurements of Mn concentrations to full depth along the SR3 transect, between Tasmania and Antarctica. Results revealed both low dMn and pMn concentrations along most of the transect. The ratio of labile to total pMn indicated that this Southern Ocean region might be characterized by a different pMn composition compared to other ocean basins. Low surface dMn concentrations were likely due to biological uptake. Strong correlations between Mn and PO_4^{3-} were observed in the dissolved fraction above the Antarctic slope suggesting strong biological control of dMn in this region. The total particulate Mn:P ratios measured in the Polar Front Waters and Antarctic Zone indicated the presence of Fe stressed diatoms. Higher ratios in the Subantarctic Zone and above the Antarctic Slope suggested Mn supply relative to PO_4^{3-} . The results suggest Mn may co-limit phytoplankton along SR3, south of the North-Polar Front, but further studies need to be performed to confirm this hypothesis. Manganese concentrations were locally increased by sedimentary inputs, close to the Tasmanian and Antarctic continental shelves, and by hydrothermal inputs above the Southeast Indian Ridge. At least two hydrothermal dMn plumes were observed, identified in Low Circumpolar Deep Water. The sources could be located west of the SR3 transect, where hydrothermal inputs have been previously described. The upward movement of hydrothermally enriched waters were observed within a cyclonic eddy, and while no supply of dMn into surface waters was observed, it is possible that this might have occurred prior the sampling period.

3. CHAPTER 3 – Biological uptake, water mass dilution and scavenging prevent transport of manganese-rich waters from the Antarctic shelf

Latour, P.; van Der Merwe, P.; Wuttig, K.; Townsend, A. T.; Corkill, M.; M.; Holmes, T. M.; Rintoul, S. R.; Schlitzer, R.; Weldrick, C.; Noble, T. L.; Strzepek, R. F.; Gault-Ringold, & Bowie, A. R. (submitted to *Global Biogeochemical Cycles*). **Biological uptake, water mass dilution and scavenging prevent transport of manganese-rich waters from the Antarctic shelf.**

3.1. Introduction

Manganese (Mn) is a key bioactive trace metal essential for the growth of phytoplankton in the ocean (Armstrong 2008; Middag et al. 2011). It is required for the oxygen evolving complex that produces electrons via photosynthesis (Armstrong 2008), and is also involved in the defence against reactive oxygen species (Peers and Price 2004; Wolfe-Simon et al. 2006). Despite being the 12th most abundant element in the Earth's crust (Wedepohl, 1995), Mn is found at very low concentrations in seawater, typically in the nanomolar range (Klinkhammer and Bender, 1980; Westerlund and Öhman 1991; Middag et al. 2013; Browning et al. 2014). These low concentrations can lead to Mn (co-)limitation of phytoplankton growth, especially in High-Nutrient Low-Chlorophyll (HNLC) regions such as the Southern Ocean where phytoplankton growth is already iron (Fe) limited (Wu et al. 2019; Browning et al. 2021). This limitation directly impacts the carbon cycle through modification of the strength of the ocean's biological carbon pump (Boyd et al. 2000). Knowing the distribution, sources, sinks and cycling of bioactive trace metals such as Mn remains essential to predict future changes in the marine carbon cycle using biogeochemical models.

In seawater, Mn distribution is controlled by its complex redox cycle and external sources/sinks. Manganese is often studied by separating its dissolved and particulate phases, by a 0.2 µm filtration (Cutter 2017). The dissolved phase is expected to be composed of the most reduced Mn species (Mn(II)) while pMn is mainly composed of Mn oxides (Sunda and Huntsman 1988; Twining et al. 2015) but can also include Mn within phytoplankton or minerals (Sunda and Huntsman 1994). Multiple external sources have been identified to supply dissolved and particulate Mn to seawater such as sediment resuspension/dissolution (Middag et al. 2011; Cheize et al. 2019), hydrothermal vents (Holmes et al., 2017), atmospheric deposition (Xu and Gao 2014), riverine outflow (Aguilar-Islas and Bruland 2006), glacial discharge (Bhatia et al. 2021) and sea-ice melting (Grotti et al. 2005). In addition, redox mobilization from sediments, associated with diagenetic processes and bacterial degradation of organic matter, has been described as a strong source of dissolved Mn (dMn) (Sundby et al. 1986; Burdige 1993). Yet, these complex processes near the sediment/water interface are tightly linked to oxygen concentrations and can either increase or remove dMn through Mn oxides dissolution or dMn precipitation, respectively (Sundby et al. 1986). Overall, sediments are usually identified as Mn sources,

associated with Mn-enriched subsurface plumes often observed along coastlines (Landing and Bruland 1980; Oldham et al. 2017; Morton et al. 2019).

In the Southern Ocean, dMn concentrations are controlled by biological uptake in the surface layer, remineralization below the photic zone, scavenging at greater depths and external inputs near the seafloor (Middag et al. 2011; 2013). The Mn particulate fraction has rarely been studied in open waters of the Southern Ocean (Bowie et al. 2009; 2010; van der Merwe et al. 2019; Latour et al. 2021) and the distribution between labile and refractory pools even less so. From studies to date, the total particulate fraction is characterised by very low surface concentrations, increasing with depth with a marked increase near the seafloor. A small excess of labile pMn relative to refractory fractions was noted in samples collected from the Australian sector of the Southern Ocean (51-63%; Latour et al. 2021). The labile particulate fraction is expected to be more bioavailable for phytoplankton uptake, while the refractory fraction is thought to be inaccessible (Berger et al. 2008). Overall, low Southern Ocean trace metal concentrations have been attributed to the oceanic isolation of the Antarctic continent by the Antarctic Circumpolar Current (ACC) and to low atmospheric inputs due to the vast distance from ice-free land masses (Wagener et al. 2008).

At higher latitudes, Antarctica represents a source of lithogenic material, yet studies documenting the export of trace metals in lithogenic material remain scarce (Measures et al. 2013). In particular, very few studies have described the dissolved and particulate trace metal concentrations in seawater off the Adélie and George V Lands, in East Antarctica, with most studies focusing on sea-ice concentrations (Lannuzel et al. 2011; 2014; Duprat et al. 2020). Smith et al. (2021) presented the first seawater concentrations in dMn in the Mertz Glacier region with relatively high dMn concentrations observed over the shelf (> 0.4 nM), attributed to sediment inputs. Dissolved and particulate Mn concentrations have also been reported in the Ross Sea (Fitzwater et al. 2000; Corami et al. 2005), although spatial variability between coastal Antarctic regions are expected (Angino 1966), necessitating further studies. The continental shelf adjacent to Adélie and George V land is characterised by several banks and depressions influencing the regional oceanic circulation (Rintoul 1998; Beaman et al. 2011). This area also includes the Mertz polynya, which is a region of high sea-ice production and bottom water formation (Rintoul 1998), as well as high primary productivity (Liniger et al. 2020). As Antarctic coastal areas represent important ecological hot spots and efficient carbon sinks (Arrigo et al. 2015), identifying trace metal distributions in these regions is vital for understanding the bottom-up control of biological carbon assimilation. In addition, high concentrations of Mn and other trace metals abundant in the lithosphere may be exported toward open Southern Ocean waters in the deep ocean through bottom water movement, or to shallow waters via northwestward coastal currents.

In this study, we present dissolved and particulate Mn concentrations along three latitudinal transects along Adélie and George V Lands (with a zonal section along 62° S joining them), in addition to three

stations located on the periphery of the Adélie Bank. Specifically, we test the hypothesis that northward transport of heavily Mn-enriched waters from the East Antarctic coast is limited due to efficient utilisation by phytoplankton and removal processes in bottom waters.

3.2. Material and methods

3.2.1. SAMPLING AREA

Multiple stations were sampled off the East Antarctic coast during the GEOTRACES voyage IN2018-V01 in the austral summer 2018, onboard the RV *Investigator*, between 62°S-66.4°S and 132°E-150°E (Figure 3.1). Samples were collected along three latitudinal transects, located at 132°E, 140°E and 150°E, hereafter referred to as 132, 140 and 150, respectively. The Mn distribution along 140, which is the southern end of the GEOTRACES-SR3 transect, has previously been reported by Latour et al. (2021). The three transects were joined by several sections along the zonal S4 section (~62-64°S). Additionally, three stations were sampled on the edge of the Adélie Bank, hereafter referred to as “shelf” stations.

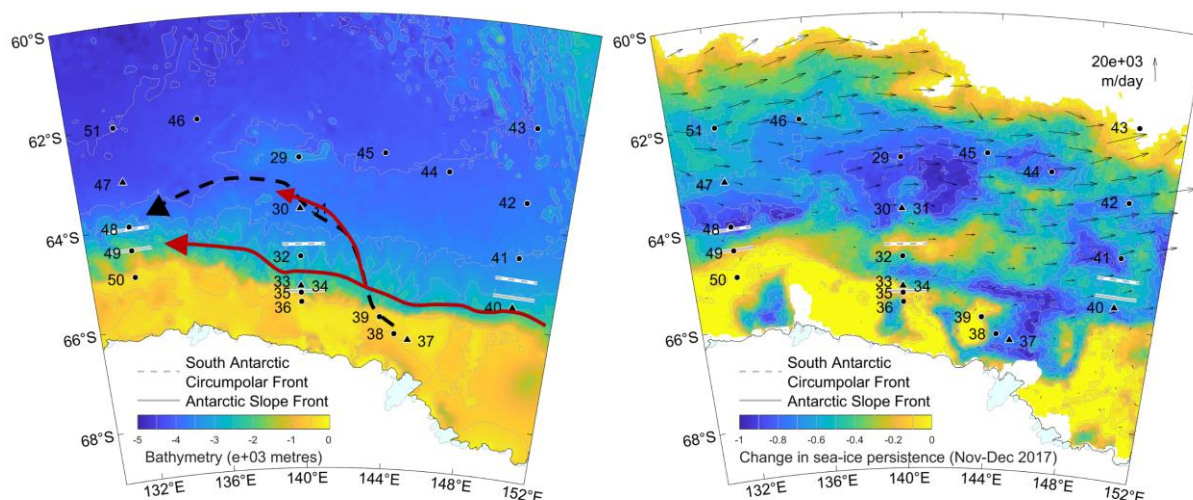


Figure 3.1: Map of the study area showing the bathymetry background colour (from Arndt et al. 2013) overlaid with TMR station locations (black dots) (a). The triangle shows stations where in-situ pumps were deployed. The large arrows indicate bottom water movement characterized in this region by Foppert et al. (2021): in red the Ross Sea Bottom Water (RSBW) and in black the Adélie Land Bottom Water (ALBW). On the right panel (b), the colour shows the change in sea-ice persistence between November and December 2017, prior to our occupation (Spreen et al., 2008). A value of 0 indicates no change in the proportion of sea-ice occurred between November and December while a value of -1 indicate that where sea-ice was present for all of November, it was absent for all of December. Overlaid small black arrows represent the average sea-ice velocity for November and December (Kimura 2004). The South Antarctic Circumpolar Front and the Antarctic Slope Front are indicated on each panel.

The hydrology of the region was studied through multiple deployments of a 36-bottle Conductivity-Temperature-Depth (CTD) rosette, also measuring oxygen, fluorescence, photosynthetically active radiation (PAR) and transmittance (Sea-Bird Electronics sensors: SBE4C, SBE3T, SBE9plus, SBE43, FLBBNTU, QCP – 2300 HP and Wetlabs CSTAR 25cm). Temperature and salinity measurements were

used to identify water masses. The combination of fluorescence, PAR and transmittance was used to locate higher biomass and identify non-photochemical quenching (Horton et al. 1996). This phenomenon occurs when phytoplankton are exposed to high light intensities and divert energy through heat rather than fluorescence. In this case, fluorescence sensors can display a ‘false deep chlorophyll maximum’. By combining fluorescence, PAR and transmittance, these ‘false deep chlorophyll maxima’ can be easily identified with transmittance, confirming the presence of particles (likely phytoplankton) in the top layer. Stations in Figure 3.1 were sampled for dissolved trace metal concentrations using a trace metal rosette (TMR). Five stations were studied for suspended particulate trace metal concentrations through deployments of in-situ pumps for high-volume sampling (ISPs, triangles in Figure 3.1; McLane Research Laboratories, WTS_LV). A chemical leach following the method of Berger et al. (2008) of ISP samples in the laboratory yielded both labile and refractory particulate fractions. Discrete (4L) samples for total particulate trace metal concentrations were also collected from the TMR to compliment the ISP sampling and expand the spatial resolution of particulate trace metal samples.

3.2.2. SAMPLE PROCESSING AND ANALYSIS

The processing of both dissolved and particulate trace metal samples followed GEOTRACES recommendations (Cutter et al. 2017). A detailed method for equipment preparation, sample handling, sample storage and analysis associated with this voyage has been described previously (Latour et al. 2021). Briefly, all sample processing was performed inside an ISO Class 5 containerized laboratory onboard the ship. Samples for dissolved trace metal concentrations were filtered through a 0.2 μm trace-metal clean filter cartridge (AcroPak™ 200, Pall). Filtered samples were then acidified using distilled (Savillex DST-1000 acid purification system) hydrochloric acid to a final pH of 1.8 and stored at room temperature until analysis. Dissolved trace metal concentrations in each sample were analysed after preconcentration and matrix removal using an automated offline seaFAST system (SC-4 DX seaFAST S2 / pico, ESI, USA) following Wuttig et al. (2019). Trace metal concentrations were determined using a Thermo Fisher ELEMENT 2 Sector Field Inductively Coupled Plasma Mass Spectrometry (SF-ICP-MS) (Central Science Laboratory, University of Tasmania). A medium spectral resolution was selected for the analysis of Mn and Ti. Rhodium (Rh) was added as an internal standard during seaFAST processing. Titanium was used as a lithogenic tracer rather than aluminium, as the seaFAST preconcentration system was optimised for Mn, and Ti extraction at pH 6.4 (Wuttig et al. 2019).

The 4 L discrete total particulate trace metal samples were filtered directly onboard using a custom-made filtration apparatus. Briefly, seawater was filtered through paired 25 mm acid-cleaned 0.8 μm SUPOR® (PES) filters with an effective size cut-off of 0.4 μm (Bishop et al. 2012) matching the ISPs. The filters were then digested using a mixture of strong acids (hydrochloric, nitric and hydrofluoric acid) following Bowie et al. (2010). Filters from the ISPs were subjected to a weak chemical leach, designed to extract labile trace metals from the refractory material (Berger et al. 2008). A total digestion

was used to quantify the remaining refractory fraction, using the same strong acids mentioned above. Dried and resuspended digest solutions were then quantified using SF-ICP-MS in a 10% nitric acid matrix. Additional details about this method are described in van der Merwe et al. (2019) and Latour et al. (2021).

3.2.3. HYDROLOGY

On the shelf, temperature and salinity were used to calculate neutral density and potential density, and all four parameters were used to identify different water masses (Orsi and Wiederwohl 2009; Silvano et al. 2017). Water masses of stations located over or north of the shelf break were characterized using neutral density and salinity (Pardo et al. 2017 and references therein). Both water mass (on shelf vs off shelf) characterisations can be found in Table S3.1 (Appendix B). Two fronts were identified: the South Antarctic Circumpolar Front (SACCF), by the southernmost extension of oxygen minimum (Pardo et al. 2017); and the Antarctic Slope Front (ASF), as the northernmost extension of cold shelf waters (potential temperature < -1.6°C) (Rintoul 1998) (Figure S3.1 in Appendix B).

As part of the discussion, we calculated the proportion of Antarctic Bottom Water (AABW) and Low Circumpolar Deep Water (LCDW) for samples within AABW. As these two water masses mix along a straight line in the temperature-salinity diagram (see Figure 3.2), this was done using potential temperature values in the following equation:

$$\text{proportion of } I = \frac{b}{a + b}$$

Where I is the water mass of interest, and a and b are the temperature differences between the sample potential temperature and the potential temperature endmembers of the mixing water masses two water masses studied and the specific depth point.

3.3. Results and discussion

3.3.1. HYDROLOGY

The potential temperature – salinity relationship reveals four water masses (Figure 3.2). Antarctic Surface Water (AASW), formed through warming of the surface layer during the austral summer was observed in shallow waters. Winter Water (WW), which is a cold remnant of the surface mixed layer created during the winter season, was observed between AASW and approximately 200 m. Below the WW, Circumpolar Deep Water (CDW) occupies most of the water column below 200 m depth. The CDW is made up of two water masses with distinct water properties and origins: LCDW coincides with a deep salinity maximum and has its origins in the North Atlantic, while Upper CDW coincides with an oxygen minimum that reflects a long transit through the deep Indian and Pacific Oceans (Lynn and Reid 1968). CDW penetrates onto the shelf in some locations, where it is known as modified CDW (mCDW)

because its properties are modified by mixing as it moves from the open ocean to the shelf (Orsi and Wiederwohl 2009). Finally, close to the seafloor, AABW was identified.

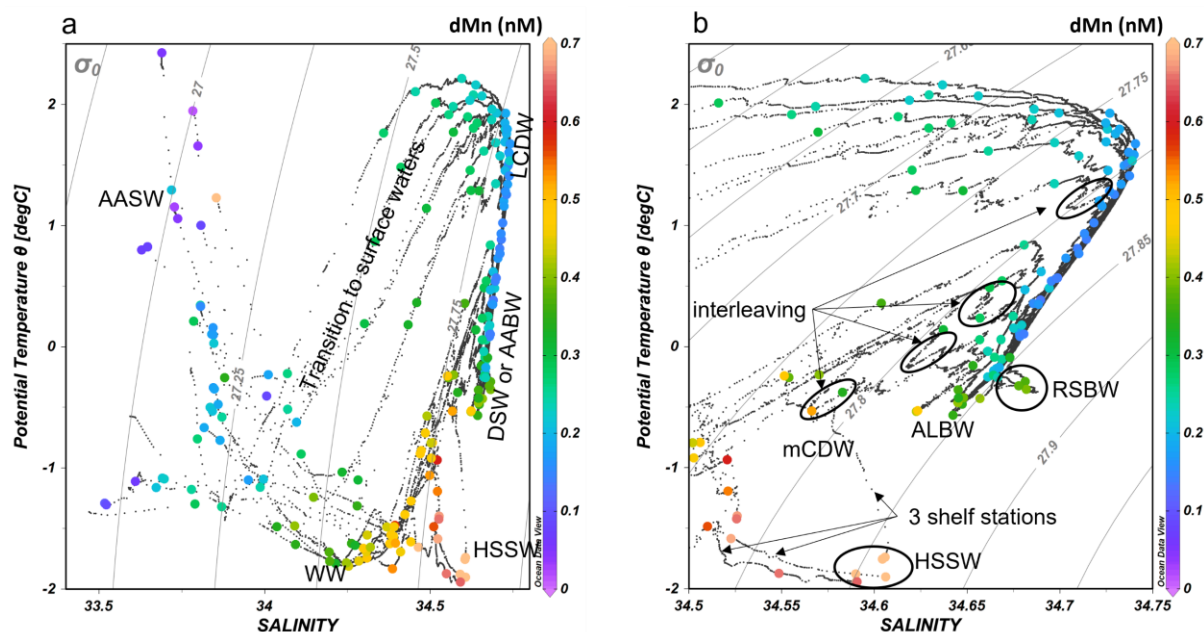


Figure 3.2: Potential temperature-salinity plot for a) the full dataset and b) the same dataset focusing on bottom waters, with salinities ranging from 34.5 to 34.75. Overlaid coloured dots represent dissolved Mn concentrations.

AABW forms when Dense Shelf Water (DSW), a cold and salty water mass formed on the continental shelf by cooling and brine rejection in winter, is exported from the shelf and mixes with CDW as it sinks to the seafloor (Gordon and Tchernia 1972). Two varieties of AABW were sampled on the voyage: relatively salty Ross Sea Bottom Water (RSBW) flowing west across 150, and a mixture of RSBW and fresher Adélie Land Bottom Water (ALBW) observed at 140 and 132 (Rintoul, 1998) (Figure 3.2b). The DSW that supplies ALBW is formed in the Mertz Polynya near 144°E on the Adélie Land coast. DSW with relatively high salinity ($S > 34.5$) was observed in some areas on the shelf near the Mertz Polynya. However, heavy sea ice prevented access to the Adélie Depression (between 142.5°E and 145°E), where the DSW that contributes to ALBW formation is found (Rintoul 1998). Therefore, we cannot describe the initial (end-member) conditions of the DSW that supplies ALBW. Interleaving observed in Figure 3.2b indicates mixing between relatively cold, fresh and oxygen-rich waters on the Antarctic continental shelf and slope with relatively warm, salty and oxygen-poor waters offshore.

The Southern Antarctic Circumpolar Current Front (SACCF; Orsi et al. 1995) and Antarctic Slope Front (ASF; Whitworth et al. 1985) crossed the transects at 132, 140 and 150. The latitude of the fronts and their separation varied between transects with the two fronts separated by a minimum of 39 km along 150 and by a maximum of 103 km along 140. Southern Ocean fronts, including the SACCF and ASF, often coincide with strong lateral gradients in physical and biogeochemical properties (Orsi et al., 1995) and therefore we anticipate that their presence may influence the distribution of Mn in this region. In particular, the ASF coincides with a jump between cold, fresh waters typical of the Antarctic continental

shelf and slope, and warmer, saltier offshore waters. Potential density anomalies showed that the 140 section was characterised by a strong density gradient near the ASF, highlighted by the depression in the isopycnals (Figure S3.1 in Appendix B). Strong mixing is expected at the base of this feature (Jacobs 1991), and may influence water movement along this transect. Generally, higher velocity westward currents are expected over the slope, compared to shelf currents (Jacobs 1991).

Previous studies have examined the circulation of shelf water masses in this region. A combined modelling and in-situ study showed summer circulation to be dominated by a shelf wide northwestward coastal current, composed of AASW and mCDW, with limited evidence of DSW (Snow et al. 2016). A weak southeastward flow of mCDW and AASW was found to reach the shelf, east of the Adélie sill (Snow et al. 2016). This on-shelf flow of mCDW was observed at our western shelf sites, with station 39 (located at 143.64°E) composed of warmer waters at intermediate depths (Figure 3.2b). A slight signal of mCDW was observed at station 37. However, no such signal was observed at station 38, highlighting the spatial variability of mCDW in this region. These oceanographic differences between transects described above, namely front locations and spatial variability of water masses, may influence the distribution of Mn and other trace metals. Below, we will focus our study on AASW and AABW considering these two water masses may be subjected to northward travel and hence drive export of Mn-enriched shelf waters toward the Southern Ocean.

3.3.2. MANGANESE CYCLE OF THE ADÉLIE AND GEORGE V LANDS

Dissolved Mn concentrations followed a common shape which agrees well with previous observations made in the Atlantic and Australian sectors of the Southern Ocean (further north) and in the Weddell Sea (Middag et al. 2011; Middag et al. 2013; Latour et al. 2021) (Figure 3.3). Surface dMn concentrations were generally low, ranging in average from 0.15 ± 0.1 nM north of the SACCF to $0.30-0.33 \pm 0.1$ nM over the shelf and the slope. Along all sections, lower dMn concentrations were observed north of the SACCF with the lowest value recorded being 0.014 nM at station 47 at 14 m. To the best of our knowledge, the previous open ocean lowest dMn value was 0.034 nM measured in the Drake Passage (Browning et al. 2014). Below low surface dMn concentrations, most stations were characterized by subsurface maxima around 200 m, with peak concentrations ranging from 0.30 ± 0.02 nM north of the SACCF to 0.61 ± 0.1 nM over the shelf. These high subsurface maxima have previously been attributed to particle remineralization (Middag et al. 2011). However, little is known about these features. Below the dMn peak, decreasing concentrations were observed with depth, resulting in overall low deep dMn concentrations, especially north of the SACCF (< 0.2 nM, Figure 3.3). Uniform low deep dMn concentrations are commonly attributed to scavenging processes which lead to short residence time of dMn in the deep ocean (Bruland and Lohan 2003). Near the seafloor, elevated dMn concentrations were observed at all stations (Figure 3.3) which are likely related to sedimentary inputs (Middag et al. 2011).

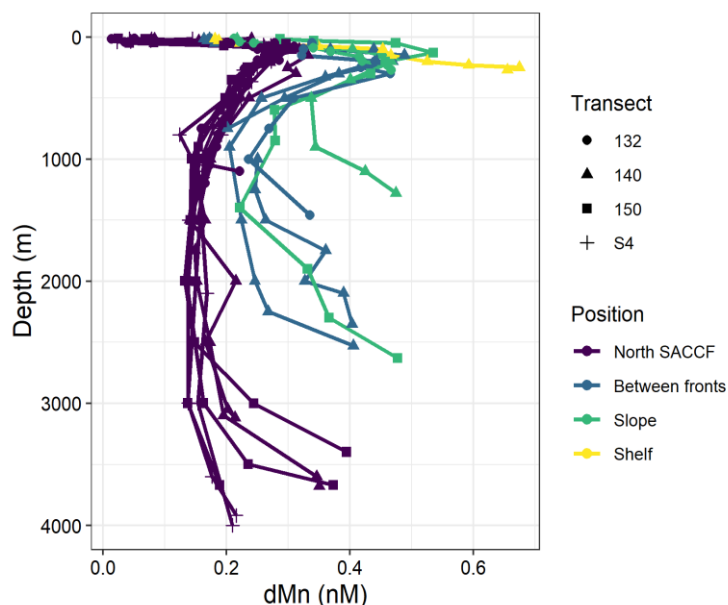


Figure 3.3: Depth profiles of dissolved Mn (dMn) along each transect, the colours represent the position of the station relative to both fronts, the slope and the shelf, the shape represents the four transects: 132, 140 and 150 (three main) and S4 which joins all the transects.

Overall, increasing dMn concentrations observed toward the shelf suggest the presence of strong external sources. Sediment resuspension (Lannuzel et al. 2011; 2014; Smith et al. 2021) or melting sea-ice (Grotti et al. 2005) likely increase dMn shelf concentrations. However, Lannuzel et al. (2011) observed up to an order of magnitude lower dMn and pMn concentrations within sea ice relative to Fe and suggested low inputs of dMn would occur through sea ice melting in this region. Another potential source may be the supply of highly reactive subglacially eroded material to the shelf (e.g., Hawking et al., 2020) from the nearby Mertz and Ninnis glaciers. We hypothesize that this East Antarctic region, characterized by high on-shelf Mn concentrations, may act as a source of Mn and potentially fertilise depleted open ocean waters, as previously seen in other regions (Measures et al. 2013). To study the potential export of Mn-enriched waters from this region, we assumed that if dMn is exported within a specific watermass, it may follow a dilution mixing line. By using salinity as a conservative parameter, we looked at the evolution of dMn, salinity and the ratio between dMn and salinity with distance from the coast to verify this (Figure 3.4).

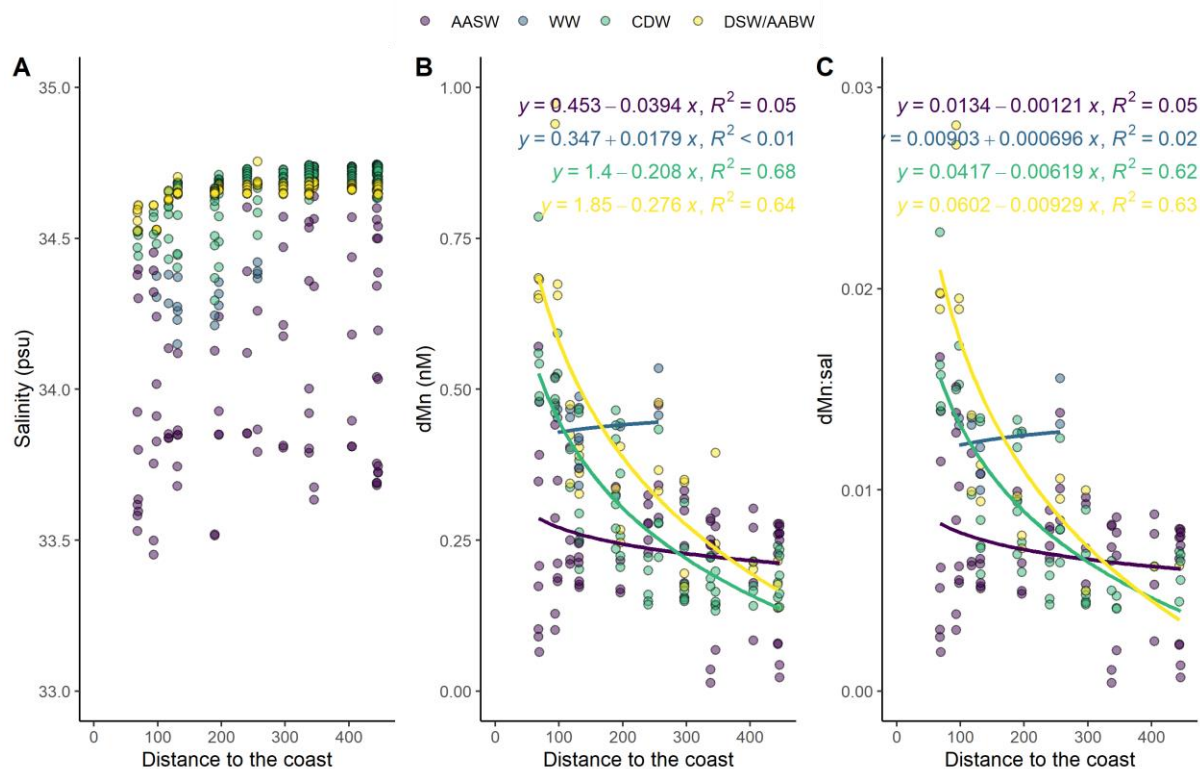


Figure 3.4: Scatter plot showing the evolution of salinity (A), dMn (B) and the ratio between dMn:salinity (C) with distance from the coast. Logarithmic regression lines are added in panel B and C with the corresponding equation and R-squared. The colours represent the water masses: AASW, Antarctic Surface Water; WW, Winter Water, CDW; Circumpolar Deep Water and DSW/AABW for Dense Shelf Water/Antarctic Bottom Water.

We observed a decrease in dMn concentrations with distance from the coast for all water masses except WW while salinity remained relatively stable in comparison (Figure 3.4A, B). The largest variations in salinity were observed in AASW and may be related to sea-ice melting (Duprat et al. 2020). The ratio of dMn per unit of salinity followed the trend of dMn (Figure 3.4C), indicating that processes other than dilution specifically impact dMn distribution by decreasing its concentration with distance from the coast. Considering we aim to study the export of dMn from this East Antarctic region, we focused our investigation on water masses subjected to northward travel; the AASW and DSW/AABW (Snow et al. 2016; Foppert et al. 2021; see section 3.1). We divided our discussion into two sections focusing on processes limiting Mn export (Biological uptake in surface waters and Removal of dMn in bottom waters) before attempting to quantify it (Export of Mn-enriched waters).

Biological uptake in surface waters

Southern Ocean dMn distribution is commonly characterized by low surface concentrations attributed to biological uptake and few external sources (Klinkhammer and Bender 1980; Middag et al. 2011). In this study, we observed low surface dMn concentrations at all stations but the lower values (< 0.1 nM) were recorded north of the SACCF (Figure 3.3). By combining chlorophyll fluorescence, PAR and transmittance, NPQ can be seen in surface waters on days of high PAR (stations 44, 46 and 47) yet transmittance highlights a well-mixed layer to 40 m. Therefore, F_0 and transmittance can be used here

as a proxy for phytoplankton biomass. While F_o was inversely correlated with dMn north of the SACCF ($R^2 = 0.20$; $p = 0.15$), transmittance versus dMn reveals a significant correlation ($R^2 = 0.49$; $p < 0.05$), most likely caused by biological uptake of dMn.

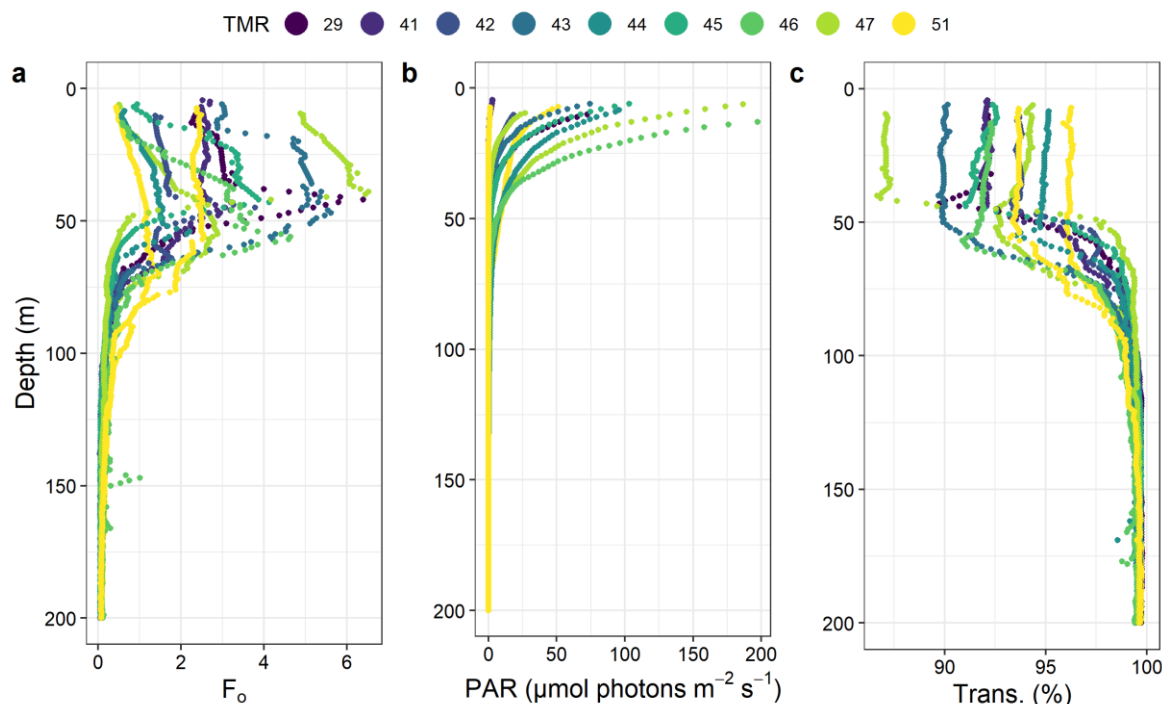


Figure 3.5: Depth profiles of fluorescence (F_o) (a), Photosynthetic Active Radiation (PAR in $\mu\text{mol photons m}^{-2} \text{sec}^{-1}$) (b) and transmittance (trans. in %) (c) between 0-200 m, north of the SACCF, where the lower surface dMn concentrations were observed.

In addition, ratios between Mn, phosphate (P) and Ti supported the hypothesis of increasing biological uptake with distance from the coast (Table 3.1). Lower dissolved Mn:P and Mn:Ti ratios were observed in the northern part of the study while conversely, increasing particulate Mn:Ti ratios were observed with distance from the coast. This particulate Mn enrichment relative to Ti combined with the decrease in dissolved Mn ratios suggests a transfer of Mn from the dissolved toward the particulate fraction, which may indicate: i) biological uptake; ii) formation of Mn oxides; iii) scavenging of dMn onto particles; or iv) a combination of these. In addition, the decrease in total particulate Mn:P ratio with distance from the coast combined with the increase in lability supported the hypothesis of increasing biological influence over the Mn cycle. Conversely, high ratios of refractory particulate Mn:P on the shelf suggest recent weathering of lithogenic Mn sources (van der Merwe et al. 2019). North of the SACCF, we measured comparable particulate Mn:P ratios to Twining et al. (2004) for Fe-stressed diatoms (0.42 mmol/mol). Diatoms and *Phaeocystis* sp. have been observed to increase their Mn requirement under Fe stress (Peers and Price 2004) or to accumulate Mn in their mucilage in the case of *Phaeocystis* (Davidson and Marchant, 1987). Therefore, surface dMn may have been depleted and transferred into the particulate phase after a bloom of such species. Profiles of silicic acid with depth showed depleted surface levels at stations 47 and 51, supporting the hypothesis of dMn drawdown

resulting from a diatom bloom (Figure S3.2 in Appendix B). Nitrate (N) to P (N:P) ratios, which may indicate the dominance of one phytoplankton group over the other (e.g. diatoms vs *Phaeocystis*), remain intermediate north of the SACCF (ranging from 15.2 to 16.4) and therefore could not be used as an additional proxy of phytoplankton community composition (Arrigo et al. 2015).

Table 3.1: Dissolved and particulate Mn concentrations with various ratios in the dissolved and total particulate fractions between Mn, P and Ti, measured in Antarctic Surface Waters (AASW).

<i>Fraction</i>	<i>Parameter</i>	<i>Shelf</i>	<i>Slope</i>	<i>Between fronts</i>	<i>North SACCF</i>
<i>Dissolved</i>	dMn (nM)	0.31 ± 0.17	0.33 ± 0.11	0.29 ± 0.11	0.15 ± 0.10
	dMn:dP	0.149 ± 0.07	0.174 ± 0.04	0.14 ± 0.04	0.074 ± 0.04
	dMn:dTi	0.045 ± 0.03	0.039 ± 0.01	0.041 ± 0.02	0.022 ± 0.01
<i>Particulate</i>	pMn (nM)	0.023 ± 0.01	-	0.03 ± 0.01	0.04 ± 0.02
	pMn:pP	1.91 ± 2.21	-	1.37 ± 1.5	0.47 ± 0.20
	pMn:pTi	0.177 ± 0.06	-	1.03 ± 0.99	2.85 ± 1.73
<i>Labile:tot. particulate</i>	LpMn:totpM	42.7 ± 5	50.4 ± 7	42.4 ± 15	57.9 ± 10
	n				

Sea-ice coverage is expected to influence the start of the bloom season. When the ice melts, increased light and nutrient availability will favour phytoplankton growth (Deppeler and Davidson 2017). Surface dMn concentrations may first increase due to sea-ice melt (Lannuzel et al. 2014), but uptake by phytoplankton should then lead to decreasing dMn and other trace metal concentrations throughout the bloom season (Kanna et al. 2020). Here, sea ice melted north of the SACCF prior to our occupation along all three longitudinal transects, as shown by the sea-ice persistence (Figure 3.1b). These results imply phytoplankton uptake started earlier north of the SACCF along each transect and agree with the observed lower dMn concentrations (Figure 3.3). Nonetheless, sea-ice movement represents a potential source of Mn and other trace metals as it may transport nutrients north of the SACCF and locally stimulate phytoplankton growth (Kanna et al. 2020). These local inputs are expected to vary seasonally with higher local enrichment/fertilization in the early season (austral spring/summer). Sea-ice advection for the period of this study indicated sea-ice was carried eastward by the ACC (Figure 3.1b). Hence, sea-ice coming from the west of this region could potentially increase local trace metal concentrations.

Removal of dissolved manganese in bottom waters

The sharpest decrease in dMn with distance from the coast was observed in bottom waters (Figure 3.4C). This suggested a removal process of dMn which was surprising considering dMn concentrations are often hypothesized to increase near the seafloor due to inputs from sediment resuspension or redox mobilization (Middag et al. 2011; Cheize et al. 2018; Morton et al. 2019). Hence, two hypotheses derive from this observation: i) one or several process(es) remove(s) dMn in bottom waters and ii) the elevated dMn concentrations observed near the seafloor (Figure 3.3) originate from the shelf and are carried downstream with the flow of AABW and not from constant sediment inputs, otherwise AABW dMn:salinity ratio would increase with distance from the coast and we observed the opposite trend (Figure 3.4C). As biological uptake is unlikely at these depths, dMn removal may result from two processes: i) scavenging of dMn onto particles and/or ii) dilution of dMn-rich AABW with overlying Mn-depleted LCDW, as previously observed in the Weddell Sea (Middag et al. 2013). To separate both processes, the fraction of LCDW was calculated for each dMn datapoint within the AABW layer using the temperature endmember within the core of AABW and LCDW (identified in Figure 3.2a) to calculate the relative proportion of LCDW in each AABW sample (Figure 3.6).

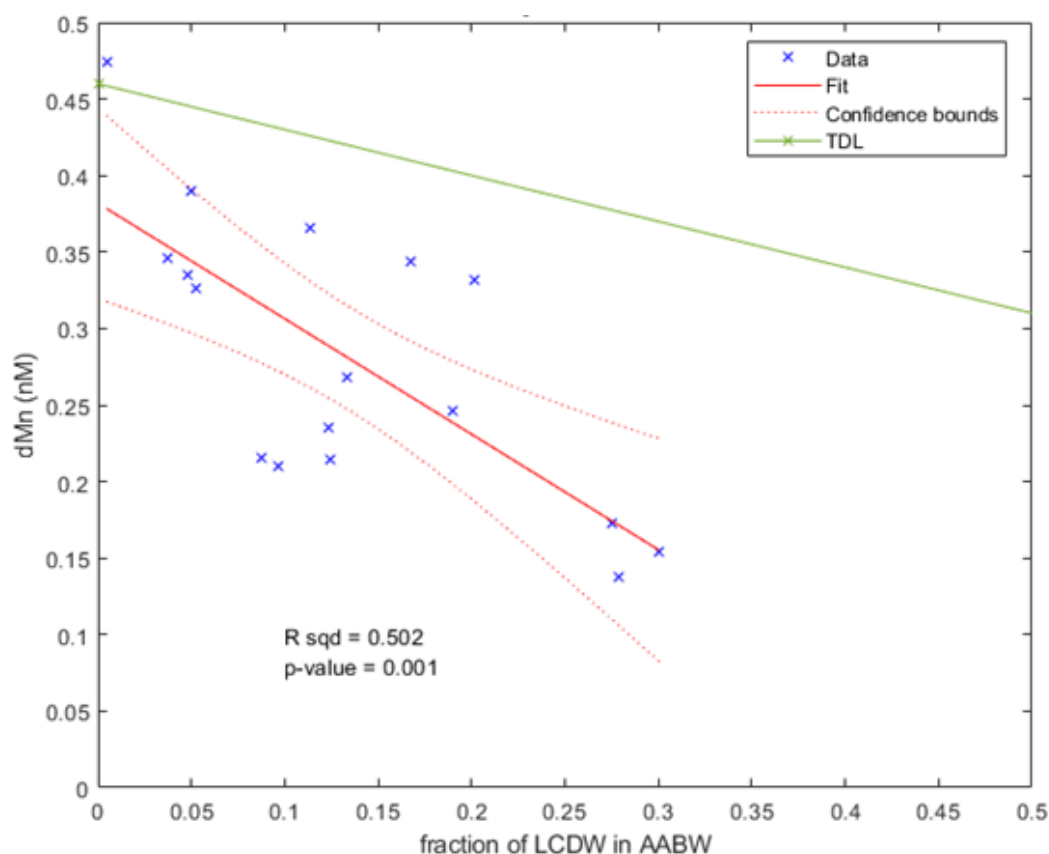


Figure 3.6: Dissolved manganese (dMn) concentrations measured in Antarctic Bottom Water (AABW) against the fraction of Low Circumpolar Deep Water (LCDW) in AABW. Linear regression with 95% confidence interval, R2 and p-value are displayed. The theoretical dilution line (TDL) is shown for a theoretical mixture of AABW and LCDW with dMn endmembers set as the mean of all off shelf dMn observations within each water mass. The TDL assumes no losses or enrichments during mixing.

Results indicated that as the contribution of LCDW increased in AABW samples, the associated dMn concentrations decreased (Figure 3.6). This result confirms that dilution of AABW with the overlying LCDW partly controls the concentration of dMn in our observations. However, almost all measurements of dMn concentrations in AABW are lower than the TDL (Figure 3.6). This suggests that final dMn concentrations are lower than expected from a direct mix between these water masses. We hypothesize that this reduction in dMn is due to scavenging in bottom waters.

Scavenging implies an adsorption of dMn onto particles, transferring Mn from the dissolved into the particulate phase. With distance from the coast, pMn concentrations within DSW/AABW remained relatively stable with local high concentrations observed on the shelf. This is in agreement with high particle content near the Antarctic shelf, where sources of both dMn and pMn are abundant. Particulate Mn is often primarily composed of Mn oxides, which are known as strong scavengers, able to decrease surrounding dissolved Mn and other trace metal levels (Goldberg 1954; Tonkin et al. 2004). High concentrations of dissolved constituents on the shelf, coincident with high pMn, indicate strong scavenging will be occurring in this region. The high fraction of refractory pMn observed on the shelf and gradual reduction in the proportion of refractory material with distance from the coast in all water masses (Figure 3.7) is consistent with higher density particles settling out to sediments preferentially near the coast soon after supply, while lower density, labile (often biogenic/detritus) particles, which are also produced in-situ, remain suspended for longer within the water column.

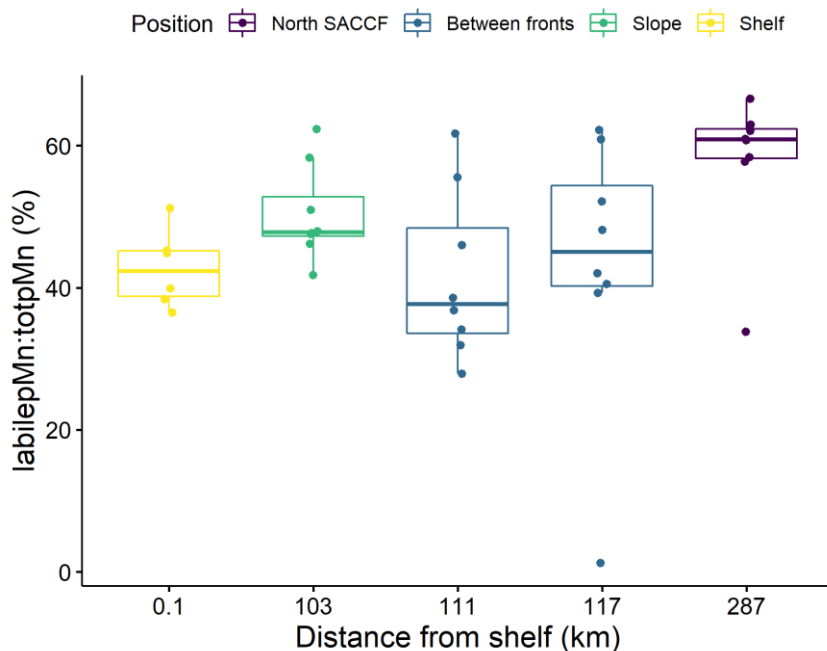


Figure 3.7: Ratio between labile particulate manganese (labilepMn) to total particulate manganese (totpMn) in % with distance from the coast at all depths (and all water masses). The colours represent the position of the station relative to both fronts, the slope and the shelf.

In the deep ocean, Mn oxides formation can occur under biotic or abiotic influence. However, abiotic Mn(II) oxidation is known to be much slower compared to the microbially-mediated Mn(II) oxidation and consequently, most Mn oxides are considered biogenic (Sunda and Huntsman 1988; Morgan 2005). Rates of Mn(II) oxidation have not yet been determined in this region, although a recent study observed a lack of Mn oxides in the Ross Sea, attributed to unique Mn redox cycle and persistence of Mn(III) ligands complexes (Oldham et al. 2021). In the present study, conservative or increasing dMn depth-profiles were also observed over the East Antarctic shelf (Figure S3.4 in Appendix B), suggesting either that i) dMn sources and inputs compensate dMn loss by scavenging or that ii) this region may also be characterized by low scavenging rates on the shelf as Oldham et al. (2021) observed in the Ross Sea. In the deep ocean, microbially-mediated Mn(II) oxidation rates have been observed to vary, especially within hydrothermal plumes with faster reactions compared to surrounding background waters, resulting from different bacterial communities (Dick et al. 2009). Hence, biotic scavenging rates may vary widely between coastal and offshore regions but also depending on specific microbial communities. Estimating Mn(II) oxidation rates remains necessary to evaluate the potential export of dMn within AABW.

Export of Manganese-enriched waters

The primary aim of this study was to identify if this East Antarctic region may act as a source of dMn for depleted Southern Ocean waters. Despite high dMn concentrations observed over the shelf; our results suggest dMn export from this region is limited, particularly in surface waters. We suggest biological uptake reduces surface dMn concentrations while mixing with overlying depleted-waters and scavenging limit export of dMn within bottom waters. Overall, we observed that between 0.1 (AASW) to 0.2 nM (DSW/AABW) of dMn were transported north of the SACCF, toward Southern Ocean open waters. This estimated export is in good agreement with the study from Middag et al. (2011), which measured similar surface concentrations in the Weddell Gyre. This suggests limited export of dMn may occur around Antarctic regions. However, we suggest the horizontal advection of Mn-enriched waters as subsurface dMn maxima may constitute a major source of dMn for surface waters following strong wind-mixing and/or upwelling induced by eddies.

Subsurface dMn maxima are common features of the Southern Ocean (Middag et al. 2011). At all stations, we observed subsurface dMn maxima located between 73 to 300 m with higher values recorded near the shelf (Figure S3.5 in Appendix B). This East Antarctic region is characterized by a shelf depth varying between 200 and 400 m (Beaman et al. 2011) which suggests that processes on the shelf provide a source of dMn at intermediate depth and could partly explain the presence of subsurface dMn maxima in Southern Ocean waters (Dinniman et al. 2019; Smith et al. 2021). The identification of these features further north indicate this Mn-enriched plume may travel to great distance at intermediate depths (Middag et al. 2011; Latour et al. 2021). Similar subsurface features were observed in the Western Antarctic Peninsula and attributed to sediment inputs (Sherrell et al. 2018). However, previous studies

associated these dMn subsurface maxima with remineralization of particulate organic matter (Middag et al. 2011). It is likely both processes - lateral advection of Mn-enriched waters and remineralization - help maintain these subsurface features at intermediate depths with varying degrees of contribution from each source, depending on proximity to shelf regions. In the present study, lower oxygen concentrations measured near these subsurface maxima support the hypothesis that particles are remineralized at that depth (Figure 3.8).

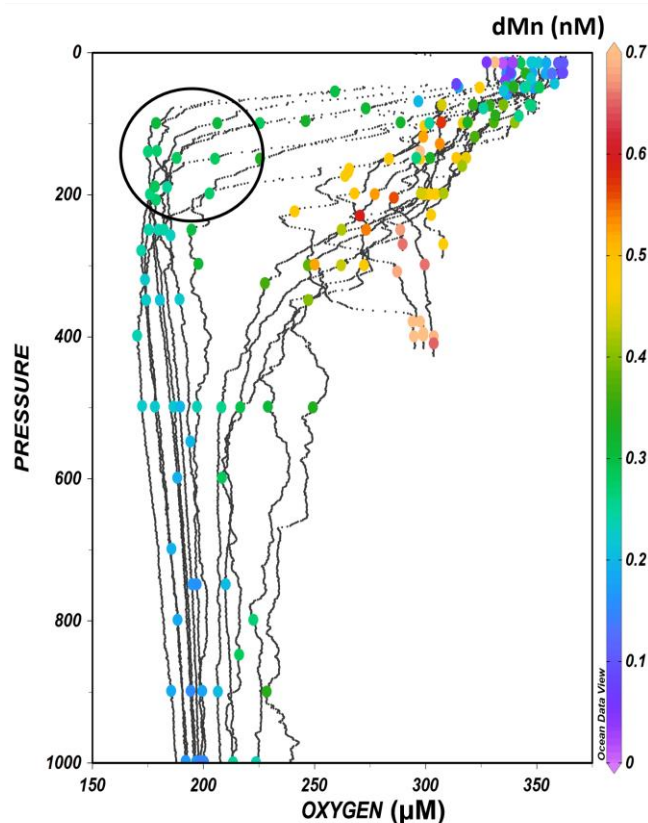


Figure 3.8: Depth profiles of oxygen concentrations (in μM) measured by the CTD sensors for the three main transects and the three 3 shelf stations with overlaid coloured dots showing dissolved Mn concentrations (in nM). The black circle shows low oxygen concentrations coincident with relatively high dMn concentrations.

Estimating a precise budget and flux of dMn from this region remains complex. Overall, our data suggest dMn export is limited in both surface and bottom waters. However, the advection of subsurface maxima constitutes a potential important source for surface waters following strong-wind-mixing and/or upwelling induced by eddies (Figure 3.9). Considering bottom water transport, the main limit of this study resides in the fact that we did not follow the path of a specific AABW plume. Instead, the present three latitudinal transects cut across several AABW plumes (Figure 3.1A; Foppert et al. 2021). To confirm the hypothesis of dMn loss within bottom waters, it remains essential to follow a specific plume, along with characterizing particles composition and estimating Mn(II) oxidation rates.

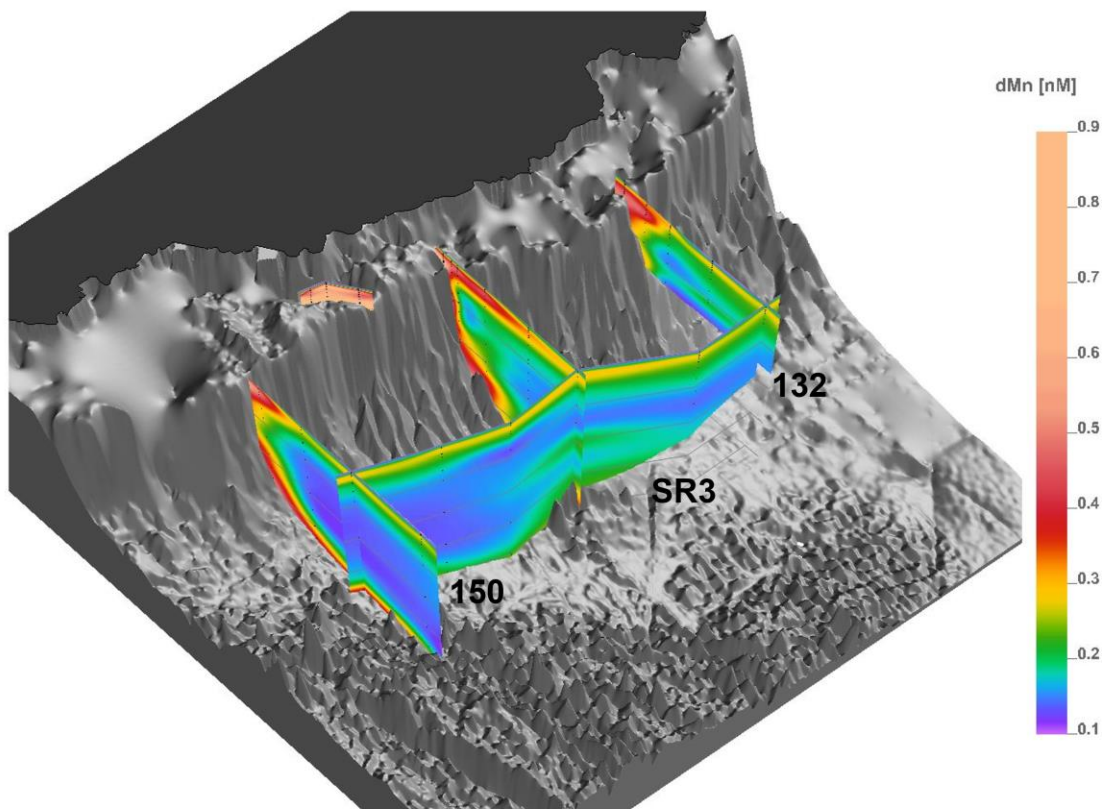


Figure 3.9: 3D plot showing dissolved Mn concentrations (in nM) along the three perpendicular sections measured (132, 140 and 150). While dMn seem elevated in bottom waters, we observed a decrease of dMn with distance from the coast. We suggest subsurface dMn maxima may represent an important source of dMn for surface waters.

3.4. Conclusion

We investigated the potential northward export of Mn-enriched Antarctic shelf waters. High Mn concentrations were found on the shelf and likely attributed to sedimentary sourced and glacial discharges. We found that dMn export in surface waters was limited due to biological uptake and dMn concentrations strongly decreased north of the SACCF. This sharp decrease in Mn was linked to the timing of sea-ice melting, which occurs earlier in the spring, north of the SACCF and stimulates phytoplankton growth and uptake of bioessential trace metals including dMn. We observed a subsurface dMn maximum at all stations north of the shelf break and suggest it may be linked to advection of enriched shelf waters near the Antarctic shelf and particle remineralization further north. However, a combination of both processes cannot be ruled out. After factoring in dilution of AABW with overlying LCDW, export of dMn via bottom water formation and advection off the shelf is hypothesized to be limited by both Mn(II) oxidation and scavenging associated with Mn oxides. This result was surprising due to the expectation that input from sediments would enrich bottom water concentrations downstream. Overall, export of Mn-enriched waters toward Southern Ocean open waters was limited. These results improve our understanding of the Southern Ocean's status as an HNLC region and relate to previous

studies which measured very low Mn concentrations in open waters of this region. This lack of Mn export may have implications regarding phytoplankton growth (co-)limitation by Mn, but also by other important biologically essential trace metals previously expected to be exported alongside Mn, such as Fe.

4. CHAPTER 4 – Seasonality of phytoplankton growth limitation by iron and manganese in subantarctic waters

The following chapter has been published as a preprint in the Earth and Space Science Open Archive (ESSOAr). In addition, this chapter was submitted to *Frontiers in Marine Science* for peer-review.

Latour, P.; Strzepek, R. F.; Wuttig, K.; van Der Merwe, P.; Eggins, S.; Bach, L.; Boyd, P.; Ellwood, M. J. & Bowie, A. R. 2022. **Seasonality of iron and manganese phytoplankton growth limitation in subantarctic waters.** <https://doi.org/10.1002/essoar.10511502.1>

4.1. Introduction

Phytoplankton play a major role in the marine carbon cycle by driving the transfer of carbon dioxide from the atmosphere into the ocean through photosynthesis. This process is part of the biological carbon pump, and its strength varies between and within oceanic regions (Lenton et al. 2013; Deppeler and Davidson 2017). The Southern Ocean is comprised of several biogeochemical regions with contrasting hydrographic and nutrient conditions: the subantarctic zone, the polar front zone, the Antarctic zone, and the seasonal sea ice zone, each delimited by fronts (Orsi et al. 1995). South of the subtropical front, phytoplankton growth is mainly limited by very low concentrations of iron (Fe) (Boyd et al. 2000; Deppeler and Davidson 2017). Other factors may also limit phytoplankton growth, such as low light and temperature, or specifically north of the polar front, low silicic acid levels (Boyd 2002; Bowie et al. 2009; Strzepek et al. 2012). These limiting factors (alone or combined) directly impact the strength of regional biological carbon pump and hence need to be identified to project changes to the oceanic carbon cycle during the Anthropocene.

Interest in nutrient co-limitation of Southern Ocean phytoplankton has recently grown (Middag et al. 2013; Browning et al. 2014; Browning et al. 2021). Specifically, several studies have identified Fe and manganese (Mn) co-limitation in both coastal (Wu et al. 2019) and open ocean waters (Browning et al. 2021) of the Southern Ocean. Co-limitation occurs when two or more elements limit phytoplankton growth simultaneously, and several kinds of co-limitation have been identified. Saito et al. (2008) classified Mn co-limitation as a type II “Biochemical substitution co-limitation”, in which two elements are expected to substitute for each other for the same active site of an enzyme, for example, Fe and Mn within the superoxide dismutase enzyme. Manganese is an essential element for phytoplankton growth, used in the oxygen-evolving complex for the water-splitting reaction of photosynthesis and in the superoxide dismutase enzyme to defend against reactive oxygen species (ROS) (Sunda et al. 1983; Peers and Price 2004). Therefore, phytoplankton growth may be limited in regions where dissolved Mn (dMn) concentrations are particularly low, such as the Southern Ocean (Westerlund and Öhman 1991; Middag et al. 2011, 2013; Latour et al. 2021). Importantly, phytoplankton Mn requirements may vary depending on Fe conditions. Peers and Price (2004) observed that diatoms increased their Mn content under Fe stress, presumably to produce more superoxide dismutase enzyme to counter the additional ROS production associated with Fe limitation. If Fe limitation increases the cellular requirement for

Mn, Mn (co-)limitation may be expected in Southern Ocean phytoplankton limited by Fe (Boyd et al. 2000; Deppeler and Davidson 2017). However, several earlier shipboard incubation experiments in Southern Ocean waters did not observe an effect of Mn addition in either coastal or open waters of the Southern Ocean during the austral spring and summer (Buma et al. 1991; Scharek et al. 1997; Sedwick et al. 2000), suggesting that Mn (co-)limitation is not pervasive within the Southern Ocean and may vary between regions and seasons.

The subantarctic zone, the northernmost region of the Southern Ocean, sustains the strongest carbon uptake of all the Southern Ocean biogeochemical regions (Lenton et al. 2013). In terms of biology, this region sees the transition from phytoplankton communities containing coccolithophores and fewer diatoms in northern waters towards more diatoms and less coccolithophores in polar waters (Trull et al. 2001). Usually, pico- and nanoplankton dominate phytoplankton communities in terms of cell counts, but high grazing pressure keeps their abundance relatively low with little seasonal variability (Deppeler and Davidson 2017 and references therein). In this region, Fe was demonstrated as the main factor limiting phytoplankton growth, with silicic acid possibly (co-)limiting diatoms (Boyd et al. 1999; Westwood et al. 2011; Eriksen et al. 2018). Until now, the study of Fe-Mn co-limitation of phytoplankton growth has been restricted to a few polar Southern Ocean sites (Buma et al. 1991; Scharek et al. 1997; Sedwick et al. 2000; Wu et al. 2019; Browning et al. 2021), with only the Browning et al. (2021) study looking at potential co-limitation within subantarctic waters. A recent study showed that dMn concentrations are low in subantarctic waters south of Tasmania, with an average concentration of 0.24 nM measured within the surface mixed layer during the austral summer 2018 (Latour et al., 2021). In this region, Mn, like Fe, may be delivered to the ocean through atmospheric inputs from Tasmania and mainland Australia or sedimentary inputs from the Tasmanian shelf. Southward advection of subtropical waters has also been observed to supply Fe and Mn enriched waters to the subantarctic zone (Sedwick et al. 2008; Bowie et al. 2009; Latour et al. 2021). To date, no studies have investigated Fe and Mn co-limitation in the Australian sector of the Southern Ocean. Additionally, to our knowledge, there has been no prior study of the seasonality of Mn or Fe-Mn (co-)limitation in any subantarctic region.

This study presents the results of three shipboard incubation experiments performed in subantarctic waters in the Australian sector of the Southern Ocean examining Fe-Mn co-limitation in austral spring, summer, and autumn. We expect that following wind-mixing in winter, both dissolved Fe (dFe) and dMn levels should be higher in surface waters during spring due to supply from deeper waters/subsurface maxima and external sources (e.g. about 0.3-0.4 nM for dFe and dMn; Bowie et al. 2009; Latour et al. 2021). Therefore, we hypothesize Fe and Mn will not (co-)limit phytoplankton growth in spring. In summer, dFe and dMn should decrease due to biological uptake and reduced vertical nutrient inputs resulting from stronger stratification. Hence, Fe limitation of phytoplankton growth will likely occur. Iron stress may increase phytoplankton Mn requirements (Peers and Price

2004), and due to the decrease of dMn concentrations from biological uptake during the spring season, dMn may (co-)limit phytoplankton growth. In autumn, trace metal levels should be at their lowest, hence we hypothesize Mn, Fe or both will strongly limit phytoplankton growth, depending on the ratios of both elements relative to biological demand.

4.2. Material and Methods

4.2.1. SAMPLING

The bioassay experiments were performed onboard the RV *Investigator* during three voyages, IN2018-V04 (September/October 2018, austral spring), IN2019-V02 (March/April 2019, austral autumn) and IN2020-V08 (December/January 2020-21, austral summer). The first experiment was conducted at Process Station 2 (PS2) of the East Australian Current voyage IN2018-V04 (45.44°S, 153.31°E) and the following two experiments at the Southern Ocean Time Series (SOTS) station (46.80°S, 141.884°E) (Figure 4.1). Both sites are within the subantarctic zone to the southeast and southwest of Tasmania, respectively (Bowie et al. 2011).

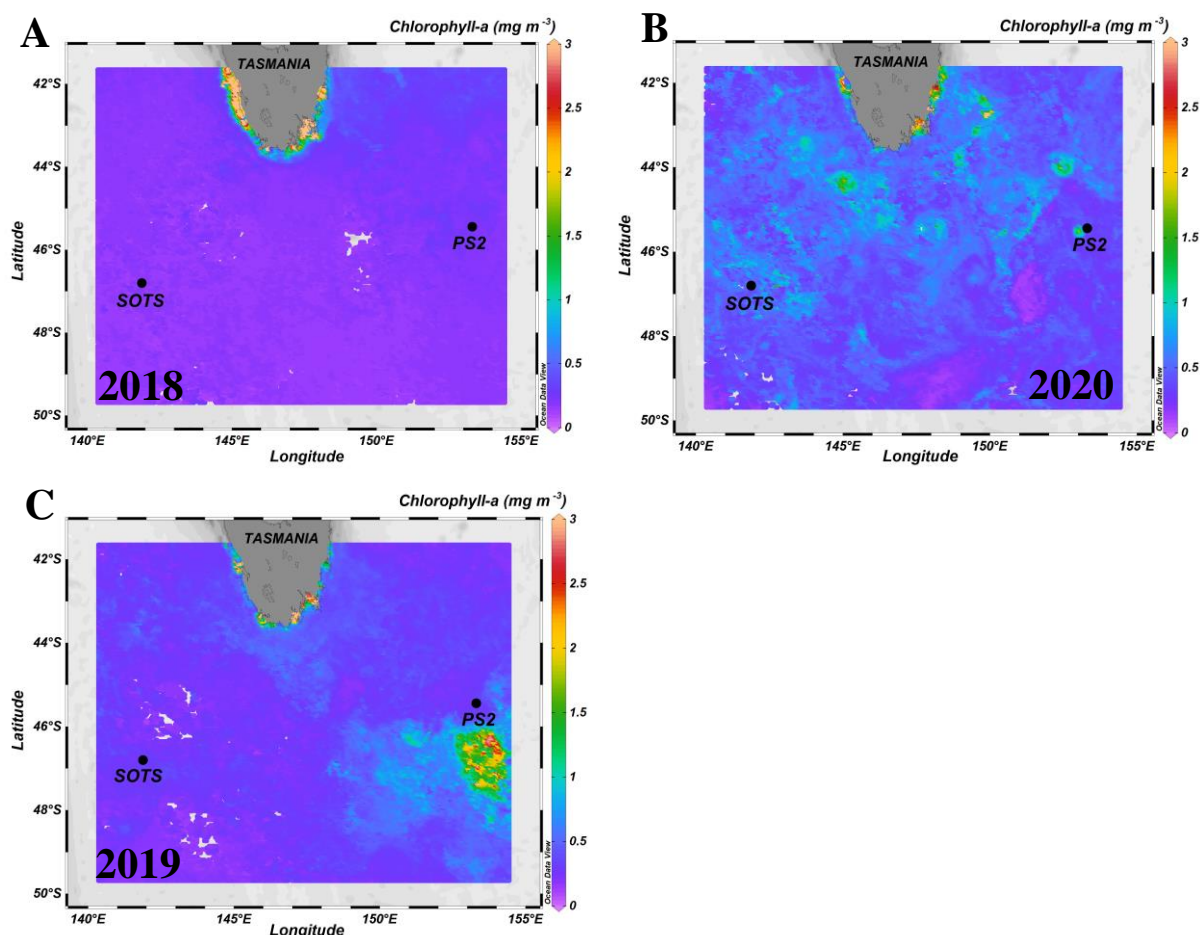


Figure 4.1: Sites sampled for each experiment. The background image colour shading represents the average surface chlorophyll-a concentrations measured by satellite (MODIS-Aqua, 8-day average 4 km) for the month when each of the bioassay experiments was performed. A: phytoplankton incubations at PS2 during the spring voyage (IN2018-V04), monthly average for September 2018. B: phytoplankton incubations at SOTS during the summer voyage (IN2020-V08), monthly average for December 2020. C: phytoplankton incubations at SOTS during the autumn voyage (IN2019-V02), monthly average for March 2019.

Seawater used for the bioassay experiments was collected at 15 m depth for the first two experiments (spring and autumn) and at 20 m for the summer experiment using a polyurethane powder-coated aluminium rosette, or “Trace Metal Rosette” (TMR), directly from the Niskin bottles adapted for trace metal sampling (Sea-bird Scientific, USA; Holmes et al. 2020). Samples for macronutrients, flow cytometry and photophysiology analyses were collected from the TMR to characterise the initial phytoplankton communities. Polycarbonate bottles used for the incubations were washed with Neutracon detergent for 48h, and then in 10% hydrochloric acid (HCl) for 7 days to remove trace metal contamination. After multiple Milli-Q water rinses, bottles were dried overnight in an ISO Class 5 laminar flow hood before being double-bagged in plastic. Onboard, the bottles were rinsed three times with the incubation seawater before filling them inside an ISO Class 5 containerized clean room. The seawater was unamended (Control) or spiked with a solution of Fe, Mn or a combination of both. The Fe and Mn spikes were prepared in 0.01 M Ultrapure HCl using ultrapure salts of FeCl₃ (or FeNO₃ for the spring experiment) and MnCl₂. Triplicates were used for each treatment, resulting in 12 bottles for 4 treatments, named hereafter: Control, +Fe, +Mn, and +FeMn. Concentrations of Fe and Mn were adjusted to reach a final concentration of at least 2 nM, which we considered as nutrient-replete conditions (Browning et al. 2021). The bottles were then incubated in deck board incubators inside mesh bags to reproduce the light penetrating the surface ocean, at approximately 15 m (80% of incident irradiance). Deck board incubators allowed the algal communities to follow their regular diel light:dark cycles. The temperature of the incubators was maintained by a continuous flow of seawater, keeping the bottles at the same temperature as the surrounding surface (~ 7 m) seawater. Sampling was done at day 7 for macronutrients, flow cytometry and photophysiology analyses for each experiment. Flow cytometry samples were fixed using 2% (v/v) glutaraldehyde (Electron-microscope grade, 25%), for phytoplankton samples collected during the second voyage in autumn 2019. For the summer 2020 voyage, a mixture of formaldehyde-hexamine (18%:10% v/w) was used to preserve phytoplankton samples. Due to a technical issue, flow cytometry samples from the spring 2018 voyage were lost and are therefore not presented in this study. All bacteria samples were fixed using 2% glutaraldehyde (Electron-microscope grade, 25%). All flow cytometry samples were held at 4°C in the dark for 25-30 min after being fixed and were then flash-frozen in liquid nitrogen and stored in a -80°C freezer until analyses back onshore.

Following the subsampling, a portion of the remaining seawater was dispensed into 300 mL acid-washed polycarbonate bottles and spiked with 16-20 µCi of Sodium ¹⁴C-bicarbonate (NaH¹⁴CO₃; specific activity 1.85 GBq mmol⁻¹; PerkinElmer, USA) and 0.2 nM of an acidified ⁵⁵Fe solution (⁵⁵FeCl₃ in 0.1 M Ultrapure HCl; specific activity 30 MBq mmol⁻¹; PerkinElmer; Ellwood et al. 2020). Bottles were then incubated in the deck board incubators for another 24 h, under the same conditions as the bioassay experiments. The spiked samples were then filtered sequentially through 0.2, 2 and 20 µm polycarbonate filters (47 mm diameter; Poretics, USA), separated by 200 µm nylon mesh spacers. The

filters were washed with Titanium(III) EDTA – citrate reagent for 5 min to dissolve Fe (oxy)hydroxides and remove extracellular particle-bound ferric ions and rinsed three times with 15 mL of 0.2 µm-filtered seawater. Finally, filters were placed in 20 mL glass vials (Wheaton Industries, USA) and acidified with 200 µL of 1.2 M HCl. These filters were then stored at room temperature for analyses on shore.

4.2.2. ANALYSIS

Dissolved macronutrients were analysed onboard using segmented flow analysis (Rees et al. 2018). One silicic acid measurement was removed from the analysis due to an inconsistent result (autumn experiment, in the “Mn” treatment). In summer, several silicic acid concentrations measured had a value below the detection limit (0.2 µM) and were therefore replaced by this same value. Final nitrate concentrations are not presented due to the use of an FeNO₃ solution for the Fe spike during the spring experiment. However, initial nitrate concentrations are mentioned in the discussion. Phosphate and silicic acid uptake rates were calculated by subtracting the final value measured in each bottle from the initial concentrations to calculate an average uptake rate per week over the 7-day period of incubation. Initial dissolved trace metal concentrations were measured through Sector Field Inductively Coupled Plasma mass spectrometry (SF-ICP-MS) after preconcentration and matrix removal through seaFAST at the Australian National University (Canberra, Australia). Dissolved Fe and Mn concentrations were used to estimate Mn deficiency relative to Fe as $Mn^* = dMn-dFe/R_{Fe:Mn}$, where $R_{Fe:Mn}$ is the average Fe:Mn ratio of phytoplankton (Moore 2013; Browning et al. 2021). If $Mn^* > 0.1$, this suggests Mn replete conditions.

Fast Repetition Rate Fluorometry (FRRF) was used to determine the maximum photochemical efficiency (F_v/F_m) and functional absorption cross section (σ_{PSII}) of photosystem II (PSII) using a Light-induced Fluorescence Transients Fast Repetition Rate (LIFT-FRR) fluorometer (Soliense, USA). After low light (2 µmol photons m⁻² s⁻¹) acclimation for ~30 minutes, samples were exposed to 140 flashes of light every 2.5 µsec (saturation sequence) to saturate PSII and the first stable electron acceptor, Q_A after which the time interval between flashes was increased exponentially (relaxation sequence) for 90 flashes. F_v/F_m (where $F_v = F_m - F_o$) was calculated from F_o and F_m , which refer to the minimum and maximum fluorescence in the dark-acclimated state, respectively. F_v/F_m and σ_{PSII} were determined from the mean of 200 iterations of the fluorescence induction and relaxation protocol measured at 470 nm. At least 10 acquisitions were measured for each sample and used to calculate the average value of F_v/F_m and σ_{PSII} . Due to recalibration of the instrument between voyages, no direct comparison of the initial fluorescence (F_o) results can be made between seasons, but only between treatments for the same season.

Flow cytometry samples were analysed at Menzies Institute for Medical Research (University of Tasmania, Hobart), using an Aurora Cytek flow cytometer. This instrument can measure particles ranging from 200 nm up to at least 60 µm. It is likely that this instrument can capture cells larger than 60 µm, but we acknowledge that the larger cells (up to 300 µm) may have been under sampled. However,

we cannot quantify this as the largest size particles possibly measured by this instrument has not yet been determined. Briefly, frozen samples were thawed at 37°C for 5-10 minutes before running 500 µL of unstained samples at flow rates of ~50 µL per minute, using Milli-Q water as sheath fluid. Violet and blue excitation lights were used to differentiate main phytoplankton groups through their fluorescence pigments: chlorophyll with red fluorescence and phycoerythrin with orange fluorescence, respectively, against forward scatter (FSC). All scatter and fluorescence parameters were analysed based on values from the integrated area of the excitation peak. Results obtained from both the summer and autumn voyages were analysed using SpectroFlo software. For an overall comparison between the two seasons, phytoplankton communities were divided into three gates: picoeukaryotes, nanoeukaryotes and large phytoplankton (microeukaryotes), identified on the violet channel (V12, 405 nm excitation, 692 nm emission) against FSC. If the signal from V12 was saturated, we used another excitation wavelengths (B7, 488 nm excitation, 661 nm emission). Picocyanobacteria were isolated on another fluorescence channel (B4, 488 nm excitation, 581 nm emission) due to the presence of phycoerythrin (Marie et al. 1999). Cell counts per unit volume were determined from the instrument through the known volume analysed. We then used the cell counts to calculate the relative importance of each group in terms of population size (*Fpop* described below) by comparing their size (FSC) and abundance, using the following equation from Bach et al. (2018):

$$F_{pop} = \frac{N_{pop} \times FSC_{pop}}{N_{all} \times FSC_{all}} \quad (1)$$

Where F represent the fraction of size (size is here represented by the parameter FSC) produced by a specific population (pop). N represents an abundance via cell count of a specific population or all phytoplankton cells (all).

Heterotrophic bacterial counts were performed after the addition of SYBR Green I stain (1000-fold dilution) on thawed fixed samples. Samples were incubated with the stain for 15 minutes at room temperature in the dark. Then, a 50 µL aliquot of stained sample was run on the instrument at high flow rate. Bacteria were identified using blue excitation and green fluorescence (B2, 488 nm excitation, 525 nm emission). Cell counts were determined as described above for phytoplankton.

Iron uptake and net primary productivity (carbon uptake) were determined by measuring disintegrations per minute (DPM) on a liquid scintillation counter (PerkinElmer Tri-Carb 2910 TR). Filters were incubated at least 24h prior analysis in 10 mL of Ultima Gold liquid scintillation cocktail (Perkin Elmer). Daily carbon incorporation rates were estimated following Hoppe et al. (2017). The uptake of ⁵⁵Fe and ¹⁴C were corrected for ambient dFe and dissolved inorganic carbon concentrations.

4.2.3. STATISTICAL TESTS

Statistical analyses were performed in R (R “stats” package; R Core Team 2020). Datasets were initially examined for homogeneity of variance using a Levene’s test, and normality using a Shapiro-Wilk.

Where data were both normally distributed and homoscedastic, significant differences between treatments were investigated using a one-way analysis of variance (ANOVA) with a Tukey’s HSD post hoc test. Otherwise, a Kruskal-Wallis test was performed followed by a Wilcoxon signed-rank test where the former result was significant. A p-value of 0.05 was used to identify significant difference between treatments.

During the autumn experiment, no statistical tests could be performed on the Fe uptake results for the +Fe treatment due to a mistake in the radioisotope additions.

4.3. Results

4.3.1. INITIAL HYDROGRAPHIC AND NUTRIENT CONDITIONS

Oceanographic conditions differed between the three experiments across temperature, salinity and silicic acid profiles (Figure 4.2). In spring, the surface ocean was characterized by a deep mixed layer depth (MLD), down to 200 m. Temperature, salinity and silicic acid concentrations were constant within the mixed layer with values at about 10.5°C, 34.9 g kg⁻¹ and < 3 μM, respectively. In summer, stronger stratification was observed with the MLD reaching just below 100 m. The surface temperature was like spring but lower below 25 m (about 10°C). In summer, the salinity was much lower than in spring (< 34.6 g kg⁻¹). Similarly, silicic acid concentrations were lower in summer, down to 1 μM in surface waters. In autumn, the MLD reached 100 m, where the temperature was ≥ 11°C and the salinity was like summer conditions. Silicic acid concentrations were the lowest, with less than 1 μM in surface waters.

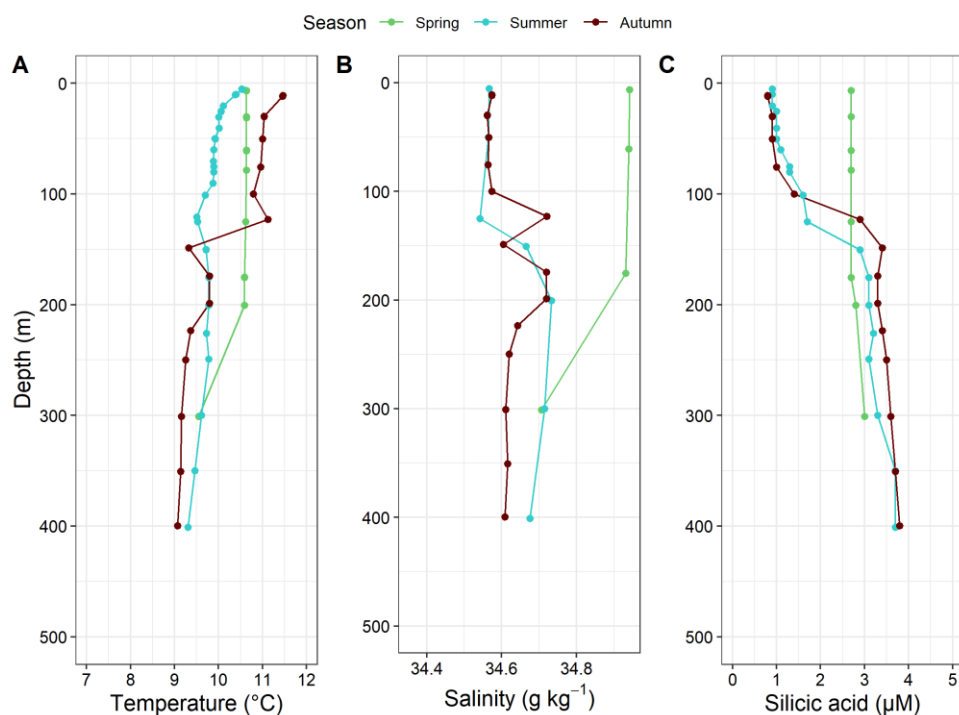


Figure 4.2: Temperature (A), salinity (B) and silicic acid concentrations (C) depth profiles measured at the sites of the incubations: PS2 (spring, in green) and SOTS (summer in blue and autumn in brown).

Initial dFe and dMn concentrations present in the incubated seawater were slightly different between seasons (Table 4.1). The dFe concentration was the highest in summer, with intermediate values measured in spring and lowest concentrations in autumn. Similarly, the lowest dMn concentration was also recorded in autumn. However, both the spring and summer experiments had similar initial dMn concentrations. The calculated Mn* values were high (0.16-0.25) with the lowest Mn* observed in autumn (Table 4.1).

Table 4.1: Initial mean dFe and dMn concentrations with standard deviations measured in (or near) the seawater incubated for the three experiments and the calculated Mn* according to Browning et al. (2021): spring at PS2 in 2018 (n = 2), summer at SOTS in 2020 (n = 1) and autumn at SOTS in 2019 (n = 3). *Single measurements were performed for dFe and dMn in summer and dMn in autumn, in these cases the method error is indicated. In autumn, both dFe and dMn values came from a near cast.

Experiment	Spring (PS2)	Summer (SOTS)	Autumn (SOTS)
Depth of water collected (m)	15	20	15
dFe (nM)	0.31 ± 0.001	0.50 ± 0.03*	0.15 ± 0.04
dMn (nM)	0.37 ± 0.032	0.44 ± 0.03*	0.26 ± 0.03*
Mn*	0.25	0.25	0.16

4.3.2. MACRONUTRIENT DRAWDOWN

Both initial phosphate and silicic acid concentrations present in the seawater incubated for each experiment, along with the final concentrations measured after 7 days of incubations are presented in Figure 4.3. Focusing on the initial conditions, phosphate concentrations ranged from 0.71 to 0.82 μM , with the lowest value observed in autumn and the highest in spring. Similarly, the lowest initial silicic acid concentrations were observed in autumn (0.8 μM) and the highest in spring (2.8 μM).

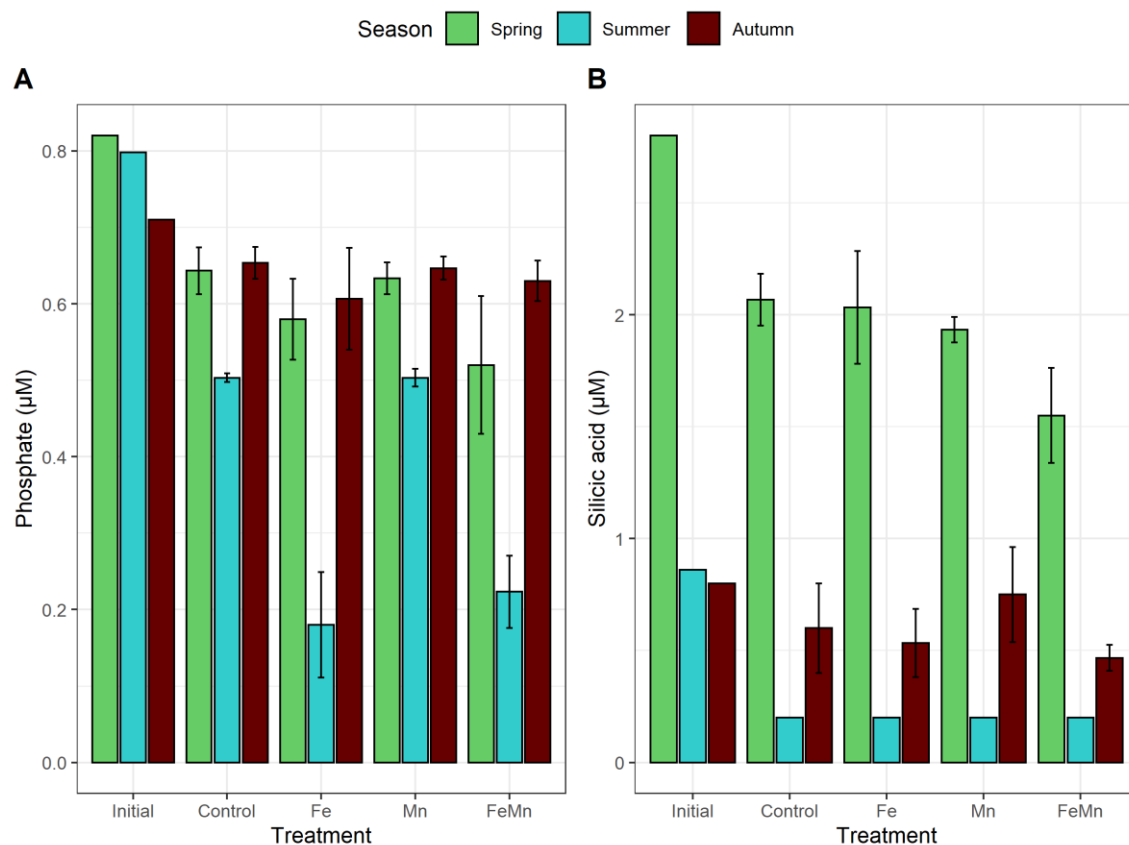


Figure 4.3: Phosphate (A) and silicic acid (B) concentrations (μM) measured in the initial water incubated ("Initial"), and after seven days of incubations for each treatment: Control ("Control"), +Fe ("Fe"), + Mn ("Mn"), +FeMn ("FeMn"). The colour represents the season of the experiment: green for spring, blue for summer and brown for autumn. Error bars represent the standard deviations and are smaller than the symbols when not visible ($n = 3$, except for the initial treatment where $n = 1$).

Phosphate and silicic acid concentrations decreased over the 7-day incubation, across all seasons and treatments. However, the uptake of both nutrients between each treatment varied seasonally. In spring, no significant differences were observed by day 7 in phosphate and silicic acid concentrations, between the control and the other treatments (ANOVA). In summer, we observed a significant decrease in phosphate concentrations only in the treatments where Fe was added (+Fe and +FeMn), compared to the control ($p\text{-value} < 0.05$, Tukey's HSD). No significant drawdown of phosphate was observed in the Mn treatment, compared to the control. In summer, all treatments were characterized by final silicic acid concentrations below the detection limit ($0.2 \mu\text{M}$). In autumn, no significant differences were observed in either phosphate or silicic acid concentrations between treatments (ANOVA).

The uptake ratios for both phosphate and silicic acid differed seasonally (Table 2). In spring, no significant differences in phosphate and silicic acid uptake rate were observed between treatments (ANOVA). In summer, both Fe additions (+Fe and +FeMn) resulted in a very strong increase in the phosphate uptake rate, which doubled compared to the control and Mn treatments ($p\text{-value} < 0.05$, Tukey's HSD). During this season, the treatment effects are impossible to interpret for the silicic acid uptake rates as concentrations were drawn down below the detection limit ($0.2 \mu\text{M}$) (Figure 4.3 and

Table 4.2). In autumn, we did not observe any significant differences in the uptake rates for either phosphate or silicic acid between treatments (ANOVA).

Table 4.2: Average uptake rates of phosphate and silicic acid ($\mu\text{M week}^{-1}$) and standard deviations for each treatment calculated over the 7-day incubation period for each experiment ($n=3$). *In summer, all final silicic acid concentrations were below the detection limit ($0.2 \mu\text{M}$) and hence replaced with $0.2 \mu\text{M}$. Consequently, the calculated uptake rate is identical in each treatment and cannot be interpreted.

	Treatment	Control	+Fe	+Mn	+FeMn
Phosphate	Spring	0.18 ± 0.03	0.24 ± 0.05	0.19 ± 0.02	0.30 ± 0.09
	Summer	0.04 ± 0.001	0.09 ± 0.01	0.04 ± 0.002	0.08 ± 0.01
	Autumn	0.06 ± 0.02	0.10 ± 0.07	0.06 ± 0.02	0.08 ± 0.03
Silicic acid	Spring	0.73 ± 0.12	0.77 ± 0.26	0.87 ± 0.06	1.25 ± 0.21
	Summer	$0.66^* \pm \text{NA}$	$0.66^* \pm \text{NA}$	$0.66^* \pm \text{NA}$	$0.66^* \pm \text{NA}$
	Autumn	0.20 ± 0.20	0.27 ± 0.15	0.05 ± 0.20	0.33 ± 0.06

In addition, nitrate to phosphate (N:P) and nitrate to silicic acid (N:Si) ratios were calculated for the summer and autumn experiments (Figure S4.2). In summer, N:P ratios significantly decreased under both Fe additions (+Fe and +FeMn) compared to the control and +Mn treatments ($p\text{-value} < 0.05$, Tukey's HSD). No significant differences were observed in N:Si ratios (Wilcoxon signed-rank test) but this may result from final silicic acid concentrations being below the detection limit. In autumn, no significant differences in N:P and N:Si ratios were observed between treatments (ANOVA).

4.3.3. PHOTOPHYSIOLOGY

The photochemical efficiency of PSII (F_v/F_m) differed between treatments and seasons (Figure 4.4A). In spring, no significant differences in final F_v/F_m values were measured between treatments (ANOVA). In summer, only the treatments with Fe additions (+Fe and +FeMn) maintained F_v/F_m values as high as the initial community, and significantly higher than the control and +Mn treatments ($p\text{-value} < 0.05$, Tukey's HSD). In autumn, we measured significantly higher F_v/F_m values in both treatments with Fe additions (+Fe and +FeMn) compared to the +Mn treatment ($p\text{-value} < 0.05$, Tukey's HSD). However, F_v/F_m values measured in both Fe treatments were not significantly higher than the control (ANOVA).

The functional absorption cross section of PSII (σ_{PSII}) differed between seasons (Figure 4.4B). The initial value was higher in summer compared to spring and autumn. In spring, we observed a significant decrease in σ_{PSII} only in the +FeMn treatment, compared to the other treatments ($p\text{-value} < 0.05$, Tukey's HSD). In summer, both treatments with Fe additions (+Fe and +FeMn) were characterized by a decrease in σ_{PSII} compared to the control and +Mn treatments ($p\text{-value} < 0.05$, Tukey's HSD). In autumn, no significant differences in σ_{PSII} were observed between treatments (ANOVA).

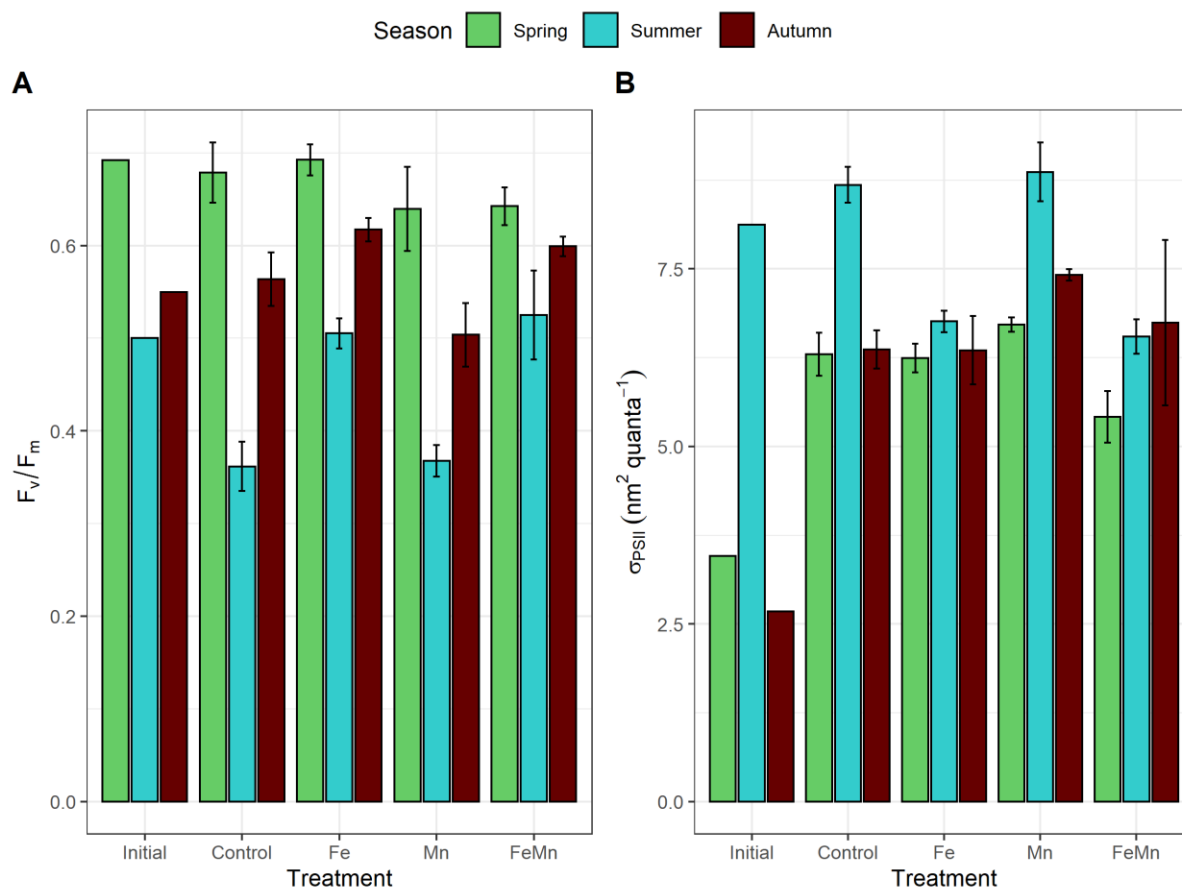


Figure 4.4: A) Photochemical efficiency of photosystem II (F_v/F_m) and B) functional absorption cross section of PSII (σ_{PSII}) in $\text{nm}^2 \text{ quanta}^{-1}$, measured for the initial algal communities incubated (“Initial”) and after 7 days of incubation, in each treatment: Control, +Fe (“Fe”), + Mn (“Mn”), +FeMn (“FeMn”). The three colours show the different seasons: green for spring, blue for summer and brown for autumn. Error bars represent the standard deviations ($n = 3$, except for the initial treatment where $n = 1$).

4.3.4. FLOW CYTOMETRY

Notable differences in phytoplankton community composition were observed between summer and autumn. In summer, picoeukaryotes dominated the cell counts (Table 4.3). However, nanoeukaryotes dominated community population size, as defined by equation (1) in the method section (Figure 4.5A). In autumn, cyanobacteria dominated the counts (Table 4.3) while nanoeukaryotes dominated the community population size (Figure 4.5B).

Table 4.3: Counts of phytoplankton cell (cell mL^{-1}) measured in the main gated populations: picoeukaryotes (“Picoeuk.”), cyanobacteria (“Cyano.”), nanoeukaryotes (“Nanos.”), large phytoplankton (“Large phyto.”) and bacteria for the summer and autumn experiments, in each treatment. The mean value along with the standard deviation ($n=3$) is presented.

Summer					
Treatment	<i>Picoeuk.</i>	<i>Cyano.</i>	<i>Nanos.</i>	<i>Large phyto.</i>	<i>Bacteria</i>
Initial	10880	4150	5630	130	620400
Control	4820 ± 683	5517 ± 1142	15540 ± 560	213 ± 32	379703 ± 92672
Fe	4847 ± 3032	4980 ± 1802	21070 ± 2208	650 ± 191	401147 ± 32324

Mn	5203 ± 942	5883 ± 924	12430 ± 1311	170 ± 36	410350 ± 29142
FeMn	6317 ± 3163	5967 ± 1438	25593 ± 12130	593 ± 15	388403 ± 79888
Autumn					
Treatment	<i>Pico.</i>	<i>Cyano.</i>	<i>Nano.</i>	<i>Large phyto.</i>	<i>Bacteria</i>
Initial	22230	25240	2260	80	655040
Control	12733 ± 3958	18743 ± 5479	4473 ± 2789	67 ± 21	734727 ± 123795
Fe	14220 ± 9869	27023 ± 2675	4230 ± 1897	77 ± 15	1080060 ± 764544
Mn	23865 ± 460	65405 ± 30823	4800 ± 891	55 ± 35	1280305 ± 323593
FeMn	12830 ± 1193	29450 ± 16046	4987 ± 876	117 ± 32	940517 ± 219637

After 7 days of incubation, no significant difference in cell counts were observed between treatments across seasons (ANOVA), but some small changes occurred in the sized-based metric. In autumn, the addition of Mn led to an increase in the cyanobacteria population size relative to the whole phytoplankton community (p -value < 0.05, Tukey's HSD). This change was not observed during the summer experiment.

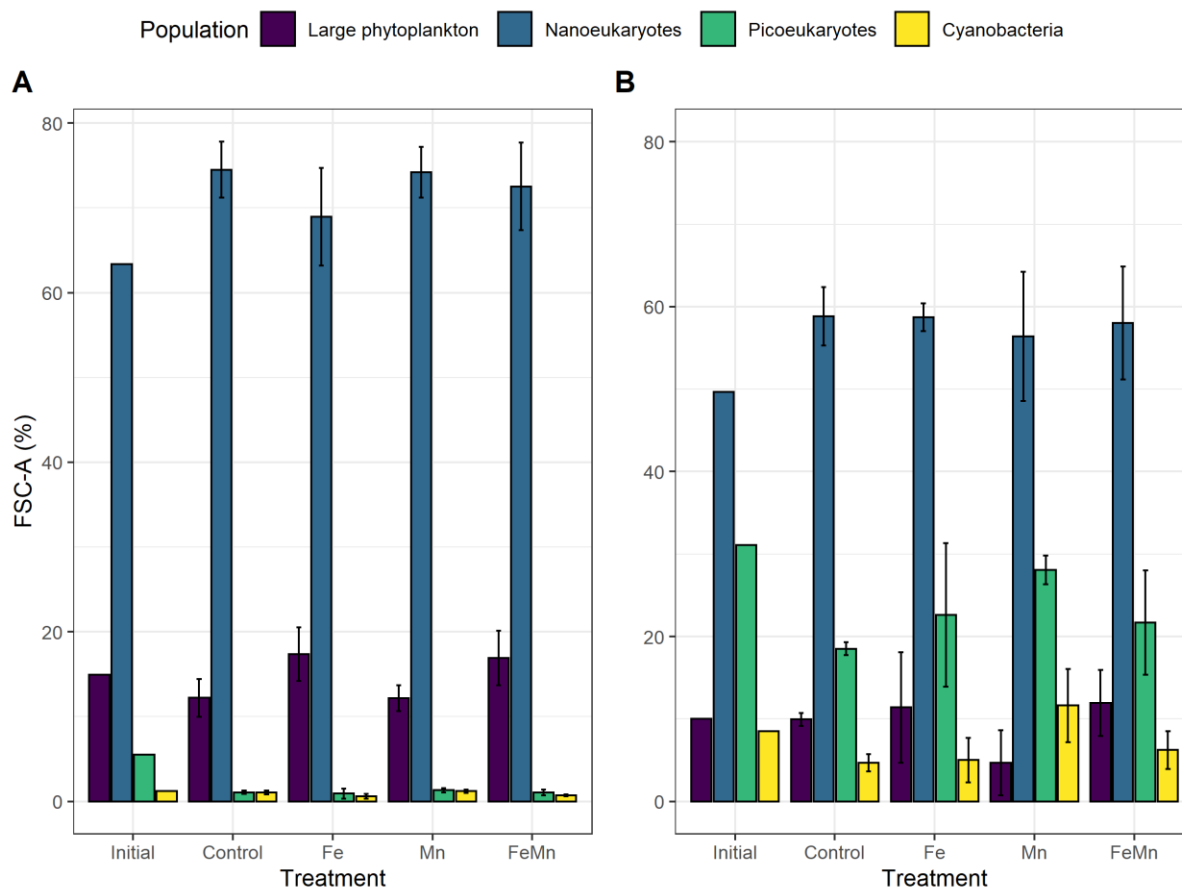


Figure 4.5: Relative contribution of four gated populations compared to all phytoplankton cells captured by the instrument: large phytoplankton (microeukaryotes), nanoeukaryotes, picoeukaryotes and cyanobacteria in terms of population size (FSC), as defined in equation (1) for summer (A) and autumn (B). These values were calculated according to the equation of Bach et al. (2018). Error bars represent the standard deviations ($n = 3$, except for the initial treatment where $n = 1$).

4.3.5. IRON AND CARBON UPTAKE

Different rates of Fe uptake were observed between seasons and size fractions (Figure 4.6). Focusing on the 0.2-2 μm size fraction, no significant differences were observed between treatments across seasons. However, in summer and autumn, Fe uptake rates increased under Fe additions, with higher average values in the +Fe addition alone. The highest Fe uptake was observed in autumn (396.8 \pm 169 pM d^{-1}), whereas mean Fe uptake was lower when both Fe and Mn were added (174.6 \pm 27 pM d^{-1}). No significant difference was observed between treatments in autumn, likely resulting from a small dataset (only 2 data points for the +Fe treatment).

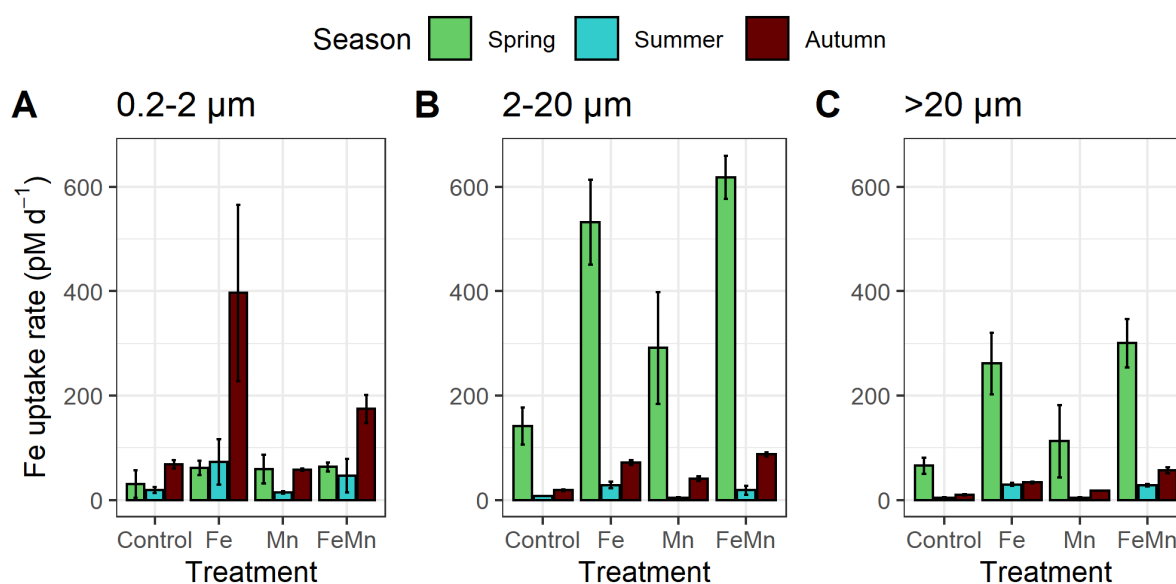


Figure 4.6: Fe uptake (pM d^{-1}) measured in each size fraction and for the three seasons: spring in green, summer in blue and autumn in brown. During the autumn experiment, only two datapoints were recorded for the +Fe treatment. Error bars represent the standard deviations and are smaller than the symbols when not visible ($n = 3$).

In the 2-20 μm size class (Figure 4.6B), Fe uptake was highest in spring with significantly higher Fe uptake under both Fe additions compared to the control and +Mn treatments ($p\text{-value} < 0.05$, Tukey's HSD). The +Mn treatment induced an increase in Fe uptake. However, it was not significantly higher than the control. In comparison, both summer and autumn seasons were characterized by much lower Fe uptake in the 2-20 μm size fraction. In summer, Fe uptake rates were significantly higher than the control only in the +Fe treatment, with a mean value four times higher than Fe uptake in the control ($p\text{-value} < 0.05$, Tukey's HSD). The combined +FeMn addition did not result in a significant stimulation of Fe uptake compared to the control ($p\text{-value} = 0.06$, Tukey's HSD). In autumn, no significant differences in Fe uptake were observed between treatments (Kruskal-Wallis test).

The >20 μm size class (Figure 4.6C) was also characterized by higher Fe uptake values measured in the spring. In both spring and summer, Fe uptake was significantly higher in both treatments with Fe additions (+Fe and +FeMn), compared to the control and +Mn treatments ($p\text{-value} < 0.05$, Tukey's

HSD). In autumn, no significant differences in Fe uptake were observed between treatments, which could result from a low number of data points (Kruskal-Wallis test).

Net primary productivity, measured through carbon uptake, also strongly varied between seasons and size fractions (Figure 4.7). In spring, no significant difference in carbon uptake rates were observed between treatments in the small size fraction (ANOVA). In summer, we measured the highest carbon uptake for picoeukaryotes in the +Fe treatment compared to the control (p -value < 0.05, Tukey's HSD). In addition, both Fe treatments (+Fe and +FeMn) had significantly higher carbon uptake rates than the +Mn treatment (p -value < 0.05, Tukey's HSD). In autumn, no significant differences in carbon uptake were observed in the 0.2-2 μ m size class (Kruskal-Wallis test).

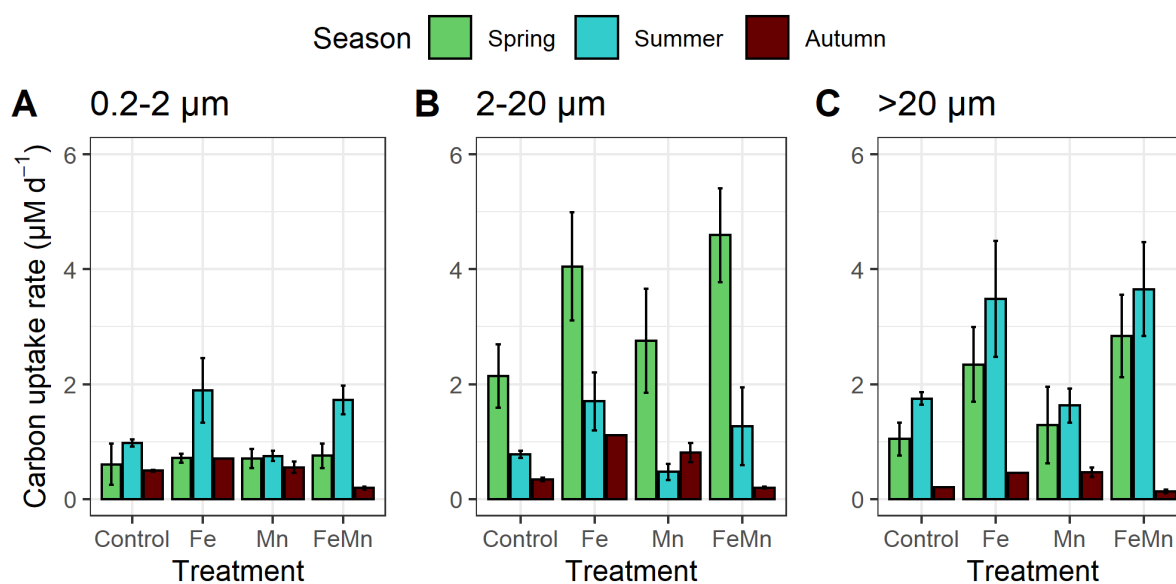


Figure 4.7: Carbon uptake ($\mu\text{M d}^{-1}$) measured in each size fraction and for the three seasons: spring in green, summer in blue and autumn in brown. Due to a manipulation mistake during the autumn experiment, only one datapoint was recorded for the +Fe treatment. For the other treatments, error bars represent the standard deviations and are smaller than the symbols when not visible ($n = 3$).

For the nanoeukaryotes (2-20 μm) during the spring season, only the +FeMn treatment had higher carbon uptake rates than the control (p -value < 0.05, Tukey's HSD). In summer, a significant difference between carbon uptake was only observed between the +Fe and +Mn treatments (p -value < 0.05, Tukey's HSD), with higher carbon uptake with Fe addition alone. In autumn, no significant differences were observed between treatments (Kruskal-Wallis test).

In the >20 μm size class, there was no significant difference in carbon uptake between treatments in spring (Kruskal-Wallis test). In summer, carbon uptake was only significantly higher in the +FeMn treatment compared to the control treatment (p -value < 0.05, Tukey's HSD). The carbon uptake rates measured in the +Fe treatment, while elevated, were not significantly different than the control (p -value = 0.05, Tukey's HSD). However, both +Fe and +FeMn treatments had a higher carbon uptake than in

the +Mn treatment (p -value < 0.05, Tukey's HSD). In autumn, no significant differences were observed in the carbon uptake between treatments within this size class (Kruskal-Wallis test).

Iron to carbon (Fe:C) uptake ratios differed between seasons and treatments, with overall higher ratios measured in autumn (Figure 4.8). Across all sizes, Fe:C ratio ranged between 33 to 153 $\mu\text{mol mol}^{-1}$ in spring, 1 to 18 $\mu\text{mol mol}^{-1}$ in summer and from 34 to 915 $\mu\text{mol mol}^{-1}$ in autumn. In the 0.2-2 μm size fraction, no significant differences were observed between treatments across seasons (ANOVA for spring and summer; and Kruskal-Wallis test for autumn).

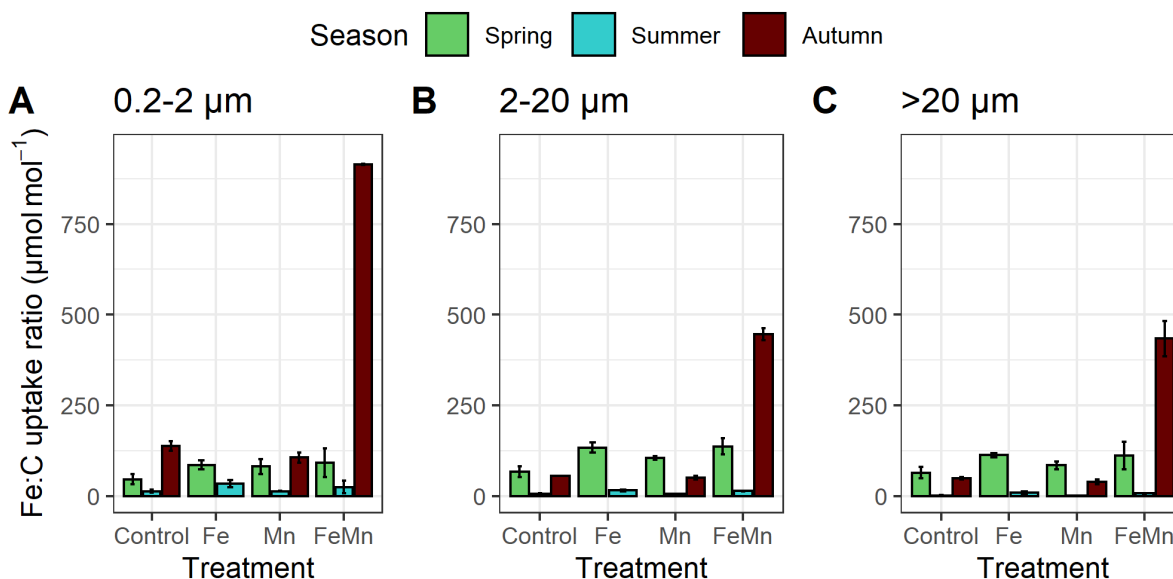


Figure 4.8: Iron to carbon (Fe:C) uptake ratio ($\mu\text{mol mol}^{-1}$) measured in each size fraction and for the three seasons: spring in green, summer in blue and autumn in brown. The Fe:C ratio from the +Fe treatment in autumn was not included due to missing data. Error bars represent the standard deviations and are smaller than the symbols when not visible ($n = 3$).

For the nanoeukaryotes (2-20 μm), spring Fe:C uptake ratios were higher in +Fe and +FeMn treatments compared to the control treatment (p -value < 0.05, Tukey's HSD). In summer, Fe:C ratios measured in +Fe and +FeMn treatments were higher than ratios measured in both the control and +Mn treatments (p -value < 0.05, Tukey's HSD). In autumn, no significant differences were observed, likely resulting from a small dataset (Kruskal-Wallis test).

No significant differences in Fe:C uptake ratios for the microeukaryotes (>20 μm) were observed during the spring experiment (ANOVA), while Fe:C ratios were higher under +Fe and +FeMn compared to the control and +Mn treatments in summer (p -value < 0.05, Tukey's HSD). In autumn, no significant differences were observed but again, this may result from a small dataset (Kruskal-Wallis test).

4.4. Discussion

4.4.1. DIFFERING HYDROGRAPHIC CONDITIONS

Contrasting results may be expected between experiments due to the different locations of the spring experiment, done at PS2, and the two other experiments (summer and autumn), performed at SOTS. The intrusion of warmer and saltier waters from the subtropical zone are commonly observed in the northern part of the subantarctic zone near SOTS and can originate from either the mixing with waters from the Zeehan Current or mixing with waters and eddies from the East Australian Current (Bowie et al. 2011). In this study, the PS2 station, located southeast of Tasmania, is much more likely to be influenced by the East Australian Current, compared to the SOTS site. This explains the strong difference in salinity observed in the spring experiment compared to the two other experiments. However, autonomous seasonal records of phytoplankton communities from the SOTS station revealed no change in community composition due to the input of subtropical waters in the subantarctic zone (Eriksen et al. 2018). Hence, we suggest that the results of the three experiments are comparable, despite the influence of subtropical waters at PS2 in the spring experiment.

The three experiments undertaken were characterized by different initial macronutrient concentrations. Higher phosphate and silicic acid concentrations were observed at the beginning of the spring experiment, which is a characteristic of the early season following winter mixing of surface waters (Rintoul and Trull 2001). In contrast, macronutrient concentrations were lowest in autumn. Phosphate concentrations decrease during the summer season due to biological uptake but are expected to remain higher than limiting levels (Rintoul and Trull 2001). On the other hand, silicic acid concentrations decrease during the growth season, due to consumption from silicifying phytoplankton such as diatoms, silicoflagellates and radiolarians (Deppeler and Davidson 2017; Eriksen et al. 2018). In autumn, silicic acid concentrations reached limiting levels, down to 0.8 μM (Paasche 1973; Hutchins et al. 2001; Westwood et al. 2011). Therefore, silicic acid growth limitation of silicifying organisms may be expected during the autumn experiment. Nitrate concentrations are not presented here but initial levels were not considered limiting (nitrate + nitrite: 11.0 μM in spring, 10.2 μM in summer, 8.3 μM in autumn).

Initial trace metal concentrations were highest in spring for dMn and summer for dFe. It is surprising to observe higher summer dFe concentrations compared to the spring experiment. Usually, higher dissolved concentrations are recorded in the early season, resulting from i) aerosol depositions coming from proximal land (Perron et al. 2020), ii) southern advection of Fe and Mn enriched subtropical waters from the East Australian Current (Sedwick, et al. 2008; Bowie et al. 2009) and/or iii) replete trace metal levels present after the winter season associated with wind-mixing (Bowie et al. 2009). At the SOTS site, higher dFe concentrations observed in summer may result from entrainment following wind-mixing events while decreasing autumn concentrations for both elements likely result from biological consumption.

Initial phytoplankton biomass in summer and autumn was dominated by pico- and nanoplankton, as previously observed in this subantarctic region (Fourquez et al. 2020). In summer, picoeukaryotes dominated phytoplankton abundance while picocyanobacteria were relatively important in autumn (Figure 4.5). It is likely that *Synechococcus* sp. dominated the picocyanobacteria, as has been previously observed at SOTS (Cassar et al. 2015; Fourquez et al. 2020). In all seasons, *in-situ* light limitation of phytoplankton growth is expected due to the deep mixed layer depths present (Figure 4.2). Indeed, Rintoul and Trull (2001) previously observed that a mixed layer depth of 75 to 100 m was deep enough to light limit phytoplankton growth in this region. Here, the mixed layer depth was at or ≥ 100 m (Figure 4.2). Initial physiological measurements indicated that the bulk phytoplankton communities were relatively healthy ($F_v/F_m > 0.5$) at all seasons (Figure 4.4). However, our data indicated various degrees of Fe limitation.

4.4.2. SEASONALITY OF IRON LIMITATION

Phytoplankton growth in subantarctic waters is usually assumed to be Fe limited (Boyd et al. 1999; Sedwick et al. 1999; Hutchins et al. 2001; Petrou et al. 2011). However, our experiments demonstrate that the degree of Fe limitation is seasonal. A previous review suggested Fe may limit subantarctic phytoplankton communities in spring (Boyd 2002). Contrasting with this hypothesis, no clear evidence of Fe stress was observed in our spring experiment. This may result from relatively elevated dFe concentrations in the early season, sufficient to maintain optimal phytoplankton growth at that time. This was supported by the high F_v/F_m values measured in all treatments (Figure 4.4A), suggesting efficient light utilization in PSII (Greene et al. 1992; Hopkinson and Barbeau 2008). Unfortunately, the lack of flow cytometry data for this season means that the initial composition of the phytoplankton community and how it evolved with Fe and Mn additions were not assessed. Previous reports showed this subantarctic region is characterized by a succession from large diatoms in spring toward weakly silicified diatoms in summer/autumn (Eriksen et al. 2018). From our Fe and carbon uptake results, it was observed that most of the Fe and carbon uptake came from nano- and microplankton in spring (Figure 4.6 and 4.7). Hence, it is possible the spring experiment took place during the transition from large diatoms ($> 20 \mu\text{m}$) toward smaller (2-20 μm) and more weakly silicified diatoms in response to decreasing ambient dFe and silicic acid concentrations (Eriksen et al. 2018).

The strongest signal of Fe limitation was observed during the summer experiment as highlighted by i) the drawdown of phosphate concentrations in both treatments where Fe was added (Figure 4.3A), and ii) the increase F_v/F_m and the decrease in σ_{PSII} with Fe additions (Figure 4.4). These results suggest that the addition of Fe alleviated phytoplankton stress (Greene et al. 1992; Petrou et al. 2011). In addition, final N:P ratios indicated Fe additions greatly stimulated nitrate consumption during this season (Figure S4.2). These results agree with previous suggestion of dominant Fe limitation in summer (Boyd 2002). Although nitrate levels were greatly drawn down by the end of the experiment within both Fe treatments (between 0.6 to 2 μM in 5 replicate bottles, and down to $<$ detection limit levels in 1 replicate bottle),

co-limitation from Fe and silicic acid may more likely occur toward the end of the experiment due to silicic acid depletion (Figure 4.3B). Flow cytometry results indicated that nanoeukaryotes dominated the initial population size and remained the dominant group throughout the experiment in all treatments (Figure 5A). Combined with the high uptake of silicic acid observed in summer (Figure 4.3B), these results suggest the growth stimulation of relatively small diatoms, within the nanoeukaryote size range, in agreement with previous results (Eriksen et al. 2018). Despite an overall dominance of smaller diatoms, large phytoplankton (>20 μm) dominated primary productivity (Figure 4.7C). Microeukaryotes comprised about 15% of the population size (Figure 4.5) and may be composed of large diatoms and large dinoflagellates, as previously observed in subantarctic waters (Cassar et al. 2015; Eriksen et al. 2018). Coincident with this relatively high carbon uptake, very low Fe uptake rates were measured in both the nano- and micro- size classes, which suggest that these large summer phytoplankton species, likely diatoms, have low cellular Fe requirements (Strzepek et al. 2011; Gao et al. 2021). This assertion was supported by the very low Fe:C uptake ratios observed during summer in all size classes (Figure 4.8), implying that diatoms were able to sustain growth and substantial carbon assimilation with very low Fe requirements. Similarly, it is notable that the 0.2-2 μm size class had carbon uptake rates as high as the 2-20 μm size fraction, implying a similar efficiency in assimilating carbon between both size classes (Figure 4.7). However, relatively higher Fe uptake rates observed in the 0.2-2 μm size class may indicate higher efficiency in Fe uptake, possibly due to their lower surface area volume ratio (Sunda and Huntsman 1995; Strzepek et al. 2011). Notably, this size fraction also includes Fe uptake by heterotrophic bacteria but their contribution to Fe uptake was not determined.

In autumn, Fe limitation was evident, supported by the increase in F_v/F_m with Fe addition (Figure 4.4; +Fe treatment only) but to a lesser extent than in summer. In contrast to the summer experiment, phosphate and silicic acid drawdown remained much lower in autumn (Table 4.2), indicating that a factor other than Fe may be (co-)limiting phytoplankton growth. Given the low initial silicic acid levels observed (0.8 μM), silicic acid may be the primary variable limiting the growth of silicified organisms (Hutchins et al. 2001; Eriksen et al. 2018) and not dFe concentrations or other macronutrients considering phosphate (0.71 μM) and nitrate + nitrite levels (8.3 μM) remained above limiting levels (Sedwick et al. 1999; Rintoul and Trull 2001). However, the possibility of Fe and silicic acid co-limitation of diatoms growth cannot be excluded (Boyd 2002). A previous study in the subantarctic zone suggested a seasonal succession of limiting variables, with both Fe and silicic acid concentrations limiting the growth of heavily silicified diatoms in late summer and autumn, leading to a community shift toward non-silicified and/or lightly silicified diatoms with low Fe requirements (Hutchins et al. 2001). Relatively high Fe uptake rates were measured in all size classes during the autumn experiment compared to summer (Figure 4.6), possibly due to an upregulation of Fe acquisition in response to chronic Fe limitation in these late season phytoplankton communities. In the >20 μm size class, it is possible dinoflagellates dominated phytoplankton abundance as silicic acid levels were likely limiting

the growth of large diatoms (Eriksen et al. 2018). Unfortunately, we cannot confirm the phytoplankton community composition of the medium and small size class as additional information would be necessary, such as pigments analyses, microscopy or molecular approaches. Flow cytometry did allow the identification of picocyanobacteria, which represented an important group during this season.

In autumn, picocyanobacteria, most likely *Synechococcus* sp. (Cassar et al. 2015) numerically dominated the phytoplankton community (Table 4.3). Previous flow cytometric analyses showed picocyanobacteria are a significant group within the subantarctic phytoplankton community, contributing about 20% to total phytoplankton biomass in mid-late summer (Cassar et al. 2015). In autumn, the contribution of picocyanobacteria to the population size doubled with +Mn addition (Figure 4.5). The photophysiology of picocyanobacteria differs from diatoms and other major phytoplankton groups (Suggett et al. 2009). This is mostly due to their use of phycobilisomes as light-harvesting pigments which results in lower maximum PSII photochemical efficiency (Suggett et al. 2004). Previous studies reported F_v/F_m values ranging from 0.1 to 0.6 for picocyanobacteria (Campbell et al. 1998; Koblížek et al. 2001; Suggett et al. 2009). Hence, it is not straight-forward to link relatively low F_v/F_m values with Fe limitation within a phytoplankton community dominated by cyanobacteria. The increase in F_v/F_m observed in the +Fe treatment (Figure 4.4A) may indicate that a different population with an intrinsically higher F_v/F_m responded to Fe addition. The slightly higher silicic acid uptake rates observed with Fe additions (Table 4.2) suggest the growth of silicified organisms, possibly weakly silicified diatoms in this late season. However, it was previously shown that picocyanobacteria can accumulate silicon intracellularly as a hydrated siliceous network, associated with magnesium or calcium (Ohnemus et al. 2018). Hence, the higher silicic acid uptake may have also resulted from picocyanobacteria stimulation. These results highlight the complexity of identifying nutrient stress conditions from a bulk phytoplankton community dataset, where signals from specific taxonomic groups can get easily lost (Suggett et al. 2009). However, our findings provide evidence for a strong seasonality of Fe limitation and a seasonal succession of various phytoplankton groups, associated with their responses to key environmental constraints, particularly dFe and silicic acid concentrations (Eriksen et al. 2018). In addition, seasonality in phytoplankton responses to Mn additions were also observed.

4.4.3. SIGNAL OF IRON-MANGANESE CO-LIMITATION

Overall, these seasonal experiments did not show a clear signal of Fe-Mn co-limitation, in comparison to the strong responses observed from Fe additions. This outcome concurred with the high Mn^* values calculated for the three seasons (Table 4.1), fitting within the range of Browning et al. (2021) (0.16 - 0.31 nM) for which Fe was limiting but not Mn. However, we observed some interesting responses to Mn addition, particularly from picocyanobacteria. In autumn, the addition of Mn noticeably stimulated the growth of picocyanobacteria (Figure 4.5). The lower bulk F_v/F_m value observed in this treatment may support the hypothesis of a dominant contribution from cyanobacteria, which often have an

intrinsically lower F_v/F_m than eukaryotic algae (Campbell et al. 1998; Koblížek et al. 2001; Suggett et al. 2009). The stimulation of the picocyanobacterial population under Mn addition may indicate that Mn was limiting cyanobacterial growth. However, the F_v/F_m parameter is not a reliable indicator of PSII efficiency in cyanobacteria as they have more flexible electron transport systems (Campbell et al. 1998) and PSII is poorly excited by the wavelength (470 nm) used in this study. Cyanobacterial Mn requirements are still poorly understood. Previous laboratory studies of *Synechocystis* (a freshwater cyanobacteria) showed that dMn concentrations ≤ 100 nM reduces oxygen evolution capacity and results in the accumulation of partially assembled PSII systems, and changes in the organization of photosystem I complexes (Salomon and Keren 2011). In their most limiting Mn treatment, Salomon and Keren (2011) measured a background dMn concentration of 1.8 nM, which is still much higher than what is commonly observed in Southern Ocean open waters. However, oceanic strains may have adapted to lower surrounding dMn concentrations by lowering their Mn requirements. This was previously shown in cyanobacteria regarding adaptation to Fe limitation (Ferreira and Straus 1994). Twining et al. (2010) reported Mn cell quotas (normalised to phosphate) ranging from 0.46 to 0.81 mmol/mol in *Synechococcus* sp. cells from the Sargasso Sea, with strong variations between cyclonic/anticyclonic eddies and mode waters. In Fe-limited Southern Ocean waters, for which there are no data on cyanobacteria, much lower Mn to phosphate ratios were measured in autotrophic flagellates and, unlike diatoms, the ratio increased once Fe stress was alleviated (Twining et al. 2004). Overall, there is insufficient information on the Mn requirements of subantarctic cyanobacterial strains to predict the dMn concentrations at which they become limited. However, our results provide the first evidence that Mn may limit cyanobacteria growth in autumn, when small picoplankton dominate the biomass and surrounding dMn concentrations are lowest. This implies Mn may be linked to deep carbon export as cyanobacteria have been observed to significantly contribute to downward carbon export in subantarctic waters through aggregation (Waite et al. 2000; Cassar et al. 2015) which increases their sinking rate (Jackson 2005). Hence, there may be seasonality in the importance of Mn in stimulating phytoplankton growth, associated with specific phytoplankton taxa such as cyanobacteria.

Another interesting result associated with Mn additions was the significant stimulation of carbon uptake within the 2-20 μm size class in spring and within the >20 μm size class in summer, only occurring under combined Fe and Mn additions (Figure 4.7). Increased carbon fixation and hence, photosynthesis, suggest that these size classes of the phytoplankton community benefited from the combined addition and may be Fe-Mn co-limited. Phytoplankton Mn requirements are directly linked to photosynthesis by two processes: i) the number of PSII reaction centres, due to the central role of Mn in the oxygen-evolving complex of PSII (Armstrong 2008) and, ii) the need for Mn to produce the superoxide dismutase enzyme, to detoxify the cell of superoxide produced during photosynthesis (Peers and Price 2004; Wolfe-Simon et al. 2006). Increased Mn requirements were previously observed in Fe-limited diatoms, due to additional ROS production associated with Fe limitation (Peers and Price 2004). Hence,

stimulation of carbon uptake observed under combined Fe and Mn additions during the summer experiment may be linked to ROS production and increased Mn requirement, knowing that phytoplankton communities were strongly Fe-limited (see previous section). Conversely, stimulation of carbon fixation measured under combined addition in spring is surprising considering phytoplankton communities were not Fe-limited. Instead, this enhanced carbon fixation may result from higher Mn demands associated with higher Fe requirements observed in these early phytoplankton communities.

Our results support the hypothesis that Mn concentrations may be low enough to limit the growth of a subset of the primary producers in this subantarctic region and hence to influence phytoplankton community composition. However, these effects appear to vary seasonally, and are subtle. Here, the evaluation of primary productivity through size-fractionated carbon uptake measurements coupled with flow cytometry helped us to identify these co-limitation signals but this approach is not commonly used. This highlights the need to use a combination of existing techniques, and to develop new tools, to identify Mn (co-)limitation within subpopulations of the phytoplankton community. For example, molecular approaches may prove a valuable tool to target specific subpopulations. In the Ross Sea, Wu et al. (2019) identified Mn co-limitation in *Phaeocystis antarctica* through proteomic measurements. Hence, this technique may be applied to multiple phytoplankton species after identifying specific changes in their proteome resulting from Mn limitation.

4.5. Conclusion

In conclusion, the signal of Mn (co-)limitation observed during these multi-seasonal experiments was masked by the strong seasonality and responses associated with Fe limitation. Our results suggest spring Fe and Mn concentrations were high enough to not limit phytoplankton growth. Conversely, phytoplankton communities were strongly Fe limited in summer. In autumn, we suggest low silicic acid levels limited diatom growth. However, the possibility that silicic acid and Fe were co-limiting diatom growth cannot be excluded. Manganese additions induced subtle community and physiological changes. In autumn, the addition of Mn alone stimulated the growth of cyanobacteria, most likely *Synechococcus* sp. These results suggest cyanobacteria may be Mn-limited in autumn when they constitute an important part of resident phytoplankton biomass and dMn concentrations are lowest following the phytoplankton growth season. In spring and summer, combined Fe and Mn additions stimulated carbon fixation in the nano- and micro- size classes, respectively. This was hypothesized to be due to the high Mn requirements of the spring community and ROS production linked to Fe limitation in summer. These results indicate that Mn may play an important role in controlling/stimulating specific phytoplankton taxa, with seasonal variability. In addition, our results show that Mn (co-)limitation signal may be hard to capture in conventional bioassays, especially when pronounced Fe responses are observed.

5. CHAPTER 5 – Characterization of a Southern Ocean deep chlorophyll maximum: responses of phytoplankton to light, iron and manganese

Latour, P.; Eggins, S.; van Der Merwe, P.; Bach, L.; Boyd, P.; Ellwood, M. J.; Wuttig, K.; Bowie, A. R. & Strzepek, R. F. (*in prep*). **Characterization of a Southern Ocean deep chlorophyll maximum: responses of phytoplankton to light, iron and manganese.**

5.1. Introduction

Southern Ocean phytoplankton play a key role in transferring carbon from the atmosphere into the ocean through the biological carbon pump. Yet, the ocean surrounding the Antarctic continent presents harsh living conditions. Iron (Fe) limitation of phytoplankton growth is now widely known (Boyd et al. 2007). Indeed, low Fe concentrations are thought to be the main factor keeping phytoplankton from consuming the high ambient macronutrient concentrations, making the Southern Ocean one of the High-Nutrient Low-Chlorophyll regions (Boyd et al. 2007). In addition, other parameters may limit phytoplankton growth in this region such as cool temperatures, low light or low silicic acid concentrations (Hutchins et al. 2001; Boyd 2002). However, specific local environments may lead to more favourable growth conditions. These include local Fe fertilisation, alleviating Fe stress (Blain et al. 2007), water column stabilisation, reducing light variability (Smith et al. 2000) or a more favourable combination of light and nutrient conditions at depth, leading to a subsurface chlorophyll accumulation, known as deep or subsurface chlorophyll maxima (DCM or SCM) (Parslow et al. 2001; Holm-Hansen et al. 2005; Baldry et al. 2020).

Deep chlorophyll-a maxima are common features of tropical waters, forming above the pycnocline where they receive just enough light and nutrients to stimulate phytoplankton growth (Cullen 1982; 2015). In contrast to tropical DCM, Southern Ocean DCM are usually located at or deeper than the pycnocline, and surface waters are replete in macronutrients (Baldry et al. 2020). Southern Ocean DCM have been associated with Fe limitation and low chlorophyll-a concentrations in surface waters, as well as the temperature minimum layer, a remnant of Antarctic surface waters (Parslow et al. 2001; Holm-Hansen et al. 2005). In addition, Southern Ocean DCM are characterized by phytoplankton communities that differ from surface waters and are usually composed of large diatoms (Parslow et al. 2001; Gomi et al. 2010). Several processes are thought to control these features, such as water column stratification, grazing from higher trophic levels, and diatom buoyancy regulation (Holm-Hansen et al. 2005; Baldry et al. 2020). Yet, many questions related to the formation, ecology and persistence of Southern Ocean DCM remain. Currently, the most efficient way to study these features is to estimate chlorophyll biomass using fluorescence sensors mounted on BGC Argo floats or elephant seals, thus capturing deep or subsurface fluorescence maxima (DFM or SFM) (Carranza et al. 2018; Baldry et al. 2020). Southern Ocean SFM have been repeatedly observed during summer, with about 60 % of fluorescence profiles reporting these features, suggesting DCM may be recurrent features in this region that influence the

carbon cycle and the structure of Southern Ocean ecosystems (Carranza et al. 2018; Baldry et al. 2020). However, non-photochemical quenching of chlorophyll fluorescence that occurs during the day can result in a SFM where a SCM would not really exist, mis-identifying these deep features (Baldry et al. 2020). Hence, direct measurements of phytoplankton physiology and biomass remain essential to fully understand Southern Ocean DCM.

When a deep chlorophyll build-up is observed and identified as a DCM, uncertainties remain about their occurrence and potential impact on carbon biogeochemistry. For example, increases in cellular chlorophyll concentration due to photoacclimation or changes in phytoplankton community composition can result in an accumulation of chlorophyll that is uncoupled from changes in carbon-based biomass (Rembauville et al. 2016). Differentiating between these processes remains complex without chlorophyll to carbon ratio measurements or microscopic analyses and few studies performed these measurements in Southern Ocean DCM (Baldry et al. 2020). The deep location of DCM, sometimes near 100 m deep, also raises the question of their efficiency in terms of primary productivity, as the low light found at this depth (~ 1% of incident irradiance) is expected to strongly limit phytoplankton carbon fixation (Parslow et al. 2001; Baldry et al. 2020). Furthermore, interactions between low light levels and concurrent low Southern Ocean Fe concentrations raise the following question: are low light conditions inducing an increase in phytoplankton cellular Fe requirements? It was previously shown in laboratory cultures that cellular Fe requirements can increase under low light, due to the increased number of Fe-rich photosynthetic units as cells photoacclimate (Sunda and Huntsman 1997). Conversely, Southern Ocean phytoplankton can modify the size, instead of the number, of their photosynthetic units to avoid increasing their Fe requirements under low light conditions (Strzepek et al. 2012; Strzepek et al. 2019). In Southern Ocean DCM, large light-harvesting antennae complexes have been observed in bulk photophysiological measurements and were associated with low Fe and light conditions (Hopkinson et al. 2007; Hopkinson and Barbeau 2008). The only additional experiment performed at Southern Ocean DCMs showed that phytoplankton communities may be Fe limited, especially large diatoms (Hopkinson et al. 2007). Field studies investigating Fe/light co-limitation in DCM of the Pacific Ocean found a range of responses, from strict light limitation to combined light and Fe co-limitation, with large diatoms often responding strongly to elevated Fe and light conditions (Hopkinson and Barbeau 2008; Johnson et al. 2010). Still, the combined role of Fe and light in mediating Southern Ocean DCM is unclear, especially in the Southern Ocean where it has not been studied (Baldry et al. 2020). In addition, trace metal co-limitation has not been previously studied at Southern Ocean DCM. Recently, manganese (Mn) was observed to limit phytoplankton growth in both coastal and open waters of the Southern Ocean (Wu et al. 2019; Browning et al. 2021) but still little is known about its potential role in limiting phytoplankton growth in polar waters. Manganese is an essential element for photosynthetic organisms, used in the oxygen evolving complex for the water-splitting reaction of photosystem II (PSII) (Armstrong 2008). Manganese is also used in the superoxide

dismutase (SOD) enzyme, in the defence against reactive oxygen species (ROS). In the Southern Ocean, surface and deep dissolved Mn (dMn) concentrations are extremely low but usually characterized by subsurface dMn maxima around 200 m (Middag et al. 2011; Latour et al. 2021). Hence, deep phytoplankton communities may display different Mn requirement as local dMn inputs following internal waves/mixing may occur more often than in surface waters.

To improve our understanding of the environmental controls on Southern Ocean DCM, we performed a 10-day shipboard bioassay in waters south of the Polar Front. Phytoplankton communities collected from a DCM were incubated with the addition of Fe at two light levels: one reproducing the ambient light at the DCM depth and the other one reproducing a shallower depth. We tested the hypothesis that phytoplankton Fe requirements may be higher under low light conditions, due to the potential increase of Fe-rich photosynthetic units arising from photoacclimation. In addition, we tested the hypothesis that manganese (Mn) may limit the growth of part of the phytoplankton community. Due to its use in the oxygen evolving complex and in antioxidant processes, phytoplankton Mn requirement may increase under low light conditions, due to an increase in PSII units or increase under high light due to upregulation of SOD to defend against ROS.

5.2. Material and methods

5.2.1. EXPERIMENTAL SET UP

The experiment was performed during the Southern Ocean Large Area Carbon Export (SOLACE) voyage onboard RV *Investigator* (IN2020-V08) during the austral summer (December 2020). Seawater was collected at the first of the two southern sites surveyed (55.47°S 138.34°E) at 87m, where an SFM was captured by the fluorescence sensor (FLBBNTU, WET Labs, USA) deployed on the Conductivity-Temperature-Depth (CTD) rosette. Trace-metal clean seawater was collected using a trace metal rosette (TMR) to minimise trace metal contamination and was processed in an ISO Class 5 containerized laboratory. Initial seawater was sampled for macronutrients and dissolved trace metal concentrations, as well as photophysiology and flow cytometry to characterize the initial phytoplankton community. Depth profiles of Fe and carbon uptake measurements were also performed on initial communities, assessed over a 24h period within deck board incubators using mesh bags to reproduce the respective depth of each phytoplankton community. Acid-washed, two-litre polycarbonate bottles were filled with unfiltered seawater directly from Niskin bottles in the containerized clean-laboratory before being spiked with Fe and/or Mn to reach a final concentration of at least 2 nM within the bottles, which is considered replete for both elements (Browning et al. 2021). Iron and Mn spikes were prepared in 0.01 M hydrochloric acid (HCl) using ultrapure salts of FeCl₃ and MnCl₂. Triplicates were used for each of the four treatments: control, +Fe, +Mn and +FeMn. The bottles were then incubated in shipboard temperature-controlled incubators and maintained close to the initial in-situ DCM temperature (2.7°C). Throughout the experiment, the incubators temperature was on average $3.4 \pm 0.24^\circ\text{C}$ (n = 12). The deck

board incubators allowed the algal communities to follow their regular diel light:dark cycles although two light settings were reproduced. The low and high light treatments were designed to mimic irradiance at the DCM and simulated shoaling, respectively, and were calculated from the proximate CTD Photosynthetic Active Radiation (PAR) profile (Figure 5.1).

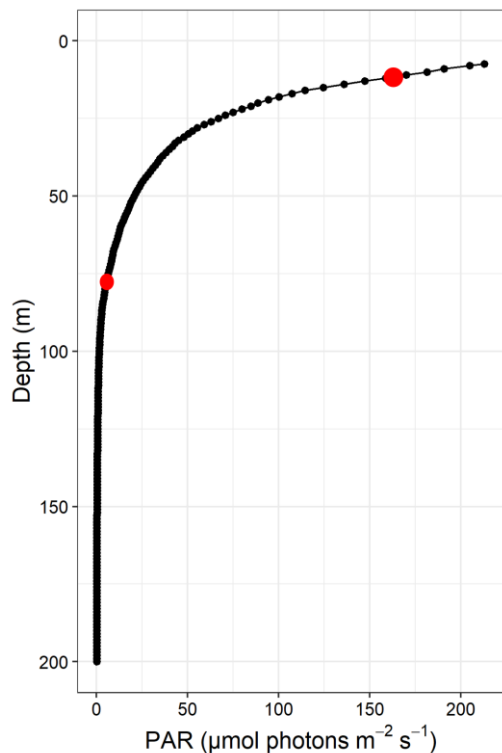


Figure 5.1: Photosynthetic Active Radiation (PAR in $\mu\text{mol photons m}^{-2} \text{s}^{-1}$) showing the decrease in PAR with depth. The two red points represent the two depths used for the calculation of the light attenuation coefficient K .

Briefly, we derived a light attenuation coefficient K (in m^{-1}) and an attenuation depth from the equation:

$$K = \frac{D(\ln(PAR))}{D(z)}$$

where $D(\ln(PAR))$ is the difference between $\ln(PAR)$ measured between two depths points (here we used 10 and 76 m; Figure 5.1), and $D(z)$ the difference between the two depths. From the coefficient K , we calculated the attenuation depth as $1/K$. Then, we measured the incident irradiance (I_0) within different sets of neutral density mesh bags and calculated the factor of attenuation depth as $-\ln(\text{incident irradiance})$. Finally, we calculated the depth reproduced by the mesh bags, by multiplying the factor of attenuation depth by the attenuation depth ($1/K$) (Table 5.1). In this way two light treatments were achieved: one that reproduced the irradiance at 87 m (the depth of the DCM), while the elevated light treatment reproduced the irradiance measured at 40 m (Table 5.1). This method was also used to assess depth profiles of carbon and Fe uptake measurements associated with initial communities (see Figure 5.2G and H below).

Table 5.1: Incident irradiance (I_0), factor of attenuation depth (AD) and derived depth (m) calculated for the different light treatments used during the field incubations. For the present work, we used either 1- (high light) or 3-layers (low light) of mesh to attenuate light.

Treatment	I_0	Factor of AD	Depth (m)
1 mesh	0.124	2.09	40.7
2 mesh	0.034	3.38	65.8
3 mesh	0.011	4.49	87.4
4 mesh	0.003	5.87	114

5.2.2. SAMPLE COLLECTION

After five days of incubation, each bottle was sampled for photophysiology, macronutrients and flow cytometry. Flow cytometry samples were fixed with a mix of formaline:hexamine (18%:10% v/w) for the study of phytoplankton and 2% glutaraldehyde (Electron-microscope grade, 25%) for heterotrophic bacteria composition. After fixation, the samples were flash-frozen and stored at -80°C until analysis onshore. The sampling was repeated after 10 days with the addition of sampling for chlorophyll-*a* (Chl-*a*) using GF/F filters, particulate organic carbon (POC) using precombusted (450°C for 4h) GF/F filters, and biogenic silicate (BSi) concentrations using $2.0\ \mu\text{m}$ polycarbonate filters.

Following the last subsampling, 300 mL of the remaining seawater was dispensed into acid-washed polycarbonate bottles and spiked with 16-20 μCi of Sodium ^{14}C -bicarbonate ($\text{NaH}^{14}\text{CO}_3$; specific activity $1.85\ \text{GBq}\ \text{mmol}^{-1}$; PerkinElmer, USA) and 0.2 nM of an acidified ^{55}Fe solution ($^{55}\text{FeCl}_3$ in 0.1 M Ultrapure HCl; specific activity $30\ \text{MBq}\ \text{mmol}^{-1}$; PerkinElmer). Bottles were then incubated in the shipboard incubators for another 24h, under the same conditions as the bioassay experiments. For the initial sampling, Fe and carbon uptake rates were measured at 6 light levels (simulated depth profile) and in a dark control, which was subtracted from the carbon uptake rates. The spiked samples were then filtered sequentially through 20, 2 and $0.2\ \mu\text{m}$ polycarbonate filters (47 mm diameter; Poretics, USA), separated by $200\ \mu\text{m}$ nylon mesh spacers. For the simulated Fe and carbon uptake depth profile, carbon uptake was also measured without size-fractionation by collecting the entire sample on a $0.2\ \mu\text{m}$ polycarbonate filter. This allowed comparison between the sum of the filter fractions and the ‘total’ carbon uptake. The filters were washed with Titanium(III) Ethylenediaminetetraacetic acid (EDTA) – citrate reagent for 5 min to dissolved Fe (oxy)hydroxides and remove ferric ions bound to particle surfaces and rinsed three times with 15 mL of $0.2\ \mu\text{m}$ -filtered seawater three times. Finally, filters were placed in 20 mL glass vials (Wheaton Industries, USA) and acidified with 200 μL of 1.2 M HCl. These filters were then stored at room temperature for analysis on shore.

5.2.3. SAMPLE ANALYSIS

Photophysiology and macronutrients were directly measured onboard as described in Chapter 4 using a Soliense Light-induced Fluorescence Transients (LIFT) Fast Repetition Rate Fluorometry (FRRF) and segmented flow analysis, respectively (Rees et al. 2018). However, the maximum photochemical efficiency (F_v/F_m) and functional absorption cross section (σ_{PSII}) were determined using the 445 nm excitation wavelength for this experiment. Chlorophyll-*a* concentrations were also measured onboard. Briefly, pigments were extracted in 90% acetone for 18 to 24 hours at -20°C before reading the fluorescence prior to and after the addition of 10% HCl on a Turner Trilogy fluorometer. The remaining samples were analysed back onshore.

Biogenic silicate concentrations were determined through spectrophotometry following the method described in Paasche (1973). Briefly, BSi was converted to silicic acid through leaching with 0.1 M sodium hydroxide at 85°C for 2.25 h before determination of silicic acid concentrations spectrophotometrically. Filters for POC determination were exposed to fuming HCl for about 12h to remove carbonates. Then, total carbon concentrations were determined using a Sercon-Callisto continuous flow isotope ratio mass spectrometer (CF-IRMS).

Iron uptake and net primary productivity (carbon uptake) were determined by measuring disintegrations per minute (DPM) on a liquid scintillation counter (PerkinElmer Tri-Carb 2910 TR). Filters were incubated at for least 24h prior analysis in 10 mL of Ultima Gold liquid scintillation cocktail (Perkin Elmer). Daily carbon incorporation rates were estimated following Hoppe et al. (2017). The uptake of ^{55}Fe and ^{14}C were corrected for ambient dissolved (dFe) and dissolved inorganic carbon concentrations. Iron and carbon uptake rates were normalized per cell using cell counts measured by flow cytometry, matching the Fe and carbon size-fractionated results to flow cytometry group counts as follows: 0.2-2 μm with picoeukaryotes and heterotrophic bacteria counts (for carbon uptake, bacterial counts were removed), 2-20 μm with nanoeukaryotes and >20 μm with large phytoplankton.

Flow cytometry samples were analysed using an Aurora Cytek flow cytometer at the Menzies Institute for Medical Research (University of Tasmania, Hobart). This instrument can measure particles ranging from 200 nm up to at least 60 μm . It is likely that this instrument can capture cells larger than 60 μm , but we acknowledge that the larger cells (up to 300 μm) may have been under sampled. However, we cannot quantify this as the largest size particles possibly measured by this instrument has not yet been determined. Frozen samples were thawed at 37°C for 5-10 minutes before running 500 μL of sample through the instrument, using a high flow rate and MilliQ-water as sheath fluid. Three main populations were gated in each sample: i) picoeukaryotes, ii) nanoeukaryotes and iii) large phytoplankton using the violet channel (V12, red fluorescence channel) against forward scatter (FSC) (similarly as Figure S4.1 in Appendix C for Chapter 4). Position of gates were adjusted per light level as cells had higher fluorescence resulting from higher pigment content per cell under low light treatments (i.e.,

phytoplankton cells collected deeper in the water column) due to photoacclimation (Cullen 2015; Rembauville et al. 2016). Under high light conditions, we observed differences in the fluorescence intensity between treatments and adjusted the gates to fit the three groups mentioned previously. Cell counts were measured directly during the sample analysis, by running a known volume of sample (here 500 μ L). Then, we calculated the relative importance of each group in terms of community size (FSC) and chlorophyll fluorescence (B7), following the equation from Bach et al. (2018):

$$F_{pop} = \frac{N_{pop} \times FSC_{pop}}{N_{all} \times FSC_{all}}$$

Where F represent the fraction of size (size is here represented by the parameter FSC) produced by a specific population. N represents an abundance via cell count of a specific population or all phytoplankton cells (all). With this equation, FSC can be replaced by another parameter, for example chlorophyll fluorescence (blue excitation wavelength, B7), which would then indicate the fraction of chlorophyll fluorescence associated with a specific population.

Bacterial counts were measured on the same instrument after the staining of samples with SYBRG I (1000-fold dilution) after a dark incubation period of 15 minutes at room temperature (Marie et al. 1999). Then, 50 μ L of stained sample was run on the instrument at high flow rate. Bacteria were identified using blue excitation light (channel B2) and measuring green fluorescence.

5.2.4. STATISTICAL ANALYSES

To test for treatment and size effects, we performed a one-way analysis of variance (ANOVA) using R software (R “stats” packages, R Core Team 2020) with a post hoc Tukey test. Dataset was first tested for homogeneity using a Levene’s test and normal distribution using a Shapiro-Wilk test. When one of the assumption was violated, a Kruskal-Wallis test was performed followed by a Wilcoxon signed-rank test if the former result was significant. A p-value of 0.05 was used to determine significance.

5.3. Results

5.3.1. CHARACTERISTICS OF THE DCM

Fluorescence profiles measured during the CTD deployment indicated an increase at about 87 m (Figure 5.2A). Chlorophyll-*a* concentrations measured along the same depth profile indicated a coincident pigment accumulation at the same depth, along with an increase in the amount of Chl-*a* per cell (Figure 5.2B and Table 5.2). Despite the increase in Chl-*a*, the fluorescence per chlorophyll-*a* ($F_{\text{chl-a}}$) ratio increased at the DCM (Figure 5.2C). Biogenic silicate concentrations peaked at a shallower depth (70 m) than the peak in fluorescence and Chl-*a* concentrations (Figure 5.2D). Similarly, POC results showed elevated concentrations at 70 m (Table 5.2). This resulted in a Chl-*a* to POC ratio (Chl-*a*: C) of 0.15 and 0.16 at 70 and 87 m, respectively (Figure 5.2E and Table 5.2). Silicic acid concentrations twice as high as surface waters were observed at about 87 m (Figure 5.2F), coinciding with the top layer of a colder water mass (Table 5.2). Initial net primary productivity was dominated by the large size class at

all depths (Figure 5.2G), with a maximum carbon uptake measured at the light treatment simulating the 42 m depth. Below this, decreasing carbon uptake rates were observed with increasing depth. Iron uptake was dominated by the small size fraction (0.2-2 μm) at all depths (Figure 5.2H). Carbon and Fe uptake measured at the simulated 92 m depth represented 12% and 5% of the total euphotic zone rates, respectively.

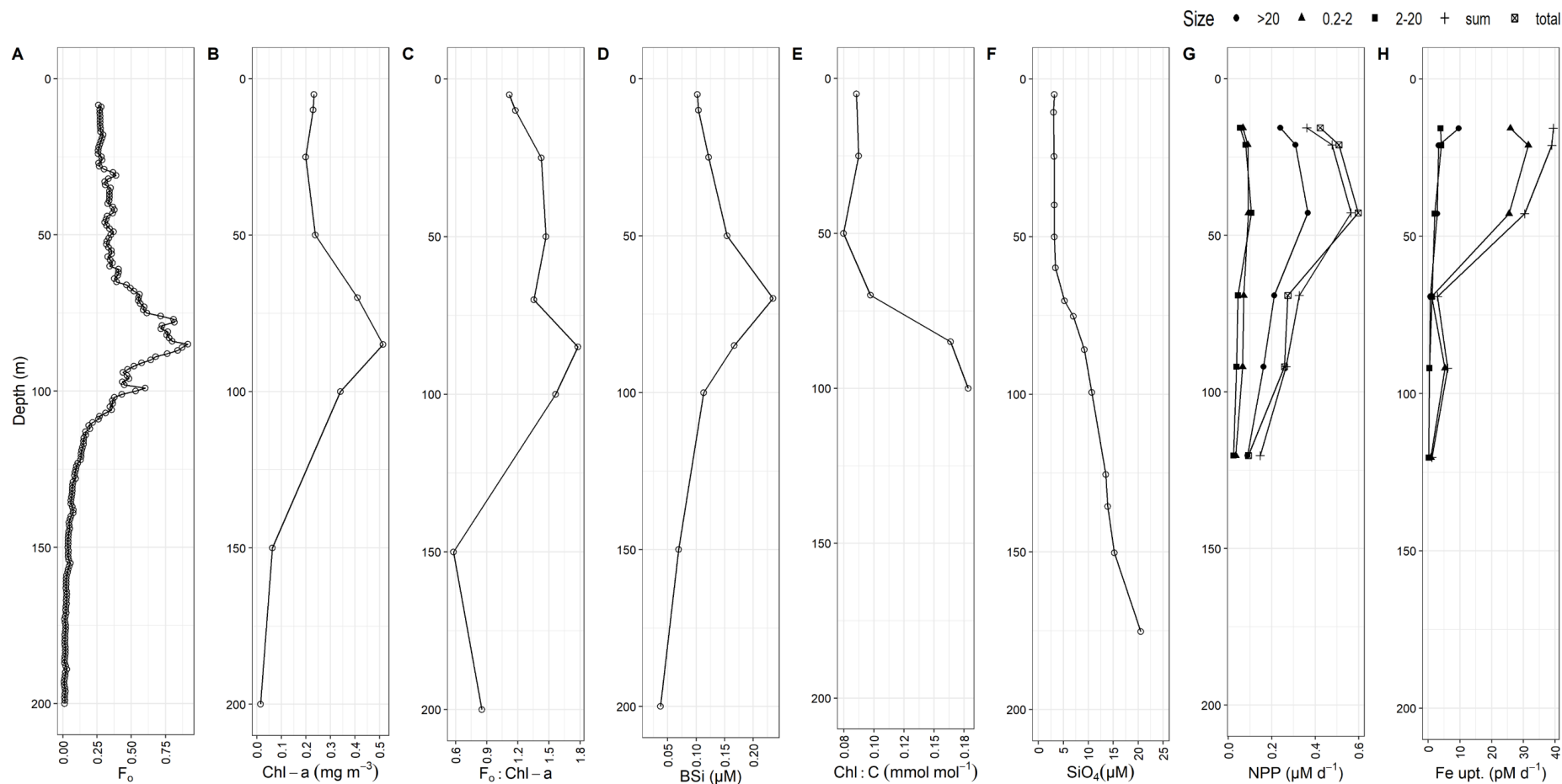


Figure 5.2: Depth profiles of A) fluorescence (F_0) measured by the CTD sensors; B) chlorophyll-*a* (Chl-*a*) concentrations in mg m^{-3} ; C) ratio of fluorescence per chlorophyll-*a* ($F_0:\text{Chl-}a$); D) biogenic silicate (BSi) concentrations in μM ; E) ratio of chlorophyll-*a* per particulate organic carbon (Chl:C) in mmol mol^{-1} ; F) silicic acid concentrations (μM); G) net primary productivity (NPP) measured through carbon uptake ($\mu\text{M d}^{-1}$); H) intracellular Fe uptake (pM d^{-1}). The legend of shapes only relates to the different sizes measured for the NPP and Fe uptake (G and H).

Trace metal samples revealed dFe and dissolved Mn (dMn) concentrations of 0.24 nM and 0.33 nM respectively, at 87 m (Table 5.2). Lower dFe concentrations were measured near the surface (0.20 nM). However, higher values were observed at intermediate depths (50 m; Table 5.2). Dissolved Mn concentrations varied little within the euphotic zone (Table 5.2). Photophysiological measurements showed decreasing F_v/F_m with depth, reaching 0.48 at 80 m (Table 5.2). The functional absorption cross section of PSII (σ_{PSII}) was lower in surface waters and higher at depth ≥ 50 m (Table 5.2).

Table 5.2: Characteristics of the DCM and overlying waters: dissolved Fe (dFe), dissolved Mn (dMn), chlorophyll-*a* concentrations (Chl-*a*), temperature (“Temp.”), chlorophyll-*a* concentrations per cell (Chl:cell), biogenic silica (BSi), particulate organic carbon (POC or C in ratio), photochemical efficiency of PSII (F_v/F_m) and functional absorption cross section of PSII (σ_{PSII}). ‘/’ indicates no data were collected.

Depth (m)	dFe (nM)	dMn (nM)	Chl- <i>a</i> (mg m ⁻³)	Temp. (°C)	Chl:cell (ng/cell)	BSi (µM)	POC (µM)	Chl:C (mmol mol ⁻¹)	F_v/F_m	σ_{PSII} (nm ² quanta ⁻¹)
10	0.20	0.31	0.23	4.07	71.9	0.10	/	/	0.61	6.68
25	/	/	0.20	4.07	/	0.12	2.54	0.09	/	/
50	0.31	0.30	0.24	4.01	67.1	0.15	3.56	0.07	0.58	9.39
70	/	/	0.41	3.50	/	0.23	4.71	0.10	/	/
87	0.24	0.33	0.51	2.68	200.7	0.17	3.51	0.16	0.48	9.28

Flow cytometry measurements showed picoeukaryotes dominated cell counts at 15 and 50 m while nanoeukaryotes dominated cell counts at 87 m (Figure 5.3A). At 15, 50 and 87 m, nanoeukaryotes were more important in terms of Chl-*a* biomass, followed by equal contributions from picoeukaryotes and large phytoplankton at 15 and 50 m (Figure 5.3B). At 87 m, large phytoplankton contributed more to Chl-*a* biomass than picoeukaryotes (Figure 5.3B).

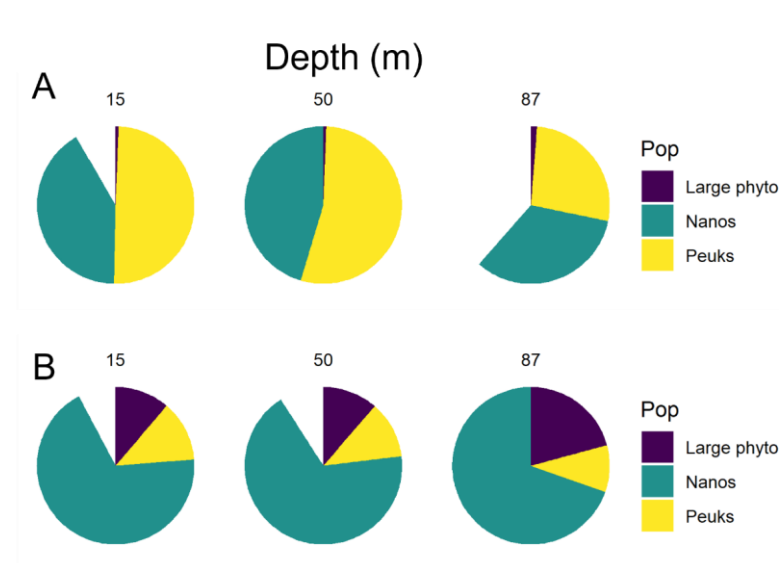


Figure 5.3: A) Cell counts (cell mL⁻¹) and B) relative importance in terms of chlorophyll-*a* fluorescence (%) for the three main populations gated: picoeukaryotes (“Peuks”), nanoeukaryotes (“Nanos”), large phytoplankton

(“Large phyto”) at the initial TMR cast where the DCM was sampled (at 87 m). The white pie slices indicate cells that were not included in the three main gates.

5.3.2. LOW AMBIENT DCM LIGHT TREATMENT

After 10 days of incubation at low light levels, final concentrations were similar to initial levels and no significant decrease in macronutrients concentrations nor different nutrient uptake rates of phosphate and silicic acid were observed between treatments (ANOVA; Figure 5.4A, B, C and Table 5.3). We did observe a significant difference in nitrate consumption with higher nitrate uptake rates in the control and +Fe treatments compared to the +Mn and +FeMn treatments (ANOVA and post hoc Tukey; $p < 0.05$; Table 5.3). In all treatments, final POC concentrations decreased after 10 days of incubations but no significant changes in POC concentrations or POC synthesis rates were observed between treatments under low light (ANOVA; Figure 5.4E and Table 5.3). However, higher Chl-*a* concentrations were measured under both low-light Fe additions compared to the control and +Mn treatments (ANOVA and post hoc Tukey; $p < 0.05$; Figure 5.4D and Table 5.3), which had similar Chl-*a* concentrations as initial levels. This resulted in higher Chl-*a*:C ratios in +Fe and +FeMn treatments (ANOVA and post hoc Tukey; $p < 0.05$; Table 5.3).

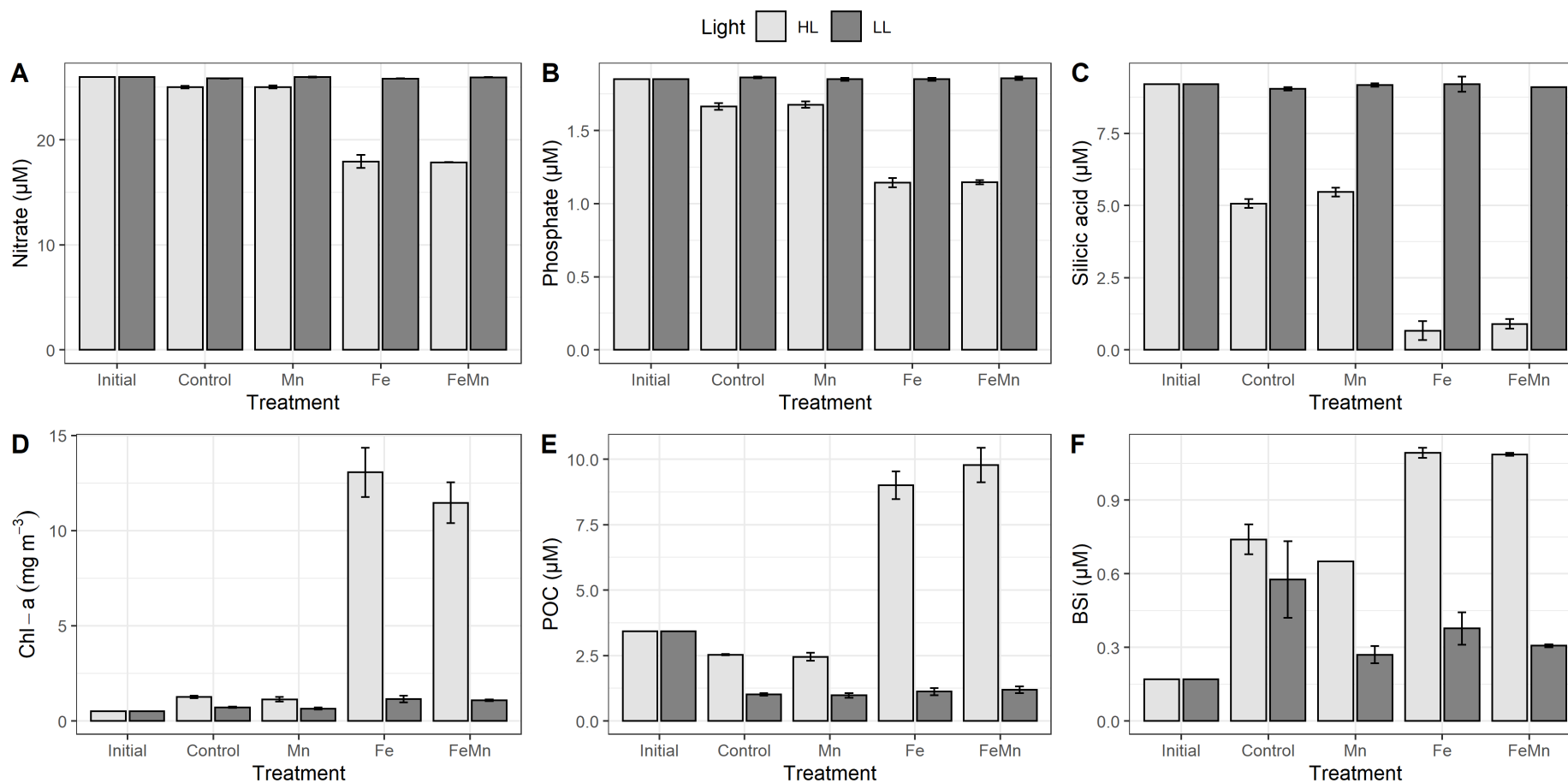


Figure 5.4: Concentrations of nitrate (A), phosphate (B), silicic acid (C), chlorophyll-*a* (D), particulate organic carbon (POC, E) and biogenic silicate (BSi, F) measured in the initial water incubated (“Initial”) and after 10 days of incubations, in each treatment: Control, +Fe (“Fe”), +Mn (“Mn”), +FeMn (“FeMn”). The two colours represent the light treatments: light grey for high light (HL) and dark grey for low light (LL).

Table 5.3: Nutrient consumption rates of nitrate (ΔN), phosphate (ΔP), silicic acid (ΔSi) in $\mu M d^{-1}$ and rate of chlorophyll-a ($\Delta Chl-a$) and POC production in $mg m^{-3} d^{-1}$ and $\mu M/day$, respectively.

Light condition	Parameter	Control	Mn	Fe	FeMn
LL	ΔN	0.013 ± 0.001	0.001 ± 0.001	0.014 ± 0.001	0.003 ± 0.002
	ΔP	-0.001	0.000	0.000	-0.001
	ΔSi	0.017 ± 0.010	0.003 ± 0.000	0 ± 0.000	0.010 ± 0.000
	$\Delta Chl-a$	0.020 ± 0.002	0.013 ± 0.004	0.064 ± 0.014	0.057 ± 0.003
	ΔPOC	1.882 ± 0.216	1.649 ± 0.450	2.482 ± 0.648	2.915 ± 0.613
HL	ΔN	0.097 ± 0.010	0.094 ± 0.013	0.804 ± 0.050	0.813 ± 0.002
	ΔP	0.019 ± 0.002	0.017 ± 0.002	0.071 ± 0.002	0.070 ± 0.002
	ΔSi	0.413 ± 0.012	0.373 ± 0.012	0.853 ± 0.026	0.83 ± 0.014
	$\Delta Chl-a$	0.075 ± 0.006	0.062 ± 0.010	1.255 ± 0.106	1.095 ± 0.088
	ΔPOC	10.8 ± 0.1	10.3 ± 0.7	49.0 ± 2.6	53.6 ± 3.2

Another response to Fe addition was the significant decrease in σ_{PSII} under both Fe additions compared to the control and +Mn treatments (ANOVA and post hoc Tukey; p -value < 0.05; Table 5.4). We observed a decrease in BSi in all low-light treatments, compared to the control (ANOVA and post hoc Tukey; p -value < 0.05; Figure 5.4F). However, we did not observe any significant difference in the BSi:C and BSi:Chl-*a* ratios between treatments (Table 5.4). Small and non-significant variations were observed in the remaining parameters. High F_v/F_m values were measured in all treatments by the end of the experiment (>0.55; Table 5.4), all higher than the initial F_v/F_m of 0.48 measured at the DCM (Table 5.2). The $F_o:Chl-a$ ratio did not show any significant difference between treatments (ANOVA; Table 5.4). Flow cytometry results indicated that the contribution of each phytoplankton group was similar to initial DCM conditions after 10 days of incubation under low light levels. Picoeukaryotes dominated phytoplankton cell counts in all treatments while nanoeukaryotes were the dominant group in terms of Chl-*a* biomass across all treatments (Table 5.5 and Figure 5.5). No significant difference in phytoplankton and bacterial cell counts were observed between treatments (ANOVA; Table 5.5).

Under low-light, net primary productivity was dominated by the large size fraction (> 20 μm) with higher carbon uptake under combined Fe and Mn additions compared to the control and +Mn treatments (ANOVA and post hoc Tukey test, p -value < 0.05; Figure 5.6A-C). No significant differences were observed between treatments in the other size classes (ANOVA). In addition, we did not observe any significant differences in cellular carbon uptake between treatments in any size class (ANOVA; Figure 5.7A-C). Iron uptake rates were low under low light conditions (< 3 $pM d^{-1}$) with higher apparent Fe uptake observed with +Fe additions compared to the control and +Mn treatments in the medium (2-20 μm) and large (>20 μm) size classes (Figure 5.6E-F). However, the difference was not significant according to the statistic test (Wilcoxon signed-rank test), which may result from a low number of data

points. Under combined +FeMn additions, Fe uptake was also higher than both the control and +Mn treatments in the medium size class, but only higher than the control in the large size fraction. In the small size class (2-20 μm), only the +Mn treatment was characterized by a significantly higher Fe uptake rate than the control (ANOVA and post hoc Tukey test, $p\text{-value} < 0.05$; Figure 5.6D). Higher cellular Fe uptake was also observed in the large size class under +Fe and +FeMn additions compared to the control and +Mn treatments (ANOVA and post hoc Tukey test, $p\text{-value} < 0.05$; Figure 5.7F). In the medium size class, higher cellular Fe uptake was only observed with +FeMn additions compared to the control and Mn treatments (ANOVA and post hoc Tukey test, $p\text{-value} < 0.05$; Figure 5.7E). No significant difference in cellular Fe uptake was observed in the small size class between treatments (ANOVA; Figure 5.7D). However, volumetric Fe:C uptake ratios were higher in the small size fraction (Figure 5.6G-I), with a significantly higher ratio only observed in the +Mn treatment compared to the control (ANOVA and post hoc Tukey test, $p\text{-value} < 0.05$; Figure 5.6G). Similarly, cellular Fe:C uptake rates were higher in the +Mn treatment compared to the control and the +FeMn treatments in this size fraction (ANOVA and post hoc Tukey test, $p\text{-value} < 0.05$; Figure 5.7G). In the medium size class, higher volumetric and cellular Fe:C uptake ratios were measured under both Fe additions (ANOVA and post hoc Tukey test, $p\text{-value} < 0.05$; Figure 5.6H and Figure 5.7H). In the large size class, volumetric and cellular Fe:C ratios were higher under +Fe and +FeMn additions compared to the control, with Fe:C ratio in +FeMn not significantly higher than in the +Mn treatment (ANOVA; Figure 5.6I and Figure 5.7I).

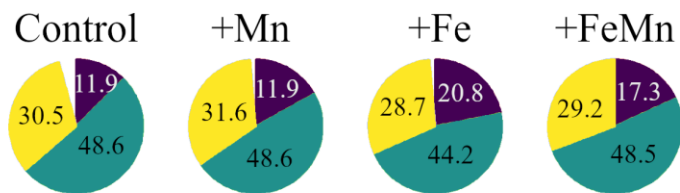
Table 5.4: Multiple variables characterising phytoplankton communities at the DCM prior to and after 10 days of incubations in each treatment and under the two light treatments with F_o : fluorescence, Chl-*a*: chlorophyll-*a*, C: particulate organic carbon, BSi: biogenic silica, Si: silicic acid, N: nitrate, P: phosphate, F_v/F_m : photochemical efficiency of PSII and σ_{PSII} : functional absorption cross section of PSII. The units are as: Chl-*a*:C (mmol mol^{-1}); BSi:C (mol mol^{-1}); BSi:Chl-*a* (mol mol^{-1}); Si:N (mol mol^{-1}); N:P (mol mol^{-1}) and σ_{PSII} ($\text{nm}^2 \text{quanta}^{-1}$).

Light condition	Parameter	Initial	Control	Mn	Fe	FeMn
LL	F_o :Chl- <i>a</i>	15028	4593 \pm 1437	5565 \pm 2278	3271 \pm 765	4613 \pm 447
	Chl- <i>a</i> :C	0.160	0.79 \pm 0.05	0.75 \pm 0.07	1.15 \pm 0.03	1.03 \pm 0.11
	BSi:C	0.050	0.57 \pm 0.14	0.28 \pm 0.01	0.34 \pm 0.02	0.26 \pm 0.02
	BSi:Chl- <i>a</i>	296	713 \pm 137	373 \pm 41	291 \pm 16	253 \pm 8
	Si:N	0.354	0.35 \pm 0.002	0.35 \pm 0.002	0.36 \pm 0.009	0.35 \pm 0.000
	N:P	14.0	13.9 \pm 0.03	14.0 \pm 0.06	14.0 \pm 0.05	14.0 \pm 0.06
	F_v/F_m	0.47	0.62 \pm 0.04	0.61 \pm 0.04	0.68 \pm 0.01	0.64 \pm 0.02
	σ_{PSII}	9.28	9.06 \pm 0.52	9.22 \pm 0.34	6.18 \pm 0.83	7.08 \pm 0.32
HL	F_o :Chl- <i>a</i>	15028	4809 \pm 802	3791 \pm 1803	1112 \pm 90	1050 \pm 72
	Chl- <i>a</i> :C	0.160	0.56 \pm 0.02	0.52 \pm 0.06	1.62 \pm 0.06	1.32 \pm 0.14
	BSi:C	0.050	0.29 \pm 0.02	0.27 \pm 0.01	0.12 \pm 0.01	0.11 \pm 0.01
	BSi:Chl- <i>a</i>	296	523 \pm 13	517 \pm 43	75 \pm 6	85 \pm 6
	Si:N	0.354	0.20 \pm 0.01	0.22 \pm 0.01	0.04 \pm 0.01	0.05 \pm 0.01
	N:P	14.0	15.0 \pm 0.10	14.9 \pm 0.20	15.7 \pm 0.01	15.6 \pm 0.20
	F_v/F_m	0.47	0.36 \pm 0.01	0.41 \pm 0.07	0.54 \pm 0.01	0.58 \pm 0.01
	σ_{PSII}	9.28	10.35 \pm 0.85	8.88 \pm 0.78	6.25 \pm 0.14	6.01 \pm 0.04

Initial communities



Low light



High light

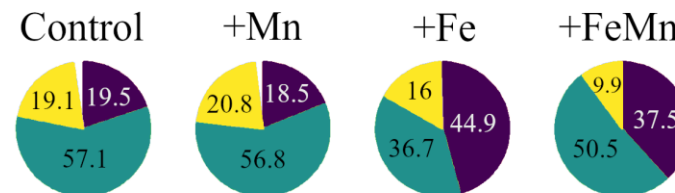


Figure 5.5: Relative contributions to chlorophyll-*a* fluorescence of the three main gated phytoplankton populations: large phytoplankton (“Large phyto”), nanoeukaryotes (“Nanos”) and picoeukaryotes (“Peuks”) for the initial communities incubated (“Initial”) and after 10 days of incubation in each treatment: Control, +Fe (“Fe”), + Mn (“Mn”), +FeMn (“FeMn”). The results are separated by light treatments.

Table 5.5: Cell counts (cell mL⁻¹) for the four gated populations for the initial community incubated (“Initial”) and after 10 days of incubation in each treatments: Control, +Fe (“Fe”), + Mn (“Mn”), +FeMn (“FeMn”), separated by light conditions.

	DCM		LL			HL			
Treatment	Initial	Control	Mn	Fe	FeMn	Control	Mn	Fe	FeMn
Large phyto.	40	17 ± 6	27 ± 6	37 ± 12	33 ± 12	57 ± 12	57 ± 6	593 ± 64	497 ± 76
Nanos.	600	573 ± 78	693 ± 103	757 ± 110	790 ± 72	3240 ± 85	3500 ± 656	5213 ± 1411	7540 ± 741
Pico.	1200	1663 ± 270	2263 ± 696	2063 ± 414	1940 ± 274	7493 ± 690	8683 ± 1888	14890 ± 6422	11357 ± 3812
Bacteria	264950	226400 ± 25904	288057 ± 68769	274033 ± 29872	277583 ± 67753	340520 ± 10352	359493 ± 12147	393763 ± 32585	417773 ± 37496

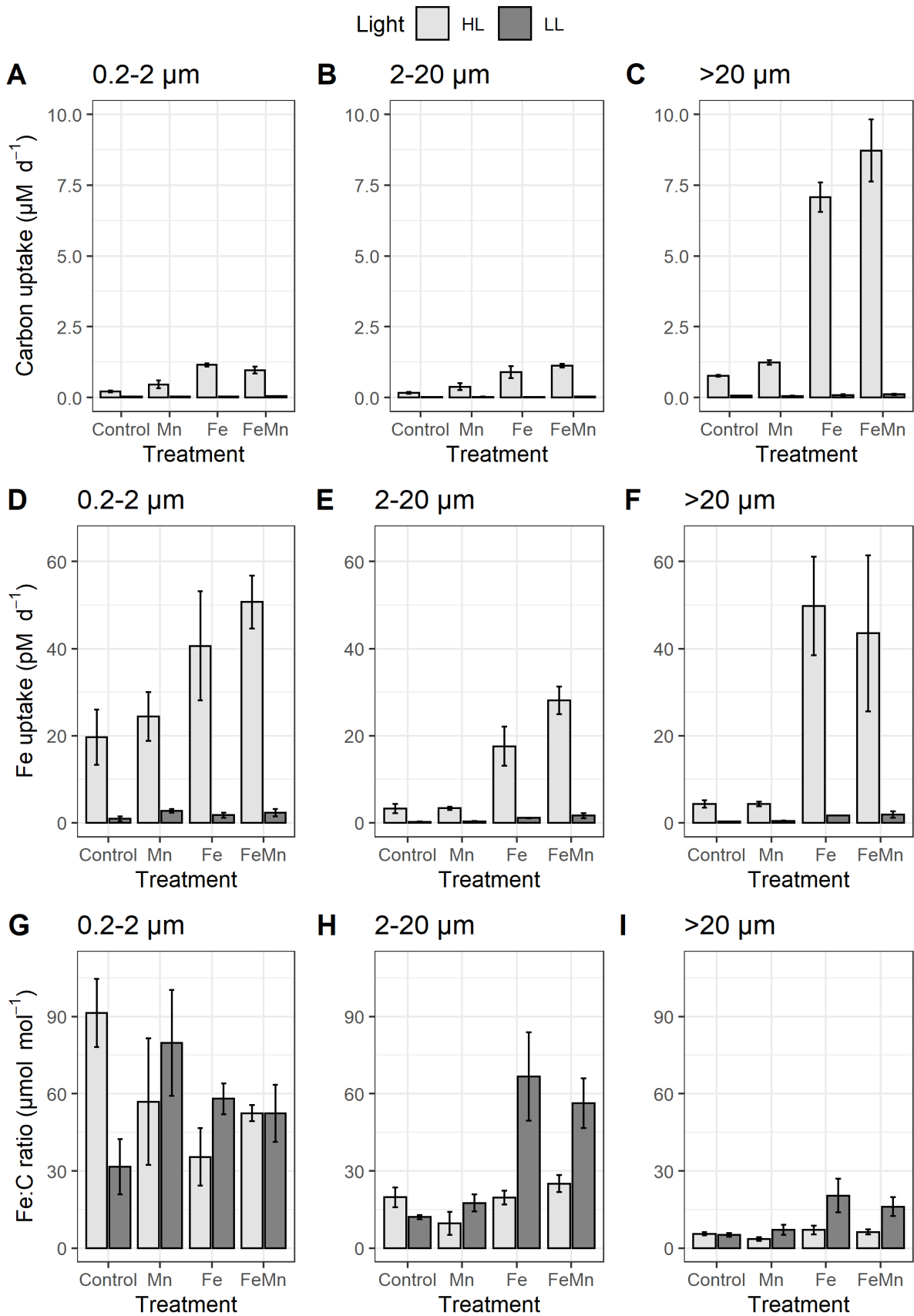


Figure 5.6: Carbon uptake in $\mu\text{M d}^{-1}$ (A-C), Fe uptake in pM d^{-1} (D-F) and Fe:C ratios in $\mu\text{mol mol}^{-1}$ (G-I) per size class (0.2-2 μm , 2-20 μm , >20 μm), treatment (Control, Mn, Fe, FeMn) and light condition (low light, LL vs high light, HL) assessed over a 24 h period on subsamples collected after 10 days of incubation.

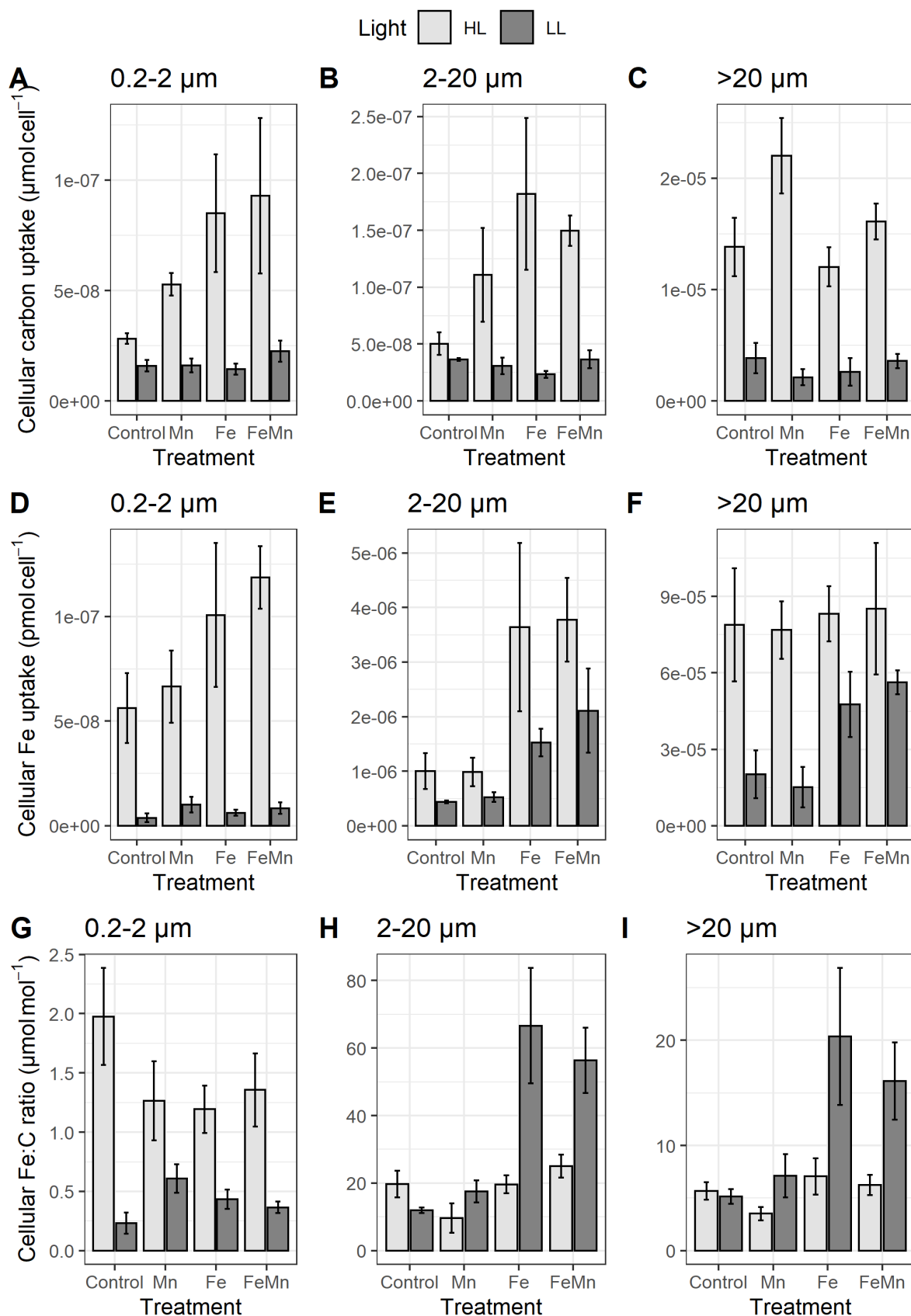


Figure 5.7: Cellular carbon uptake in $\mu\text{mol cell}^{-1} \text{d}^{-1}$ (A-C), cellular Fe uptake in $\text{pmol cell}^{-1} \text{d}^{-1}$ (D-F) and cellular Fe:C ratios in $\mu\text{mol mol}^{-1}$ (G-I) per size class (0.2-2 μm , 2-20 μm , >20 μm), treatment (Control, Mn, Fe, FeMn)

CHAPTER 5 – Characterization of a Southern Ocean deep chlorophyll maximum: responses of phytoplankton to light, iron and manganese

and light condition (low light, LL vs high light, HL) assessed over a 24 h period on subsamples collected after 10 days of incubation.

5.3.3. HIGH LIGHT TREATMENT

After ten days of incubation under higher light levels, macronutrient concentrations decreased in all treatments, with significantly lower nitrate, phosphate, and silicic acid concentrations measured under both Fe additions compared to the control and +Mn treatments (ANOVA and post hoc Tukey test, p -value < 0.05; Figure 5.4A-C). Thus, the derived rates of nitrate, phosphate, and silicic acid consumption were higher with +Fe and +FeMn additions (ANOVA and post hoc Tukey test, p -value < 0.05; Table 5.3). By the end of the experiment, we observed an increase in Chl-*a* in all treatments while POC concentrations decreased in the control and +Mn treatments compared to initial levels. However, both Fe treatments were characterized by significantly higher production in Chl-*a* and POC (ANOVA and post hoc Tukey test, p -value < 0.05; Figure 5.4D, E), resulting in significantly higher Chl-*a*:C ratios under +Fe compared to all other treatments (ANOVA and post hoc Tukey test, p -value < 0.05; Table 5.4). The +FeMn treatment was also characterized by higher Chl-*a*:C ratio compared to the control and +Mn treatments (ANOVA and post hoc Tukey test, p -value < 0.05; Table 5.4). Final BSi concentrations were higher in all treatments compared to initial levels. Coincident significantly higher BSi concentrations were measured with both Fe additions compared to the control and +Mn treatments. However, BSi concentrations were higher in the control compared to the Mn treatment (ANOVA and post hoc Tukey test, p -value < 0.05; Figure 5.4F). Interestingly, the strong decrease in silicic acid levels observed with +Fe and +FeMn additions (about 8 μ M; Figure 5.4C) was accompanied by a comparatively small production of BSi (< 1 μ M; Figure 5.4F).

Similarly, stronger variations in phytoplankton physiology between treatments were observed in the high light treatment. Fluorescence to Chl-*a* (F_0 :Chl-*a*) ratios decreased in all treatments compared to initial DCM values with significantly lower final values under both +Fe and +FeMn additions (ANOVA and post hoc Tukey test, p -value < 0.05; Table 5.4). Lower F_v/F_m values were measured in the control and +Mn treatments after 10 days of incubations compared to initial conditions. However, higher F_v/F_m were measured under Fe additions compared to the control and +Mn treatments with 0.54 and 0.58 measured in +Fe and +FeMn, respectively (ANOVA and post hoc Tukey test, p -value < 0.05; Table 5.4). Compared to the initial DCM value, we observed a decrease in σ_{PSII} for all treatments except the control. Significantly lower σ_{PSII} were observed with Fe additions (ANOVA and post hoc Tukey test, p -value < 0.05; Table 5.4). Flow cytometry results showed significantly higher cell counts after 10 days of incubation under high light compared to initial DCM counts. By the end of the experiment, picoeukaryotes dominated phytoplankton cell counts followed by nanoeukaryotes and large phytoplankton (Table 5.5). No difference in picoeukaryotes counts were observed between treatments. However, large phytoplankton cell counts significantly increased with +Fe and +FeMn additions (ANOVA and post hoc Tukey test, p -value < 0.05; Table 5.5) while nanoeukaryotes cell counts

significantly increased only with +FeMn additions, compared to the control and +Mn treatments (ANOVA and post hoc Tukey test, p -value < 0.05; Table 5.5). Nanoeukaryotes, which initially dominated the Chl-*a* biomass at the DCM, remained dominant in the control, +Mn and +FeMn treatments but their contribution significantly decreased in the +Fe treatment while the large phytoplankton contribution significantly increased under both Fe treatments (ANOVA and post hoc Tukey test, p -value < 0.05; Figure 5.5). Large phytoplankton dominated Chl-*a* biomass in the +Fe treatment (Figure 5.5). High-light incubation bacterial counts showed a strong increase in all treatments. However, only the combined addition of Fe and Mn resulted in a significant increase in bacterial counts compared to the control (ANOVA and post hoc Tukey test, p -value < 0.05; Table 5.5).

Under high light, volumetric carbon uptake was dominated by the large size class, and we observed a significant increase in carbon uptake in both Fe addition treatments in all size classes (ANOVA and post hoc Tukey test, p -value < 0.05; Figure 5.6A-C). Cellular carbon uptake was also dominated by the large size class, in which +Mn addition alone stimulated carbon uptake compared to the control and +Fe treatments (ANOVA and post hoc Tukey test, p -value < 0.05; Figure 5.7C). In the medium size fraction, cellular carbon uptake was higher under +Fe compared to the control while the +FeMn treatment stimulated cellular carbon uptake in the small size fraction (ANOVA and post hoc Tukey test, p -value < 0.05; Figure 5.7B). High volumetric Fe uptake was observed in both the small and large size classes (Figure 5.6D-F). Within the small size class, higher Fe uptake was only observed in the +FeMn treatment compared to the control and +Mn treatments (ANOVA and post hoc Tukey test, p -value < 0.05; Figure 5.6D). In the medium and large size classes, higher Fe uptake was observed in both Fe additions treatments compared to the control and +Mn treatments (ANOVA and post hoc Tukey test, p -value < 0.05; Figure 5.6E-F). Similarly, both Fe addition treatments strongly increased cellular Fe uptake in the medium size class compared to the control and +Mn treatments (ANOVA and post hoc Tukey test, p -value < 0.05; Figure 5.7E), resulting in lower cellular Fe:C uptake ratio in the +Mn treatment compared to the three other treatments (ANOVA and post hoc Tukey test, p -value < 0.05; Figure 5.7H). A similar difference was observed for volumetric ratios (Figure 5.6H). In the small size class, only the combined addition of Fe and Mn resulted in a significant increase in cellular Fe uptake compared to the control (ANOVA and post hoc Tukey test, p -value < 0.05; Figure 5.7D) but no significant differences were observed in cellular Fe:C uptake ratios between treatments. In this size class, volumetric Fe:C uptake ratios were higher in the control compared to the +Fe treatment. Similarly, no significant differences in cellular Fe uptake were observed between treatments in the large size class (ANOVA) which resulted in lower Fe:C uptake ratio in the +Mn treatment compared to the +Fe addition only (ANOVA and post hoc Tukey test, p -value < 0.05; Figure 5.7I). A similar difference was observed for volumetric ratios (Figure 5.6I).

5.4. Discussion

This study aimed to further our understanding of Southern Ocean DCM, and to test the hypothesis that phytoplankton Fe and Mn requirements may change under varying light conditions. Our results indicated that the initial DCM phytoplankton community was light-limited but healthy. We observed a strong phytoplankton growth stimulation under high Fe and light conditions while Mn addition did not stimulate growth or nutrient utilization. This could result from sufficiently high initial dMn concentrations. However, specific responses in carbon and Fe uptake rates along with flow cytometry results suggested part of the phytoplankton community benefited from Mn additions. Below, we discuss the initial setting and conditions of the DCM before describing specific responses to light, Fe and Mn additions.

Coincident measurements of increased fluorescence and Chl-*a* concentrations confirmed the presence of an SFM and DCM at about 87 m (Figure 5.2A-B). Elevated POC concentrations at the DCM (Table 5.2) also suggested real biomass build-up although other particles, such as heterotrophs and sinking particles, may increase POC concentrations (Hopkinson et al. 2007). Elevated BSi concentrations observed near the DCM supported the hypothesis of a diatom-dominated DCM, as has been observed previously in the Southern Ocean (Parslow et al. 2001; Gomi et al. 2010; Baldry et al. 2020). In addition, higher silicic acid concentrations found at the DCM depth indicated more favourable conditions for diatom growth as surface levels were likely limiting ($< 5 \mu\text{M}$) (Westwood et al. 2011). The increase in the Chl-*a*:C ratio observed at the DCM may support two hypothesis: i) an increase in Chl-*a* pigments per cell due to photoacclimation or ii) a community shift toward phytoplankton species with higher Chl-*a* content per cell (Hopkinson et al. 2007; Cullen 2015; Rembauville et al. 2016). Diatoms have previously been observed to have higher chlorophyll content per cell (Rembauville et al. 2016). Considering the initial dataset strongly suggests the presence of diatoms, through BSi concentrations (Figure 5.2D) and increase in large phytoplankton cell counts (Figure 5.3A), it is possible the increase in Chl-*a*:C ratio resulted from a community shift from smaller organisms to large diatoms with higher chlorophyll content per cell. This was supported by the increase in Chl-*a* per cell, almost 3-fold higher, observed at the DCM depth. However, we are unable to differentiate between community shifts and photoacclimation processes without additional data.

The depth profile of temperature showed the DCM was found below the pycnocline, in the shallower portion of the temperature minimum layer which is a remnant of Antarctic Surface Water (Table 5.2; Parslow et al. 2001; Holm-Hansen et al. 2005). Previous studies suggested the temperature minimum layer may have higher dFe concentrations supporting phytoplankton growth at depth (Holm-Hansen et al. 2005). However, our data do not support this hypothesis as we measured lower dFe concentrations at the DCM compared to overlying waters (Table 5.2). The observed increase of F_o :Chl-*a* ratio at the DCM depth may indicate some degree of Fe stress (Schallenberg et al; *in prep*). However, the high photochemical efficiency of PSII ($F_v/F_m = 0.47$; Table 5.2) measured at the DCM indicated that bulk

phytoplankton community were relatively healthy (Hopkinson et al. 2007). The high σ_{PSII} (Table 5.2) agreed with previous studies that found large light-harvesting complexes in these deep features, associated with interaction between Fe and light limitation (Hopkinson et al. 2007; Hopkinson and Barbeau 2008). It has been hypothesized that large antennae complexes allow the cell to capture more photons without increasing their number of photosynthetic units and hence Fe requirements (Strzepek et al. 2019).

5.4.1. LIGHT CONTROLS PHYTOPLANKTON GROWTH AT THE DCM

Under low light, the lack of macronutrients drawdown and POC accumulation compared to elevated light (see discussion below) strongly supported the hypothesis that phytoplankton communities were primarily light limited within the DCM (Figure 5.4A-C, E; Holm-Hansen et al. 2005; Hopkinson and Barbeau 2008). The bulk high F_v/F_m values measured in all treatments by the end of the experiment indicated efficient light utilization in PSII (Table 5.4; Greene et al. 1992; Hopkinson and Barbeau 2008), suggesting that under low light, most of the phytoplankton community was not strongly limited by Fe. However, the small response observed with Fe additions, with increased Chl-*a* production (Figure 5.4D) and decreased σ_{PSII} (Table 5.4) indicated some degree of Fe stress. Increasing Chl-*a* concentrations with Fe addition strongly support the hypothesis that part of the DCM phytoplankton community was Fe limited for photoacclimation processes, suggesting that photoacclimation relied in part on an increase in PSII unit numbers to counter low light conditions (Sunda and Huntsman 1997). Changes in σ_{PSII} may be related to modified light environment, Fe-limitation, or changes in species composition (Hopkinson and Barbeau 2008; Suggett et al. 2009). Our results suggest σ_{PSII} was more strongly controlled by Fe than light in our experiment. In addition, higher cellular Fe uptake measured under both Fe additions in the medium and large size classes may result from the upregulation of Fe transport within the cell observed under Fe limitation (Hudson and Morel 1990; Strzepek et al. 2011).

Overall, these results showed that light was the proximal parameter controlling phytoplankton growth at the DCM (Hopkinson and Barbeau 2008) and agree with recent hypothesis that Southern Ocean phytoplankton Fe requirements may not increase under limiting light conditions (Strzepek et al. 2019; Vives et al. 2022). Volumetric and cellular carbon uptake was dominated by the large size fraction (>20 μm ; Figure 5.6, 5.7), indicating that despite being less important in terms of cell counts and chlorophyll fluorescence biomass (Figure 5.5), large diatoms present at the DCM may still drive strong carbon export, as previously suggested (Boyd and Newton 1999; Hopkinson and Barbeau 2008). However, primary productivity remained generally low under low light, in accordance with a previous study in this region where Westwood et al. (2011) measured gross primary productivity $<10 \text{ mg C m}^{-3} \text{ d}^{-1}$ at two summer DCM. In comparison, net primary productivity measured here initially at the DCM (Figure 5.2G) and after 10 days of incubation under low light (Figure 5.6A-C) remained below $3.6 \text{ mg C m}^{-3} \text{ d}^{-1}$. These results suggest that over a short period of time, the studied DCM has low productivity despite the presence of healthy cells. Previous studies have observed that DCM deepen and become less

productive as the season progresses and light limitation becomes too great to support photosynthesis (Griffiths et al. 1999; Parslow et al. 2001). Despite the sampling of this feature in mid-summer, its already deep position and associated light limitation resulted in low productivity. While most of the phytoplankton community seemed healthy under low light, the small response with Fe addition still suggested some degree of Fe limitation (Hopkinson and Barbeau 2008).

5.4.2. ONCE LIGHT SHINES, IRON LIMITS

After light limitation was relieved, we observed an initial decrease in macronutrient concentrations in the treatments without Fe (Figure 5.4A-C). Nutrient consumption, especially silicic acid, and BSi production (Figure 5.4C, F) indicated natural Fe concentrations were high enough to support the growth of diatoms under increased light levels (Table 5.3). However, the lower F_v/F_m values observed by the end of the experiment in the control and +Mn treatments indicated Fe was likely depleted throughout the experiment and reached levels limiting efficient light utilization in PSII (Table 5.4; Greene et al. 1992; Hopkinson and Barbeau 2008). The decrease in σ_{PSII} but also in the $F_o:Chl-a$ ratio observed with Fe additions also supported the hypothesis that Fe stress was relieved in the high light incubations (Hopkinson and Barbeau 2008; Schallenberg et al. *in prep*).

Under high light and with Fe additions, phytoplankton growth was drastically stimulated, as shown by the strong decrease in macronutrient concentrations and the increased production in Chl-*a* and POC (Figure 5.4A-E). The shift in the community toward large phytoplankton (Figure 5.5) coincident with an increase in BSi concentrations (Figure 5.4F) supported the hypothesis that Fe stimulated the growth of large diatoms, a group known to respond quickly to Fe fertilisation (Hopkinson et al. 2007; Hopkinson and Barbeau 2008). These results agree with previous DCM field studies which observed strong response from large diatoms to increasing Fe and light conditions, associated with high Fe costs of synthesising photosynthetic reaction centres and electron transport proteins (Hopkinson and Barbeau 2008). Our results agree with this hypothesis as higher volumetric and cellular Fe uptake rates were observed in the large size class (> 20 μm) under both Fe additions. The higher Chl-*a*:C ratios measured with Fe additions suggest these large diatoms responded to Fe by increasing Chl-*a* content per cell (Table 5.4; Hopkinson and Barbeau 2008; Rembauville et al. 2016). However, the high volumetric and cellular carbon uptake rates coincided with relatively low Fe:C uptake ratios (Figure 5.6, 5.7), suggesting that these large diatoms may be particularly effective at carbon drawdown per unit Fe. In the context of a natural DCM, this suggests natural Fe fertilization will more strongly stimulate phytoplankton growth (especially large diatoms) and associated high carbon drawdown, when light levels increase and so when isopycnal shoaling occurs, for example due to an eddy or intense mixing (Hopkinson and Barbeau 2008).

High light conditions also likely stimulated Fe uptake by heterotrophic bacteria, supported by the elevated Fe:C uptake ratios observed in the small size class (Figure 5.6G, 5.7G). These high Fe:C uptake

ratios result from combined Fe uptake from heterotrophic bacteria and small phytoplankton within this size fraction, while only phytoplankton predominately assimilate carbon. Interestingly, the higher Fe:C ratio observed in the control compared to the +Fe treatment (Figure 5.6G) may indicate some competition between heterotrophic bacteria and phytoplankton. Indeed, Fourquez et al. (2017) observed that heterotrophic bacteria and phytoplankton may compete for Fe uptake once carbon limitation of bacterial growth is relieved. Such competition may impact phytoplankton growth, especially when Fe concentrations become depleted, for example in the late stage of a bloom.

Different Fe uptake rates between the two light conditions may also result from a different Fe speciation. The reduced Fe(II) species is thought to be more bioavailable for phytoplankton and bacterial consumption (Lueder et al. 2020) but in seawater, dFe is primarily present as complexed by ligands as it quickly tends to precipitate under seawater pH and oxygen conditions (Boye et al. 2001; Canfield et al. 2005). Hence, the speciation of the Fe solution added (Fe(III)) during this experiment will likely change and may produce different response than natural Fe fertilization (Lannuzel et al. 2011). Sunlight-induced reactions may lead to a change in Fe speciation through direct ligand to metal charge transfer or superoxide, which can reduce Fe(III) to Fe(II) (Lueder et al. 2020). While higher Fe demand under high light due to strong phytoplankton growth stimulation was likely, Fe supply was probably also higher than compared to the low light experiment if photolabile complexes were present. Hence, differences in Fe speciation between our two light settings may have occurred and influenced Fe uptake by the phytoplankton and bacterial communities.

5.4.3. RESPONSES TO MANGANESE ADDITIONS

A clear signal of Mn (co-)limitation was lacking based on final photochemical efficiencies, nutrient utilization and POC synthesis. Using the equation from Browning et al. (2021) to evaluate Mn deficiency relative to Fe, as $Mn^* = dMn - dFe / R_{Fe:Mn}$, with $R_{Fe:Mn}$ being the average Fe:Mn ratio of phytoplankton (Moore 2013; Browning et al. 2021), we calculated $Mn^* = 0.23$. This value fits within the range described by Browning et al. (2021) for Fe-limited sites, but not Mn. This suggests initial dMn levels were high enough to not limit phytoplankton growth. Yet, several signals in the Fe/carbon uptake and flow cytometry results suggested small responses to Mn additions.

Under high light, addition of Mn alone stimulated cellular carbon uptake in the large size class while the combined +FeMn addition stimulated both Fe and carbon uptake in the small size fraction. In addition, combined Fe and Mn induced a community shift (nanoeukaryotes dominant) compared to Fe addition alone (large phytoplankton dominant). These results suggest that Mn can subtly influence multiple phytoplankton species across a wide size range. The stimulation of cellular carbon and Fe uptake with Mn additions may indicate some degree of initial Mn limitation. As previously mentioned, the Mn requirement is directly linked to the number of photosynthetic units and to the defence against ROS via the production of superoxide dismutase enzyme (Armstrong 2008; Peers and Price 2004;

Wolfe-Simon et al. 2006). A lack of Mn for the synthesis of oxygen evolving complexes would likely result in more uniform physiological stress within a rapidly growing phytoplankton community, as all phototrophs are expected to use Mn in the oxygen evolving complex (Raven 1990; Armstrong 2008), but with the caveat that the number of PSII reaction centres can differ between phytoplankton species (Strzepek and Harrison; Strzepek et al. 2019). Hence, it seems more likely that any variation in phytoplankton response to Mn addition observed during this experiment may more likely be related to the Mn needed for SOD synthesis and other antioxidant molecules. Furthermore, Mn has also been observed to be used in non-proteinaceous complexes as a back-up for SOD enzymes (Aguirre and Culotta 2012). With a strong biomass build-up, such as the one observed under high light levels, an increase in ROS production is expected and may modify phytoplankton Mn requirements (Peers and Price 2004; Diaz and Plummer 2018). In the Fe/Mn superoxide dismutase class, Fe and Mn can substitute for each other due to the similarity of their active sites, despite SOD being metal specific (Whittaker 2003; Aguirre and Culotta 2012). This results in non-activation of the enzyme, for example when Fe binds a Mn-SOD (Aguirre and Culotta 2012). As cellular Fe is in great excess compared to cellular Mn (Twining and Baines 2013), Fe may bind Mn-SOD and reduce the cell's ability to defend itself against oxidative stress. In addition, the use of Fe-SOD may possibly increase oxidative stress through Fenton chemistry during which hydroxyl radicals may be produced after Fe(II) reacts with hydrogen peroxide (Aguirre and Culotta 2012). Most of the research on Mn-SOD has been done on bacteria but eukaryotes are also assumed to rely on Mn-SOD (Aguirre and Culotta 2012). Yet, little information is known about ROS in the Southern Ocean and associated antioxidant processes from phytoplankton in this region. Phytoplankton Mn-SOD have been studied in temperate coastal diatoms (Peers and Price 2004; Wolfe-Simon et al. 2006), where dMn concentrations are expected to be high compared to Southern Ocean open waters. Aguirre and Culotta (2012) suggested Mn-SOD evolving in low Fe environment may be more likely to bind Fe and remain inactive. As Southern Ocean waters are characterized by both low Fe and Mn concentrations, phytoplankton may be confronted by i) a supply of dMn too low to produce Mn-SOD and /or ii) an issue with Fe binding Mn-SOD, making it inactive. Hence, it is possible some Southern Ocean phytoplankton species have adapted to the low surrounding dMn concentrations by using different metal co-factors for their SOD, such as Cu/Zn or Ni (Fridovich 1997; Lesser 2006; Morel et al. 2020). Nickel-SOD may be particularly important as Ni is found at relatively high concentrations in the Southern Ocean (> 8 nM at the present DCM) and its high content in diatoms frustule has been hypothesized to be related to frustule-associated Ni-SOD (Twining et al. 2012; McCain and Bertrand 2022). In the context of the present experiment, it is possible these subtle differences observed between phytoplankton classes indicate different Mn requirement related to Mn-SOD and Mn non-proteinaceous complexes production. However, laboratory-based studies looking at Southern Ocean phytoplankton Mn requirement and SOD production remain necessary to confirm this hypothesis.

The shift in communities observed under combined +FeMn addition with elevated light may suggest some interspecific competition for micronutrients between different size groups. It is surprising that adding Mn with Fe was unfavourable for large diatoms; however, as mentioned above, phytoplankton Mn requirements may vary between species depending on the SOD class they rely on. Usually in Southern Ocean addition experiments, large diatoms respond quickly to Fe. The fact that under combined Fe and Mn additions, smaller diatoms remained the dominant group may suggest that adding Mn maintained their competitiveness for Fe uptake. This could indicate a higher Mn requirement from the diatoms present within the nanoeukaryote range but could also support the hypothesis that large Fe-responding diatoms have a lower Mn requirement, possibly related to the use of different SOD, for example Ni-SOD. The higher bacterial count observed only under combined Fe and Mn addition may also support this hypothesis as competition between microbes and phytoplankton for Fe uptake has been previously observed (Fourquez et al. 2020).

Overall, responses to Mn additions were subtle and may easily be missed during conventional experiments, as carbon and Fe uptakes are rarely measured. This highlights the need for field studies using multiple techniques. From this experiment, stronger responses were observed with high light levels and the strong increase in biomass, likely associated with increased oxidative stress. We hypothesize Mn may control part of the primary productivity depending on species Mn requirements. We suggest this may be related to each species reliance on Mn-SOD as it is possible some Southern Ocean phytoplankton adapted to low dMn concentrations by using a different class of SOD. In the context of the DCM, the lack of responses to Mn additions observed under low light conditions strongly suggests that initial dMn concentrations were high enough to not limit phytoplankton growth found at this depth, and that photoacclimation to low light did not appreciably increase cellular Mn demand. Hence, we hypothesize Mn will more likely limit phytoplankton growth in shallower water, where higher light levels stimulate growth and lead to higher ROS production. In addition, Mn (co-)limitation may be more prominent in the late season, after depletion of dMn through biological uptake.

5.5. Conclusion

During this experiment, we aimed to characterize a mid-summer Southern Ocean DCM found in polar waters. We found that light was the proximal environmental variable limiting phytoplankton growth at the DCM, but our results suggested initial communities were relatively healthy. Despite this, the DCM was not strongly productive. When light limitation was relieved, the strongest phytoplankton growth response was observed under Fe additions, and especially for large diatoms. These results show that the large diatoms responding to Fe were co-limited by Fe and light. These results suggest that natural Fe fertilization of similar DCM phytoplankton communities will have more impact when light levels are also increased, for example when isopycnals shoal due to an eddy or strong mixing. No clear signal of Mn(co-)limitation was observed but subtle changes under Mn addition indicated part of the phytoplankton community may have been Mn-limited. We hypothesize subtle responses to Mn may be

CHAPTER 5 – Characterization of a Southern Ocean deep chlorophyll maximum: responses of phytoplankton to light, iron and manganese

associated with differing Mn requirement from Southern Ocean phytoplankton for the synthesis of Mn-SOD. However, laboratory-based studies looking at Mn requirement from various phytoplankton polar taxa in combination with their trace metal requirement for SOD production remain essential to confirm this hypothesis. Specifically, identifying which SOD family key phytoplankton groups rely upon for growth and how they change under limiting conditions would greatly advance our knowledge and understanding on how Mn can control Southern Ocean phytoplankton growth.

6. CHAPTER 6 – Summary and future directions

Manganese has received much interest since the discovery of its central roles in the oxygen evolving complex and in cellular antioxidant activity (Raven 1990; Armstrong 2008; Peers and Price 2004; Wolfe-Simon et al. 2006; Aguirre and Culotta 2012). In the Southern Ocean, the very low Mn concentrations have early on raised the question of its potential role in limiting phytoplankton growth but first results were inconclusive (Martin et al. 1990; Buma et al. 1991; Scharek et al. 1997; Sedwick, et al. 2000). About a decade later, the hypothesis of Mn co-limitation was revisited (Middag et al. 2013; Browning et al. 2014). Identifying which parameters limit phytoplankton growth in the Southern Ocean is especially relevant considering the importance of this region for the carbon cycle, and consequently for the climate of the planet (Caldeira and Duffy 2000; Gruber et al. 2009; Lenton et al. 2013). Yet, very few data related to Mn have been reported in this vast region, due to its remoteness and inaccessibility (Westerlund and Öhman 1991; Sedwick et al. 1997; Bowie et al. 2009; Middag et al. 2011, 2013), keeping us from fully understanding its spatial, temporal and seasonal variations. Constraining Mn distributions, cycling and control on phytoplankton growth in this biogeochemically important region is essential to identify its role in controlling primary productivity, and consequently, the climate. To address this, we examined Mn distribution in the Australian sector of the Southern Ocean, before looking at its potential role in limiting phytoplankton growth in subantarctic and polar waters.

6.1. Summary of key results

This thesis is divided into four main chapters, aiming to address the following questions: i) how does Mn distribution vary spatially in the Australian sector of the Southern Ocean and ii) does Mn limit primary productivity in this region? Each of these questions are answered across two chapters.

In Chapter 2, entitled “Manganese biogeochemistry in the Southern Ocean, from Tasmania to Antarctica”, we described the first full-depth dataset of dissolved and particulate Mn concentrations in this region. We measured extremely low dissolved Mn (dMn) concentrations in surface waters (< 0.25 nM), attributed to few external inputs and biological uptake. We observed biological uptake strengthened southward, resulting in lower dMn concentrations near the Antarctic continent. Our examination of Mn:P ratios suggested the presence of Fe-stressed diatoms south of the SAF. Particulate Mn (pMn) concentrations were also low, with a lower than expected proportion of labile material, suggesting the Southern Ocean may have a unique pMn composition in comparison to other ocean basins (Twining et al. 2015). Two main external sources were identified: hydrothermal vents above the Southeast Indian Ridge and sediment inputs near the Tasmanian and Antarctic shelves, locally increasing both dMn and pMn concentrations.

In Chapter 3: “Biological uptake, water mass dilution and scavenging prevent transport of Mn-rich waters from the Antarctic shelf”, we examined the export of Mn-enriched Antarctic coastal waters toward Southern Ocean open waters. We found that despite high Mn concentrations found on the shelf, limited offshore transport of Mn occurred. In surface waters, this was due to removal through biological uptake while dilution of Mn-rich Antarctic Bottom Water (AABW) with overlying Mn-depleted Low Circumpolar Deep Water (LCDW) and scavenging limited Mn export in bottom waters. These results could be associated with other metals expected to be high on the Antarctic shelf (e.g., Fe) and further our understanding of the Southern Ocean as a High-Nutrient Low-Chlorophyll region (HNLC).

In Chapter 4: “Seasonality of phytoplankton growth limitation by iron and manganese in subantarctic waters”, we found that Mn addition stimulated carbon fixation in medium and large phytoplankton classes, in spring and summer respectively. Manganese addition strongly stimulated the growth of cyanobacteria in autumn, suggesting this population may be commonly Mn-limited late in the growth season. Overall, our study suggested Mn may control specific phytoplankton taxa with a seasonal variability, but signals of Mn limitation were subtle and easily masked by the strong phytoplankton responses associated with Fe limitation.

In Chapter 5, entitled “Characterization of a Southern Ocean deep chlorophyll maximum: responses of phytoplankton to light, iron and manganese”, we examined phytoplankton communities from a polar DCM. We found light was the primary parameter limiting the growth of phytoplankton, however, large diatoms were co-limited by Fe and light. Responses to Mn additions were subtle and indicated Mn may limit primary productivity when shoaling of isopycnals occur and phytoplankton communities receive higher light levels. At higher irradiance, growth is strongly stimulated and may be associated with increased oxidative stress, and we speculate that Mn requirements may then consequentially increase.

6.2. Significance of findings

6.2.1. NEW KNOWLEDGE REGARDING THE MANGANESE CYCLE

This thesis highlighted the very low Mn concentrations found in this under-studied Southern Ocean region. In surface waters, we found biological uptake was the main factor controlling Mn concentrations. Conversely, Mn was resupplied in the system through sediment and hydrothermal inputs. However, the former source increased Mn concentrations near the shelves only, except when transported through bottom water movement. The lack of export of Mn-enriched surface waters from the Antarctic continent toward open waters was surprising but may enhance the HNLC characteristic of the Southern Ocean as transport of Mn, but also other crustal-abundant elements, such as Fe, must be limited to (at least partly) explain the pervasive low trace metal concentrations found in this region. Bottom water transport of Mn was also limited by water masses mixing and scavenging processes but additional study evaluating Mn(II) oxidation rates remain essential to confirm the latter hypothesis. In addition, future modifications of Antarctic Bottom Waters (AABW) may alter this potential transport pathway of Mn

and other crustal-abundant elements toward Southern Ocean open waters, as increased freshening has been suggested to slow down AABW formation (Lago and England 2019). In this region, it seems hydrothermal inputs above the Southeast Indian Ridge may be more important than sedimentary sources to resupply Mn into the system although their transport to the surface ocean layer, where they can stimulate phytoplankton growth, depends on isopycnals shoaling (Tagliabue et al. 2022). Results from this thesis also showed that the observed low Mn concentrations may lead to some degree of seasonal and species-specific phytoplankton growth limitation. Overall, our results suggest that Mn co-limitation is nuanced and may control part of the primary productivity and hence influence the carbon cycle.

6.2.2. IMPORTANCE FOR GLOBAL CARBON CYCLE

The discovery of the subtle impact and potential control of Mn on phytoplankton communities in the SAZ and polar waters may be directly linked to the oceanic carbon cycle. Manganese was recently observed to (co-)limit phytoplankton growth in both coastal and open waters of the Southern Ocean (Wu et al. 2019; Browning et al. 2021). However, the signals of Mn limitation observed during the present work were far from being as clear as the observations of Browning et al. (2021) during similar addition experiments in the Drake Passage. This suggests that Mn control on Southern Ocean primary productivity may be restricted to specific regions, seasons, and select phytoplankton taxa. It is first important to locate these regions where Mn may control phytoplankton growth to incorporate this information into biogeochemical models aiming to predict future changes in the oceanic carbon cycle. Yet, identifying where Mn may limit primary productivity is not sufficient and variations in phytoplankton Mn requirements associated with current, but also predicted changes in the conditions of the Southern Ocean should be assessed.

There are multiple forecasts for possible future changes in the Southern Ocean. In the subantarctic zone (SAZ), warming and freshening is predicted to decrease phytoplankton productivity through more stratification of the water column, and a decrease in nutrient supply from deeper waters, leading to a community shift toward small phytoplankton communities, such as nanoflagellates (Marinov et al. 2010; Boyd et al. 2016; Deppeler and Davidson 2017). On the other hand, an increase in temperature and wind strength, associated with increased frequency of dust events into the SAZ has been hypothesized to stimulate diatom growth and primary productivity (Boyd et al. 2016; IPCC 2021). Within these two predicted scenarios, Mn may impact phytoplankton growth, and hence carbon drawdown in several ways. First, a decrease in nutrient supply through more stratification may result in strengthened Mn limitation through i) less dMn supply from subsurface dMn maxima (features commonly observed in the Southern Ocean, Chapters 2 and 3) and ii) a possible increase in phytoplankton Mn requirements through intensification of Fe limitation (Peers and Price 2004). Another potential change in the influence of Mn may be due to increased phytoplankton exposure to ultraviolet (UV) radiation associated with stronger stratification (Gao et al. 2012; Häder et al. 2015; Deppeler and Davidson 2017). Under elevated light or longer exposure to UV radiation, photodamage can occur and lead to higher

production of reactive oxygen species (ROS). Through this process, phytoplankton exposed to UV-A and UV-B experience increased oxidative stress. The more damaging UV-B has been associated with superoxide production and enhanced superoxide dismutase (SOD) enzyme activity in phytoplankton (Martínez 2007). As increased stratification will likely result in higher phytoplankton exposure to UV and enhanced SOD activity, limited nutrient supply to the surface ocean layer could exacerbate Mn limitation if most Southern Ocean phytoplankton taxa rely on Mn-SOD. Yet, little information is known about this (see next section).

In polar waters, increased productivity is expected to result from enhanced mixing and nutrient supply; however, associated light-limitation with a deeper mixed layer may also decrease primary productivity (Deppeler and Davidson 2017; IPCC 2021). Near the Antarctic shelf, increased productivity is expected due to enhanced nutrient and stratification from melting sea-ice (Deppeler and Davidson 2017; IPCC 2021). In these scenarios, Mn will likely not limit phytoplankton growth due to higher nutrient inputs from either subsurface dMn maxima (polar waters, Chapter 2) or sediment inputs (Chapter 3) and sea-ice melting near the Antarctic shelf (Lannuzel et al. 2014). However, the predicted decrease in sea-ice extent (IPCC 2021) may lead to a decrease in the supply of Mn and other micronutrients from melting sea-ice at the current edge of sea-ice extension. This could result in strengthened Mn limitation in open waters adjacent to the Antarctic shelf. Overall, we suggest Mn control on primary productivity and indirectly on the carbon cycle may be more prominent in oceanic regions where a decrease in nutrient supply and increase in UV exposure is predicted, such as open waters of the SAZ. Considering the SAZ currently sustains the strongest carbon uptake within the Southern Ocean (Lenton et al. 2013), incorporating Mn effects on phytoplankton growth in biogeochemical models aiming to predict future evolution of the oceanic carbon cycle is essential.

6.3. Future directions

Our understanding of the Mn cycle and the control of this element on Southern Ocean primary productivity has been strongly advanced with recent research (Middag et al. 2013; Wu et al. 2019; Browning et al. 2021; Oldham et al. 2021; Smith et al. 2021) and the work presented in this thesis. However, information is still lacking to fully know the role Mn plays in impacting biogeochemical cycles and Southern Ocean phytoplankton growth.

The results presented in Chapters 4 and 5 of this thesis indicate that Mn may contribute to limiting Southern Ocean primary productivity. While flow cytometry and size fractionated carbon and Fe uptake results gave us indications on which phytoplankton group may respond to Mn additions, we still cannot confirm which species may be Mn-limited. Yet, to better understand how Mn limitation may drive changes in deep carbon export, identifying which species are more likely to be Mn-limited is essential. To further resolve this, Mn requirements from a wide range of Southern Ocean phytoplankton species should be studied under laboratory-controlled conditions, especially species isolated from low Mn

regions. In addition, more interest should be given to ROS production by Southern Ocean phytoplankton, especially superoxide, as it is hypothesized that Fe limitation may modify phytoplankton Mn requirement for SOD enzyme (Peers and Price 2004). In Chapter 5, we hypothesized some Southern Ocean phytoplankton species may have adapted to the low surrounding Mn concentrations by using a different SOD class such as Ni-SOD. However, many questions related to antioxidant processes remain and highlight the need for additional studies looking at interaction between antioxidants and phytoplankton metal quotas (McCain and Bertrand 2022). In addition, combining knowledge of the trace metal requirements of Southern Ocean phytoplankton with *in-situ* trace metal concentrations is essential to predict the future evolution of the carbon cycle.

Information on Southern Ocean Mn speciation is also limited. Indeed, identifying the dominant Mn species in the dissolved and particulate phase is important to constrain other trace metal cycles. Since Mn(III) was observed to be maintained in oxygenated seawater through binding with strong ligands as Mn(III)-L complexes (Oldham et al. 2017), only one additional study has looked at Mn speciation in the Southern Ocean in detail (Oldham et al. 2021). In this study on the shelf of the Ross Sea, Oldham et al. (2021) observed Mn(III)-L dominated the dMn pool and suggested that Mn(III) stabilization by ligands prevented MnOx formation which then limited scavenging of other elements. The results from Chapters 2 and 3 of this dissertation suggested that the portion of MnOx in the pMn pool was lower than results from previous studies in other ocean basins. In addition, a non-scavenged profile was observed on the East Antarctic shelf (Chapter 3), in agreement with previous observation of lesser MnOx in this region (Oldham et al. 2021). Hence, to increase our understanding of the Mn cycle, specific measurements of MnOx and Mn(III) in open waters of the Southern Ocean are necessary to further our understanding of other trace elements subject to scavenging, such as Fe and cobalt (Co). Currently, such measurements are limited in Southern Ocean waters due to the high detection limit of techniques used to measure Mn(III) concentrations (50 nM, Madison et al. 2011; 0.3-0.5 nM Oldham et al. 2017; 2021) compared to the expected low dMn concentrations found in this region (< 0.5 nM, Middag et al. 2011, 2013; Chapters 2 and 3 of this thesis). Hence, the development of new techniques targeting specific Mn species with low detection limits adapted for Southern Ocean measurements are necessary. It would be interesting to see if any differentiation of dMn species using the combined methods of seaFAST and ICP-MS is possible. In addition, such measurements of Mn(III) in Southern Ocean waters would further our knowledge of the Fe cycle as Mn(III) has been observed to bind to similar ligands as Fe, sometimes with even higher affinity than Fe(III) (Luther et al. 2015; Oldham et al. 2017). As ligands may be saturating near the Antarctic coast (Thuróczy et al. 2012) and because Fe solubility depends on its complexation with ligands (Boye et al. 2001; Lannuzel et al. 2015), the binding of Mn(III) to Fe-binding ligands may potentially decrease Fe solubility and intensify Fe limitation of phytoplankton growth.

In conclusion, this thesis has enhanced our understanding of the Mn cycle in the Southern Ocean. Yet, several questions related to Mn control of primary productivity, Mn speciation and the resultant impacts on biogeochemical cycles remain. In addition, large regions of the Southern Ocean are under-studied for Mn and other trace metal concentrations. For example, a large portion of the Pacific sector has still not been studied for micronutrients (see Introduction, Figure 1.8). The results from this thesis have shown subtle, nuanced effects of Mn control on primary productivity and hence potentially on the oceanic carbon cycle. As this is directly related to the spatial variations in the Mn cycle and the adaptations of local phytoplankton communities, additional studies looking at Mn concentrations, speciation and control on primary productivity in under-studied regions are essential to produce better predictions of the oceanic carbon cycle.

Appendices

Appendix A – Chapter 2

Manuscript from Latour et al. (2021): <https://aslopubs.onlinelibrary.wiley.com/doi/10.1002/lno.11772>

Appendix B – Chapter 3

Table S3.1: Classification of water masses observed during this expedition, separated by their position toward the shelf. Abbreviations: AASW, Antarctic Surface Waters; mCDW, modified Circumpolar Deep Water; WW, Winter Water; DSW, Dense Shelf Water; UCDW, Upper Circumpolar Deep Water; LCDW, Low Circumpolar Deep Water; AABW, Antarctic Bottom Waters.

Region	References Orsi and Wiederwohl 2009; Silvano et al. 2017; Pardo et al. 2017 and references herein				
	Water mass	Potential density	Potential temperature	Neutral density	Salinity
On shelf	AASW	< 27.55	–	< 28.0	–
	mCDW	> 27.7		$28 \leq \Upsilon_n < 28.27$	
	WW	$27.55 < \rho_h < 27.7$	$-1.92 < \theta < -1.75$	–	
	DSW	–	–	> 28.27	
Off shelf	AASW	–	–	< 27.7	< 34.3
	UCDW			$27.7 \leq \Upsilon_n < 28.18$	≥ 34.3
	LCDW			$28.18 \leq \Upsilon_n < 28.25$	–
	AABW			≥ 28.25	

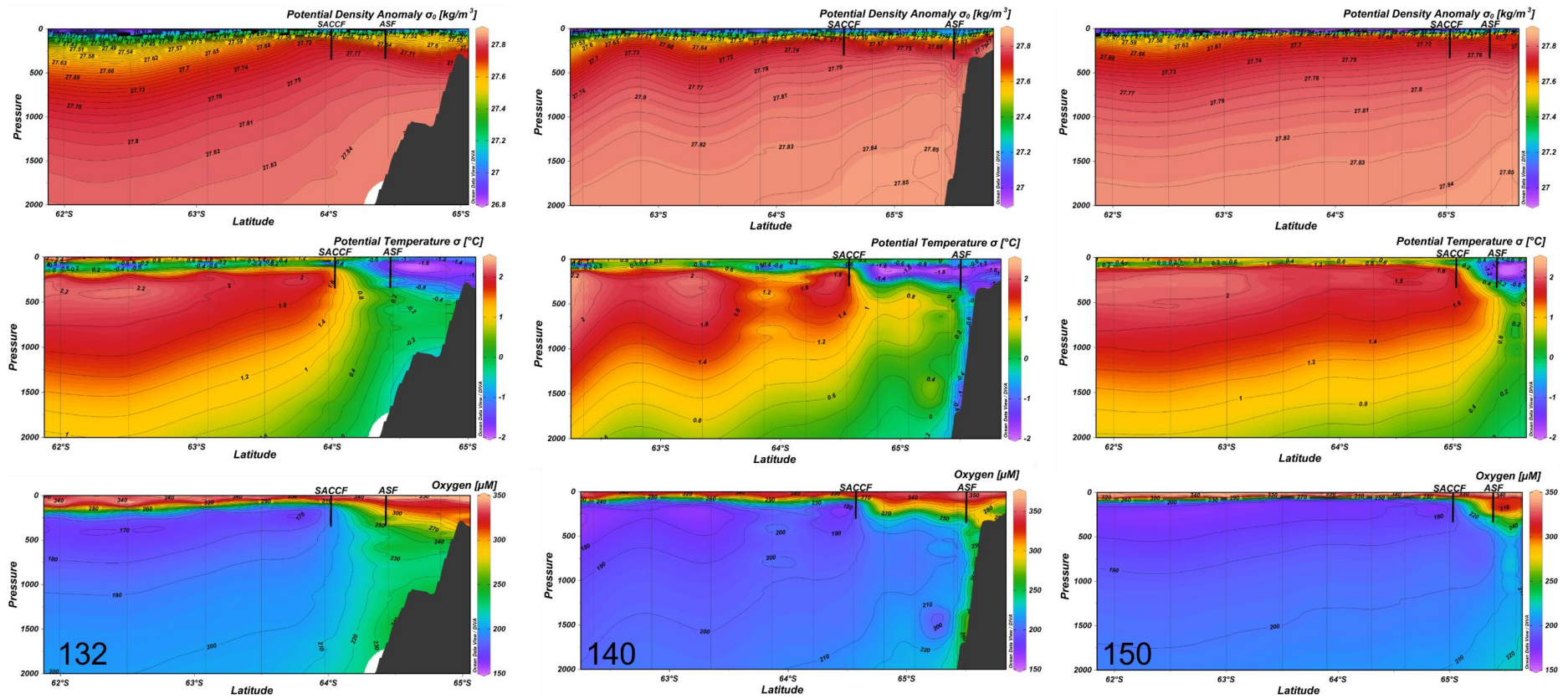


Figure S3.1: Potential density anomaly, potential temperature and oxygen concentrations along the three main transects, with the 2 fronts identified: South Antarctic Circumpolar Front (SACCF) and Antarctic Slope Front (ASF). Depression of isopycnals can be seen along 140 at the ASF.

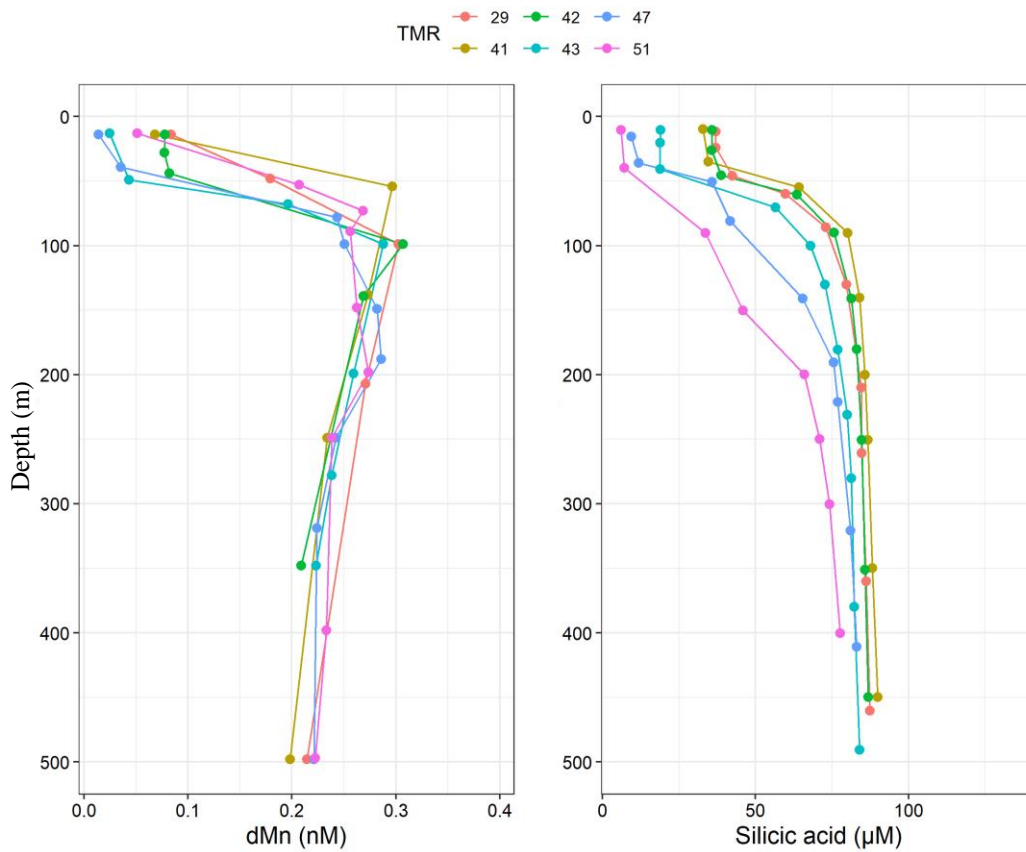


Figure S3.2: Depth profiles of dissolved Mn (dMn) in nM (a) and silicic acid in μM (b) at the TMR stations north of the Southern Antarctic Circumpolar Current Front, characterized by lower surface dMn concentrations, between 0 and 500 m.

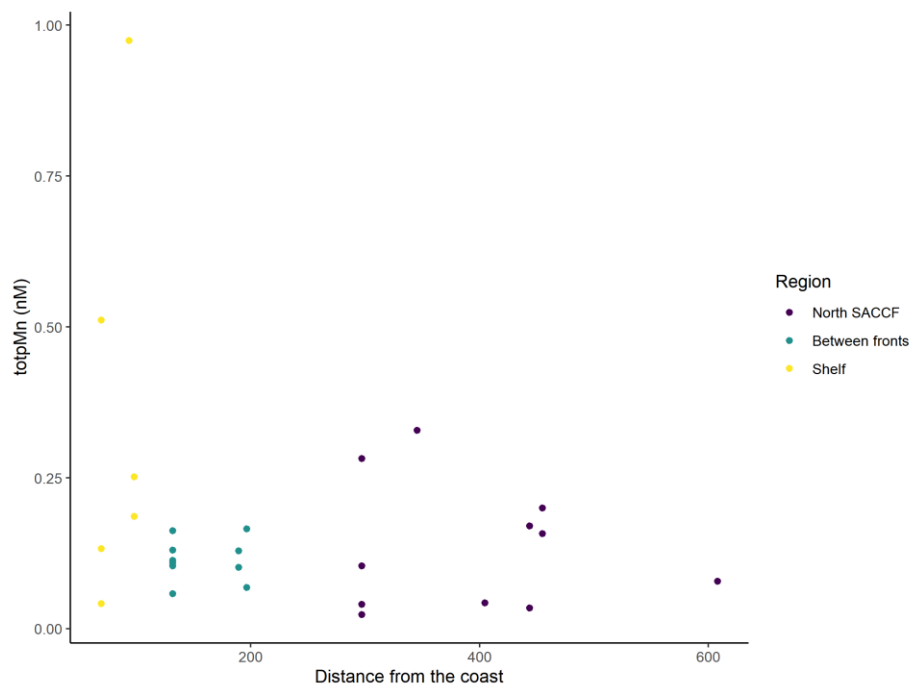


Figure S3.3: Depth profiles of dissolved Mn (dMn) in nM (a) and silicic acid in μM (b) at the TMR stations north of the Southern Antarctic Circumpolar Current Front, characterized by lower surface dMn concentrations, between 0 and 500 m.

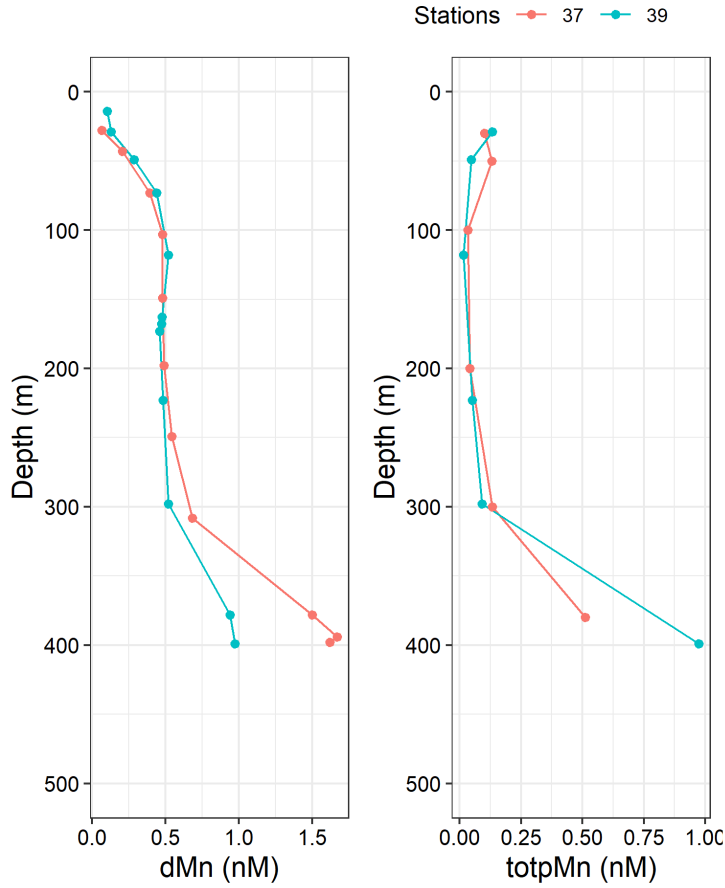


Figure S3.4: Depth profiles of dissolved Mn (dMn) and particulate Mn (pMn) in nM for the remaining two trace metal rosette stations sampled on the Adélie Bank (TMR 37 and 39). Conservative/increasing depth profiles can be observed.

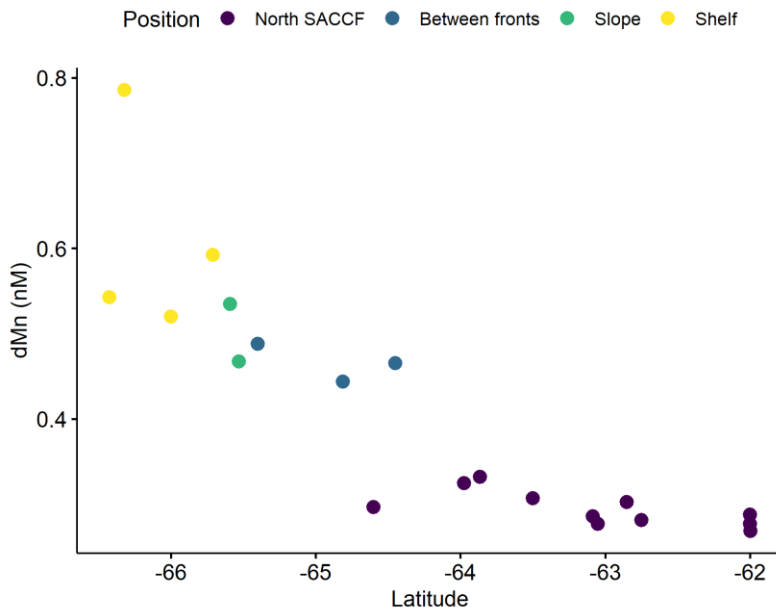


Figure S3.5: Evolution of subsurface dMn maxima values (in nM) compared to latitude. The colours represent the position of the stations relative to fronts: north of the South Antarctic Circumpolar Front (North SACCF), between the two fronts (Between fronts), over the slope (Slope) and on the shelf (Shelf).

Appendix C – Chapter 4

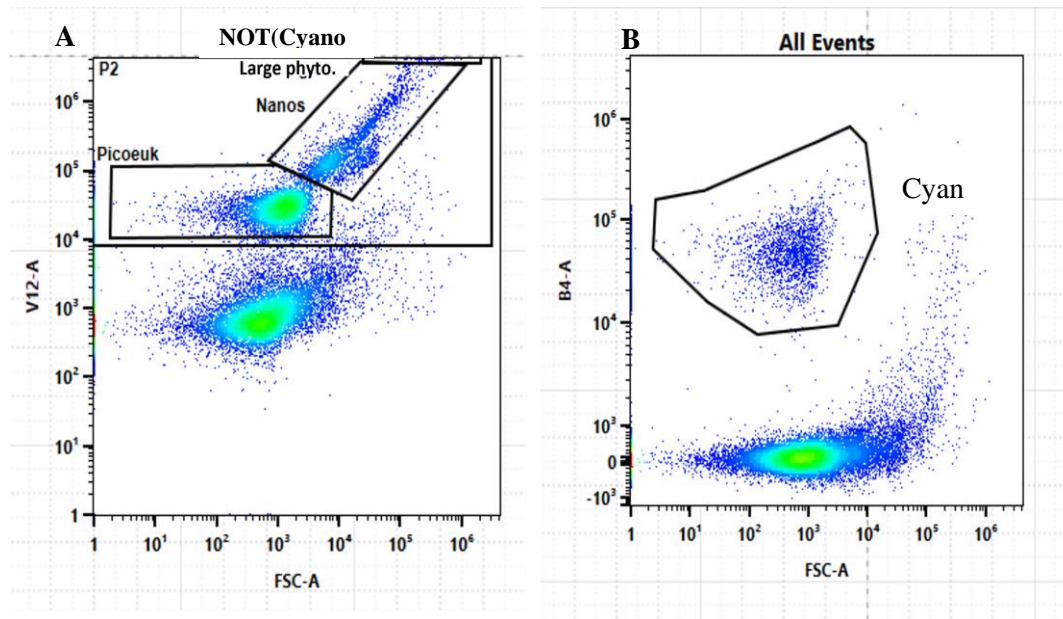


Figure S4.1: Gates used to group phytoplankton community into four main populations: large phytoplankton (large phyto), nanoeukaryotes (Nanos), picoeukaryotes (Picoeuk) (A) and cyanobacteria (Cyan) (B). First, cyanobacteria were gated on the B4 channel. Then the points within this gate were removed from the remaining data to avoid double-gating. The three other populations were gated on the V12 channel. For the determination of each population contribution to chlorophyll biomass, the channel B7 was used due to saturation of the V12 signal from large phytoplankton (as can be seen in the right corner of plot A).

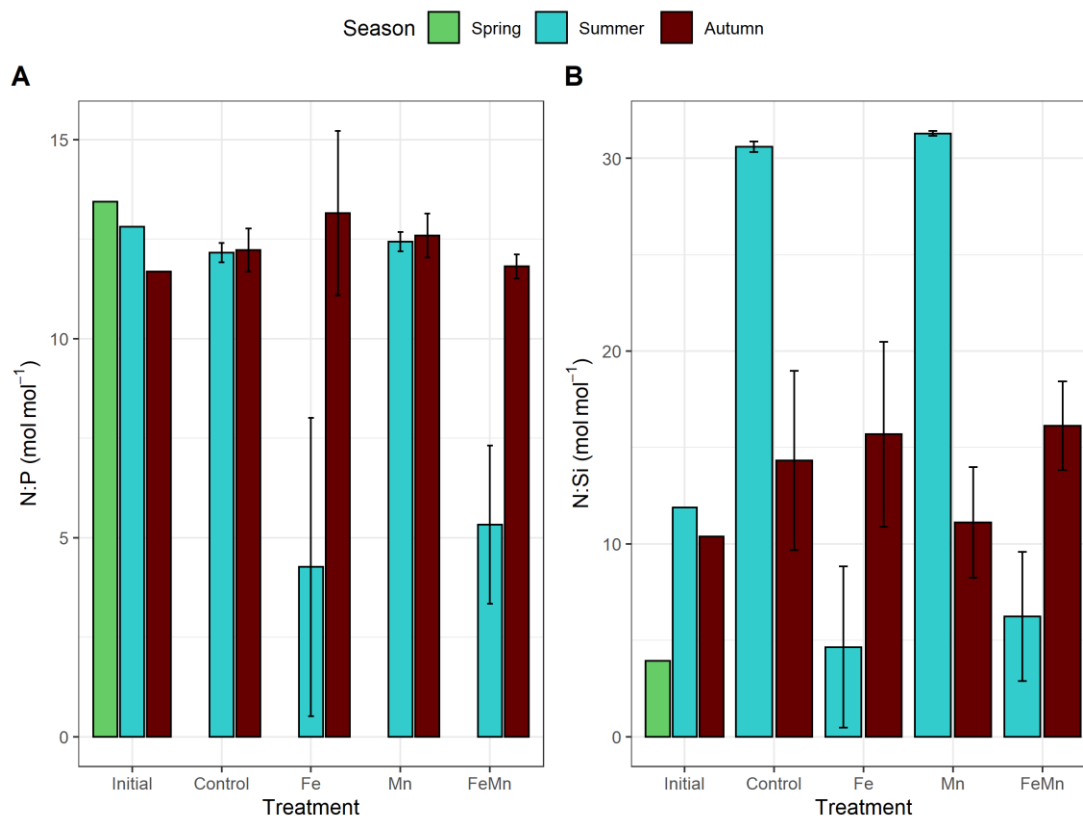


Figure S4.2: Nitrate to phosphate (N:P) and nitrate to silicic acid (N:Si) ratios measured in summer and autumn after 7 days of incubation. The spring results are not presented due to the use of an FeNO_3 solution for the Fe spike.

Table S4.1: Macronutrient data (in μM) for the seasonal study in subantarctic waters, measured at day = 7.

Voyage	Season	Site	Treatment	Bottle	Time	NOx	Phosphate	Silicic ac.	Ammonia	Nitrite
IN2019-V02	Autumn	SOTS	Initial	Initial	Initial	8.3	0.71	0.8	NaN	NaN
IN2019-V02	Autumn	SOTS	C	C3	T7	8.04	0.63	0.8	0.45	0.158
IN2019-V02	Autumn	SOTS	C	C2	T7	7.71	0.66	0.4	0.39	0.139
IN2019-V02	Autumn	SOTS	C	C1	T7	8.19	0.67	0.6	0.32	0.151
IN2019-V02	Autumn	SOTS	Fe	Fe3	T7	8.23	0.53	0.4	0.4	0.18
IN2019-V02	Autumn	SOTS	Fe	Fe2	T7	7.75	0.64	0.5	0.22	0.139
IN2019-V02	Autumn	SOTS	Fe	Fe1	T7	7.68	0.65	0.7	0.48	0.143
IN2019-V02	Autumn	SOTS	Mn	Mn3	T7	8.18	0.63	0.9	0.11	0.168
IN2019-V02	Autumn	SOTS	Mn	Mn2	T7	8.34	0.65	2	0.99	0.163
IN2019-V02	Autumn	SOTS	Mn	Mn1	T7	7.89	0.66	0.6	0.13	0.134
IN2019-V02	Autumn	SOTS	FeMn	FeMn3	T7	7.51	0.65	0.4	0.14	0.141
IN2019-V02	Autumn	SOTS	FeMn	FeMn2	T7	7.29	0.6	0.5	0.18	0.133
IN2019-V02	Autumn	SOTS	FeMn	FeMn1	T7	7.52	0.64	0.5	0.11	0.129
IN2020-V08	Summer	SOTS	Initial	Initial	Initial	10.22	0.798	0.86	0.124	0.2156
IN2020-V08	Summer	SOTS	C	C1	T7	6.13	0.5	0	0.06	0.131
IN2020-V08	Summer	SOTS	C	C2	T7	6.06	0.51	0	0.07	0.128
IN2020-V08	Summer	SOTS	C	C3	T7	6.17	0.5	0	0.06	0.122
IN2020-V08	Summer	SOTS	Fe	Fe1	T7	0.02	0.1	0.1	0.01	0.031
IN2020-V08	Summer	SOTS	Fe	Fe2	T7	1.1	0.22	0	0.03	0.058
IN2020-V08	Summer	SOTS	Fe	Fe3	T7	1.67	0.22	0	0.09	0.049
IN2020-V08	Summer	SOTS	Mn	Mn1	T7	6.28	0.51	0	0.07	0.13
IN2020-V08	Summer	SOTS	Mn	Mn2	T7	6.23	0.49	0	0.06	0.125
IN2020-V08	Summer	SOTS	Mn	Mn3	T7	6.26	0.51	0	0.08	0.133
IN2020-V08	Summer	SOTS	FeMn	FeMn1	T7	0.6	0.17	0	0.04	0.048
IN2020-V08	Summer	SOTS	FeMn	FeMn2	T7	1.2	0.24	0	0.08	0.052
IN2020-V08	Summer	SOTS	FeMn	FeMn3	T7	1.94	0.26	0.1	0.04	0.061
IN2018-V04	Spring	PS2	Initial	Initial	Initial	11.02	0.82	2.8	0.01	0.196
IN2018-V04	Spring	PS2	C	C1	T7	NaN	0.65	2	0.01	0.067

IN2018-V04	Spring	PS2	C	C2	T7	NaN	0.61	2	0.01	0.049
IN2018-V04	Spring	PS2	C	C3	T7	NaN	0.67	2.2	0.01	0.055
IN2018-V04	Spring	PS2	Fe	Fe1	T7	NaN	0.6	2	0.01	0.109
IN2018-V04	Spring	PS2	Fe	Fe2	T7	NaN	0.52	1.8	0.01	0.108
IN2018-V04	Spring	PS2	Fe	Fe3	T7	NaN	0.62	2.3	0.01	0.09
IN2018-V04	Spring	PS2	Mn	Mn1	T7	NaN	0.64	1.9	0	0.039
IN2018-V04	Spring	PS2	Mn	Mn2	T7	NaN	0.61	1.9	0.01	0.05
IN2018-V04	Spring	PS2	Mn	Mn3	T7	NaN	0.65	2	0.01	0.056
IN2018-V04	Spring	PS2	FeMn	FeMn1	T7	NaN	0.43	1.4	0.01	0.116
IN2018-V04	Spring	PS2	FeMn	FeMn2	T7	NaN	0.52	1.7	0.01	0.119
IN2018-V04	Spring	PS2	FeMn	FeMn3	T7	NaN	0.61	2.9	0.01	0.141

Table S4.2: Photophysiological measurements for the seasonal study in subantarctic waters, measured at day = 7. In the thesis, we presented results for photochemical efficiency of PSII (F_v/F_m) and functional absorption cross section of PSII (σ_{PSII}) in $\text{nm}^2 \text{quanta}^{-1}$.

Voyage	Season	Treatment	Bottle	Time	Fo	Fm	Fv	Fv/Fm	Fv/Fo	Sigma
EAC	Spring	Initial	Initial	T7	1.92	6.24	4.32	0.69	2.26	345.73
EAC	Spring	Control	C1	T7	13.20	45.05	31.85	0.71	2.41	598.41
EAC	Spring	Control	C2	T7	17.57	49.26	31.69	0.64	1.81	658.85
EAC	Spring	Control	C3	T7	8.96	28.51	19.55	0.69	2.18	632.04
EAC	Spring	Fe	Fe1	T7	11.10	36.39	25.29	0.70	2.28	625.05
EAC	Spring	Fe	Fe2	T7	16.08	49.43	33.35	0.67	2.07	644.55
EAC	Spring	Fe	Fe3	T7	11.51	39.37	27.87	0.71	2.42	604.03
EAC	Spring	FeMn	FeMn1	T7	28.94	85.43	56.50	0.66	1.95	510.22
EAC	Spring	FeMn	FeMn2	T7	24.15	68.10	43.95	0.65	1.82	533.76
EAC	Spring	FeMn	FeMn3	T7	17.22	45.34	28.12	0.62	1.64	581.56
EAC	Spring	Mn	Mn1	T7	14.49	40.19	25.70	0.64	1.77	678.85
EAC	Spring	Mn	Mn2	T7	11.91	37.82	25.91	0.69	2.18	659.93
EAC	Spring	Mn	Mn3	T7	15.26	37.59	22.34	0.59	1.47	675.61
SOTS	Autumn	Initial	Initial	T7	2.80	6.31	3.50	0.55	1.28	267.40
SOTS	Autumn	Control	C1	T7	6.93	14.82	7.89	0.53	1.15	619.94

SOTS	Autumn	Control	C2	T7	7.66	18.69	11.03	0.59	1.46	621.87
SOTS	Autumn	Control	C3	T7	10.58	24.54	13.96	0.57	1.32	667.37
SOTS	Autumn	Fe	Fe1	T7	6.56	16.49	9.93	0.60	1.53	593.86
SOTS	Autumn	Fe	Fe2	T7	5.87	15.56	9.69	0.62	1.68	624.17
SOTS	Autumn	Fe	Fe3	T7	11.32	30.27	18.95	0.63	1.69	687.95
SOTS	Autumn	FeMn	FeMn1	T7	10.87	26.33	15.46	0.59	1.43	802.44
SOTS	Autumn	FeMn	FeMn2	T7	9.54	24.08	14.54	0.60	1.54	575.65
SOTS	Autumn	FeMn	FeMn3	T7	6.08	15.45	9.37	0.61	1.58	644.46
SOTS	Autumn	Mn	Mn1	T7	10.91	23.82	12.91	0.54	1.20	742.65
SOTS	Autumn	Mn	Mn2	T7	12.05	22.96	10.90	0.47	0.91	733.16
SOTS	Autumn	Mn	Mn3	T7	11.66	23.11	11.44	0.49	0.98	749.29
SOLACE	Summer	Initial	Initial	T7	2610.70	5667.90	3057.30	0.50	1.20	812.20
SOLACE	Summer	Control	C1	T7	5396.59	8871.80	3475.21	0.39	0.64	858.25
SOLACE	Summer	Control	C2	T7	4365.36	6633.16	2267.80	0.34	0.52	897.21
SOLACE	Summer	Control	C3	T7	5175.19	7978.70	2803.51	0.35	0.54	849.85
SOLACE	Summer	Fe	Fe1	T7	6512.90	13556.82	7043.92	0.52	1.08	677.76
SOLACE	Summer	Fe	Fe2	T7	5374.62	10493.68	5119.06	0.49	0.95	690.41
SOLACE	Summer	Fe	Fe3	T7	5257.42	10693.25	5435.83	0.51	1.03	660.24
SOLACE	Summer	FeMn	FeMn1	T7	2723.98	6485.45	3761.47	0.58	1.38	645.33
SOLACE	Summer	FeMn	FeMn2	T7	4532.83	8923.22	4390.39	0.49	0.97	636.48
SOLACE	Summer	FeMn	FeMn3	T7	6157.99	12395.53	6237.54	0.50	1.01	682.29
SOLACE	Summer	Mn	Mn1	T7	4596.79	7179.62	2582.83	0.36	0.56	854.41
SOLACE	Summer	Mn	Mn2	T7	3490.19	5697.23	2207.04	0.39	0.63	872.22
SOLACE	Summer	Mn	Mn3	T7	6136.10	9535.40	3399.31	0.36	0.55	933.05

Table S4.3: Flow cytometry data for the summer and autumn experiments in subantarctic waters. Six gates are indicated: all fluorescent cells, large phytoplankton, picoeukaryotes, nanoeukaryotes, cyanobacteria and bacteria.

Voyage	Season	Treatment	Bottle	Gate	Cell count per μL	Mean FSC-A	Mean B7-A
IN2020-V08	Summer	Initial	Initial	Cyanobacteria	4.15	731	21867
IN2020-V08	Summer	Initial	Initial	Large phytoplankton	0.13	280882	1169218
IN2020-V08	Summer	Initial	Initial	All fluorescent cells	19.96	12268	27050
IN2020-V08	Summer	Initial	Initial	Picoeukaryotes	10.88	1240	5029
IN2020-V08	Summer	Initial	Initial	Nanoeukaryotes	5.63	27571	56735
IN2020-V09	Summer	Initial	Initial	Bacteria	620.4	NaN	NaN
IN2020-V08	Summer	Control	C1	Cyanobacteria	5.91	1048	19021
IN2020-V08	Summer	Control	C1	Large phytoplankton	0.2	362275	1243072
IN2020-V08	Summer	Control	C1	All fluorescent cells	22.87	25385	44802
IN2020-V08	Summer	Control	C1	Picoeukaryotes	5.11	1276	4180
IN2020-V08	Summer	Control	C1	Nanoeukaryotes	14.93	28123	49898
IN2020-V09	Summer	Control	C1	Bacteria	428.14	NaN	NaN
IN2020-V08	Summer	Control	C2	Cyanobacteria	6.41	1086	18048
IN2020-V08	Summer	Control	C2	Large phytoplankton	0.19	288786	1079209
IN2020-V08	Summer	Control	C2	All fluorescent cells	24.01	23166	45859
IN2020-V08	Summer	Control	C2	Picoeukaryotes	5.31	1275	4080
IN2020-V08	Summer	Control	C2	Nanoeukaryotes	15.66	27808	54263
IN2020-V09	Summer	Control	C2	Bacteria	438.12	NaN	NaN
IN2020-V08	Summer	Control	C3	Cyanobacteria	4.23	1139	20030
IN2020-V08	Summer	Control	C3	Large phytoplankton	0.25	340989	1387839
IN2020-V08	Summer	Control	C3	All fluorescent cells	22.41	26680	55239
IN2020-V08	Summer	Control	C3	Picoeukaryotes	4.04	1302	4508
IN2020-V08	Summer	Control	C3	Nanoeukaryotes	16.03	27184	53810
IN2020-V09	Summer	Control	C3	Bacteria	272.85	NaN	NaN
IN2020-V08	Summer	Fe	Fe1	Cyanobacteria	3.99	1553	31039
IN2020-V08	Summer	Fe	Fe1	Large phytoplankton	0.85	342872	974707
IN2020-V08	Summer	Fe	Fe1	All fluorescent cells	26.75	51855	93913

IN2020-V08	Summer	Fe	Fe1	Picoeukaryotes	2.8	2487	5428
IN2020-V08	Summer	Fe	Fe1	Nanoeukaryotes	18.8	46496	87985
IN2020-V09	Summer	Fe	Fe1	Bacteria	371.09	NaN	NaN
IN2020-V08	Summer	Fe	Fe2	Cyanobacteria	3.89	1398	30724
IN2020-V08	Summer	Fe	Fe2	Large phytoplankton	0.63	297180	959511
IN2020-V08	Summer	Fe	Fe2	All fluorescent cells	29.09	42353	81250
IN2020-V08	Summer	Fe	Fe2	Picoeukaryotes	3.41	2405	5812
IN2020-V08	Summer	Fe	Fe2	Nanoeukaryotes	21.2	40247	81769
IN2020-V09	Summer	Fe	Fe2	Bacteria	397.01	NaN	NaN
IN2020-V08	Summer	Fe	Fe3	Cyanobacteria	7.06	1382	30181
IN2020-V08	Summer	Fe	Fe3	Large phytoplankton	0.47	363510	996516
IN2020-V08	Summer	Fe	Fe3	All fluorescent cells	36.21	29693	56063
IN2020-V08	Summer	Fe	Fe3	Picoeukaryotes	8.33	2010	6802
IN2020-V08	Summer	Fe	Fe3	Nanoeukaryotes	23.21	34534	63713
IN2020-V09	Summer	Fe	Fe3	Bacteria	435.34	NaN	NaN
IN2020-V08	Summer	Mn	Mn1	Cyanobacteria	6.26	1054	19763
IN2020-V08	Summer	Mn	Mn1	Large phytoplankton	0.2	345457	1251659
IN2020-V08	Summer	Mn	Mn1	All fluorescent cells	21.24	24728	45264
IN2020-V08	Summer	Mn	Mn1	Picoeukaryotes	5.03	1223	3973
IN2020-V08	Summer	Mn	Mn1	Nanoeukaryotes	13.83	28934	48852
IN2020-V09	Summer	Mn	Mn1	Bacteria	384.82	NaN	NaN
IN2020-V08	Summer	Mn	Mn2	Cyanobacteria	6.56	1021	14881
IN2020-V08	Summer	Mn	Mn2	Large phytoplankton	0.13	396399	1256901
IN2020-V08	Summer	Mn	Mn2	All fluorescent cells	21.52	22953	38274
IN2020-V08	Summer	Mn	Mn2	Picoeukaryotes	6.22	1261	3612
IN2020-V08	Summer	Mn	Mn2	Nanoeukaryotes	12.23	30549	50196
IN2020-V09	Summer	Mn	Mn2	Bacteria	442.1	NaN	NaN
IN2020-V08	Summer	Mn	Mn3	Cyanobacteria	4.83	1044	13447
IN2020-V08	Summer	Mn	Mn3	Large phytoplankton	0.18	366434	1422342
IN2020-V08	Summer	Mn	Mn3	All fluorescent cells	18.2	28005	46548
IN2020-V08	Summer	Mn	Mn3	Picoeukaryotes	4.36	1376	3836

IN2020-V08	Summer	Mn	Mn3	Nanoekaryotes	11.23	32106	49904
IN2020-V09	Summer	Mn	Mn3	Bacteria	404.13	NaN	NaN
IN2020-V08	Summer	FeMn	FeMn1	Cyanobacteria	7.31	1326	29780
IN2020-V08	Summer	FeMn	FeMn1	Large phytoplankton	0.59	368946	967295
IN2020-V08	Summer	FeMn	FeMn1	All fluorescent cells	54.36	28281	52497
IN2020-V08	Summer	FeMn	FeMn1	Picoekaryotes	9.92	2187	6546
IN2020-V08	Summer	FeMn	FeMn1	Nanoekaryotes	39.6	30442	55692
IN2020-V09	Summer	FeMn	FeMn1	Bacteria	360.28	NaN	NaN
IN2020-V08	Summer	FeMn	FeMn2	Cyanobacteria	6.14	1619	33144
IN2020-V08	Summer	FeMn	FeMn2	Large phytoplankton	0.58	338642	943985
IN2020-V08	Summer	FeMn	FeMn2	All fluorescent cells	26.99	45206	78477
IN2020-V08	Summer	FeMn	FeMn2	Picoekaryotes	4	2287	5623
IN2020-V08	Summer	FeMn	FeMn2	Nanoekaryotes	18.52	46378	81955
IN2020-V09	Summer	FeMn	FeMn2	Bacteria	478.55	NaN	NaN
IN2020-V08	Summer	FeMn	FeMn3	Cyanobacteria	4.45	1567	25453
IN2020-V08	Summer	FeMn	FeMn3	Large phytoplankton	0.61	378840	950596
IN2020-V08	Summer	FeMn	FeMn3	All fluorescent cells	27.34	41309	73562
IN2020-V08	Summer	FeMn	FeMn3	Picoekaryotes	5.03	2065	6633
IN2020-V08	Summer	FeMn	FeMn3	Nanoekaryotes	18.66	41613	74746
IN2020-V09	Summer	FeMn	FeMn3	Bacteria	326.38	NaN	NaN
IN2019-V02	Autumn	Initial	Initial	Cyanobacteria	25.24	631	11395
IN2019-V02	Autumn	Initial	Initial	Large phytoplankton	0.08	234623	826577
IN2019-V02	Autumn	Initial	Initial	All fluorescent cells	29.76	6303	17529
IN2019-V02	Autumn	Initial	Initial	Nanoek	2.26	41225	98868
IN2019-V02	Autumn	Initial	Initial	Picoekaryotes	22.23	2625	7879
IN2019-V02	Autumn	Initial	Initial	Bacteria	655.04	NaN	NaN
IN2019-V02	Autumn	Control	C1	Cyanobacteria	15.59	663	17753
IN2019-V02	Autumn	Control	C1	Large phytoplankton	0.06	427977	924858
IN2019-V02	Autumn	Control	C1	All fluorescent cells	22.06	11094	23943
IN2019-V02	Autumn	Control	C1	Nanoek	3.28	41422	72533
IN2019-V02	Autumn	Control	C1	Picoekaryotes	13.44	3538	11614

IN2019-V03	Autumn	Control	C1	Bacteria	684.62	NaN	NaN
IN2019-V02	Autumn	Control	C2	Cyanobacteria	15.57	716	21202
IN2019-V02	Autumn	Control	C2	Large phytoplankton	0.05	391821	1006791
IN2019-V02	Autumn	Control	C2	All fluorescent cells	16.14	11781	27990
IN2019-V02	Autumn	Control	C2	Nanoeuk	2.48	44779	71663
IN2019-V02	Autumn	Control	C2	Picoeukaryotes	8.47	4030	13953
IN2019-V03	Autumn	Control	C2	Bacteria	643.84	NaN	NaN
IN2019-V02	Autumn	Control	C3	Cyanobacteria	25.07	743	22085
IN2019-V02	Autumn	Control	C3	Large phytoplankton	0.09	476900	691569
IN2019-V02	Autumn	Control	C3	All fluorescent cells	31.91	14898	26125
IN2019-V02	Autumn	Control	C3	Nanoeuk	7.66	38851	49906
IN2019-V02	Autumn	Control	C3	Picoeukaryotes	16.29	5305	14252
IN2019-V03	Autumn	Control	C3	Bacteria	875.72	NaN	NaN
IN2019-V02	Autumn	Fe	Fe1	Cyanobacteria	9.06	735	16326
IN2019-V02	Autumn	Fe	Fe1	Large phytoplankton	0.09	492350	798866
IN2019-V02	Autumn	Fe	Fe1	All fluorescent cells	13.01	17999	28502
IN2019-V02	Autumn	Fe	Fe1	Nanoeuk	2.79	48149	55360
IN2019-V02	Autumn	Fe	Fe1	Picoeukaryotes	6.76	5232	13639
IN2019-V03	Autumn	Fe	Fe1	Bacteria	578.9	NaN	NaN
IN2019-V02	Autumn	Fe	Fe2	Cyanobacteria	14.83	725	19238
IN2019-V02	Autumn	Fe	Fe2	Large phytoplankton	0.06	399979	863076
IN2019-V02	Autumn	Fe	Fe2	All fluorescent cells	18.85	13841	26194
IN2019-V02	Autumn	Fe	Fe2	Nanoeuk	3.52	44926	59978
IN2019-V02	Autumn	Fe	Fe2	Picoeukaryotes	10.49	5121	13633
IN2019-V03	Autumn	Fe	Fe2	Bacteria	701.23	NaN	NaN
IN2019-V02	Autumn	Fe	Fe3	Cyanobacteria	57.18	886	25440
IN2019-V02	Autumn	Fe	Fe3	Large phytoplankton	0.08	478513	499537
IN2019-V02	Autumn	Fe	Fe3	All fluorescent cells	47.09	13367	24257
IN2019-V02	Autumn	Fe	Fe3	Nanoeuk	6.38	57427	55398
IN2019-V02	Autumn	Fe	Fe3	Picoeukaryotes	25.41	7971	16827
IN2019-V03	Autumn	Fe	Fe3	Bacteria	1960.05	NaN	NaN

IN2019-V02	Autumn	Mn	Mn2	Cyanobacteria	43.61	696	13431
IN2019-V02	Autumn	Mn	Mn2	Large phytoplankton	0.08	333703	716839
IN2019-V02	Autumn	Mn	Mn2	All fluorescent cells	33.12	10793	18706
IN2019-V02	Autumn	Mn	Mn2	Nanoeuk	4.17	43601	62788
IN2019-V02	Autumn	Mn	Mn2	Picoeukaryotes	24.19	3966	10198
IN2019-V03	Autumn	Mn	Mn2	Bacteria	1051.49	NaN	NaN
IN2019-V02	Autumn	Mn	Mn3	Cyanobacteria	87.2	685	14014
IN2019-V02	Autumn	Mn	Mn3	Large phytoplankton	0.03	252927	907091
IN2019-V02	Autumn	Mn	Mn3	All fluorescent cells	41.56	9749	21515
IN2019-V02	Autumn	Mn	Mn3	Nanoeuk	5.43	46224	63015
IN2019-V02	Autumn	Mn	Mn3	Picoeukaryotes	23.54	5044	13187
IN2019-V03	Autumn	Mn	Mn3	Bacteria	1509.12	NaN	NaN
IN2019-V02	Autumn	FeMn	FeMn1	Cyanobacteria	47.52	725	16382
IN2019-V02	Autumn	FeMn	FeMn1	Large phytoplankton	0.13	458364	672520
IN2019-V02	Autumn	FeMn	FeMn1	All fluorescent cells	29.99	14554	26121
IN2019-V02	Autumn	FeMn	FeMn1	Nanoeuk	5.84	46388	52621
IN2019-V02	Autumn	FeMn	FeMn1	Picoeukaryotes	13.03	5973	14912
IN2019-V03	Autumn	FeMn	FeMn1	Bacteria	1177.72	NaN	NaN
IN2019-V02	Autumn	FeMn	FeMn2	Cyanobacteria	23.96	736	17829
IN2019-V02	Autumn	FeMn	FeMn2	Large phytoplankton	0.14	466373	745857
IN2019-V02	Autumn	FeMn	FeMn2	All fluorescent cells	25.75	15294	26373
IN2019-V02	Autumn	FeMn	FeMn2	Nanoeuk	4.09	53403	64791
IN2019-V02	Autumn	FeMn	FeMn2	Picoeukaryotes	13.91	5242	12617
IN2019-V03	Autumn	FeMn	FeMn2	Bacteria	899.64	NaN	NaN
IN2019-V02	Autumn	FeMn	FeMn3	Cyanobacteria	16.87	738	18006
IN2019-V02	Autumn	FeMn	FeMn3	Large phytoplankton	0.08	287406	917369
IN2019-V02	Autumn	FeMn	FeMn3	All fluorescent cells	22.11	13964	28216
IN2019-V02	Autumn	FeMn	FeMn3	Nanoeuk	5.03	39865	57533
IN2019-V02	Autumn	FeMn	FeMn3	Picoeukaryotes	11.55	5161	13779
IN2019-V03	Autumn	FeMn	FeMn3	Bacteria	744.19	NaN	NaN

Table S4.4: Results of carbon and Fe uptake (in $\mu\text{M d}^{-1}$ and pM d^{-1} , respectively) measured in the three size fractions: $>20 \mu\text{m}$, $2\text{-}20 \mu\text{m}$, $0.2\text{-}2 \mu\text{m}$.

Voyage	Season	Treatment	Bottle	Size (μm)	Fe_pM	C_uM	Fe:C
IN2018-V04	Spring	Control	Control1	20	81.07	1.00	81.05
IN2018-V04	Spring	Control	Control1	2	172.46	2.08	82.99
IN2018-V04	Spring	Control	Control1	0.2	14.44	0.32	44.75
IN2018-V04	Spring	Control	Control2	20	65.99	1.35	48.92
IN2018-V04	Spring	Control	Control2	2	150.55	2.72	55.26
IN2018-V04	Spring	Control	Control2	0.2	15.90	0.48	32.82
IN2018-V04	Spring	Control	Control3	20	49.37	0.79	62.80
IN2018-V04	Spring	Control	Control3	2	102.73	1.62	63.46
IN2018-V04	Spring	Control	Control3	0.2	61.53	1.01	61.09
IN2018-V04	Spring	Fe	Fe1	20	219.52	1.94	112.94
IN2018-V04	Spring	Fe	Fe1	2	599.46	5.08	117.96
IN2018-V04	Spring	Fe	Fe1	0.2	45.86	0.63	73.36
IN2018-V04	Spring	Fe	Fe2	20	329.15	3.09	106.48
IN2018-V04	Spring	Fe	Fe2	2	441.74	3.23	136.71
IN2018-V04	Spring	Fe	Fe2	0.2	72.37	0.74	97.79
IN2018-V04	Spring	Fe	Fe3	20	236.58	2.00	118.55
IN2018-V04	Spring	Fe	Fe3	2	555.23	3.83	144.88
IN2018-V04	Spring	Fe	Fe3	0.2	66.23	0.77	86.21
IN2018-V04	Spring	Mn	Mn1	20	54.71	0.75	72.75
IN2018-V04	Spring	Mn	Mn1	2	302.36	2.86	105.57
IN2018-V04	Spring	Mn	Mn1	0.2	88.62	0.85	104.76
IN2018-V04	Spring	Mn	Mn2	20	189.60	2.03	93.21
IN2018-V04	Spring	Mn	Mn2	2	392.43	3.60	108.91
IN2018-V04	Spring	Mn	Mn2	0.2	53.66	0.74	72.72
IN2018-V04	Spring	Mn	Mn3	20	94.02	1.07	87.87
IN2018-V04	Spring	Mn	Mn3	2	178.95	1.80	99.45

IN2018-V04	Spring	Mn	Mn3	0.2	34.32	0.52	66.35
IN2018-V04	Spring	FeMn	FeMn1	20	296.60	3.64	81.52
IN2018-V04	Spring	FeMn	FeMn1	2	654.69	5.47	119.65
IN2018-V04	Spring	FeMn	FeMn1	0.2	53.72	0.96	56.09
IN2018-V04	Spring	FeMn	FeMn2	20	256.29	2.61	98.14
IN2018-V04	Spring	FeMn	FeMn2	2	573.42	4.46	128.57
IN2018-V04	Spring	FeMn	FeMn2	0.2	65.01	0.77	84.60
IN2018-V04	Spring	FeMn	FeMn3	20	347.71	2.26	153.95
IN2018-V04	Spring	FeMn	FeMn3	2	626.02	3.84	162.82
IN2018-V04	Spring	FeMn	FeMn3	0.2	71.03	0.53	134.52
IN2019-V02	Autumn	Control	Control1	20	9.41	0.20	46.42
IN2019-V02	Autumn	Control	Control1	2	20.18	0.36	55.35
IN2019-V02	Autumn	Control	Control1	0.2	73.59	0.50	147.32
IN2019-V02	Autumn	Control	Control2	20	10.61	0.21	51.26
IN2019-V02	Autumn	Control	Control2	2	17.71	0.32	56.14
IN2019-V02	Autumn	Control	Control2	0.2	62.53	0.48	129.26
IN2019-V02	Autumn	Fe	Fe1	20	32.60	NaN	NaN
IN2019-V02	Autumn	Fe	Fe1	2	68.12	NaN	NaN
IN2019-V02	Autumn	Fe	Fe1	0.2	516.19	NaN	NaN
IN2019-V02	Autumn	Fe	Fe2	20	35.13	NaN	NaN
IN2019-V02	Autumn	Fe	Fe2	2	75.19	NaN	NaN
IN2019-V02	Autumn	Fe	Fe2	0.2	277.32	NaN	NaN
IN2019-V02	Autumn	Fe	Fe3	20	NaN	0.45	NaN
IN2019-V02	Autumn	Fe	Fe3	2	NaN	1.11	NaN
IN2019-V02	Autumn	Fe	Fe3	0.2	NaN	0.70	NaN
IN2019-V02	Autumn	Mn	Mn1	20	17.64	0.40	43.83
IN2019-V02	Autumn	Mn	Mn1	2	37.18	0.69	53.66
IN2019-V02	Autumn	Mn	Mn1	0.2	56.12	0.48	116.22
IN2019-V02	Autumn	Mn	Mn2	20	18.06	0.52	34.63
IN2019-V02	Autumn	Mn	Mn2	2	43.96	0.92	47.64
IN2019-V02	Autumn	Mn	Mn2	0.2	59.64	0.62	96.18

IN2019-V02	Autumn	FeMn	FeMn1	20	61.04	0.15	399.47
IN2019-V02	Autumn	FeMn	FeMn1	2	84.38	0.18	457.26
IN2019-V02	Autumn	FeMn	FeMn1	0.2	193.62	0.21	914.72
IN2019-V02	Autumn	FeMn	FeMn2	20	52.72	0.11	468.14
IN2019-V02	Autumn	FeMn	FeMn2	2	90.12	0.21	434.82
IN2019-V02	Autumn	FeMn	FeMn2	0.2	155.66	0.17	912.38
IN2020-V08	Summer	Control	Control1	20	5.26	1.66	2.13
IN2020-V08	Summer	Control	Control1	2	7.41	0.71	7.00
IN2020-V08	Summer	Control	Control1	0.2	24.70	0.92	18.07
IN2020-V08	Summer	Control	Control2	20	3.98	1.72	1.55
IN2020-V08	Summer	Control	Control2	2	7.25	0.78	6.23
IN2020-V08	Summer	Control	Control2	0.2	20.02	1.03	13.00
IN2020-V08	Summer	Control	Control3	20	4.99	1.87	1.79
IN2020-V08	Summer	Control	Control3	2	7.42	0.83	5.97
IN2020-V08	Summer	Control	Control3	0.2	13.49	0.98	9.27
IN2020-V08	Summer	Fe	Fe1	20	28.07	4.30	5.98
IN2020-V08	Summer	Fe	Fe1	2	28.66	1.43	18.30
IN2020-V08	Summer	Fe	Fe1	0.2	41.25	1.42	26.49
IN2020-V08	Summer	Fe	Fe2	20	32.69	2.35	12.73
IN2020-V08	Summer	Fe	Fe2	2	34.75	2.28	13.94
IN2020-V08	Summer	Fe	Fe2	0.2	122.59	2.51	44.65
IN2020-V08	Summer	Fe	Fe3	20	28.74	3.80	6.92
IN2020-V08	Summer	Fe	Fe3	2	22.08	1.38	14.60
IN2020-V08	Summer	Fe	Fe3	0.2	54.95	1.72	29.17
IN2020-V08	Summer	Mn	Mn1	20	4.02	1.40	1.92
IN2020-V08	Summer	Mn	Mn1	2	2.73	0.33	5.62
IN2020-V08	Summer	Mn	Mn1	0.2	12.00	0.66	12.13
IN2020-V08	Summer	Mn	Mn2	20	5.45	1.96	1.87
IN2020-V08	Summer	Mn	Mn2	2	5.04	0.61	5.52
IN2020-V08	Summer	Mn	Mn2	0.2	17.25	0.84	13.74
IN2020-V08	Summer	Mn	Mn3	20	4.06	1.52	1.79

IN2020-V08	Summer	Mn	Mn3	2	3.55	0.47	5.04
IN2020-V08	Summer	Mn	Mn3	0.2	13.83	0.74	12.50
IN2020-V08	Summer	FeMn	FeMn1	20	31.18	4.30	6.63
IN2020-V08	Summer	FeMn	FeMn1	2	28.19	2.04	12.65
IN2020-V08	Summer	FeMn	FeMn1	0.2	31.57	1.98	14.60
IN2020-V08	Summer	FeMn	FeMn2	20	26.09	2.74	8.71
IN2020-V08	Summer	FeMn	FeMn2	2	11.63	0.78	13.57
IN2020-V08	Summer	FeMn	FeMn2	0.2	83.74	1.72	44.46
IN2020-V08	Summer	FeMn	FeMn3	20	27.53	3.92	6.42
IN2020-V08	Summer	FeMn	FeMn3	2	16.08	0.97	15.21
IN2020-V08	Summer	FeMn	FeMn3	0.2	24.31	1.48	15.05

Appendix D – Chapter 5

Table S5.1: Various parameters used for the deep chlorophyll maximum (DCM) experiment in polar waters, measured at day = 10. Macronutrients (NOx), phosphate, silicic acid, nitrite, particulate organic carbon (POC) and biogenic silica (BSi) are presented in μM . Chlorophyll-*a* (Chl-*a*) concentrations are in mg m^{-3} .

Voyage	Sample ID	Time	Light	Treatment	Nox	Phosphate	Silicic ac.	Nitrite	POC	Chl- <i>a</i>	Bsi
IN2020-V08	Initial_85.8m	T10	LL	Initial	26.18	1.85	9.20	0.21	3.43	0.51	0.17
IN2020-V08	2SOLTEE_LL_C1_TF	T10	LL	Control	26.05	1.86	9.10	0.21	1.06	0.69	0.41
IN2020-V08	2SOLTEE_LL_C2_TF	T10	LL	Control	26.07	1.87	9.00	0.22	0.98	0.75	0.72
IN2020-V08	2SOLTEE_LL_C3_TF	T10	LL	Control	26.05	1.86	9.00	0.22	1.01	0.71	0.60
IN2020-V08	2SOLTEE_LL_Mn1_TF	T10	LL	Mn	26.24	1.85	9.20	0.22	0.93	0.59	0.25
IN2020-V08	2SOLTEE_LL_Mn2_TF	T10	LL	Mn	26.18	1.86	9.20	0.21	1.08	0.66	0.31
IN2020-V08	2SOLTEE_LL_Mn3_TF	T10	LL	Mn	26.16	1.84	9.10	0.21	0.92	0.69	0.25
IN2020-V08	2SOLTEE_LL_Fe1_TF	T10	LL	Fe	26.02	1.84	9.50	0.21	1.28	1.36	0.45
IN2020-V08	2SOLTEE_LL_Fe2_TF	T10	LL	Fe	26.06	1.86	9.10	0.22	1.06	1.06	0.32
IN2020-V08	2SOLTEE_LL_Fe3_TF	T10	LL	Fe	26.05	1.85	9.00	0.22	1.02	1.04	0.36
IN2020-V08	2SOLTEE_LL_FeMn1_TF	T10	LL	FeMn	26.18	1.87	9.10	0.22	1.32	1.05	0.31
IN2020-V08	2SOLTEE_LL_FeMn2_TF	T10	LL	FeMn	26.17	1.85	9.10	0.22	1.18	1.09	0.30
IN2020-V08	2SOLTEE_LL_FeMn3_TF	T10	LL	FeMn	26.14	1.85	9.10	0.22	1.07	1.12	0.31
IN2020-V08	2SOLTEE_HL_C1_TF	T10	HL	Control	25.11	1.65	5.10	0.21	2.54	1.29	0.78
IN2020-V08	2SOLTEE_HL_C2_TF	T10	HL	Control	25.16	1.65	4.90	0.21	2.55	1.31	0.77
IN2020-V08	2SOLTEE_HL_C3_TF	T10	HL	Control	25.35	1.69	5.20	0.21	2.51	1.18	0.67
IN2020-V08	2SOLTEE_HL_Mn1_TF	T10	HL	Mn	25.36	1.66	5.50	0.21	2.39	1.05	0.65
IN2020-V08	2SOLTEE_HL_Mn2_TF	T10	HL	Mn	25.07	1.67	5.60	0.22	2.35	1.27	0.65
IN2020-V08	2SOLTEE_HL_Mn3_TF	T10	HL	Mn	25.29	1.70	5.30	0.21	2.63	1.07	0.65
IN2020-V08	2SOLTEE_HL_Fe1_TF	T10	HL	Fe	18.29	1.15	0.90	0.25	8.88	12.22	1.07
IN2020-V08	2SOLTEE_HL_Fe2_TF	T10	HL	Fe	18.71	1.17	0.80	0.23	8.55	12.40	1.11
IN2020-V08	2SOLTEE_HL_Fe3_TF	T10	HL	Fe	17.56	1.11	0.30	0.29	9.60	14.56	1.10
IN2020-V08	2SOLTEE_HL_FeMn1_TF	T10	HL	FeMn	18.09	1.15	1.10	0.25	10.45	11.79	1.09
IN2020-V08	2SOLTEE_HL_FeMn2_TF	T10	HL	FeMn	18.12	1.16	0.80	0.26	9.77	10.26	1.08
IN2020-V08	2SOLTEE_HL_FeMn3_TF	T10	HL	FeMn	18.07	1.13	0.80	0.25	9.12	12.34	1.09

Table S5.2: Photophysiological measurements for the deep chlorophyll maximum (DCM) experiment. In the thesis, we presented results for photochemical efficiency of PSII (F_v/F_m) and functional absorption cross section of PSII (σ_{PSII}) in $\text{nm}^2 \text{ quanta}^{-1}$.

Voyage	Treatment	Rep	Light	Time	F_o	F_m	F_v	F_v.F_m	F_v.F_o	σ_{PSII}
IN2020-V08	Initial	1	HL	T10	7720.27	14707.95	6987.68	0.47	0.91	928.22
IN2020-V08	Contol	1	HL	T10	7280.26	11529.44	4249.19	0.37	0.58	939.64
IN2020-V08	Contol	2	HL	T10	4886.64	7710.93	2824.29	0.37	0.58	1019.57
IN2020-V08	Contol	3	HL	T10	6020.30	9280.32	3260.02	0.35	0.54	1145.89
IN2020-V08	Fe	1	HL	T10	14567.85	32603.24	18035.38	0.55	1.24	644.81
IN2020-V08	Fe	2	HL	T10	12246.07	26553.13	14307.07	0.54	1.17	615.53
IN2020-V08	Fe	3	HL	T10	16853.19	36253.77	19400.59	0.54	1.15	614.30
IN2020-V08	FeMn	1	HL	T10	11857.58	28233.97	16376.40	0.58	1.38	607.32
IN2020-V08	FeMn	2	HL	T10	10182.25	23917.56	13735.32	0.57	1.35	599.18
IN2020-V08	FeMn	3	HL	T10	14208.83	34787.98	20579.16	0.59	1.45	597.04
IN2020-V08	Mn	1	HL	T10	6583.79	9744.25	3160.46	0.32	0.48	990.74
IN2020-V08	Mn	2	HL	T10	2551.12	4807.34	2256.22	0.47	0.88	865.35
IN2020-V08	Mn	3	HL	T10	3320.37	5852.17	2531.80	0.43	0.76	804.30
IN2020-V08	Initial	1	LL	T10	7720.27	14707.95	6987.68	0.47	0.91	928.22
IN2020-V08	Contol	1	LL	T10	4312.99	10674.82	6361.83	0.60	1.49	973.43
IN2020-V08	Contol	2	LL	T10	3600.76	8840.98	5240.22	0.59	1.48	847.89
IN2020-V08	Contol	3	LL	T10	1953.81	5880.09	3926.29	0.67	2.02	895.30
IN2020-V08	Fe	1	LL	T10	4242.78	13747.80	9505.02	0.69	2.24	500.59
IN2020-V08	Fe	2	LL	T10	4528.63	13485.19	8956.57	0.66	1.98	672.40
IN2020-V08	Fe	3	LL	T10	2523.89	8132.49	5608.60	0.69	2.24	681.76
IN2020-V08	FeMn	1	LL	T10	4333.55	12485.76	8152.22	0.65	1.88	732.62
IN2020-V08	FeMn	2	LL	T10	5674.49	14868.38	9193.89	0.62	1.62	663.13
IN2020-V08	FeMn	3	LL	T10	5029.88	13948.36	8918.48	0.64	1.77	728.30
IN2020-V08	Mn	1	LL	T10	2376.73	6458.78	4082.05	0.63	1.72	885.03
IN2020-V08	Mn	2	LL	T10	2562.19	7065.63	4503.44	0.64	1.78	966.25
IN2020-V08	Mn	3	LL	T10	6100.72	13994.30	7893.57	0.56	1.30	913.56

Table S5.3: Flow cytometry data for the deep chlorophyll maximum (DCM) experiment. Five gates are indicated: all fluorescent cells, large phytoplankton, picoeukaryotes, nanoeukaryotes and bacteria.

Voyage	Light	Treatment	Rep.	Gate	Cell count per uL	Mean FSC-A	Mean B7-A
IN2020-V08	HL	Initial	1	All fluorescent cells	2.71	33521	71879
IN2020-V08	HL	Initial	1	Large phytoplankton	0.04	705598	1237155
IN2020-V08	HL	Initial	1	Bacteria	264.95	NaN	NaN
IN2020-V08	HL	Initial	1	Picoeukaryotes	1.2	4829	36563
IN2020-V08	HL	Initial	1	Nanoeukaryotes	0.6	38103	152503
IN2020-V08	HL	Control	1	All fluorescent cells	13.21	19655	29883
IN2020-V08	HL	Control	1	Large phytoplankton	0.05	369544	1116992
IN2020-V08	HL	Control	1	Bacteria	328.91	NaN	NaN
IN2020-V08	HL	Control	1	Picoeukaryotes	7.1	3864	10094
IN2020-V08	HL	Control	1	Nanoeukaryotes	3.16	36088	77595
IN2020-V08	HL	Control	2	All fluorescent cells	12.34	18729	31903
IN2020-V08	HL	Control	2	Large phytoplankton	0.05	379180	1212154
IN2020-V08	HL	Control	2	Bacteria	343.86	NaN	NaN
IN2020-V08	HL	Control	2	Picoeukaryotes	7.09	3491	10601
IN2020-V08	HL	Control	2	Nanoeukaryotes	3.33	34114	72397
IN2020-V08	HL	Control	3	All fluorescent cells	13.34	16224	35216
IN2020-V08	HL	Control	3	Large phytoplankton	0.07	416661	1939291
IN2020-V08	HL	Control	3	Bacteria	348.79	NaN	NaN
IN2020-V08	HL	Control	3	Picoeukaryotes	8.29	3714	11279
IN2020-V08	HL	Control	3	Nanoeukaryotes	3.23	34269	69841
IN2020-V08	HL	Mn	1	All fluorescent cells	12.42	20963	37165
IN2020-V08	HL	Mn	1	Large phytoplankton	0.05	349015	1761798
IN2020-V08	HL	Mn	1	Bacteria	349.15	NaN	NaN
IN2020-V08	HL	Mn	1	Picoeukaryotes	7.07	3697	10377
IN2020-V08	HL	Mn	1	Nanoeukaryotes	3.22	42611	87117
IN2020-V08	HL	Mn	2	All fluorescent cells	17.49	14211	27829
IN2020-V08	HL	Mn	2	Large phytoplankton	0.06	379513	1207558

IN2020-V08	HL	Mn	2	Bacteria	356.46	NaN	NaN
IN2020-V08	HL	Mn	2	Picoeukaryotes	10.76	3963	11798
IN2020-V08	HL	Mn	2	Nanoekaryotes	4.25	24876	65521
IN2020-V08	HL	Mn	3	All fluorescent cells	13.54	18673	28280
IN2020-V08	HL	Mn	3	Large phytoplankton	0.06	328341	1381318
IN2020-V08	HL	Mn	3	Bacteria	372.87	NaN	NaN
IN2020-V08	HL	Mn	3	Picoeukaryotes	8.22	3749	9534
IN2020-V08	HL	Mn	3	Nanoekaryotes	3.03	30469	66107
IN2020-V08	HL	Fe	1	All fluorescent cells	20.9	46065	71296
IN2020-V08	HL	Fe	1	Large phytoplankton	0.52	840915	1272086
IN2020-V08	HL	Fe	1	Bacteria	389.35	NaN	NaN
IN2020-V08	HL	Fe	1	Picoeukaryotes	11.83	7381	18229
IN2020-V08	HL	Fe	1	Nanoekaryotes	4.78	53208	119806
IN2020-V08	HL	Fe	2	All fluorescent cells	19.68	48833	78615
IN2020-V08	HL	Fe	2	Large phytoplankton	0.63	798851	1255612
IN2020-V08	HL	Fe	2	Bacteria	363.61	NaN	NaN
IN2020-V08	HL	Fe	2	Picoeukaryotes	10.57	6587	18587
IN2020-V08	HL	Fe	2	Nanoekaryotes	4.07	52738	127360
IN2020-V08	HL	Fe	3	All fluorescent cells	34.65	29552	57722
IN2020-V08	HL	Fe	3	Large phytoplankton	0.63	727211	1242855
IN2020-V08	HL	Fe	3	Bacteria	428.33	NaN	NaN
IN2020-V08	HL	Fe	3	Picoeukaryotes	22.27	6143	18716
IN2020-V08	HL	Fe	3	Nanoekaryotes	6.79	47049	112473
IN2020-V08	HL	FeMn	1	All fluorescent cells	25.91	41807	72110
IN2020-V08	HL	FeMn	1	Large phytoplankton	0.55	721130	1243552
IN2020-V08	HL	FeMn	1	Bacteria	455.89	NaN	NaN
IN2020-V08	HL	FeMn	1	Picoeukaryotes	13.38	6526	16506
IN2020-V08	HL	FeMn	1	Nanoekaryotes	8.3	46886	113311
IN2020-V08	HL	FeMn	2	All fluorescent cells	19.82	43262	66805
IN2020-V08	HL	FeMn	2	Large phytoplankton	0.41	726214	1084875
IN2020-V08	HL	FeMn	2	Bacteria	380.93	NaN	NaN

IN2020-V08	HL	FeMn	2	Picoeukaryotes	6.96	4204	12512
IN2020-V08	HL	FeMn	2	Nanoekaryotes	7.5	43315	100796
IN2020-V08	HL	FeMn	3	All fluorescent cells	26.35	43547	60566
IN2020-V08	HL	FeMn	3	Large phytoplankton	0.53	834228	1278118
IN2020-V08	HL	FeMn	3	Bacteria	416.5	NaN	NaN
IN2020-V08	HL	FeMn	3	Picoeukaryotes	13.73	6536	13287
IN2020-V08	HL	FeMn	3	Nanoekaryotes	6.82	51634	103372
IN2020-V08	LL	Control	1	All fluorescent cells	3.71	22348	56066
IN2020-V08	LL	Control	1	Large phytoplankton	0.02	291644	1118355
IN2020-V08	LL	Control	1	Bacteria	254.87	NaN	NaN
IN2020-V08	LL	Control	1	Picoeukaryotes	1.93	5141	34191
IN2020-V08	LL	Control	1	Nanoekaryotes	0.66	43574	150121
IN2020-V08	LL	Control	2	All fluorescent cells	3.04	32364	49666
IN2020-V08	LL	Control	2	Large phytoplankton	0.01	515464	1897184
IN2020-V08	LL	Control	2	Bacteria	204.22	NaN	NaN
IN2020-V08	LL	Control	2	Picoeukaryotes	1.39	6147	30633
IN2020-V08	LL	Control	2	Nanoekaryotes	0.51	48762	140807
IN2020-V08	LL	Control	3	All fluorescent cells	3.34	26989	43716
IN2020-V08	LL	Control	3	Large phytoplankton	0.02	575868	897781
IN2020-V08	LL	Control	3	Bacteria	220.11	NaN	NaN
IN2020-V08	LL	Control	3	Picoeukaryotes	1.67	5752	27639
IN2020-V08	LL	Control	3	Nanoekaryotes	0.55	42537	134360
IN2020-V08	LL	Mn	1	All fluorescent cells	5.19	24772	48145
IN2020-V08	LL	Mn	1	Large phytoplankton	0.03	256346	1279551
IN2020-V08	LL	Mn	1	Bacteria	362.06	NaN	NaN
IN2020-V08	LL	Mn	1	Picoeukaryotes	3.02	5158	28647
IN2020-V08	LL	Mn	1	Nanoekaryotes	0.78	44521	139380
IN2020-V08	LL	Mn	2	All fluorescent cells	3.17	31560	63237
IN2020-V08	LL	Mn	2	Large phytoplankton	0.03	400315	1638452
IN2020-V08	LL	Mn	2	Bacteria	226.12	NaN	NaN
IN2020-V08	LL	Mn	2	Picoeukaryotes	1.65	5150	31254

IN2020-V08	LL	Mn	2	Nanoeukaryotes	0.58	43369	150922
IN2020-V08	LL	Mn	3	All fluorescent cells	3.82	25268	49666
IN2020-V08	LL	Mn	3	Large phytoplankton	0.02	305620	787966
IN2020-V08	LL	Mn	3	Bacteria	275.99	NaN	NaN
IN2020-V08	LL	Mn	3	Picoeukaryotes	2.12	6022	30711
IN2020-V08	LL	Mn	3	Nanoeukaryotes	0.72	40618	134687
IN2020-V08	LL	Fe	1	All fluorescent cells	4.81	36053	58019
IN2020-V08	LL	Fe	1	Large phytoplankton	0.03	667622	1888599
IN2020-V08	LL	Fe	1	Bacteria	290.58	NaN	NaN
IN2020-V08	LL	Fe	1	Picoeukaryotes	2.54	6951	32325
IN2020-V08	LL	Fe	1	Nanoeukaryotes	0.87	45200	142846
IN2020-V08	LL	Fe	2	All fluorescent cells	3.57	30947	55118
IN2020-V08	LL	Fe	2	Large phytoplankton	0.03	391971	1118481
IN2020-V08	LL	Fe	2	Bacteria	291.97	NaN	NaN
IN2020-V08	LL	Fe	2	Picoeukaryotes	1.86	6981	32889
IN2020-V08	LL	Fe	2	Nanoeukaryotes	0.65	44629	137700
IN2020-V08	LL	Fe	3	All fluorescent cells	3.45	37358	77811
IN2020-V08	LL	Fe	3	Large phytoplankton	0.05	621340	1348160
IN2020-V08	LL	Fe	3	Bacteria	239.55	NaN	NaN
IN2020-V08	LL	Fe	3	Picoeukaryotes	1.79	6574	38510
IN2020-V08	LL	Fe	3	Nanoeukaryotes	0.75	44164	151959
IN2020-V08	LL	FeMn	1	All fluorescent cells	4.06	22945	55461
IN2020-V08	LL	FeMn	1	Large phytoplankton	0.02	517327	1081284
IN2020-V08	LL	FeMn	1	Bacteria	331.95	NaN	NaN
IN2020-V08	LL	FeMn	1	Picoeukaryotes	2.25	6820	33294
IN2020-V08	LL	FeMn	1	Nanoeukaryotes	0.85	37999	139352
IN2020-V08	LL	FeMn	2	All fluorescent cells	3.79	29985	69409
IN2020-V08	LL	FeMn	2	Large phytoplankton	0.04	347061	1459382
IN2020-V08	LL	FeMn	2	Bacteria	299.12	NaN	NaN
IN2020-V08	LL	FeMn	2	Picoeukaryotes	1.84	6904	38354
IN2020-V08	LL	FeMn	2	Nanoeukaryotes	0.81	44225	144659

IN2020-V08	LL	FeMn	3	All fluorescent cells	3.58	36870	57581
IN2020-V08	LL	FeMn	3	Large phytoplankton	0.04	684145	1031003
IN2020-V08	LL	FeMn	3	Bacteria	201.68	NaN	NaN
IN2020-V08	LL	FeMn	3	Picoeukaryotes	1.73	6971	32877
IN2020-V08	LL	FeMn	3	Nanoeukaryotes	0.71	46873	140283

Table S5.4: Fe and carbon uptake rates data (in $\mu\text{M d}^{-1}$ and pM d^{-1} , respectively) for the deep chlorophyll maximum (DCM) experiment.

Voyage	Light	Treatment	Replicates	Size fraction	Fe (pM d^{-1})	C ($\mu\text{M d}^{-1}$)	Fe:C ($\mu\text{mol mol}^{-1}$)
IN2020-V08	HL	Control	1	20	5.21E+00	8.00E-01	6.10E+00
IN2020-V08	HL	Control	1	2	3.07E+00	1.39E-01	2.21E+01
IN2020-V08	HL	Control	1	0.2	1.45E+01	1.85E-01	7.85E+01
IN2020-V08	HL	Control	2	20	3.52E+00	7.29E-01	4.83E+00
IN2020-V08	HL	Control	2	2	2.30E+00	1.51E-01	1.52E+01
IN2020-V08	HL	Control	2	0.2	1.78E+01	1.96E-01	9.06E+01
IN2020-V08	HL	Control	3	20	4.34E+00	7.65E-01	5.68E+00
IN2020-V08	HL	Control	3	2	4.36E+00	1.99E-01	2.19E+01
IN2020-V08	HL	Control	3	0.2	2.68E+01	2.55E-01	1.05E+02
IN2020-V08	HL	Fe	1	20	3.69E+01	7.18E+00	5.13E+00
IN2020-V08	HL	Fe	1	2	2.15E+01	1.13E+00	1.91E+01
IN2020-V08	HL	Fe	1	0.2	5.43E+01	1.16E+00	4.70E+01
IN2020-V08	HL	Fe	2	20	5.49E+01	6.51E+00	8.44E+00
IN2020-V08	HL	Fe	2	2	1.86E+01	8.27E-01	2.25E+01
IN2020-V08	HL	Fe	2	0.2	3.78E+01	1.09E+00	3.48E+01
IN2020-V08	HL	Fe	3	20	5.76E+01	7.54E+00	7.64E+00
IN2020-V08	HL	Fe	3	2	1.26E+01	7.29E-01	1.73E+01
IN2020-V08	HL	Fe	3	0.2	2.98E+01	1.21E+00	2.46E+01
IN2020-V08	HL	Mn	1	20	4.30E+00	1.28E+00	3.35E+00
IN2020-V08	HL	Mn	1	2	3.56E+00	2.42E-01	1.47E+01
IN2020-V08	HL	Mn	1	0.2	3.08E+01	3.74E-01	8.24E+01
IN2020-V08	HL	Mn	2	20	4.81E+00	1.14E+00	4.23E+00

IN2020-V08	HL	Mn	2	2	2.90E+00	4.31E-01	6.72E+00
IN2020-V08	HL	Mn	2	0.2	2.07E+01	6.22E-01	3.33E+01
IN2020-V08	HL	Mn	3	20	3.86E+00	1.28E+00	3.00E+00
IN2020-V08	HL	Mn	3	2	3.52E+00	4.73E-01	7.45E+00
IN2020-V08	HL	Mn	3	0.2	2.16E+01	3.92E-01	5.51E+01
IN2020-V08	HL	FeMn	1	20	5.27E+01	9.49E+00	5.55E+00
IN2020-V08	HL	FeMn	1	2	2.45E+01	1.12E+00	2.19E+01
IN2020-V08	HL	FeMn	1	0.2	5.63E+01	1.10E+00	5.12E+01
IN2020-V08	HL	FeMn	2	20	2.29E+01	NaN	NaN
IN2020-V08	HL	FeMn	2	2	2.93E+01	1.19E+00	2.46E+01
IN2020-V08	HL	FeMn	2	0.2	5.15E+01	9.20E-01	5.60E+01
IN2020-V08	HL	FeMn	3	20	5.49E+01	7.94E+00	6.92E+00
IN2020-V08	HL	FeMn	3	2	3.05E+01	1.07E+00	2.86E+01
IN2020-V08	HL	FeMn	3	0.2	4.42E+01	8.83E-01	5.01E+01
IN2020-V08	LL	Control	1	20	3.35E-01	7.54E-02	4.45E+00
IN2020-V08	LL	Control	1	2	3.08E-01	2.38E-02	1.29E+01
IN2020-V08	LL	Control	1	0.2	1.57E+00	3.64E-02	4.31E+01
IN2020-V08	LL	Control	2	20	3.08E-01	5.24E-02	5.88E+00
IN2020-V08	LL	Control	2	2	2.14E-01	1.81E-02	1.18E+01
IN2020-V08	LL	Control	2	0.2	4.40E-01	2.01E-02	2.19E+01
IN2020-V08	LL	Control	3	20	2.58E-01	5.04E-02	5.11E+00
IN2020-V08	LL	Control	3	2	2.37E-01	2.09E-02	1.13E+01
IN2020-V08	LL	Control	3	0.2	7.15E-01	2.40E-02	2.98E+01
IN2020-V08	LL	Fe	1	20	1.66E+00	1.07E-01	1.56E+01
IN2020-V08	LL	Fe	1	2	1.07E+00	2.27E-02	4.74E+01
IN2020-V08	LL	Fe	1	0.2	2.18E+00	3.59E-02	6.08E+01
IN2020-V08	LL	Fe	2	20	1.64E+00	9.27E-02	1.77E+01
IN2020-V08	LL	Fe	2	2	1.12E+00	1.55E-02	7.23E+01
IN2020-V08	LL	Fe	2	0.2	1.96E+00	3.15E-02	6.21E+01
IN2020-V08	LL	Fe	3	20	1.65E+00	5.92E-02	2.78E+01
IN2020-V08	LL	Fe	3	2	1.20E+00	1.50E-02	8.02E+01

IN2020-V08	LL	Fe	3	0.2	1.11E+00	2.17E-02	5.12E+01
IN2020-V08	LL	Mn	1	20	3.27E-01	6.76E-02	4.83E+00
IN2020-V08	LL	Mn	1	2	3.93E-01	2.82E-02	1.39E+01
IN2020-V08	LL	Mn	1	0.2	2.29E+00	3.98E-02	5.76E+01
IN2020-V08	LL	Mn	2	20	3.10E-01	4.05E-02	7.67E+00
IN2020-V08	LL	Mn	2	2	3.60E-01	1.94E-02	1.85E+01
IN2020-V08	LL	Mn	2	0.2	3.14E+00	3.20E-02	9.83E+01
IN2020-V08	LL	Mn	3	20	4.87E-01	5.53E-02	8.81E+00
IN2020-V08	LL	Mn	3	2	3.27E-01	1.62E-02	2.03E+01
IN2020-V08	LL	Mn	3	0.2	2.80E+00	3.36E-02	8.33E+01
IN2020-V08	LL	FeMn	1	20	1.02E+00	8.62E-02	1.19E+01
IN2020-V08	LL	FeMn	1	2	1.09E+00	2.33E-02	4.65E+01
IN2020-V08	LL	FeMn	1	0.2	1.82E+00	3.93E-02	4.62E+01
IN2020-V08	LL	FeMn	2	20	2.41E+00	1.31E-01	1.84E+01
IN2020-V08	LL	FeMn	2	2	2.26E+00	3.44E-02	6.58E+01
IN2020-V08	LL	FeMn	2	0.2	3.25E+00	4.99E-02	6.51E+01
IN2020-V08	LL	FeMn	3	20	2.29E+00	1.26E-01	1.81E+01
IN2020-V08	LL	FeMn	3	2	1.60E+00	2.82E-02	5.67E+01
IN2020-V08	LL	FeMn	3	0.2	1.82E+00	3.98E-02	4.57E+01

References

- Aguilar-Islas, A. M., and K. W. Bruland. 2006. "Dissolved manganese and silicic acid in the Columbia River Plume: A major source to the California Current and coastal waters off Washington and Oregon." *Marine Chemistry* 101 (3–4): 233–47. <https://doi.org/10.1016/j.marchem.2006.03.005>.
- Aguirre, J. D., and V. C. Culotta. 2012. "Battles with Iron: Manganese in Oxidative Stress Protection." *Journal of Biological Chemistry* 287 (17): 13541–48. <https://doi.org/10.1074/jbc.R111.312181>.
- Alderkamp, A-C, de Baar, H. J. W., Visser R. J. W., and K. R. Arrigo. 2010. "Can photoinhibition control phytoplankton abundance in deeply mixed water columns of the Southern Ocean?" *Limnology and Oceanography* 55 (3): 1248–64. <https://doi.org/10.4319/lo.2010.55.3.1248>.
- Allen, M. D., Kropat, J., Tottey, S., Del Campo, J. A., and S. S. Merchant. 2007. "Manganese deficiency in *Chlamydomonas* results in loss of Photosystem II and MnSOD Function, Sensitivity to Peroxides, and Secondary Phosphorus and Iron Deficiency." *Plant Physiology* 143 (1): 263–77. <https://doi.org/10.1104/pp.106.088609>.
- Angino, E. 1966. "Geochemistry of Antarctic Pelagic Sediments," *Geochimica et Cosmochimica Acta*, 1966, vol. 30, no 9, p. 939-961.
- Ardyna, M., Lacour, L., Sergi, S., d'Ovidio, F., Sallée, J-B., Rembauville, M., Blain, S., Tagliabue, A., Schlitzer, R., Jeandel, C., Arrigo, K. R., and H. Claustre. "Hydrothermal vents trigger massive phytoplankton blooms in the Southern Ocean." *Nature Communications* 10 (1). <https://doi.org/10.1038/s41467-019-09973-6>.
- Armstrong, F. A. 2008. "Why did Nature choose manganese to make oxygen?" *Philosophical Transactions of the Royal Society B: Biological Sciences* 363 (1494): 1263–70. <https://doi.org/10.1098/rstb.2007.2223>.
- Arndt, J. E, Schenke, H. W., Jakobsson, M., Nitsche, F. O. Buys, G., Goleby, B., et al. 2013. The international Bathymetric Chart of the Southern Ocean (IBCSO) Version 1.0 - A new bathymetric compilation covering circum-Antarctic waters. *Geophysical Research Letters*, 40(12), 3111-3117. doi.org/10.1002/grl.50413.
- Arrigo, K. R., van Dijken, G. L., and A. L. Strong. 2015. "Environmental controls of marine productivity hot spots around Antarctica." *Journal of Geophysical Research: Oceans* 120 (8): 5545–65. <https://doi.org/10.1002/2015JC010888>.
- Aumont, O., C. Ethé, Tagliabue A., Bopp L., and M. Gehlen. 2015. "PISCES-v2: An Ocean biogeochemical model for carbon and ecosystem Studies." *Geoscientific Model Development* 8 (8): 2465–2513. <https://doi.org/10.5194/gmd-8-2465-2015>.
- Bach, L. T., Lohbeck, K. T., Reusch, T. B. H., and U. Riebesell. 2018. "Rapid evolution of highly variable competitive abilities in a key phytoplankton species." *Nature Ecology & Evolution* 2 (4): 611–13. <https://doi.org/10.1038/s41559-018-0474-x>.
- Baker, A.R., Jickells, T.D., Witt, M. and K.L. Linge. 2006. "Trends in the Solubility of Iron, Aluminium, Manganese and Phosphorus in Aerosol Collected over the Atlantic Ocean." *Marine Chemistry* 98 (1): 43–58. <https://doi.org/10.1016/j.marchem.2005.06.004>.
- Bakker, D. C. E., Hoppema, M., Schroder, M. and W. Geibert. 2008. "A rapid transition from ice covered CO₂-rich waters to a biologically mediated CO₂ sink in the Eastern Weddell Gyre," *Biogeosciences*, 2008, vol. 5, no 5, p. 1373-1386.
- Baldry, K., Strutto, G., Hill, N. A., and P. W. Boyd. 2020. "Subsurface chlorophyll-a maxima in the Southern Ocean." *Frontiers in Marine Science* 7 (August): 671. <https://doi.org/10.3389/fmars.2020.00671>.
- Beaman, R. J., O'Brien, P. E., Post, A. L., and L. De Santis. 2011. "A new high-resolution bathymetry model for the Terre Adélie and George V continental margin, East Antarctica." *Antarctic Science* 23 (1): 95–103. <https://doi.org/10.1017/S095410201000074X>.
- Behrenfeld, M. J., Bale, A. J., Kolber, Z. S., Aiken, J., and P. G. Falkowski. 1996. "Confirmation of iron limitation of phytoplankton photosynthesis in the Equatorial Pacific Ocean." *Nature* 383 (6600): 508–11. <https://doi.org/10.1038/383508a0>.

- Berger, C. J. M., Lippiatt, S. M., Lawrence, M. G., and K. W. Bruland. 2008a. "Application of a chemical leach technique for estimating labile particulate aluminium, iron, and manganese in the Columbia River plume and coastal waters off Oregon and Washington." *Journal of Geophysical Research* 113 (August). <https://doi.org/10.1029/2007JC004703>.
- Bhatia, M. P., Waterman, S., Burgess, D. O., Williams, P. L., Bundy, R. M., Mellett, T., et al. (2021). Glaciers and nutrients in the Canadian Arctic Archipelago marine system. *Global Biogeochemical Cycles*, 35, e2021GB006976.
- Bishop, J. K.B., Lam, P. J., and T. J. Wood. 2012a. "Getting Good Particles: Accurate sampling of particles by large volume in-situ Filtration." *Limnology and Oceanography: Methods* 10 (9): 681–710. <https://doi.org/10.4319/lom.2012.10.681>.
- Blain, S., Quéguiner, B., Armand, L., Belviso, S., Bombled, B., Bopp, L., Bowie, A. R., et al. 2007. "Effect of natural iron fertilization on carbon sequestration in the Southern Ocean." *Nature* 446 (7139): 1070–74. <https://doi.org/10.1038/nature05700>.
- Boulart, C., Briais, A., Chavagnac, V., Révillon, S., Ceuleneer, G., Donval, J-P., Guyader, V., et al. 2017. "Contrasted hydrothermal activity along the South-East Indian Ridge (130°E-140°E): From crustal to ultramafic circulation." *Geochemistry, Geophysics, Geosystems* 18 (7): 2446–58. <https://doi.org/10.1002/2016GC006683>.
- Bowie, A. R., Griffiths, F. B., Dehairs, F., and T. W. Trull. 2011. "Oceanography of the Subantarctic and Polar Frontal Zones South of Australia during Summer: Setting for the SAZ-Sense Study." *Deep Sea Research Part II: Topical Studies in Oceanography* 58 (21–22): 2059–70. <https://doi.org/10.1016/j.dsr2.2011.05.033>.
- Bowie, A. R., Lannuzel, D., Remenyi, T. A., Wagener, T., Lam, P. J., Boyd, P. W., Guieu, C., Townsend, A. T., and T. W. Trull. 2009. "Biogeochemical iron budgets of the Southern Ocean south of Australia: Decoupling of iron and nutrient cycles in the subantarctic zone by the summertime supply" *Global Biogeochemical Cycles* 23 (4): n/a-n/a. <https://doi.org/10.1029/2009GB003500>.
- Bowie, A. R., Townsend, A. T., Lannuzel, D., Remenyi, T. A., and van der Merwe, P. 2010. "Modern sampling and analytical methods for the determination of trace elements in marine particulate material using magnetic sector inductively coupled plasma–mass spectrometry." *Analytica Chimica Acta* 676 (1–2): 15–27. <https://doi.org/10.1016/j.aca.2010.07.037>.
- Bown, J., Boye, M., Baker, A., Duvieilbourg, E., Lacan, Le Moigne, F., F., Planchon, F., Speich, S., and D. M. Nelson. 2011. "The biogeochemical cycle of dissolved cobalt in the Atlantic and the Southern Ocean south off the coast of South Africa." *Marine Chemistry* 126 (1–4): 193–206. <https://doi.org/10.1016/j.marchem.2011.03.008>.
- Boyd, P. W., Jickells, T., Law, C.S., Blain, S., Boyle, E.A., Buesseler, K.O., Coale, K.H., et al. 2007. "Mesoscale iron enrichment experiments 1993-2005: Synthesis and future directions." *Science* 315 (5812): 612–17. <https://doi.org/10.1126/science.1131669>.
- Boyd, P. W., and P. Newton. 1995. "Evidence of the potential influence of planktonic community structure on the interannual variability of particulate organic carbon flux." *Deep Sea Research Part I: Oceanographic Research Papers* 42 (5): 619–39. [https://doi.org/10.1016/0967-0637\(95\)00017-Z](https://doi.org/10.1016/0967-0637(95)00017-Z).
- Boyd, P. W. 2002. "Environmental factors controlling phytoplankton processes in the Southern Ocean." *Journal of Phycology* 38 (5): 844–61. <https://doi.org/10.1046/j.1529-8817.2002.t01-1-01203.x>.
- Boyd, P. W., Claustre, H., Levy, M., Siegel, D. A., and T. Weber. 2019. "Multi-faceted particle pumps drive carbon sequestration in the ocean." *Nature* 568 (7752): 327–35. <https://doi.org/10.1038/s41586-019-1098-2>.
- Boyd, P. W., Watson, A. J., Law, C. S., Abraham, E. R., Trull, T., Murdoch, R., Bakker, D. C. E., Bowie, A. R., Buesseler, K. O., Chang, Hoe, et al. 2000. "A mesoscale phytoplankton bloom in the polar Southern Ocean stimulated by iron fertilization." *Nature* 407 (6805): 695–702. <https://doi.org/10.1038/35037500>.
- Boyd, P. W., Dillingham, P. W., McGraw, C. M., Armstrong, E. A., Cornwall, C. E., Feng, Y.-y., Hurd, C. L., et al. 2016. "Physiological responses of a Southern Ocean diatom to complex future ocean conditions." *Nature Climate Change* 6 (2): 207–13. <https://doi.org/10.1038/nclimate2811>.

- Boyd, P.W. and P.P. Newton. 1999. "Does planktonic community structure determine downward particulate organic carbon flux in different oceanic provinces?" *Deep Sea Research Part I: Oceanographic Research Papers* 46 (1): 63–91. [https://doi.org/10.1016/S0967-0637\(98\)00066-1](https://doi.org/10.1016/S0967-0637(98)00066-1).
- Boye, M., Constant M.G. van den Berg, J. T.M., de Jong, H. L., Croot, P. and H. J.W. de Baar. 2001. "Organic complexation of iron in the Southern Ocean." *Deep Sea Research Part I: Oceanographic Research Papers* 48 (6): 1477–97. [https://doi.org/10.1016/S0967-0637\(00\)00099-6](https://doi.org/10.1016/S0967-0637(00)00099-6).
- Brand, L. E., Sunda, W. G., and R. R. L. Guillard. 1983. "Limitation of marine phytoplankton reproductive rates by zinc, manganese, and iron: Zn, Mn, Fe limitation in algae." *Limnology and Oceanography* 28 (6): 1182–98. <https://doi.org/10.4319/lo.1983.28.6.1182>.
- Browning, T. J., Bouman, H. A., Henderson, G. M., Mather, T. A., Pyle, D. M., Schlosser, C., Woodward, E. M. S., and C. M. Moore. 2014. "Strong Responses of Southern Ocean phytoplankton communities to volcanic ash." *Geophysical Research Letters* 41 (8): 2851–57. <https://doi.org/10.1002/2014GL059364>.
- Browning, T. J., Achterberg, E. P., Engel, A., and E. Mawji. 2021. "Manganese co-limitation of phytoplankton growth and major nutrient drawdown in the Southern Ocean." *Nature Communications* 12 (1): 884. <https://doi.org/10.1038/s41467-021-21122-6>.
- Bruland, K W, and M C Lohan. 2003. "6.02 Controls of trace metals in seawater," *Treatise on geochemistry*, vol. 6, p.625.
- Bull, C., Niederhoffer, E. C., Yoshida, T., and J. A. Fee. 1991. "Kinetic studies of superoxide dismutases: properties of the manganese-containing protein from *Thermus Thermophilus*." *Journal of the American Chemical Society* 113 (11): 4069–76. <https://doi.org/10.1021/ja00011a003>.
- Buma, A. G. J., de Baar, H. J. W., Nolting, R. F., and van Bennekom, A. J. 1991. "Metal enrichment experiments in the Weddell-Scotia Seas: Effects of iron and manganese on various plankton communities." *Limnology and Oceanography* 36 (8): 1865–78. <https://doi.org/10.4319/lo.1991.36.8.1865>.
- Burdige, David J. 1993. "The biogeochemistry of manganese and iron reduction in marine sediments." *Earth-Science Reviews* 35 (3): 249–84. [https://doi.org/10.1016/0012-8252\(93\)90040-E](https://doi.org/10.1016/0012-8252(93)90040-E).
- Butler, E. C. V. 2006. "The tail of two rivers in Tasmania: the Derwent and Huon Estuaries." In *Estuaries*, edited by Peter J. Wangersky, 5H:1–49. Berlin/Heidelberg: Springer-Verlag. https://doi.org/10.1007/698_5_022.
- Butler, E. C.V., O’Sullivan, J. E., Watson, R. J., Bowie, A. R., Remenyi, T. A., and D. Lannuzel. 2013. "Trace metals Cd, Co, Cu, Ni, and Zn in waters of the subantarctic and polar frontal zones south of Tasmania during the ‘SAZ-Sense’ Project." *Marine Chemistry* 148 (January): 63–76. <https://doi.org/10.1016/j.marchem.2012.10.005>.
- Cadenas, E. 1989. "Biochemistry of oxygen toxicity." *Annual review of biochemistry*, vol. 58, no 1, p. 79-110.
- Cairncross, B., and J. Gutzmer. 1997. "The Manganese adventure: The South African Manganese Fields (Associated Ore & Metal Corp. Ltd., Johannesburg).
- Caldeira, K., and P. B. Duffy. 2000. "The role of the Southern Ocean in uptake and storage of anthropogenic carbon dioxide." *Science* 287 (5453): 620–22. <https://doi.org/10.1126/science.287.5453.620>.
- Campbell, D., Hurry, V., Clarke, A. K., Gustafsson, P., and G. Öquist. 1998. "Chlorophyll Fluorescence Analysis of Cyanobacterial Photosynthesis and Acclimation." *Microbiology and Molecular Biology Reviews* 62 (3): 667–83. <https://doi.org/10.1128/MMBR.62.3.667-683.1998>.
- Canfield, D. E., Kristensen, E., and B. Thamdrup. The iron and manganese cycles. In : *Advances in Marine Biology*. Academic Press, 2005. p. 269-312.
- Carranza, M. M., Gille, S. T., Franks, P. J. S., Johnson, K. S., Pinkel, R., and J. B. Girton. 2018. "When mixed layers are not mixed. Storm-driven mixing and bio-optical vertical gradients in mixed layers of the Southern Ocean." *Journal of Geophysical Research: Oceans* 123 (10): 7264–89. <https://doi.org/10.1029/2018JC014416>.

- Cassar, N., Wright, S. W., Thomson, P. G., Trull, T. W., Westwood, K. J., de Salas, M., Davidson, A., Pearce, I., Davies, D. M., and R. J. Matear. 2015. “The relation of mixed-layer net community production to phytoplankton community composition in the Southern Ocean.” *Global Biogeochemical Cycles* 29 (4): 446–62. <https://doi.org/10.1002/2014GB004936>.
- Cheize, M., Planquette, H.F., Fitzsimmons, J.N., Pelleter, E., Sherrell, R.M., Lambert, C., Bucciarelli, E., Sarthou, G., Le Goff, M., Liorzou, C., Cheron, S., Viollier, E. and N. Gayet. 2018. “Contribution of resuspended sedimentary particles to dissolved iron and manganese in the ocean: an experimental study.” *Chemical Geology*, October. <https://doi.org/10.1016/j.chemgeo.2018.10.003>.
- Chisholm, S. W. (2000). Stirring times in the Southern Ocean. *Nature*, 407(6805), 685-686.
- Coale, K. H. 1991. “Effects of iron, manganese, copper, and zinc enrichments on productivity and biomass in the subarctic Pacific.” *Limnology and Oceanography* 36 (8): 1851–1864.
- Conde Pardo, P., Tilbrook, B., Langlais, C., Trull, T. W., and S. R. Rintoul. 2017a. “Carbon uptake and biogeochemical change in the Southern Ocean, south of Tasmania.” *Biogeosciences* 14 (22): 5217–37. <https://doi.org/10.5194/bg-14-5217-2017>.
- Corami, F., Capodaglio, G., Turetta, C., Soggia, F., Magi, E., and M. Grotti. 2005. “Summer distribution of trace metals in the Western sector of the Ross Sea, Antarctica.” *Journal of Environmental Monitoring* 7 (12): 1256. <https://doi.org/10.1039/b507323p>.
- Cowen, J. P., Massoth G. J., and R. A. Feely. n.d. “Scavenging rates of dissolved manganese in a hydrothermal vent plume,” . *Deep Sea Res.* 37:1619–37
- Cullen, J. J. 1982. “The Deep Chlorophyll Maximum: Comparing Vertical Profiles of Chlorophyll *a*.” *Canadian Journal of Fisheries and Aquatic Sciences* 39 (5): 791–803. <https://doi.org/10.1139/f82-108>.
- . 2015. “Subsurface chlorophyll maximum layers: enduring enigma or mystery solved?” *Annual Review of Marine Science* 7 (1): 207–39. <https://doi.org/10.1146/annurev-marine-010213-135111>.
- Cutter, G., Andersson, P., Codispoti, L., Croot, P., Francois, R., Lohan, M. C., Obata, H., and M. R. van der Loeff. 2010. *Sampling and Sample-Handling Protocols for GEOTRACES Cruises*. GEOTRACES.
- Cutter, G. 2017. “Sampling and sample-handling protocols for GEOTRACES Cruises,” 178.
- Davidson, A. T., and H. J. Marchant. 1987. “Binding of manganese by Antarctic *Phaeocystis pouchetii* and the role of bacteria in its release,”. *Marine Biology*, 95, 481-487.
- Davies, S. H., and J. J. Morgan. 1989. “Manganese(II) oxidation kinetics on metal oxide surfaces. *Journal of Colloid and Interface Science*, 1989, vol. 129, no 1, p. 63-77.
- Deppeler, S. L., and A. T. Davidson. 2017. “Southern Ocean phytoplankton in a Changing Climate.” *Frontiers in Marine Science* 4 (February). <https://doi.org/10.3389/fmars.2017.00040>.
- Diaz, J. M., and S. Plummer. 2018. “Production of extracellular reactive oxygen species by phytoplankton: Past and Future Directions.” *Journal of Plankton Research*, September. <https://doi.org/10.1093/plankt/fby039>.
- Dick, G. J., Clement, B. G., Webb, S. M., Fodrie, F. J., Bargar, J. R., and B. M. Tebo. 2009. “Enzymatic microbial Mn(II) oxidation and Mn biooxide production in the Guaymas Basin deep-Sea hydrothermal plume.” *Geochimica et Cosmochimica Acta* 73 (21): 6517–30. <https://doi.org/10.1016/j.gca.2009.07.039>.
- DiTullio, G. R., Grebmeier, J. M., Arrigo, K. R., Lizotte, M. P., Robinson, D. H., Leventer, A., Barry, J. P., VanWoert, M. L., and R. B. Dunbar. 2000. “Rapid and early export of Phaeocystis antarctica blooms in the Ross Sea, Antarctica.” *Nature* 404 (6778): 595–98. <https://doi.org/10.1038/35007061>.
- Ducklow, H., Steinberg, D., and K. Buesseler. 2001. “Upper ocean carbon export and the biological pump.” *Oceanography* 14 (4): 50–58. <https://doi.org/10.5670/oceanog.2001.06>.
- Duprat, L., Corkill, M., Genovese, C., Townsend, A. T., Moreau, S., Meiners, K. M., and D. Lannuzel. 2020. “Nutrient distribution in East Antarctic Summer sea ice: a potential iron contribution from glacial basal melt.” *Journal of Geophysical Research: Oceans* 125 (12). <https://doi.org/10.1029/2020JC016130>.

- Ehrenreich, A., and F. Widdel. 1994. "Anaerobic oxidation of ferrous iron by purple bacteria, a new type of phototrophic metabolism." *Applied and Environmental Microbiology* 60 (12): 4517–26. <https://doi.org/10.1128/aem.60.12.4517-4526.1994>.
- Eriksen, R., Trull, T. W., Davies, D., Jansen, P., Davidson, A. T., Westwood, K., and R. van den Enden. 2018. "Seasonal succession of phytoplankton community structure from autonomous sampling at the Australian Southern Ocean Time Series (SOTS) Observatory." *Marine Ecology Progress Series* 589 (February): 13–31. <https://doi.org/10.3354/meps12420>.
- Eyring, V., Gillett, N.P., Achuta, Rao, K.M., Barimalala, R., Barreiro, Parrillo, M., Bellouin, N., Cassou, C., Durack, P.J., Kosaka, Y., McGregor, S., Min, S., Morgenstern, O., and Y. Sun, 2021: Human Influence on the Climate System. In *Climate Change 2021: The Physical Science Basis. Contribution of Working Group I to the Sixth Assessment Report of the Intergovernmental Panel on Climate Change* [Masson-Delmotte, V., P. Zhai, A. Pirani, S.L. Connors, C. Péan, S. Berger, N. Caud, Y. Chen, L. Goldfarb, M.I. Gomis, M. Huang, K. Leitzell, E. Lonnoy, J.B.R. Matthews, T.K. Maycock, T. Waterfield, O. Yelekçi, R. Yu, and B. Zhou (eds.)]. Cambridge University Press. In Press.
- Ferreira, F., and N. A. Straus. 1994. "Iron deprivation in cyanobacteria." *Journal of Applied Phycology* 6 (2): 199–210. <https://doi.org/10.1007/BF02186073>.
- Findlay, A. J., Gartman, A., Shaw, T. J., and G. W. 2015. "Trace metal concentration and partitioning in the first 1.5 m of hydrothermal vent plumes along the Mid-Atlantic Ridge: TAG, Snakepit, and Rainbow." *Chemical Geology* 412 (September): 117–31. <https://doi.org/10.1016/j.chemgeo.2015.07.021>.
- Fischer, W. W., Hemp, J., and J. E. Johnson. 2015. "Manganese and the evolution of photosynthesis." *Origins of Life and Evolution of Biospheres* 45 (3): 351–57. <https://doi.org/10.1007/s11084-015-9442-5>.
- Fischer, W. W., and A. H. Knoll. 2009. "An iron shuttle for deepwater silica in Late Archean and early Paleoproterozoic iron formation." *Geological Society of America Bulletin* preprint (2008): 1. <https://doi.org/10.1130/B26328.1>.
- Fitzsimmons, J. N., John, S. G., Marsay, C. M., Hoffman, C. L., Nicholas, S. L., Toner, B. M., German, C. R., and R. M. Sherrell. 2017. "Iron persistence in a distal hydrothermal plume supported by dissolved–particulate exchange." *Nature Geoscience* 10 (3): 195–201. <https://doi.org/10.1038/ngeo2900>.
- Fitzwater, S.E, K.S Johnson, R.M Gordon, K.H Coale, and W.O Smith. 2000a. "Trace metal concentrations in the Ross Sea and their relationship with nutrients and phytoplankton growth." *Deep Sea Research Part II: Topical Studies in Oceanography* 47 (15–16): 3159–79. [https://doi.org/10.1016/S0967-0645\(00\)00063-1](https://doi.org/10.1016/S0967-0645(00)00063-1).
- Foppert, A., Rintoul, S. R., Purkey, S. G., Zilberman, N., Kobayashi, T., Sallée, J-B., Wijk, E. M., and L. O. Wallace. 2021. "Deep Argo Reveals Bottom Water Properties and Pathways in the Australian-Antarctic Basin." *Journal of Geophysical Research: Oceans* 126 (12). <https://doi.org/10.1029/2021JC017935>.
- Fourquez, M., Bressac, M., Deppeler, S. L., Ellwood, M., Obernosterer, I., Trull, T. W., and P. W. Boyd. 2020. "Microbial competition in the subpolar Southern Ocean: An Fe–C Co-Limitation Experiment." *Frontiers in Marine Science* 6 (January): 776. <https://doi.org/10.3389/fmars.2019.00776>.
- Frew, R., Bowie, A. R., Croot, P., and S. Pickmere. 2001. "Macronutrient and trace-metal geochemistry of an in situ iron-induced Southern Ocean bloom." *Deep Sea Research Part II: Topical Studies in Oceanography* 48 (11–12): 2467–2481.
- Fridovich, I. 1997. "Superoxide anion radical (O[•]2), Superoxide Dismutases, and Related Matters." *Journal of Biological Chemistry* 272 (30): 18515–17. <https://doi.org/10.1074/jbc.272.30.18515>.
- . 1998. "Oxygen toxicity: a radical explanation". *Journal of Experimental Biology*, 201, 1203–1209.
- Gao, K, Helbling, E. W., Häder, D. P., and D. Hutchins. 2012. "Responses of marine primary producers to interactions between ocean acidification, solar radiation, and warming." *Marine Ecology Progress Series* 470 (December): 167–89. <https://doi.org/10.3354/meps10043>.

- Gao, X., Bowler, C., and E. Kazamia. 2021. "Iron metabolism strategies in diatoms." Edited by Janneke Balk. *Journal of Experimental Botany* 72 (6): 2165–80. <https://doi.org/10.1093/jxb/eraa575>.
- Gerringa, L.J.A., Blain, S., Laan, P., Sarthou, G., Veldhuis, M.J.W., Brussaard, C.P.D., Viollier, E., and K.R. Timmermans. 2008. "Fe-binding dissolved organic ligands near the Kerguelen Archipelago in the Southern Ocean (Indian Sector)." *Deep Sea Research Part II: Topical Studies in Oceanography* 55 (5–7): 606–21. <https://doi.org/10.1016/j.dsr2.2007.12.007>.
- Godwin, C. M., Zehnpfennig, J. R., and D. R. Learman. 2020. "Biotic and abiotic mechanisms of manganese(II) oxidation in Lake Erie." *Frontiers in Environmental Science* 8 (May). <https://doi.org/10.3389/fenvs.2020.00057>.
- Goldberg, E. D. 1954. "Marine Geochemistry 1. Chemical Scavengers of the Sea." *The Journal of Geology* 62 (3): 249–65. <https://doi.org/10.1086/626161>.
- Gomi, Y., Fukuchi, M., and A. Taniguchi. 2010. "Diatom assemblages at subsurface chlorophyll maximum layer in the Eastern Indian sector of the Southern Ocean in summer." *Journal of Plankton Research* 32 (7): 1039–50. <https://doi.org/10.1093/plankt/fbq031>.
- Gordon, A. L. and P. Tchernia. 1972. Waters of the continental margin off Adelie coast, Antarctica. Antarctic Oceanology II, Antarctic Research Series 19, American Geophysical Union, pp. 59-69.
- Greene, R. M., Geider, R. J., Kolber, Z., and P. G. Falkowski. 1992. "Iron-induced changes in light harvesting and photochemical energy conversion processes in eukaryotic marine algae." *Plant Physiology* 100 (2): 565–75. <https://doi.org/10.1104/pp.100.2.565>.
- Griffiths, F. B., Bates, T. S., Quinn, P. K., Clementson, L. A., and J. S. Parslow. 1999. "Oceanographic context of the first Aerosol Characterization Experiment (ACE 1): A physical, chemical, and biological overview." *Journal of Geophysical Research: Atmospheres* 104 (D17): 21649–71. <https://doi.org/10.1029/1999JD900386>.
- Grotti, M., Soggia, F., Ianni, C., and R. Frache. 2005. "Trace metals distributions in coastal sea ice of Terra Nova Bay, Ross Sea, Antarctica," *Antarctic Science*, 2005, vol. 17, no 2, p. 289-300.
- Gruber, N., Gloor, M., Mikaloff Fletcher, S. E., Doney, S. C., Dutkiewicz, S., Follows, M. J., Gerber, M., Jacobson, A. R., Joos, F., Lindsay, K., Menemenlis, D., Mouchet, A., Muller, S. A. Sarmiento, J. L., and T. Takahasi. 2009. "Oceanic sources, sinks, and transport of atmospheric CO₂." *Global Biogeochemical Cycles* 23 (1): n/a-n/a. <https://doi.org/10.1029/2008GB003349>.
- Häder, D.-P., Williamson, C. E., Wängberg, S.-Å., Rautio, M., Rose, K. C., Gao, Kunshan, Walter Helbling, E. Sinha, R. P., and R. Worrest. 2015. "Effects of UV radiation on aquatic ecosystems and interactions with other environmental factors." *Photochemical & Photobiological Sciences* 14 (1): 108–26. <https://doi.org/10.1039/C4PP90035A>.
- Halfter, S., Cavan, E. L., Butterworth, P., Swadling, K. M., and P. W. Boyd. 2021. "'Sinking Dead'—How zooplankton carcasses contribute to particulate organic carbon flux in the Subantarctic Southern Ocean." *Limnology and Oceanography*, November, Ino.11971. <https://doi.org/10.1002/lno.11971>.
- Henley, S. F., Cavan, E. L., Fawcett, S. E., Kerr, R., Monteiro, T., Sherrell, R. M., Bowie, A. R., Boyd, P. W., Barnes, . K. A., Schoss, I. R., Marshall, T., Flynn, R., and S. Smith. 2020. "Changing biogeochemistry of the Southern Ocean and its ecosystem implications." *Frontiers in Marine Science* 7 (July): 581. <https://doi.org/10.3389/fmars.2020.00581>.
- Herndl, G. J., and T. Reinthaler. 2013. "Microbial control of the dark end of the biological pump." *Nature Geoscience* 6 (9): 718–24. <https://doi.org/10.1038/ngeo1921>.
- Holmes, T. M., Chase, Z., Townsend, A. T., and A. R. Bowie. 2017. "Detection, dispersal and biogeochemical contribution of hydrothermal iron in the ocean," *Marine and Freshwater Research*, 2017, vol. 68, no 12, p. 2184-2204.
- Holm-Hansen, O., Kahru, M., and C. D. Hewes. 2005. "Deep chlorophyll a maxima (DCMs) in pelagic Antarctic Waters. II. Relation to bathymetric features and dissolved iron concentrations." *Marine Ecology Progress Series* 297: 71–81. <https://doi.org/10.3354/meps297071>.

- Hopkinson, B. M., and K. A. Barbeau. 2008. "Interactive influences of iron and light limitation on phytoplankton at subsurface chlorophyll maxima in the Eastern North Pacific." *Limnology and Oceanography* 53 (4): 1303–18. <https://doi.org/10.4319/lo.2008.53.4.1303>.
- Hopkinson, B. M., Mitchell, B. G., Reynolds, R. A., Wang, H., Selph, K. E., Measures, C. I., Hewes, C. D., Holm-Hansen, O., and K. A. Barbeau. 2007. "Iron limitation across chlorophyll gradients in the Southern Drake Passage: Phytoplankton responses to iron addition and photosynthetic indicators of iron stress." *Limnology and Oceanography* 52 (6): 2540–54. <https://doi.org/10.4319/lo.2007.52.6.2540>.
- Hoppe, C.J.M., Klaas, C., Ossebaar, S., Soppa, M.A., Cheah, W., Laglera, L.M., Santos-Echeandia, J., Rost, B., Wolf-Gladrow, D. A., Bracher, A., Hoppema, M., Strass, V., and S. Trimborn. 2017. "Controls of primary production in two phytoplankton blooms in the Antarctic Circumpolar Current." *Deep Sea Research Part II: Topical Studies in Oceanography* 138 (April): 63–73. <https://doi.org/10.1016/j.dsr2.2015.10.005>.
- Horton, P., Ruban, A. V., and R. G. Walters. 1996. "Regulation of light harvesting in green plants." *Annual Review of Plant Physiology and Plant Molecular Biology* 47 (1): 655–84. <https://doi.org/10.1146/annurev.arplant.47.1.655>.
- Hudson, R. J. M., and F. M. M. Morel. 1990. "Iron transport in marine phytoplankton: Kinetics of cellular and medium coordination reactions." *Limnology and Oceanography* 35 (5): 1002–20. <https://doi.org/10.4319/lo.1990.35.5.1002>.
- Hulten, M. M. P. van, Middag, R., Dutay, J.-C., de Baar, H. J. W., Roy-Barman, M., Gehlen, M., Tagliabue, A., and A. Sterl. 2017. "Manganese in the West Atlantic Ocean in context of the first global ocean circulation model of manganese." *Biogeosciences* 14 (5): 1123–52. <https://doi.org/10.5194/bg-14-1123-2017>.
- Hutchins, D. A., Sedwick, P. N., DiTullio, G. R., Boyd, P. W., Quéguiner, B., Griffiths, F. B., and C. Crossley. 2001. "Control of phytoplankton growth by iron and silicic acid availability in the Subantarctic Southern Ocean: Experimental results from the SAZ Project." *Journal of Geophysical Research: Oceans* 106 (C12): 31559–72. <https://doi.org/10.1029/2000JC000333>.
- Ishii, M., Inoue, H. Y., Matsueda, H., and E. Tanoue. 1998. "Close coupling between seasonal biological production and dynamics of dissolved inorganic carbon in the Indian Ocean sector and the Western Pacific Ocean sector of the Antarctic Ocean." *Deep Sea Research Part I: Oceanographic Research Papers* 45 (7): 1187–1209. [https://doi.org/10.1016/S0967-0637\(98\)00010-7](https://doi.org/10.1016/S0967-0637(98)00010-7).
- Jackson, G. A. 2005. "Role of algal aggregation in vertical carbon export during SOIREE and in other low biomass environments." *Geophysical Research Letters* 32 (13): L13607. <https://doi.org/10.1029/2005GL023180>.
- Jacobs, S. S. 1991. "On the nature and significance of the Antarctic Slope Front." *Marine Chemistry* 35 (1–4): 9–24. [https://doi.org/10.1016/S0304-4203\(09\)90005-6](https://doi.org/10.1016/S0304-4203(09)90005-6).
- Jamieson, D, B Chance, E Cadenas, and A. Boveris. 1986. "The relation of free radical production to hyperoxia," *Annual review of physiology*, 1986, vol. 48, no 1, p. 703-719.
- Jin, X., Gruber, N., Dunne, J. P., Sarmiento, J. L., and R. A. Armstrong. 2006. "Diagnosing the contribution of phytoplankton functional groups to the production and export of particulate organic carbon, CaCO₃, and opal from global nutrient and alkalinity distributions." *Global Biogeochemical Cycles* 20 (2): n/a-n/a. <https://doi.org/10.1029/2005GB002532>.
- Johnson, Z. I., Shyam, R., Ritchie, A. E., Mioni, C., Lance, V. P., Murray, J. W., and E. R. Zinser. 2010. "The effect of iron- and light-limitation on phytoplankton communities of deep chlorophyll maxima of the Western Pacific Ocean." *Journal of Marine Research* 68 (2): 283–308. <https://doi.org/10.1357/002224010793721433>.
- Kanna, N., Lannuzel, D., van der Merwe, Pier., and J. Nishioka. 2020. "Size fractionation and bioavailability of iron released from melting sea ice in a Subpolar marginal sea." *Marine Chemistry* 221 (April): 103774. <https://doi.org/10.1016/j.marchem.2020.103774>.
- Kasting, J. F., and J.L Siefert. 2002. "Life and the evolution of Earth's atmosphere." *Science* 296 (5570): 1066–68. <https://doi.org/10.1126/science.1071184>.
- Kimura, N. 2004. Sea ice motion in response to surface wind and ocean current in the Southern Ocean. *Journal of the Meteorological Society of Japan*. Ser. II, 82(4), 1223-1231. doi:10.2151/jmsj.2004.1223.

- Kirschvink, J. L., Gaidos, E. J., Bertani, L. E., Beukes, N. J., Gutzmer, J., Maepa, L. N., and R. E. Steinberger. 2000. "Paleoproterozoic snowball Earth: Extreme climatic and geochemical global change and its biological consequences." *Proceedings of the National Academy of Sciences* 97 (4): 1400–1405. <https://doi.org/10.1073/pnas.97.4.1400>.
- Kirschvink, J. L., and R. E. Kopp. 2008. "Paleoproterozoic ice houses and the evolution of oxygen-mediating enzymes: The case for a late origin of Photosystem II." *Philosophical Transactions of the Royal Society B: Biological Sciences* 363 (1504): 2755–65. <https://doi.org/10.1098/rstb.2008.0024>.
- Klinkhammer, G., and A. Hudson. 1986a. "Dispersal patterns for hydrothermal plumes in the South Pacific using manganese as a tracer." *Earth and Planetary Science Letters* 79 (3–4): 241–49. [https://doi.org/10.1016/0012-821X\(86\)90182-2](https://doi.org/10.1016/0012-821X(86)90182-2).
- Klinkhammer, G. P., and M. L. Bender. 1980. "The distribution of manganese in the Pacific Ocean." *Earth and Planetary Science Letters* 46 (3): 361–384.
- Koblížek, M., Kaftan, D., and L. Nedbal. 2001. "On the relationship between the non-photochemical quenching of the chlorophyll fluorescence and the Photosystem II light harvesting efficiency. A repetitive flash fluorescence induction study," *Photosynthesis Research*, 2001, vol. 68, no 2, p. 141-152.
- Konovalov, S., Samodurov, A., Oguz, T., and L. Ivanov. 2004. "Parameterization of iron and manganese cycling in the Black Sea suboxic and anoxic environment." *Deep Sea Research Part I: Oceanographic Research Papers* 51 (12): 2027–45. <https://doi.org/10.1016/j.dsr.2004.08.005>.
- Kopp, R. E., Kirschvink, J. L., Hilburn I. A., and C. Z. Nash. 2005. "The Paleoproterozoic snowball Earth: A climate disaster triggered by the evolution of oxygenic photosynthesis." *Proceedings of the National Academy of Sciences* 102 (32): 11131–36. <https://doi.org/10.1073/pnas.0504878102>.
- Kostka, J. E., Luther, G. W., and K. H. Nealson. 1995. "Chemical and biological reduction of Mn (III) -pyrophosphate complexes: Potential importance of dissolved Mn (III) as an environmental oxidant," *Geochimica et Cosmochimica Acta*, 1995, vol. 59, no 5, p. 885-894.
- Lago, V., and M. H. England. 2019. "Projected slowdown of Antarctic Bottom Water formation in response to amplified meltwater contributions." *Journal of Climate* 32 (19): 6319–35. <https://doi.org/10.1175/JCLI-D-18-0622.1>.
- Landing, W. M., and K. W. Bruland. 1980. "Manganese in the North Pacific." *Earth and Planetary Science Letters* 49 (1): 45–56. [https://doi.org/10.1016/0012-821X\(80\)90149-1](https://doi.org/10.1016/0012-821X(80)90149-1).
- Landing, W. M., and K. W. Bruland. 1987. "The contrasting biogeochemistry of iron and manganese in the Pacific Ocean," *Geochimica et Cosmochimica Acta*, 1987, vol. 51, no 1, p. 29-43.
- Landschützer, P., Gruber, N., Bakker, D. C. E., and U. Schuster. 2014. "Recent variability of the global ocean carbon sink." *Global Biogeochemical Cycles* 28 (9): 927–49. <https://doi.org/10.1002/2014GB004853>.
- Lannuzel, D., Bowie, A. R., van der Merwe, P. C., Townsend, A. T., and V. Schoemann. 2011. "Distribution of dissolved and particulate metals in Antarctic sea ice." *Marine Chemistry* 124 (1–4): 134–46. <https://doi.org/10.1016/j.marchem.2011.01.004>.
- Lannuzel, D., Bowie, A. R., Remenyi, T., Lam, P., Townsend, A. T., Ibanami, E., Butler, E., Wagener, T., and V. Schoemann. 2011a. "Distributions of dissolved and particulate iron in the Sub-Antarctic and Polar Frontal Southern Ocean (Australian Sector)." *Deep Sea Research Part II: Topical Studies in Oceanography* 58 (21–22): 2094–2112. <https://doi.org/10.1016/j.dsr2.2011.05.027>.
- Lannuzel, D., Grotti, M., Abelmoschi, M. L., and P. van der Merwe. 2015. "Organic ligands control the concentrations of dissolved iron in Antarctic sea ice." *Marine Chemistry* 174 (August): 120–30. <https://doi.org/10.1016/j.marchem.2015.05.005>.
- Lannuzel, D., van der Merwe, P. C., Townsend, A. T., and A. R. Bowie. 2014. "Size fractionation of iron, manganese and aluminium in Antarctic fast ice reveals a lithogenic origin and low iron solubility." *Marine Chemistry* 161 (April): 47–56. <https://doi.org/10.1016/j.marchem.2014.02.006>.
- Latour, P., Wuttig, K., van der Merwe, P. C., Strzepak, R. F., Gault-Ringold, M., Townsend, A. T., Holmes, T. M., Corkill, M., and A. R. Bowie. 2021. "Manganese biogeochemistry in the

- Southern Ocean, from Tasmania to Antarctica.” *Limnol Oceanogr*, 66: 2547-2562. <https://doi.org/10.1002/lno.11772>.
- Lenton, A., Tilbrook, B., Law, R., Bakker, D. C. E., Doney, S. C., Gruber, N., Hoppema, M., Ishii, M., Lovenduski, N. S., and R. J., Matear. 2013. “Sea-Air CO₂ fluxes in the Southern Ocean for the period 1990-2009.” *Biogeosciences Discussions* 10: 285–333.
- Lesser, M. P. 2006. “Oxidative stress in marine environments: Biochemistry and Physiological Ecology.” *Annual Review of Physiology* 68 (1): 253–78. <https://doi.org/10.1146/annurev.physiol.68.040104.110001>.
- Liniger, G., Strutton, P. G., Lannuzel, D., and S Moreau. 2020. “Calving event led to changes in phytoplankton bloom phenology in the Mertz Polynya, Antarctica.” *Journal of Geophysical Research: Oceans* 125 (11). <https://doi.org/10.1029/2020JC016387>.
- Lueder, U., Jørgensen, B. B., Kappler, A., and C. Schmidt. 2020. “Photochemistry of iron in aquatic environments.” *Environmental Science: Processes & Impacts* 22 (1): 12–24. <https://doi.org/10.1039/C9EM00415G>.
- Luther, G. W. 2005. “Manganese(II) oxidation and Mn(IV) reduction in the environment—Two one-electron transfer steps versus a single two-electron step.” *Geomicrobiology Journal* 22 (3–4): 195–203. <https://doi.org/10.1080/01490450590946022>.
- . 2010. “The role of one- and two-electron transfer reactions in forming thermodynamically unstable intermediates as barriers in multi-electron redox reactions.” *Aquatic Geochemistry* 16 (3): 395–420. <https://doi.org/10.1007/s10498-009-9082-3>.
- . 2016. *Inorganic Chemistry for Geochemistry and Environmental Sciences: Fundamentals and Applications*. Chichester, UK: John Wiley & Sons. <https://doi.org/10.1002/9781118851432>.
- Luther, G. W., Madison, A. S., Mucci, A., Sundby, B., and V. E. Oldham. 2015a. “A kinetic approach to assess the strengths of ligands bound to soluble Mn(III).” *Marine Chemistry* 173 (July): 93–99. <https://doi.org/10.1016/j.marchem.2014.09.006>.
- Lynn, R. J., and J. L. Reid. 1968. “Characteristics and circulation of deep and abyssal waters.” *Deep Sea Research and Oceanographic Abstracts* 15 (5): 577–98. [https://doi.org/10.1016/0011-7471\(68\)90064-8](https://doi.org/10.1016/0011-7471(68)90064-8).
- Lyons, T. W., Reinhard, C. T., and N. J. Planavsky. 2014. “The rise of oxygen in Earth’s early ocean and atmosphere.” *Nature* 506 (7488): 307–15. <https://doi.org/10.1038/nature13068>.
- Madison, A. S., Tebo, B. M., Mucci, A., Sundby, B., and G. W. Luther. 2013. “Abundant porewater Mn(III) is a major component of the sedimentary redox system.” *Science* 341 (6148): 875–78. <https://doi.org/10.1126/science.1241396>.
- Madison, A. S., Tebo, B. M., and G. W. Luther. 2011. “Simultaneous determination of soluble manganese(III), manganese(II) and total manganese in natural (pore)waters.” *Talanta* 84 (2): 374–81. <https://doi.org/10.1016/j.talanta.2011.01.025>.
- Marie, D., Partensky, F., Vaulot, D., and C. Brussaard. 1999. “Enumeration of phytoplankton, bacteria, and viruses in marine samples.” *Current Protocols in Cytometry* 10 (1). <https://doi.org/10.1002/0471142956.cy1111s10>.
- Marinov, I., Doney, S. C., and I. D. Lima. 2010. “Response of ocean phytoplankton community structure to climate change over the 21st century: Partitioning the effects of nutrients, temperature and light.” *Biogeosciences* 7 (12): 3941–59. <https://doi.org/10.5194/bg-7-3941-2010>.
- Martin, J. H. 1990. “Glacial - Interglacial CO₂ Change: The Iron Hypothesis.” *Paleoceanography* 5 (1): 1–13. <https://doi.org/10.1029/PA005i001p00001>.
- Martin, J. H. 1991. “Iron, Liebig’s Law, and the Greenhouse.” *Oceanography* 4 (2): 52–55. <https://doi.org/10.5670/oceanog.1991.02>.
- Martin, J. H., Fitzwater, S. E., and R. M. Gordon. 1990. Iron deficiency limits phytoplankton growth in Antarctic waters, *Global Biogeochemical Cycles*, 4(1), 5– 12, doi:10.1029/GB004i001p00005.
- Martin, J. H., and R. M. Gordon. 1988. “Northeast Pacific iron distributions in relation to phytoplankton productivity.” *Deep Sea Research Part A. Oceanographic Research Papers* 35 (2): 177–96. [https://doi.org/10.1016/0198-0149\(88\)90035-0](https://doi.org/10.1016/0198-0149(88)90035-0).

- Martin, J. H., R. M. Gordon, Steve Fitzwater, and William W. Broenkow. 1989. "Vertex: Phytoplankton/iron studies in the Gulf of Alaska." *Deep Sea Research Part A. Oceanographic Research Papers* 36 (5): 649–80. [https://doi.org/10.1016/0198-0149\(89\)90144-1](https://doi.org/10.1016/0198-0149(89)90144-1).
- Martínez, R. 2007. "Effects of ultraviolet radiation on protein content, respiratory electron transport system (ETS) activity and superoxide dismutase (SOD) activity of Antarctic plankton." *Polar Biology* 30 (9): 1159–72. <https://doi.org/10.1007/s00300-007-0273-3>.
- May, B. P., and P. P. Dennis. 1989. "Evolution and regulation of the gene encoding superoxide dismutase from the Archaeobacterium Halobacterium Cutirubrum." *Journal of Biological Chemistry* 264 (21): 12253–58. [https://doi.org/10.1016/S0021-9258\(18\)63850-5](https://doi.org/10.1016/S0021-9258(18)63850-5).
- McAdam, M. E., Levelle, F., Fox, R. A., and E. M. Fielden. 1977. "A pulse-radiolysis study of the manganese-containing superoxide dismutase from *Bacillus Stearothermophilus*." *Biochemical Journal* 165 (1): 81–87. <https://doi.org/10.1042/bj1650081>.
- McCain, J. S. P. and E. M., Bertrand. 2022. Phytoplankton antioxidant systems and their contributions to cellular elemental stoichiometry. *Limnology and Oceanography Letters*, 7(2), 96-111.
- McEvoy, J. P., and G. W. Brudvig. 2006. "Water-Splitting Chemistry of Photosystem II." *Chemical Reviews* 106 (11): 4455–83. <https://doi.org/10.1021/cr0204294>.
- McKinley, G. A., Pilcher, D. J., Fay, A. R., Lindsay, K., Long, M. C., and N. S. Lovenduski. 2016. "Timescales for detection of trends in the ocean carbon sink." *Nature* 530 (7591): 469–72. <https://doi.org/10.1038/nature16958>.
- Measures, C.I., Brown, M.T., Selph, K.E., Apprill, A., Zhou, M., Hatta, M., and W.T. Hiscock. 2013. "The influence of shelf processes in delivering dissolved iron to the HNLC waters of the Drake Passage, Antarctica." *Deep Sea Research Part II: Topical Studies in Oceanography* 90 (June): 77–88. <https://doi.org/10.1016/j.dsr2.2012.11.004>.
- Metzl, N., Tilbrook, B., and A. Poisson. 1999. "The annual fCO₂ cycle and the air-sea CO₂ flux in the Sub-Antarctic Ocean." *Tellus B* 51 (4): 849–61. <https://doi.org/10.1034/j.1600-0889.1999.t01-3-00008.x>.
- Middag, R., de Baar, H. J. W., Klunder, M. B., and P. Laan. 2013. "Fluxes of dissolved aluminum and manganese to the Weddell Sea and indications for manganese co-limitation." *Limnology and Oceanography* 58 (1): 287–300. <https://doi.org/10.4319/lo.2013.58.1.0287>.
- Middag, R., de Baar, H.J.W., Laan, P., Cai, P.H., and J.C. van Ooijen. 2011. "Dissolved manganese in the Atlantic sector of the Southern Ocean." *Deep Sea Research Part II: Topical Studies in Oceanography* 58 (25–26): 2661–77. <https://doi.org/10.1016/j.dsr2.2010.10.043>.
- Mitchell, B. G., Brody, E. A., Holm-Hansen, O., McClain, C., and J. Bishop. 1991. "Light limitation of phytoplankton biomass and macronutrient utilization in the Southern Ocean." *Limnology and Oceanography* 36 (8): 1662–77. <https://doi.org/10.4319/lo.1991.36.8.1662>.
- Moore, C M. 2013. "Processes and patterns of oceanic nutrient limitation." *NATURE GEOSCIENCE*, vol. 6, no 9, p. 701-710.
- Morel, F. M.M., Lam, P. J., and M. A. Saito. 2020a. "Trace metal substitution in marine phytoplankton." *Annual Review of Earth and Planetary Sciences* 48 (1): 491–517. <https://doi.org/10.1146/annurev-earth-053018-060108>.
- Morgan, J. J. 2005. "Kinetics of reaction between O₂ and Mn(II) species in aqueous solutions." *Geochimica et Cosmochimica Acta* 69 (1): 35–48. <https://doi.org/10.1016/j.gca.2004.06.013>.
- Morton, P. L., Landing, W. M., Shiller, A. M., Moody, A., Kelly, T. D., Bizimis, M., Donat, J. R., De Carlo, E. H., and J. Shacat. 2019. "Shelf inputs and lateral transport of Mn, Co, and Ce in the Western North Pacific Ocean." *Frontiers in Marine Science* 6 (September): 591. <https://doi.org/10.3389/fmars.2019.00591>.
- Murray, J. W. 1975. "The interaction of metal ions at the manganese dioxide-solution interface." *Geochimica et Cosmochimica Acta* 39 (4): 505–19. [https://doi.org/10.1016/0016-7037\(75\)90103-9](https://doi.org/10.1016/0016-7037(75)90103-9).
- Nelson, D. M., and W. Smith. 1991. "Sverdrup revisited: Critical depths, maximum chlorophyll levels, and the control of Southern Ocean productivity by the irradiance-mixing regime." *Limnology and Oceanography* 36 (8): 1650–61. <https://doi.org/10.4319/lo.1991.36.8.1650>.

- Nico, P. S., Anastasio, C., and R. J. Zasoski. 2002. "Rapid photo-oxidation of Mn(II) mediated by humic substances." *Geochimica et Cosmochimica Acta* 66 (23): 4047–56. [https://doi.org/10.1016/S0016-7037\(02\)01001-3](https://doi.org/10.1016/S0016-7037(02)01001-3).
- Nisbet, E. G., and N. H. Sleep. 2001. "The habitat and nature of early life." *Nature* 409 (6823): 1083–91. <https://doi.org/10.1038/35059210>.
- Oldham, V. E., Chmiel, R., Hansel, C. M., DiTullio, G. R., Rao, D., and M. Saito. 2021. "Inhibited manganese oxide formation hinders cobalt scavenging in the Ross Sea." *Global Biogeochemical Cycles* 35 (5). <https://doi.org/10.1029/2020GB006706>.
- Oldham, V. E., Mucci, A., Tebo, B. M., and G. W. Luther. 2017. "Soluble Mn(III)–L complexes are abundant in oxygenated waters and stabilized by humic ligands." *Geochimica et Cosmochimica Acta* 199 (February): 238–46. <https://doi.org/10.1016/j.gca.2016.11.043>.
- Oldham, V. E., Owings, S. M., Jones, M. R., Tebo, B. M., and G. W. Luther. 2015. "Evidence for the presence of strong Mn(III)-binding ligands in the water column of the Chesapeake Bay." *Marine Chemistry* 171 (April): 58–66. <https://doi.org/10.1016/j.marchem.2015.02.008>.
- Orsi, A. H., Whitworth, T., and W. D. Nowlin. 1995. "On the meridional extent and fronts of the Antarctic Circumpolar Current." *Deep Sea Research Part I: Oceanographic Research Papers* 42 (5): 641–73. [https://doi.org/10.1016/0967-0637\(95\)00021-W](https://doi.org/10.1016/0967-0637(95)00021-W).
- Orsi, A. H., and C. L. Wiederwohl. 2009. "A recount of Ross Sea waters." *Deep Sea Research Part II: Topical Studies in Oceanography* 56 (13–14): 778–95. <https://doi.org/10.1016/j.dsr2.2008.10.033>.
- Paasche, E. 1973. "Silicon and the Ecology of Marine Plankton Diatoms. I. *Thalassiosira Pseudonana* (Cyclotella Nana) Grown in a Chemostat with Silicate as Limiting Nutrient." *Marine Biology* 19 (2): 117–26. <https://doi.org/10.1007/BF00353582>.
- Pakhomova, S. V., Hall, P. O.J., Kononets, M. Y., Rozanov, A. G., Tengberg, A., and A. V. Vershinin. 2007. "Fluxes of iron and manganese across the sediment–water interface under various redox conditions." *Marine Chemistry* 107 (3): 319–31. <https://doi.org/10.1016/j.marchem.2007.06.001>.
- Parslow, J. S., Boyd, P. W., Rintoul, S. R., and F. B. Griffiths. 2001. "A persistent subsurface chlorophyll maximum in the Interpolar Frontal Zone south of Australia: seasonal progression and implications for phytoplankton-light-nutrient interactions." *Journal of Geophysical Research: Oceans* 106 (C12): 31543–57. <https://doi.org/10.1029/2000JC000322>.
- Patel, R. S., Llort, J., Strutton, P. G., Phillips, H. E., Moreau, S., Conde Pardo, P., and A. Lenton. 2020. "The biogeochemical structure of Southern Ocean mesoscale eddies." *Journal of Geophysical Research: Oceans*, June, e2020JC016115. <https://doi.org/10.1029/2020JC016115>.
- Patel, R. S., Phillips, H. E., Strutton, P. G., Lenton, A., and J. Llort. 2019. "Meridional heat and salt transport across the Subantarctic front by cold-core eddies." *Journal of Geophysical Research: Oceans* 124 (2): 981–1004. <https://doi.org/10.1029/2018JC014655>.
- Pausch, F., Bischof, K., and S. Trimborn. 2019. "Iron and manganese co-limit growth of the Southern Ocean diatom *Chaetoceros debilis*." Edited by Bruno Jesus. *PLOS ONE* 14 (9): e0221959. <https://doi.org/10.1371/journal.pone.0221959>.
- Peers, G., and N. M. Price. 2004. "A role for manganese in superoxide dismutases and growth of iron-deficient diatoms." *Limnology and Oceanography* 49 (5): 1774–1783.
- Perelman, A., Dubinsky, Z., and R. Martínez. 2006. "Temperature dependence of superoxide dismutase activity in plankton." *Journal of Experimental Marine Biology and Ecology* 334 (2): 229–35. <https://doi.org/10.1016/j.jembe.2006.02.009>.
- Perron, M. M.G., Proemse, B. C., Strzelec, M., Gault-Ringold, M., Boyd, P. W., Sanz Rodriguez, E., Paull, B., and A. R. Bowie. 2020. "Origin, transport and deposition of aerosol iron to Australian coastal waters." *Atmospheric Environment* 228 (May): 117432. <https://doi.org/10.1016/j.atmosenv.2020.117432>.
- Petrou, K., Hassler, C. S., Doblin, M. A., Shelly, K., Schoemann, V., van den Enden, R., Wright, S., and P. J. Ralph. 2011. "Iron-limitation and high light stress on phytoplankton populations from the Australian Sub-Antarctic Zone (SAZ)." *Deep Sea Research Part II: Topical Studies in Oceanography* 58 (21–22): 2200–2211. <https://doi.org/10.1016/j.dsr2.2011.05.020>.

- Planavsky, N. J., Asael, D., Hofmann, A., Reinhard, C. T., Lalonde, S. V., Knudsen, A., Wang, X., Ossa Ossa, F., Pecoits, E., Smith, A. J. B., Beukes, N., J., Bekker, A., Johnson, T. M., Konhauser, K. O., Lyons, T. W., and O. J. Rouxel. "Evidence for oxygenic photosynthesis half a billion years before the Great Oxidation Event." *Nature Geoscience* 7 (4): 283–86. <https://doi.org/10.1038/ngeo2122>.
- R Core Team (2020). R: A language and environment for statistical computing. R Foundation for Statistical Computing, Vienna, Austria. URL <https://www.R-project.org/>.
- Raven, J. A. 1990. "Predictions of Mn and Fe use efficiencies of phototrophic growth as a function of light availability for growth and of C assimilation pathway," *New Phytologist*, 1990, vol. 116, no 1, p. 1-18.19.
- Raven, J. A, Evans, M. C. W., and R. E. Korb. 1999. "The role of trace metals in photosynthetic electron transport in O₂-evolving organisms," 39.
- Rees, C., Pender, L., Sherrin, K., Schwanger, C., Hughes, P., Tibben, S., Marouchos, A., and M. Rayner. 2018. "Methods for reproducible shipboard SFA nutrient measurement using RMNS and automated data processing." *Limnology and Oceanography: Methods*, December. <https://doi.org/10.1002/lom3.10294>.
- Rembauville, M., Blain, S., Armand, L., Quéguiner, B., and I. Salter. 2015. "Export fluxes in a naturally iron-fertilized area of the Southern Ocean – Part 2: Importance of Diatom Resting Spores and Faecal Pellets for Export." *Biogeosciences* 12 (11): 3171–95. <https://doi.org/10.5194/bg-12-3171-2015>.
- Rembauville, M., Blain, S., Caparros, J., and I. Salter. 2016. "Particulate matter stoichiometry driven by microplankton community structure in summer in the Indian sector of the Southern Ocean." *Limnology and Oceanography* 61 (4): 1301–21. <https://doi.org/10.1002/lno.10291>.
- Rigual-Hernández, A. S., Trull, T. W., Bray, S. G., Closset, I., and L. K. Armand. 2015. "Seasonal dynamics in diatom and particulate export fluxes to the deep sea in the Australian sector of the Southern Antarctic Zone." *Journal of Marine Systems* 142 (February): 62–74. <https://doi.org/10.1016/j.jmarsys.2014.10.002>.
- Rintoul, S. R. 1998. "On the origin and influence of Adélie Land Bottom Water." In *Antarctic Research Series*, edited by Stanley S. Jacobs and Ray F. Weiss, 151–71. Washington, D. C.: American Geophysical Union. <https://doi.org/10.1029/AR075p0151>.
- . 2018. "The global influence of localized dynamics in the Southern Ocean." *Nature* 558 (7709): 209–18. <https://doi.org/10.1038/s41586-018-0182-3>.
- Rintoul, S. R., and J. L. Bullister. 1999. "A late winter hydrographic section from Tasmania to Antarctica." *Deep Sea Research Part I: Oceanographic Research Papers* 46 (8): 1417–1454.
- Rintoul, S. R., and T. W. Trull. 2001. "Seasonal evolution of the mixed layer in the Subantarctic Zone south of Australia." *Journal of Geophysical Research: Oceans* 106 (C12): 31447–62. <https://doi.org/10.1029/2000JC000329>.
- Saito, M, A., and T. J. Goepfert. 2008. "Zinc-Cobalt Colimitation of *Phaeocystis Antarctica*." *Limnology and Oceanography* 53 (1): 266–75. <https://doi.org/10.4319/lo.2008.53.1.0266>.
- Saito, M. A., Goepfert, T. J., and J. T. Ritt. 2008a. "Some thoughts on the concept of colimitation: Three definitions and the importance of bioavailability." *Limnology and Oceanography* 53 (1): 276–290.
- Salomon, E., and N. Keren. 2011. "Manganese Limitation Induces Changes in the Activity and in the Organization of Photosynthetic Complexes in the Cyanobacterium *Synechocystis* Sp. Strain PCC 6803." *Plant Physiology* 155 (1): 571–79. <https://doi.org/10.1104/pp.110.164269>.
- Sarmiento, J. L., and N. Gruber. 2002. "Sinks for anthropogenic carbon." *Physics Today* 55 (8): 30–36. <https://doi.org/10.1063/1.1510279>.
- Sarmiento, J. L., Hughes, T. M. C., Stouffer, R. J., and S. Manabe. 1998. "Simulated response of the ocean carbon cycle to anthropogenic climate warming." *Nature* 393 (6682): 245–49. <https://doi.org/10.1038/30455>.
- Sauer, K. 1980. "A role for manganese in oxygen evolution in photosynthesis." *Accounts of Chemical Research* 13 (8): 249–56. <https://doi.org/10.1021/ar50152a001>.
- Schallenberg, C., Strzepak, R. F., Bestley, S., Wojtasiewicz, B. and T. W. Trull. *in prep*. "Iron limitation drives the globally extreme Fluorescence/Chlorophyll ratios of the Southern Ocean".

- Scharek, R., Van Leeuwe, M. A., and H. JW De Baar. 1997. "Responses of Southern Ocean phytoplankton to the addition of trace metals." *Deep Sea Research Part II: Topical Studies in Oceanography* 44 (1–2): 209–227.
- Schlitzer, R., Anderson, R. F., Masferrer Dodas, E., Lohan, M., Geibert, W., Tagliabue, A., A. R. Bowie, et al. 2018. "The GEOTRACES Intermediate Data Product 2017." *Chemical Geology* 493 (August): 210–23. <https://doi.org/10.1016/j.chemgeo.2018.05.040>.
- Schoemann, V., Wollast, R., Chou, L., and C. Lancelot. 2001. "Effects of photosynthesis on the accumulation of Mn and Fe by *Phaeocystis* colonies." *Limnology and Oceanography* 46 (5): 1065–76. <https://doi.org/10.4319/lo.2001.46.5.1065>.
- Schoffman, H., Lis, H., Shaked, Y., and N. Keren. 2016. "Iron–nutrient interactions within phytoplankton." *Frontiers in Plant Science* 7 (August). <https://doi.org/10.3389/fpls.2016.01223>.
- Sedwick, P. N., and G. R. Di Tullio. 1997. "Regulation of algal bloom in Antarctic shelf waters by the release of iron from melting sea ice." *Geophysical Research Letters* 24 (20): 2515–18. <https://doi.org/0094-8534/97/97 GL-02596505.00>.
- Sedwick, P. N., DiTullio, G. R., and D. J. Mackey. 2000. "Iron and manganese in the Ross Sea, Antarctica: Seasonal iron limitation in Antarctic shelf waters." *Journal of Geophysical Research: Oceans* 105 (C5): 11321–36. <https://doi.org/10.1029/2000JC000256>.
- Sedwick, P.N., Bowie, A.R., and T.W. Trull. 2008. "Dissolved iron in the Australian sector of the Southern Ocean (CLIVAR SR3 Section): Meridional and seasonal trends." *Deep Sea Research Part I: Oceanographic Research Papers* 55 (8): 911–25. <https://doi.org/10.1016/j.dsr.2008.03.011>.
- Sedwick, P.N., Edwards, P.R., Mackey, D.J., Griffiths, F.B., and J.S. Parslow. 1997. "Iron and manganese in surface waters of the Australian Subantarctic region." *Deep Sea Research Part I: Oceanographic Research Papers* 44 (7): 1239–53. [https://doi.org/10.1016/S0967-0637\(97\)00021-6](https://doi.org/10.1016/S0967-0637(97)00021-6).
- Sherrell, R. M., Annett, A. L., Fitzsimmons, J. N., Rocanova, V. J., and M. P. Meredith. 2018. "A 'shallow bathtub ring' of local sedimentary iron input maintains the Palmer Deep biological hotspot on the West Antarctic Peninsula shelf." *Philosophical Transactions of the Royal Society A: Mathematical, Physical and Engineering Sciences* 376 (2122): 20170171. <https://doi.org/10.1098/rsta.2017.0171>.
- Silvano, A., Rintoul, S. R., Peña-Molino, B., and G. D. Williams. 2017. "Distribution of water masses and meltwater on the continental shelf near the Totten and Moscow University ice shelves." *Journal of Geophysical Research: Oceans* 122 (3): 2050–68. <https://doi.org/10.1002/2016JC012115>.
- Smith, A. J. R., Ratnarajah, L., Holmes, T. M., Wuttig, K., Townsend, A. T., Westwood, K., Cox, M., Bell, E., Nicol, S., and D. Lannuzel. 2021. "Circumpolar deep water and shelf sediments support late summer microbial iron remineralization." *Global Biogeochemical Cycles* 35 (11). <https://doi.org/10.1029/2020GB006921>.
- Smith, W. O., Marra, J., Hiscock, M. R., and R. T. Barber. 2000. "The seasonal cycle of phytoplankton biomass and primary productivity in the Ross Sea, Antarctica." *Deep Sea Research Part II: Topical Studies in Oceanography* 47 (15–16): 3119–40. [https://doi.org/10.1016/S0967-0645\(00\)00061-8](https://doi.org/10.1016/S0967-0645(00)00061-8).
- Snow, K., Sloyan, B. M., Rintoul, S. R., Hogg, A. McC., and S. M. Downes. 2016. "Controls on circulation, cross-shelf exchange, and dense water formation in an Antarctic polynya." *Geophysical Research Letters* 43 (13): 7089–96. <https://doi.org/10.1002/2016GL069479>.
- Sokolov, S., and S. R. Rintoul. 2002. "Structure of Southern Ocean Fronts at 140 E." *Journal of Marine Systems* 37 (1–3): 151–184.
- . 2009. "Circumpolar Structure and Distribution of the Antarctic Circumpolar Current Fronts: 1. Mean Circumpolar Paths." *Journal of Geophysical Research* 114 (C11). <https://doi.org/10.1029/2008JC005108>.
- Spreen, G., Kaleschke L. and G. Heygster. 2008. Sea ice remote sensing using AMSR-E 89-GHz channels. *Journal of Geophysical Research: Oceans*, 113(C2). doi:10.1029/2005JC003384.
- Sproviero, E. M., Gascón, J. A., McEvoy, J. P., Brudvig, G. W., and V. S Batista. 2007. "Quantum Mechanics/Molecular Mechanics Structural Models of the Oxygen-Evolving Complex of

- Photosystem II." *Current Opinion in Structural Biology* 17 (2): 173–80.
<https://doi.org/10.1016/j.sbi.2007.03.015>.
- Stallings, W. C., Metzger, A. L., Paitridge, K. A., Fee, J. A., and M. L. Ludwig. 1991. "Structure-function relationships in iron and manganese superoxide dismutases." *Free Radical Research Communications* 12 (1): 259–68. <https://doi.org/10.3109/10715769109145794>.
- Strzepek, R. F., and P. J. Harrison. 2004. "Photosynthetic architecture differs in coastal and oceanic diatoms." *Nature* 431 (7009): 689–92. <https://doi.org/10.1038/nature02954>.
- Strzepek, R. F., Hunter K. A., Frew, R. D., Harrison, P. J., and P. W. Boyd. 2012. "Iron-light interactions differ in Southern Ocean phytoplankton." *Limnology and Oceanography* 57 (4): 1182–1200. <https://doi.org/10.4319/lo.2012.57.4.1182>.
- Strzepek, R. F., Maldonado, M. T., Hunter, K. A., Frew, R. D., and P. W. Boyd. 2011. "Adaptive strategies by Southern Ocean phytoplankton to lessen iron limitation: Uptake of organically complexed iron and reduced cellular iron requirements." *Limnology and Oceanography* 56 (6): 1983–2002. <https://doi.org/10.4319/lo.2011.56.6.1983>.
- Suggett, D. J., MacIntyre, H. L., and R. J. Geider. 2004. "Evaluation of biophysical and optical determinations of light absorption by photosystem II in phytoplankton: Evaluation of light absorption by PSII." *Limnology and Oceanography: Methods* 2 (10): 316–32. <https://doi.org/10.4319/lom.2004.2.316>.
- Suggett, D. J., Moore, C. M., Hickman, A. E., and R. J. Geider. 2009. "Interpretation of fast repetition rate (FRR) fluorescence: signatures of phytoplankton community structure versus physiological state." *Marine Ecology Progress Series* 376 (February): 1–19. <https://doi.org/10.3354/meps07830>.
- Sunda, W. G., Huntsman, S. A., and G. R. Harvey. 1983. "Photoreduction of manganese oxides in seawater and its geochemical and biological implications." *Nature* 301 (5897): 234–36. <https://doi.org/10.1038/301234a0>.
- Sunda, W. G., and S. A. Huntsman. 1983. "Effect of competitive interactions between manganese and copper on cellular manganese and growth in estuarine and oceanic species of the diatom *Thalassiosira* 1, 2." *Limnology and Oceanography* 28 (5): 924–934. <https://doi.org/10.4319/lo.1983.28.5.0924>.
- . 1988. "Effect of sunlight on redox cycles of manganese in the southwestern Sargasso Sea." *Deep Sea Research Part A. Oceanographic Research Papers* 35 (8): 1297–1317. [https://doi.org/10.1016/0198-0149\(88\)90084-2](https://doi.org/10.1016/0198-0149(88)90084-2).
- . 1994. "Photoreduction of manganese oxides in seawater." *Marine Chemistry* 46 (1–2): 133–52. [https://doi.org/10.1016/0304-4203\(94\)90051-5](https://doi.org/10.1016/0304-4203(94)90051-5).
- . 1995. "Iron uptake and growth limitation in oceanic and coastal phytoplankton." *Marine Chemistry* 50 (1–4): 189–206. [https://doi.org/10.1016/0304-4203\(95\)00035-P](https://doi.org/10.1016/0304-4203(95)00035-P).
- . 1997. "Interrelated influence of iron, light and cell size on marine phytoplankton growth." *Nature* 390 (6658): 389–92. <https://doi.org/10.1038/37093>.
- Sundby, B., Anderson, L. G., and J. Hall. 1986. "The effect of oxygen on release and uptake of cobalt, manganese, iron and phosphate at the sediment-water interface," *Geochimica et Cosmochimica Acta*, 1986, vol. 50, no 6, p. 1281-1288.
- Sung, W. M., and J. J. Morgan. 1981. "Oxidative removal of Mn(II) from solution catalysed by the FeOOH (lepidocrocite) surface." *Geochimica et Cosmochimica Acta*, 1981, vol. 45, no 12, p. 2377-2383.
- Tagliabue, A., Bowie, A. R., Holmes, T. M., Latour, P., van der Merwe, P. C., East, M., Wuttig, K., and J. A. Resing. *In press*. "Constraining the contribution of hydrothermal iron to Southern Ocean export production using deep ocean iron observations." *Frontiers in Marine Science*.
- Takahashi, T., Sweeney, C., Hales, B., Chipman, D., Newberger, T., Goddard, J., Iannuzzi, R., and S. Sutherland. 2012. "The changing carbon cycle in the Southern Ocean." *Oceanography* 25 (3): 26–37. <https://doi.org/10.5670/oceanog.2012.71>.
- Tamsitt, V., Drake, H. F., Morrison, A. K., Talley, L. D., Dufour, C. O., Gray, A. R., Griffies, S. M., Mazloff, M. R., Sarmiento, J. L., Wang, J., and W. Weijer. 2017. "Spiraling pathways of global deep waters to the surface of the Southern Ocean." *Nature Communications* 8 (1): 172. <https://doi.org/10.1038/s41467-017-00197-0>.

- Tebo, B. M., Bargar, J. R., Clement, B. G., Dick, G. J., Murray, K. J., Parker, D., Verity, R., and S. M. Webb. 2004. "Biogenic manganese oxides: Properties and mechanisms of formation." *Annual Review of Earth and Planetary Sciences* 32 (1): 287–328. <https://doi.org/10.1146/annurev.earth.32.101802.120213>.
- Tebo, B. M., Clement, B. G., and G. J. Dick. 2007. "Biotransformations of Manganese." p. 1223–1238. In C. J. Hurst, R. L. Crawford, J. L. Garland, D. A. Lipson, A. L. Mills, and L. D. Stetzenbach (ed.), *Manual of environmental microbiology*, 3rd ed. ASM Press, Washington, DC.
- Thuróczy, C-E, Alderkamp, A-C, Laan, P., Gerringa, L. J.A., Mills, M. M., Van Dijken, G. L., De Baar, H. J.W., and K. R. Arrigo. 2012. "Key role of organic complexation of iron in sustaining phytoplankton blooms in the Pine Island and Amundsen polynyas (Southern Ocean)." *Deep Sea Research Part II: Topical Studies in Oceanography* 71–76 (September): 49–60. <https://doi.org/10.1016/j.dsr2.2012.03.009>.
- Tonkin, J. W., Balistrieri, L. S., and J. W. Murray. 2004. "Modeling sorption of divalent metal cations on hydrous manganese oxide using the diffuse double layer model." *Applied Geochemistry* 19 (1): 29–53. [https://doi.org/10.1016/S0883-2927\(03\)00115-X](https://doi.org/10.1016/S0883-2927(03)00115-X).
- Trouwborst, R. E. 2006. "Soluble Mn(III) in Suboxic Zones." *Science* 313 (5795): 1955–57. <https://doi.org/10.1126/science.1132876>.
- Turekian, K. K. 1977. The fate of metals in the oceans, *Geochim. Cosmochim. Acta*, 41, 1139–1144, doi:10.1016/0016-7037(77)90109-0.
- Turner, J. T. 2002. "Zooplankton faecal pellets, marine snow and sinking phytoplankton blooms." *Aquatic Microbial Ecology* 27: 57–102. <https://doi.org/10.3354/ame027057>.
- Twining, B. S., and S. B. Baines. 2013. "The Trace Metal Composition of Marine Phytoplankton." *Annual Review of Marine Science* 5 (1): 191–215. <https://doi.org/10.1146/annurev-marine-121211-172322>.
- Twining, B. S., Baines, S. B., and N. S. Fisher. 2004. "Element stoichiometries of individual plankton cells collected during the Southern Ocean Iron Experiment (SOFEX)." *Limnology and Oceanography* 49 (6): 2115–2128.
- Twining, B. S., Baines, S. B., Vogt, S., and D. M., Nelson. 2012. Role of diatoms in nickel biogeochemistry in the ocean. *Global biogeochemical cycles*, 26(4).
- Twining, B. S., Nuñez-Milland, D., Vogt, S., Johnson, R. S., and P. N. Sedwick. 2010. "Variations in *Synechococcus* cell quotas of phosphorus, sulfur, manganese, iron, nickel, and zinc within mesoscale eddies in the Sargasso Sea." *Limnology and Oceanography* 55 (2): 492–506. <https://doi.org/10.4319/lo.2010.55.2.0492>.
- Twining, B. S., Rauschenberg, S., Morton, P. L., and S. Vogt. 2015. "Metal contents of phytoplankton and labile particulate material in the North Atlantic Ocean." *Progress in Oceanography* 137 (September): 261–83. <https://doi.org/10.1016/j.pocean.2015.07.001>.
- van der Merwe, P., Wuttig, K., Holmes, T., Trull, T. W., Chase, Z., Townsend, A. T., Goemann, K., and A. R. Bowie. 2019. "High lability Fe particles sourced from glacial erosion can meet previously unaccounted biological demand: Heard Island, Southern Ocean." *Frontiers in Marine Science* 6 (June): 332. <https://doi.org/10.3389/fmars.2019.00332>.
- Vives, C. R., Schallenberg, C., Strutton, P. G., and K. J. Westwood. 2022. "Iron and light limitation of phytoplankton growth off East Antarctica." *Journal of Marine Systems*; 103774, ISSN 0924-7963. <http://www.sciencedirect.com/science/article/pii/S0924796322000756>.
- Wagener, T., Guieu, C., Losno, R., Bonnet, S., and N. Mahowald. 2008. "Revisiting atmospheric dust export to the Southern Hemisphere Ocean: Biogeochemical implications." *Global Biogeochemical Cycles* 22 (2): n/a-n/a. <https://doi.org/10.1029/2007GB002984>.
- Waite, A. M., Safi, K. A., Hall, J. A., and S. D. Nodder. 2000. "Mass sedimentation of picoplankton embedded in organic aggregates." *Limnology and Oceanography* 45 (1): 87–97. <https://doi.org/10.4319/lo.2000.45.1.0087>.
- Walker, J. C.G., and P. Brimblecombe. 1985. "Iron and sulfur in the pre-biologic ocean." *Precambrian Research* 28 (3–4): 205–22. [https://doi.org/10.1016/0301-9268\(85\)90031-2](https://doi.org/10.1016/0301-9268(85)90031-2).
- Wedepohl, K Hans. 1995. "The Composition of the Continental Crust," *Geochimica et Cosmochimica Acta*, 59, 1217–1232.
- Westerlund, S., and P. Öhman. 1991. "Iron in the water column of the Weddell Sea." *Marine Chemistry* 35 (1–4): 199–217. [https://doi.org/10.1016/S0304-4203\(09\)90018-4](https://doi.org/10.1016/S0304-4203(09)90018-4).

- Westwood, K. J., Griffiths, F. B., Webb, J. P., and S. W. Wright. 2011. "Primary production in the Sub-Antarctic and Polar Frontal Zones south of Tasmania, Australia; SAZ-Sense Survey, 2007." *Deep Sea Research Part II: Topical Studies in Oceanography* 58 (21–22): 2162–78. <https://doi.org/10.1016/j.dsr2.2011.05.017>.
- Whitby, H., Planquette, H., Cassar, N., Bucciarelli, E., Osburn, C. L., Janssen, D. J., ... and G. Sarthou. 2020. A call for refining the role of humic-like substances in the oceanic iron cycle. *Scientific reports*, 10(1), 1-12.
- Whittaker, J.W. 2003. "The irony of manganese superoxide dismutase." *Biochemical Society Transactions* 31 (6): 1318–21. <https://doi.org/10.1042/bst0311318>.
- Whitworth, T., Orsi, A. H., Kim, S.-J., Nowlin, W. D., and R. A. Locarnini. 1985. "Water masses and mixing near the Antarctic Slope Front." In *Antarctic Research Series*, edited by Stanley S. Jacobs and Ray F. Weiss, 1–27. Washington, D. C.: American Geophysical Union. <https://doi.org/10.1029/AR075p0001>.
- Widdel, F., Schnell, S., Heising, S., Ehrenreich, A., Assmus, B., and B. Schink. 1993. "Ferrous iron oxidation by anoxygenic phototrophic bacteria." *Nature* 362 (6423): 834–36. <https://doi.org/10.1038/362834a0>.
- Wijk, Esmee M. van, and Stephen R. Rintoul. 2014. "Freshening drives contraction of Antarctic Bottom Water in the Australian Antarctic Basin." *Geophysical Research Letters* 41 (5): 1657–64. <https://doi.org/10.1002/2013GL058921>.
- Wintjens, R., Noël, C., May, A. C.W., Gerbod, D., Dufernez, F., Capron, M., Viscogliosi, E., and M. Rooman. 2004. "Specificity and phenetic relationships of iron- and manganese-containing superoxide dismutases on the basis of structure and sequence comparisons." *Journal of Biological Chemistry* 279 (10): 9248–54. <https://doi.org/10.1074/jbc.M312329200>.
- Wolfe-Simon, F., Starovoytov, V., Reinfelder, J. R., Schofield, O., and P. G. Falkowski. 2006. "Localization and role of manganese superoxide dismutase in a marine diatom." *PLANT PHYSIOLOGY* 142 (4): 1701–9. <https://doi.org/10.1104/pp.106.088963>.
- Wu, M., McCain, J. S. P., Rowland, E., Middag, R., Sandgren, M., Allen, A. E., and E. M. Bertrand. 2019. "Manganese and iron deficiency in Southern Ocean *Phaeocystis antarctica* populations revealed through taxon-specific protein indicators." *Nature Communications* 10 (1): 3582. <https://doi.org/10.1038/s41467-019-11426-z>.
- Wuttig, K., Wagener, T., Bressac, M., Dammschäuser, A., Streu, P., Guieu, C., and P. L. Croot. 2013. "Impacts of dust deposition on dissolved trace metal concentrations (Mn, Al and Fe) during a mesocosm experiment." *Biogeosciences* 10 (4): 2583–2600. <https://doi.org/10.5194/bg-10-2583-2013>.
- Wuttig, Kathrin. 2013. "Manganese biogeochemistry in the sunlit ocean." PhD Thesis, Universitätsbibliothek Kiel.
- Wuttig, K., Heller, M. I., and P. L. Croot. 2013a. "Reactivity of inorganic Mn and Mn Desferrioxamine B with O₂, O₂⁻, and H₂O₂ in Seawater." *Environmental Science & Technology*, August, 130822151350003. <https://doi.org/10.1021/es4016603>.
- Wuttig, K., Townsend, A. T., van der Merwe, Pier., Gault-Ringold, M., Holmes, T., Schallenberg, C., Latour, P., Tonnard, M., Rijkenberg, M., J., A., Lannuzel, D., and A. R. Bowie. 2019. "Critical evaluation of a SeaFAST system for the analysis of trace metals in marine samples." *Talanta* 197 (May): 653–68. <https://doi.org/10.1016/j.talanta.2019.01.047>.
- Xu, G., and Y. Gao. 2014. "Atmospheric trace elements in aerosols observed over the Southern Ocean and coastal East Antarctica." *Polar Research* 33 (1): 23973. <https://doi.org/10.3402/polar.v33.23973>.
- Zhao, W., Guo, Q., and J. Zhao. 2007. "A membrane-associated Mn-superoxide dismutase protects the photosynthetic apparatus and nitrogenase from oxidative damage in the cyanobacterium *Anabaena* Sp. PCC 7120." *Plant and Cell Physiology* 48 (4): 563–72. <https://doi.org/10.1093/pcp/pcm025>.